The synthesis of cementitious compounds in molten salts

Rashed Ahmad Sheikh

Department of Chemical Engineering
University College London

February, 2016

A thesis submitted to the University of London for the degree of
Doctor of Philosophy

EPSRC
Engineering and Physical Sciences
Research Council

UCL

Declaration

"I can confirm the work presented in this thesis is my own. Where information has been derived from other sources, this has been indicated."

Rashed Ahmad Sheikh
Department of Chemical Engineering
University College London

Abstract

This thesis describes an investigation into the synthesis of cementitious compounds in molten salts. These compounds are produced in energy-intensive industries (EIIs), such as the cement process, and are responsible for emitting significant quantities of carbon dioxide (CO_2) emissions. Molten salt synthesis (MSS) involves dissolving compounds in a molten salt and reacting in solution. If the MSS of cementitious compounds can occur at lower temperatures than EIIs, this could lead to fewer quantities of CO_2 emissions. The cementitious compounds selected for this investigation were dicalcium silicate (β-Ca_2SiO_4), tricalcium silicate (Ca_3SiO_5), disodium metasilicate (α-Na_2SiO_3), tetrasodium orthosilicate (β-Na_4SiO_4) and the salt selected was sodium chloride (NaCl).

Initally, the dissolution behaviour of the reactants; silicon dioxide (SiO_2), calcium carbonate ($CaCO_3$) and sodium carbonate (Na_2CO_3) were investigated in NaCl, using calorimetry, potentiometry, X-ray diffraction (XRD) and Scanning Electron Microscopy (SEM). The XRD and SEM data suggested Na_2CO_3 and $CaCO_3$ decomposed to CO_2, calcium oxide (CaO) and sodium oxide (Na_2O), and SiO_2 only dissolved with a limited solubility. The calorimetric data suggested the heat of mixing (ΔH_{mix}) for Na_2CO_3 in molten NaCl illustrated a maximum positive contribution of ~2 kJ mol^{-1}, and its phase diagram illustrated a eutectic point at 638°C, 47 mol% Na_2CO_3. The potentiometric data suggested the solubility products (K_{sp}) for Na_2O and CaO in NaCl were -log 1.58 and -log 1.1, demonstrating reasonably high solubilities in comparison to other melts. This information suggests the MSS of cementitious compounds could be possible in industry.

Then, the MSS of cementitious compounds were investigated using SEM and XRD and were depicted on predominance diagrams. The XRD and SEM data suggested β-Ca_2SiO_4 and α-Na_2SiO_3 can be produced, however Ca_3SiO_5 requires higher temperatures (>1100ºC). This suggests other cementitious compounds can be produced in this manner, thus paving the way for producing complete products, such as cement.

Contents

List of figures

Page

List of tables

Nomenclature

Symbol	Description.	Symbol	Description.
MSS	Molten salt synthesis.	AAS	Atomic adsorption spectroscopy.
ΔC_p	Heat capacity.	PL	Photoluminescence.
ΔH_{mix}	Heat of mixing.	UV-vis	UV-visible spectroscopy.
K_{sp}	Solubility product.	TG	Thermogravimeric analysis.
K_d	Dissociation constant.	CALPHAD	CALculation of PHAse Diagrams.
K_f	Formation constant.	BSE	Back-scatter electrons.
EDS	Energy-dispersive X-ray spectroscopy.	SEI	Secondary electron imaging.
XRD	X-ray diffraction.	NIST	National Institute of Standards and Technology.
SEM	Scanning electron microscopy.	Kα1	Radiation type.
GHG	Greenhouse gases.	Kα2	
EII	Energy-intensive industries.	PM	Particulate matter.
ΔV_d	Decomposition potential.	CKD	Cement kiln dust.
CV	Cyclic Voltammatery.	CCS	Carbon capture storage.
ISE	Ion-selective electrode.	HPGRS	High pressure roller mills.
ΔG_f	Gibbs free energy of formation.	VRM	Vertical roller mills.
ΔH_f	Enthalpy of formation.	DSC	Differential scanning calorimetery.
ΔG_{mix}	Gibbs free energies of mixing.	ARE	Aircraft Reactor Experiment.
PM	Particulate Matter.	MSRE	Molten Salt Experimental Reactor.
CKD	Cement Kiln Dust.	AEC	United States Atmoic Energy Commission.
ΔG°	Gibbs free energy of dissociation.	EDS	Energy-dispersive X-ray spectroscopy.
SEC	Specific energy consumption.	MCFC	Molten carbonate fuel cells.
UNFCCC	United Nations Convention on Climate Change.	AES	Atomic emission spectroscopy.
EU ETS	EU emission trading scheme.	FFC	Fray, Farthing and Chen.
SAM	Sequential Addition Method.	ICDD	The International Centre for Diffraction Data database.
CCGT	Combined Cycle gas Turbine.	IR	Infrared (spectroscopy).
WHRSG	Waste Heat Recovery Steam Generator.	LSF	Lime saturation factor.
Γ	Wavelength.	TEM	Transmission electron microscopy.
CCR	Calcium carbide residues.	JI	Joint Implementation Scheme.
CoP	Conference of Parties.	IGA	Integranular corrosion.
Θ	Scattering angle.	YSZ	Yttria stabilized zirconia.
UKERC	United Kingdom Energy Research Council.	CO_2	Carbon dioxide.
CDM	Clean Development Mechanism.	$[O^{2-}]$	Oxide ion activity.
CRCT	Centre for Research in Computational Thermochemistry.	ΔH_{fusion}	Enthalpy of fusion.
ΔH	Enthalpy	ΔS	Entropy.

Table N1: Nomenclature.

Units	Description
g mol^{-1}	Grammes per mole.
W	Power.
kg mol^{-1}	Kilogrammes per mole.
wt%	Weight percent.
ppm	Parts per million.
Gt	Gigatonnes.
mol%	Mole percent.
ºC	Degrees centigrade.
Mt	Metric tonnes.
kg tonne^{-1}	Kilogrammes per tonne.
mm	Millimetre.
M	Metre.
V	Voltage.
ºC min^{-1}	Degrees centigrade per minute.
kWh tonne^{-1}	Kilowatt hour per tonne.
kWh	Kilowatt hour.
torr	Torr (~133.3 Pa).
µm	Micrometre (10^{-6}).
nm	Nanometre (10^{-9}).
Z	Atomic number.
ρ	Density.
kV	Kilovolts.
E_o	Incident beam energy.
A	Atomic weight.
mW	Megawatts.
Ω	Resistivity.
atm	Atmosphere.
J mol^{-1} C^{-1}	Joule per mole centigrade.
cm^{2}	Surface area.
V s^{-1}	Volts per second.
λ	Wavelength.
eV	Electron volts.
Wh kg^{-1}	Watts hour per kilogram.
MJ kg^{-1}	Mega joules per kilogram.

Table N2: Units.

Chapter 1

Background & thesis structure

1.1 Global warming and CO_2 emissions

The concept of the molten salt synthesis (MSS) of cementitious compounds initiated in response to the phenomenon of global warming. It is well-known the global average surface temperature of the earth has risen by ~0.8ºC during the 20th century (figure 1.1) [1]. This has been attributed to an increase in quantities of greenhouse gases (GHG's) in the atmosphere, from anthropogenic sources (such as fossil fuels) and changing land use (such as deforestation) [2]. This temperature rise is linked to major catastrophes, such as hurricanes, heat waves, floods, droughts (in localised regions), evaporation of lakes, rising sea levels and the melting of ice glaciers [1-2]. It is also predicted this temperature rise will continue up to ~5.8ºC this century, which is greater than the official tipping point of ~2ºC, which scientists believe climate change becomes impossible to mitigate [3]. This makes global warming a major environmental problem.

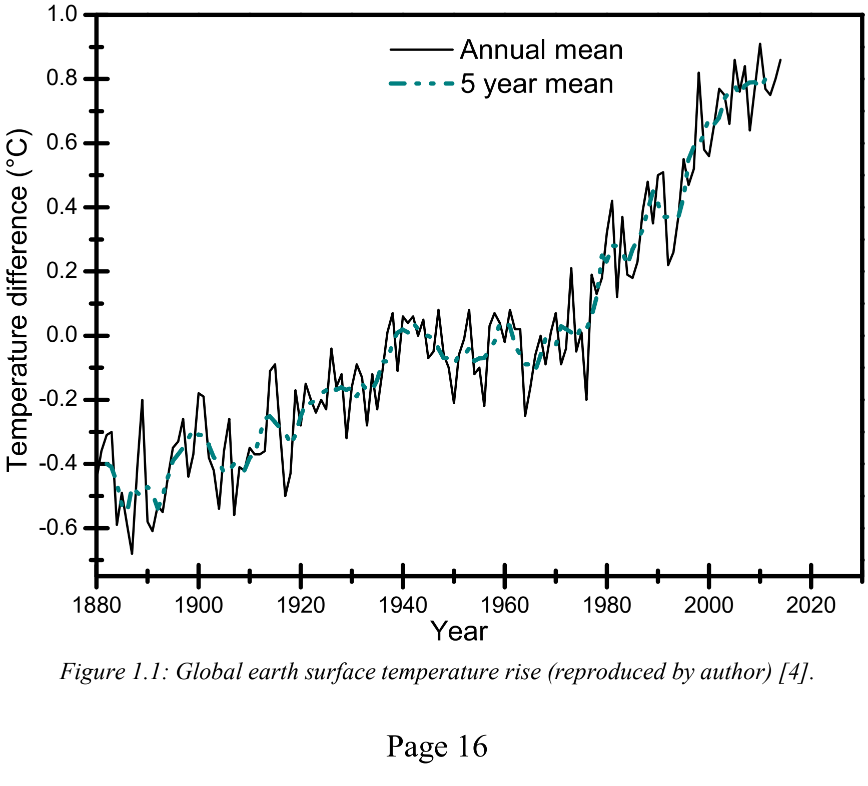

Figure 1.1: Global earth surface temperature rise (reproduced by author) [4].

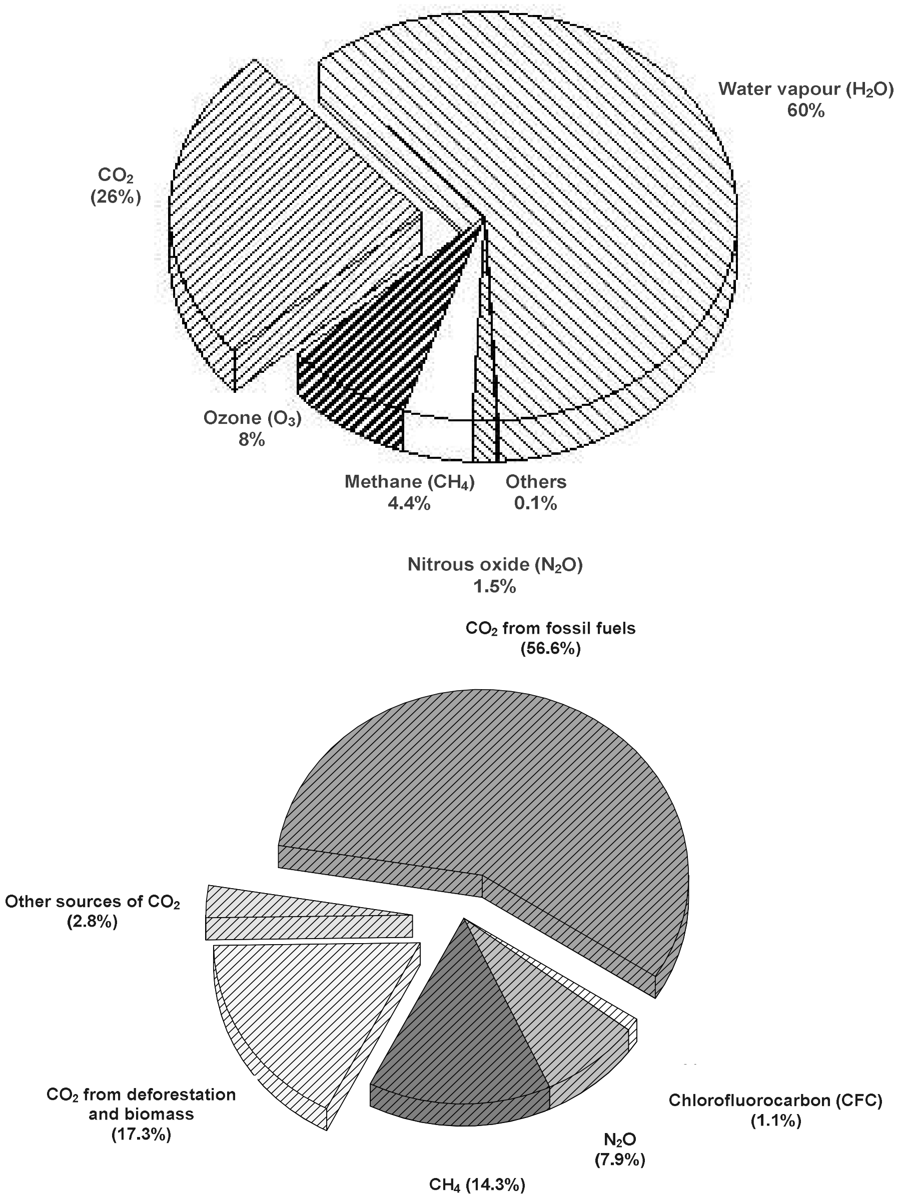

Figure 1.2: GHG's (top) and GHG's from anthropogenic sources (bottom) in the 21st century (in wt%) (reproduced by author) [5].

There are 24 GHG's in the atmosphere that contribute towards global warming (figure 1.2) [2]. The main anthropogenic GHG is CO_2 and its concentration has increased by ~10 Gt (~1.5 times) between the years 1990-2011, and its concentration in the atmosphere is rising at ~2 ppm per annum [2]. The main anthropogenic sources of CO_2 are fossil fuels (~66 wt%) from the manufacturing, power generation and transportation sectors and deforestation (33 wt%), therefore tackling these sectors is likely to reduce CO_2 emissions, and therefore global warming [6].

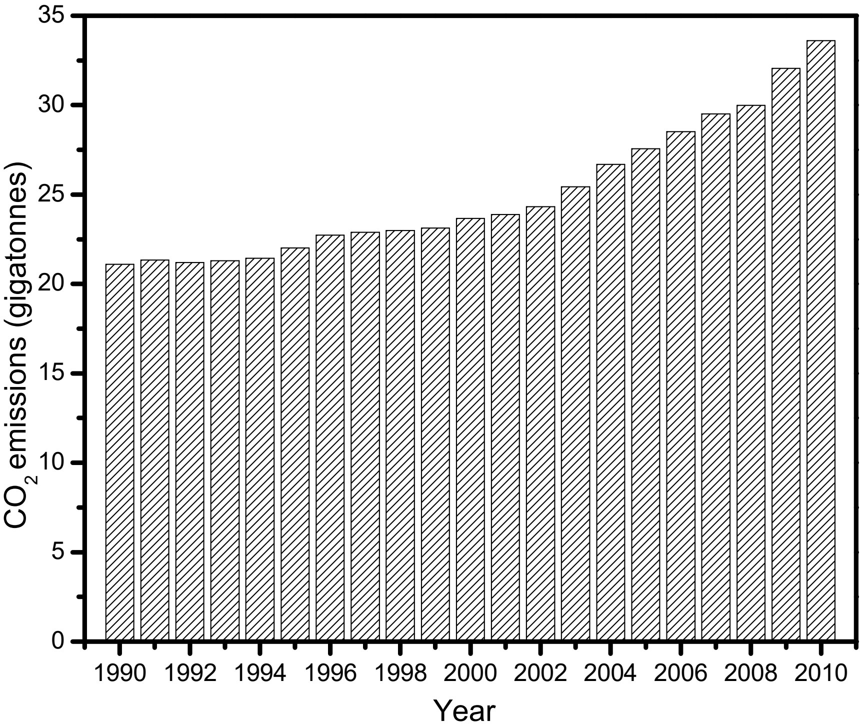

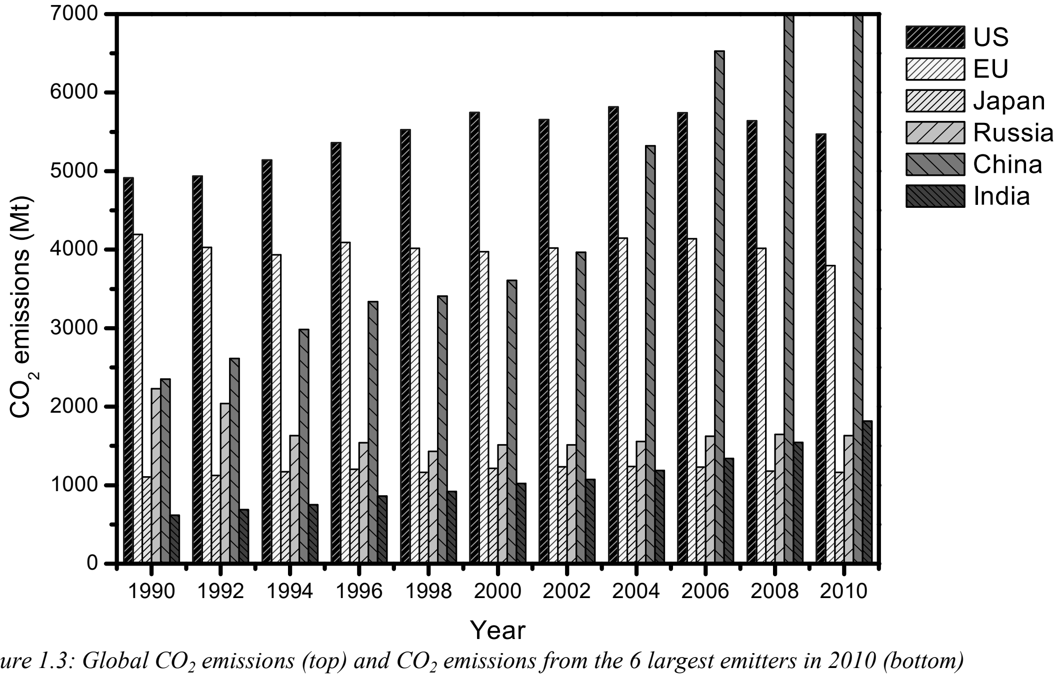

Figure 1.3: Global CO_2 emissions (top) and CO_2 emissions from the 6 largest emitters in 2010 (bottom) (reproduced by author) [5-6].

However tackling CO_2 emissions is not an easy task which can vary across the globe. This can be attributed to different population sizes, the effects of regional financial circumstances (such as recessions) and regional strategies used by governments to combat climate change (figure 1.3), for example in 2000, CO_2 emissions from the US increased (up to ~5500 Mt), probably due to an increase in natural gas prices. The gas prices caused an increase in the usage of coal that year instead of natural gas, therefore emitting more CO_2. In 2009, CO_2 emissions from Japan decreased (down to ~1100

Mt) probably due to the effects of a recession which caused its industrial processes to produce significant quantities of materials. CO_2 emissions then rose due to the increased usage of coal energy after the after the Fukushima incident. In 2002, CO_2 emissions from China increased to ~5300 Mt, probably due to a reduction in electricity prices, which caused customers to use large amounts of electricity. CO_2 emissions from the EU increased to ~4000 Mt in 1996 and 2004, probably due an increase in the usage of fossil fuel. CO_2 emissions from Russia decreased to ~1400 Mt in 2000, after increasing environmental legislation caused an increase in environmental expenditure. CO_2 emissions from India increased to ~1500 Mt probably to an increase in the usage of coal [5-8]. The overall consensus is that although regional differences vary, global CO_2 emissions are still rising and requires addressing.

1.2 Cement process

One of the main sources of CO_2 emissions are energy-intensive industries (EIIs). These emit large quantities of CO_2 directly or indirectly (through electricity usage) [9]. One example of an EII is the cement process, which accounts for 5 wt% of CO_2 emissions [9-11]. In the cement process, ~40 wt% of emissions arise from burning fossil fuels, ~50 wt% from the decomposition of limestone and ~5-10 wt% from electricity usage [11-12]. It has been estimated that the cement process emits between 0.65-0.92 kg $tonne^{-1}$ of CO_2 annually, and this figure is projected to rise at 4.7% per annum (figure 1.4) [11] [13].

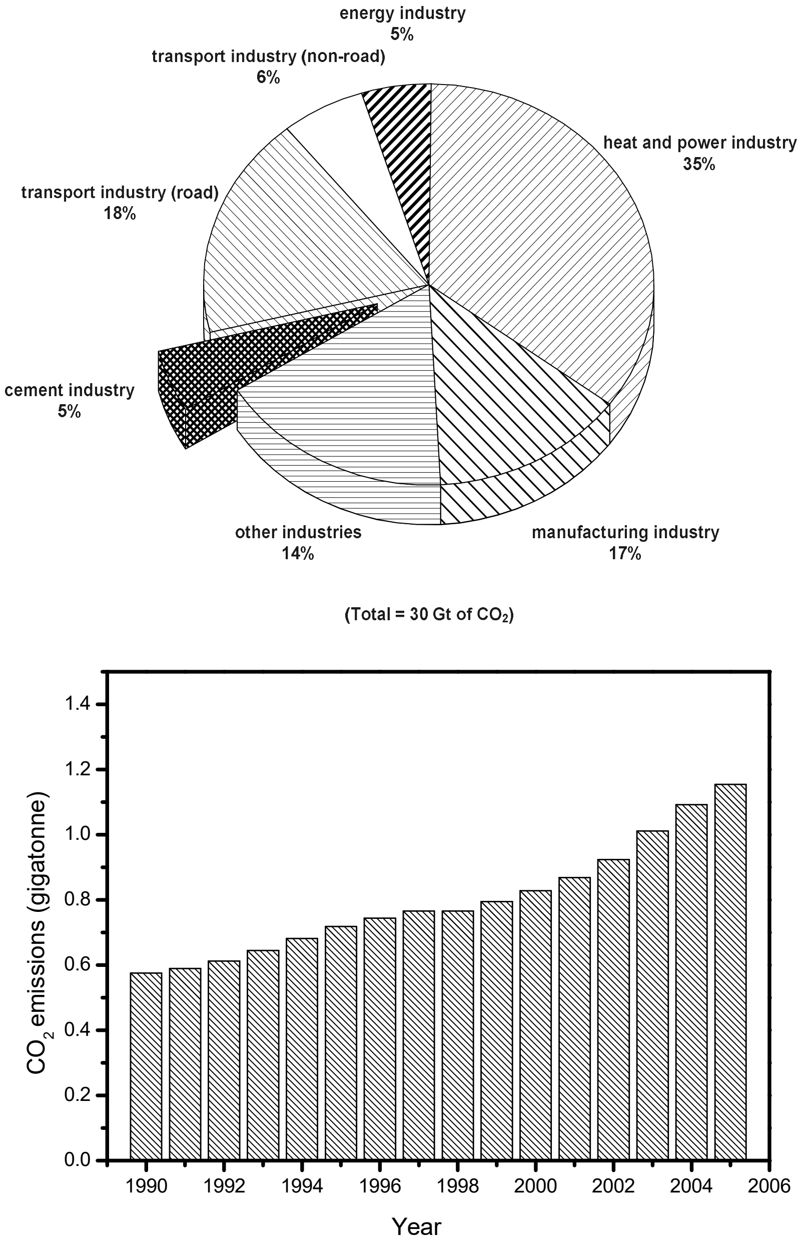

Figure 1.4 Global annual contributions to CO_2 emissions from industrial sectors (top) and the cement process (bottom) (reproduced by author) [5] [13].

To understand why the cement process is a significant contributor towards CO_2 emissions, it is important to understand cement production. Cement contains five phases (including gypsum) which provide different characteristics towards the final product (table 1.1) [14-15]. β-Ca_2SiO_4 contributes towards slow hardening and strength, β-Ca_3SiO_5 contributes towards rapid hardening and early strength, $Ca_3Al_2O_6$ contributes towards slow hardening and gives the final product its characteristic grey colour and $Ca_2(Al, Fe)_2O_5$ contributes towards quick setting and hardening, which is retarded by gypsum. Cement may also contain several minor constituents such as sulphur oxide (SO_3), Na_2O and potassium oxide (K_2O), which appear in small quantities [14-15]. The final cement product is often described by the quaternary phase system; $CaO\text{-}SiO_2\text{-}Al_2O_3\text{-}Fe_2O_3$ [14-15].

Composition (mol%)	Compound/Solid solution	Name	Compound name	CCN [1]
45-75	$\beta\text{-}Ca_3SiO_5$	Alite	Tricalcium silicate	C_3S
7-32	$\beta\text{-}Ca_2SiO_4$	Belite	Dicalcium silicate	C_2S
0-13	$Ca_3Al_2O_6$	Aluminate	Tricalcium aluminate	C_3A
0-18	$Ca_2(Al, Fe)_2O_5$ / $Ca_2(Al, Fe)_2O_{12}$	Ferrite	Calcium alumino ferrites	C_4AF / C_6A_2F
2-10	$CaSO_4 \cdot 2H_2O$	-	Gypsum	-

Table 1.1: Cement composition [14].

Cement production requires excavating limestone and clay from quarries and transporting them to a cement manufacturing site. These are then crushed and grinded in mills to reduce their particle sizes (to ~100 mm in diameter) and blended with additives (such as iron, bauxite, quartzite and/or silica) in silos to produce a “raw meal” [16]. This allows for a specific composition and consistency to be achieved before being sent to the pyroprocessing stage. The pyroprocessing stage contains many different designs according to the type of cement plant which vary according to the characteristics of the raw meal (table 1.2) [14-17].

Cement process	Raw meal type	Moisture content (wt%)	Cement kiln type
Wet	Slurry	28-43	Long
Semi-wet (preheater)	Filter cake	16-21	Long/Leopol
Semi-dry (preheater)	Pellets	10-12	Long/Leopol
Dry	Dry powder	0.5-1	Long
Dry (preheater)	Dry powder	0.5-1	Short
Dry (precalciners and preheater)	Dry powder	0.5-1	Short
Shaft	Pellets	-	Shaft

Table 1.2: Pyroprocessing stage designs and raw meal characteristics [14-17].

The wet process involves grinding and mixing the raw meal with water to produce slurry (with a moisture content of ~40 wt%) [14-17]. This allows for the reactants to be easily transported through the kiln, prevents blow back by combustion gases and

---

[1] CCN = Cement Chemist Notation

$C = CaO$, $S = SiO_2$, $A = Al_2O_3$ $F = Fe_2O_3$

allows for easier grinding of the reactants. The slurry is then sent to a drier to reduce the moisture content, or to a long cement kiln where the moisture is driven off and cement reactions occur [14-17].

The dry process involves grinding the raw meal to produce a powder (with particle sizes of ~90 μm), which is sent to a precalciner and/or preheater or long cement kiln where cement reactions occur [14-17]. [2] The preheater/precalciners allow ~40% of the raw meal to decompose before the cement kiln [14]. This allows for a reduction in energy consumption and kiln length.

The semi-dry and semi-wet process is a combination of the wet and dry process. The semi-dry process involves mixing and grinding the raw meal to produce pellets (with a moisture content of ~11 wt%) [14-15]. The wet pellets are then sent to a preheater or long cement kiln to drive off the moisture [15]. The semi-wet process involves mixing and grinding the raw meal with water to produce a filter cake (with a moisture content of ~18 wt%) [24]. The wet filter cake is then sent to either a preheater or filter cake drier before the cement kiln [14-17].

The cement kiln is a cylindrical steel tube, inclined between 1-4° to the horizontal (in most cases) [15]. The cement kiln rotates at ~3-5 revolutions per minute upon its axis, causing the reactants to travel from the upper to the lower end [14]. The lower end houses a controlled flame at temperatures exceeding ~1450ºC, which causes the reactants to melt and fuse together to produce cement clinker nodules (table 1.3) [30]. Initially limestone and clay decompose to SiO_2, aluminium(III) oxide (Al_2O_3), calcium oxide (CaO) and iron(III) oxide (Fe_2O_3) (reactions 1-4). Then these compounds react to form the main phases of cement clinker; β-Ca_2SiO_4, Ca_2(Al, Fe)$_2O_5$, and/or Ca_2(Al, Fe)$_2O_{12}$, $Ca_3Al_2O_6$) (reactions 5-8). Then β-Ca_2SiO_4 and CaO react in a secondary reaction to form Ca_3SiO_5 (reactions 9). Ca_6 (Al, Fe)$_2$ $O_{12,}$ and/or Ca_2(Al, Fe)$_2O_5$ and α-Fe_2O_3 form a liquid flux (20-30 wt% of the cement mixture). This liquid flux causes the products to aggregate into cement clinker nodules (with a diameter 1-10 mm) and helps to promote reaction kinetics [14-17].

---

[2] A preheater is a series of chambers with moving grates or gas cyclones.
A precalciner is a combustion chamber within a preheater system.

Number	Cement reactions	ΔH_R (kJ mol^{-1})	
		25 (ºC)	**1450 (ºC)**
1	$CaCO_3$ (s) $\rightarrow$ CaO (s) + CO_2 (g)	178	113
	calcium carbonate → calcium oxide + carbon dioxide		
2	$Al_2Si_4O_{10}(OH)_2$ (s) $\rightarrow$ α-Al_2O_3 (s) + $4SiO_2$ (s) + H_2O (g)	82.0	90.0
	aluminum silicate di-hydroxide (pyrophyllite) → aluminum(III) oxide + silicon dioxide + water		
3	$Al_2Si_2O_5(OH)_4$ (s) $\rightarrow$ α-Al_2O_3 (s) + $2SiO_2$ (s) + $2H_2O$ (g)	120	25.0
	aluminum silicate tetra-hydroxide (kaolinite) → aluminum(III) oxide + silicon dioxide + water		
4	$2FeO.OH$ (s) $\rightarrow$ α-Fe_2O_3 + H_2O (g)	55.2	68.0
	iron(III) hydroxide oxide → iron(III) oxide + water		
5	$2CaO$ (s) + SiO_2 (s) $\rightarrow$ β-Ca_2SiO_4 (s)	-124	-111
	calcium carbonate + silicon dioxide → dicalcium metasilicate (C_2S)		
6	$3CaO$ (s) + α-Al_2O_3 (s) $\rightarrow$ $Ca_3Al_2O_6$ (s)	-16.0	-19.0
	calcium carbonate + aluminum(III) oxide → tricalcium aluminate (C_3A)		
7	$6CaO$ (s) + 2α-Al_2O_3 (s) + α-Fe_2O_3 (s) $\rightarrow$ $Ca_6(Al, Fe)_2O_{12}$ (s)	-157	(not available) [2]
	calcium carbonate + aluminum(III) oxide + iron(III) oxide → hexacalcium aluminoferrite (C_6A_2F)		
8	$4CaO$ (s) + α-Al_2O_3 (s) + α-Fe_2O_3 (s) $\rightarrow$ $Ca_2(Al, Fe)_2O_5$ (s)	-105	-723[3]
	calcium carbonate + aluminum(III) oxide + iron(III) oxide → tetracalcium aluminoferrite (C_4AF)		
9	$3CaO$ (s) + SiO_2 (s) $\rightarrow$ Ca_3SiO_5 (s)	-155	-137
	calcium carbonate + silicon dioxide → tricalcium silicate (C_3S)		

Table 1.3: ΔH_R of cement reactions for 1 mol of cement (HSC-Chemistry 6.1) [15] [18-19].

The total residence time in the cement kiln is ~3 hours, depending upon the type of process. During this period, pollutants are driven off from the reactants/products in gaseous form or as particulate matter (PM). The main pollutants in cement kilns are nitrogen oxides (NOx), sulphur dioxide (SO_2), cement kiln dust (CKD) and CO_2 [33]. The cement clinker nodules are then cooled (to ~170ºC) and solidified in a cooler or cooling zone attached to the cement kiln [14]. The most common coolers are grate coolers, which are horizontal perforated grates with cold air blown from underneath [35]. The clinker nodules are then sent to mills where their particle sizes are reduced (to ~5 µm) [14-15]. The most common mills are ball mills which are steel tubes divided into separate chambers, rotating upon a horizontal axis. The final cement product is then mixed with additives, such as gypsum ($CaSO_4$. $2H_2O$). $CaCO_3$ or

---

[3] Data not available in HSC Chemistry 6.1

anhydrite ($CaSO_4$) (up to ~ 2-8 wt%) to achieve the desirable hydraulic properties of cement [15].

The largest energy-intensive step in the cement process is the decomposition of $CaCO_3$ in an endothermic reaction, which is quoted at ~1.76 MJ kg^{-1} at 25°C [39]. The theoretical energy requirement (TER) ranges between 1.57-1.80 MJ kg^{-1} for the wet and dry process respectively [17] [20-22]. The specific energy consumption (SEC) ranges between 3-6 MJ kg^{-1} depending upon the design of the cement process [17]. The average values for the SEC is quoted at ~3.40 GJ tonne^{-1} for the dry process and ~5.29 GJ tonne^{-1} for the wet process [17]. The electrical SEC ranges between ~75-80 kWh tonne^{-1}, however values have been reported up to ~110-120 kWh tonne^{-1} in some cases (table 1.4) [20-22].

Cement process	**SEC**	
	Thermal (MJ kg^{-1})	**Electrical (kWh tonne^{-1})**
Wet	5-7.5	25
Semi-wet (with preheater)	3.4-4	30
Semi-dry (with preheater)	3.2-3.9	30
Dry	3.6-4.5	25
Dry (with preheater)	3.1-3.5	22
Dry (with preheater and precalciner)	3.1-3.2	22
Shaft	3.7-6.6	30

Table 1.4: Energy consumption of the cement processes [15] [20-22].

The energy consumption for the cement process is considered to be a significant source of CO_2 emissions. This is mainly attributed to the burning of fossil fuels to heat the kiln, heat losses by conduction, convection and radiation (due to the design of the kiln) and electricity used to grind the final cement product [15]. These areas can be improved which could lead to significant benefits in terms of CO_2 emissions.

1.3 Strategies to reduce CO_2 emissions

There have been many strategies to reduce CO_2 emissions, which are divided into adaptation and mitigation. Mitigation strategies are actions to reduce CO_2 emissions or and/or enhance its removal from the atmosphere by switching to low-carbon energy sources (such as wind solar and geothermal) and expanding forests to remove emissions from the atmosphere (carbon sinks). Adaptation strategies are actions to offset the effects of global warming, which involve preparing coasts and river basins for rising sea levels, preparing farms for changing weather conditions and tackling the spread of diseases. The general consensus are that both mitigation and adaptation strategies should be pursued simultaneously as even if CO_2 emissions are stabilized, the effects of global warming will continue for many years [23].

There have been many initiatives to reduce CO_2 emissions. One well-known initiative is the United Nations Framework Convention on Climate Change (UNFCCC) treaty, created by the Intergovernmental Panel on Climate Change (IPCC) [24-26]. This treaty provided a framework for negotiating further international treaties and was further developed during Conference Parties (CoP) meetings [24-26]. However no emission targets or enforcement mechanisms were included thus considered non-legally binding [24-26]. [4]

Another initiative was the Kyoto Protocol treaty, which was created in 1997, at the 3rd CoP [27-28]. This treaty represented a shared commitment by 192 countries to reduce their GHG emissions by the implementation of obligatory targets and the mechanisms to tackle climate change, such as Emissions Trading (ET), the Clean Development Mechanism (CDM) and Joint Implementation (JI) scheme [27-28]. Both the CDM and the JI scheme allowed emissions in one country to be reduced by trading emissions reductions in another country. The CDM required the second country to be a developing country and the JI required the second country to be another country that

---

[4] The CoP is a committee of signatories to the treaty, formed to assess the goals of the UNFCC and establish measures for the effects of climate change [27-28].

The IPCC is an intergovernmental body containing 196 countries (to date) to stabilize GHG concentrations in the atmosphere to levels which prevent dangerous anthropogenic interferences with the climate system [27-28].

ratified the Kyoto protocol. This treaty set an average CO_2 emissions target from industrialized countries at 5.2% below the 1990 levels by 2012 and between 6-8% for most countries [50]. Unlike the UNFCCC, the US never ratified the Kyoto Protocol which was also the largest GHG emitter [27-28].

Another initiative was the EU emission trading scheme (EU ETS) which was implemented in 2005, as part of the tradable emission allowances scheme of the Kyoto Protocol [29-31]. This was the world's first international cap and trade system, covering more than 11000 factories, power stations, airlines and other installations in the EU. A limit was set on the total amount of GHG's emitted which was reduced over time until the total emissions fell. Under the cap, companies received or brought emission allowances and traded with one another as required. This scheme was solely responsible for reducing 45% of EU's CO_2 emissions and 40% of total GHG emissions by 2012 [29-31].

Another initiative was the Energy and Climate Policy in 2007, (often denoted the 20-20-20 targets) by the EU [30]. This declaration set out goals to reduce GHG emissions by 20% in comparison with the 1990 base-line by 2020 and satisfy 20% of the EU's energy needs from renewable sources by 2050. The declaration comprised of four pieces of legislation; the reform of the EU ETS, implementation of national targets for emissions not covered by the EU ETS, national targets for renewable energy sources and the introduction of carbon capture and storage (CCS). The reform of the EU ETS included the introduction of a single EU-wide cap on emission allowances to be reduced each year instead of the existing system of national caps [31]. The national targets for emissions not covered by the EU ETS included the housing, agriculture, waste and transport (excluding aviation) sectors and the national targets for renewable energy sources were binding national targets for raising the share of renewable energy by 2020. The introduction of CCS included a legal framework for the environmentally safe use of CCS technologies involves capturing of CO_2 emitted by industrial processes and storing it in underground geological formations. The directive covered all CO_2 storage in geological formations in the EU and laid down requirements over the lifetime of the storage sites [30-31].

Another initiative was the Strategic Energy Technology Plan (SET-Plan) in 2008, by the EU [32]. This set out goals to establish an energy policy for Europe by accelerating the development and deployment of low-carbon technologies, reducing costs of new technologies by co-ordinating research and helping finance projects and promoting research and innovation efforts across Europe by supporting technologies with the greatest impact on the EU's transformation to a low-carbon energy system [30-32].

Apart from initiatives, many technologies have been developed for EIIs to reduce CO_2 emissions, for example for the cement process ball mills have been replaced with vertical roller mills (VRM), high pressure roller mills (HPGRS) or high roller mills (HRM) [60]. These technologies have higher grinding capacities than conventional ball mills [33-34]. [5]

Classifiers and separators are often installed in cement plants to create “grinding circuits” to improve the energy efficiency of the grinding process [33-34]. These circuits can “open” where the feed rate of incoming clinker/raw meal is adjusted to achieve a desired particle size, or “closed” where coarser particles are separated from the finer product and returned for further grinding [33-34].

High activation grinding is a technology at a conceptual level, which is proven to increase the reactivity of blended cements [35]. High activation grinding utilizes vibratory or attrition milling. Current studies suggest activation grinding increases the surface area of the particles and/or mechanically activates compounds within blended cements and hence their reactivity [35]. [6]

Wet cement plants are often converted to dry plants in partial or complete conversions. Complete conversions involve converting the cement kiln and initial milling stage to the dry process and partial conversions involve converting solely the cement kiln [35-37]. Preheaters and precalciners are also installed to increase the residence time before the cement kiln to decompose limestone. The most common preheater is the grate preheater which is being succeeded by gas-suspension preheaters

---

5 VMR’s are rollers rotating at different speeds, HPGRS’s are rollers rotating at similar speeds, and a HRM is a roller in a rotating cylinder [33-34].

6 Vibratory mills are grinding chambers attached to vibrating motors. Attrition mills are grinding chambers attached to rotating chambers [33-34].

(with lower pressure drops). Cement kilns are also lined with refractory bricks or concrete which insulates the steel shell from the high temperatures inside the cement kiln. This protects the cement kiln from corrosive materials, such as alkali sulphates in cement and reduces heat losses from the cement kiln [35-37].

Thermal energy is often recovered by chains hanging from the cement kiln. These chains are exposed to the high temperature gas stream at the kiln exit, which capture thermal energy and recycle it through a series of heat exchangers [15]. The thermal energy is then redirected to the cement kiln, preheaters and precalciners thus lowering the energy consumption. The thermal energy can also be redirected to waste heat recovery steam generators (WHRSG) to drive an electrical generator. The electricity that is produced offsets a portion of electricity purchased from the national grid which reduces running costs [38].

The reaction temperatures in the cement kiln are often reduced using alternative raw materials that offset a portion of the limestone in the raw meal or alternative fuels. These raw materials include calcareous or decarbonated oil shale, steel or granulated blast furnace slag, fly ash or calcium carbide residues (CCR) [39-42]. Reaction temperatures are also lowered by increasing the limestone content in the raw meal (or lime saturation factor (LSF)) [39-40]. This produces cement with a lower Ca_3SiO_5 and higher β-Ca_2SiO_4, often called Belite cements. This has a lower compressive strength and different hydration characteristics than conventional cement thus lower energy consumption. The final cement product is often blended with additives such as blast furnace slag or fly ash to increase the volume of cement. It is estimated up to 25% of the final product can be diluted without changing the application of cement [39-42].

Carbon capture for cement plants is another technology being investigated at a conceptual level [43-47]. The concentration of CO_2 in flue gases in the cement process are higher (14-33 wt%) than coal power plants (12-14 wt%) or gas power plants (4 wt%) making them ideal for carbon capture [43-46]. The captured CO_2 is then compressed for transportation and taken to reservoirs for underground storage, or used in enhanced oil recovery. The various carbon capture technologies include post-combustion capture, oxy-fuel combustion capture and pre-combustion capture. Post-combustion capture technologies remove CO_2 from flue gases during the combustion of fuel using CaO (often referred to as a sorbent), which is referred to as carbonate looping technology [43-47]. Other post-combustion capture technologies use an amine solvent or biologically capture CO_2 using algae in water and involve a cleaning process after any cycles [43-47]. Oxy-fuel combustion technologies use O_2 for combustion instead of air. This produces a flue gas containing CO_2 and H_2O and results in a higher flame temperature. The O_2 is often produced by cryogenic air separation [43-47]. Pre-combustion technologies involve burning fuel in insufficient amounts of O_2 or air/steam to produce a 'synthesis gas" containing carbon monoxide (CO) and water (H_2O) via the water-gas shift reaction [82]. The CO then reacts with steam in a catalytic reactor to produce CO_2 and H_2. The CO_2 is then separated by physical or chemical absorption to produce a fuel that is rich in H_2. The fuel can also be used to generate electricity in a combined-cycle gas turbine (CCGT) [43-48].

1.4 Research objectives and thesis structure

Despite these initiatives, CO_2 emissions are continuing to rise globally and it is important that we continue to investigate new methods of reducing these emissions. One relatively new method of reducing CO_2 emissions is to reduce reaction temperatures in the cement kiln. The cement process requires $1450^{\circ}C$ for the cement reactions to occur and melt the phases; $Ca_6 (Al, Fe)_2 O_{12,}$ and/or $Ca_2(Al, Fe)_2O_5$ and α-Fe_2O_3. These phases create a liquid flux, allowing sufficient contact between the reactant/product particles for cement reactions to occur [12]. However previous solid-state experiments have suggested only $1250^{\circ}C$ is required to obtain Ca_3SiO_5 (the cement phase with the highest temperature requirement) [49]. This suggests if one is able to introduce a liquid phase into the cement kiln at lower reaction temperatures, the energy requirement and CO_2 emissions could be lowered. One method of introducing a liquid phase into the cement kiln is using a molten salt and has led to the synthesis of a variety of compounds (denoted MSS). The concept of MSS is to dissolve the reactants in a molten salt and allow them to react in solution. In this scenario the molten salt behaves as a solvent or as a reactant [50]. Therefore the objective of this thesis is to investigate whether the MSS of cementitious compounds (such as the phases of cement) are possible and whether complete products such as cement can be produced at lower reaction temperatures than industry. The cementitious compounds considered in this thesis will be α-Na_2SiO_3, β-Ca_2SiO_4,

Ca_3SiO_5 and β-Na_4SiO_4, which are found in cement and/or share a similar structural chemistry to the phases of cement. [7]

The structure of this thesis can be described as follows; **Chapter 1: Background & thesis structure** introduced the effects of global warming, CO_2 emissions and strategies to reduce these emissions. It also described the cement process, as an example of an EII that contributes towards CO_2 emissions. **Chapter 2: Literature review** describes **molten salts and their applications** to readers who are unfamiliar with this topic. It then describes previous investigations into the **dissolution of compounds in molten salts** (describing investigations into K_{sp}, ΔH_{mix} values and phase diagrams). These will help determine whether the MSS of cementitious compounds are possible in industry. This chapter also describes previous investigations into the **MSS of compounds,** which will determine which compounds/phases can be produced in this manner. Finally it will describe previous investigations into the **diagrammatic representation of molten salt reactions** (using predominance diagrams), which is a useful topic for describing MSS reactions and the interaction of container materials (crucibles) with the molten salt.

Chapter 3: Characterization, electroanalytical and calorimetric techniques & experimental setup describes the experimental techniques used to investigate the **structures and purities of the reactants in the molten salt in the molten salt, behaviour of the molten salt at the reaction conditions, dissolution of the reactants in the molten salt** and the **MSS of cementitious compounds.** These include XRD, SEM, potentiometry, Cyclic Voltammatery (CV), Drop calorimetry and Differential Scanning Calorimetry (DSC). It also provides a description of the setup for each experiment.

Chapter 4: Results & discussion describes the complete investigation into the MSS of cementitious compounds. This initiates with an investigation into the **feasibility of the synthesis of cementitious compounds**. This will be used to determine the reaction temperatures required to produce cementitious compounds and the selection

---

[7] "Cementitious compounds" have been selected to replace the phases of cement due to its multi-component nature. The lessons learnt from synthesising cementitious compounds in molten salts will be applied to all the phases of cement.

of a suitable salt for MSS. Then the **structures and purities of the reactants in the molten salt** will be investigated, which will suggest the purity and phase transitions of the reactants at the reaction conditions. Then, the **behaviour of the molten salt at the reaction conditions** will be investigated, which will be useful for describing the effects of vapour pressure upon the salt, which can have delirious effects upon the experiments. Then, the **dissolution of the reactants in the molten salt** will be investigated, which will lead to obtaining K_{sp}, ΔH_{mix} values and phase diagrams. This information will help determine whether the MSS of cementitious compounds are possible in industry. Then the **MSS of cementitious compounds** will be investigated, and depicted on predominance diagrams. This will help determine which other compounds can be produced in this manner.

Chapter 5: Conclusions & future work describes the conclusions of the thesis and future work for other researchers for the **feasibility of the synthesis of cementitious compounds, structures and purities of the reactants in the molten salt**, **behaviour of the molten salt at the reaction conditions, dissolution of the reactants in the molten salt** and **MSS of cementitious compounds.** The structure of this thesis can also be summarised in a flow diagram (figure 1.5).

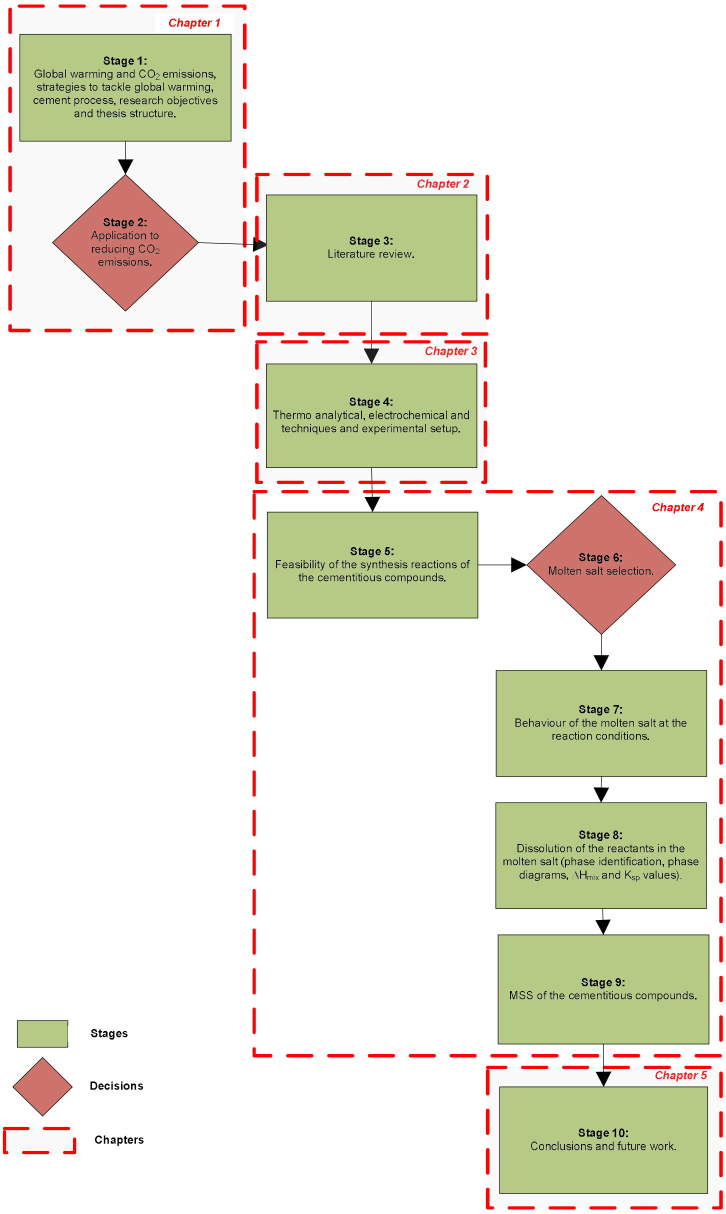

Figure 1.5: Decision tree and thesis structure.

Chapter 2

Literature review

2.1 Introduction

This chapter provides an understanding of **molten salts and their applications** to those who are unfamiliar. It then introduces previous investigations describing the **dissolution of compounds in molten salts (K_{sp}, ΔH_{mix} and phase diagrams),** the **MSS of compounds** and the **diagrammatic representation of molten salt reactions.**

2.1 Molten salts and their applications

Molten salts (also known as ionized salts) are a class of compounds that are solid at room temperature and pressure, and made liquid by heating [51]. The most common salts that have been used in literature include halides and oxyanionic salts. Halide salts are compounds with a halide ion, i.e. F^-, Cl^-, Br^- and oxyanionic salts have an O^{2-} ion, i.e. NO_3^-, SO_4^{2-}, OH^- complex ions. Complex ions are groups of ions coexisting in localized regions for appreciable periods of time [51-53]. A list of halide and oxyanionic salts can be found in table 2.1.

Halide salts (with their melting points)	
Chlorides	NaCl (801ºC), KCl (770ºC), LiCl (605ºC)
Fluorides	NaF (993ºC), KF (858ºC), LiF (845ºC)
Thiocyanate	NaSCN (287ºC), KSCN (173ºC), LSCN (unavailable)
Oxyanionic salts (with their melting points)	
Hydroxide	NaOH (318ºC), KOH (406ºC), LOH (462ºC)
Nitrate	$NaNO_3$ (308ºC), KNO_3 (334ºC), $LiNO_3$ (255ºC)
Sulphate	Li_2SO_4 (859ºC), K_2SO_4 (1069ºC) Na_2SO_4 (884ºC)
Carbonate	Li_2CO_3 (723ºC) Na_2CO_3 (851ºC) K_2CO_3 (891ºC)
Phosphate	$NaPO_3$ (627ºC), KPO_3 (450ºC), $LiPO_3$ (unavailable)
Borates	$LiBO_2$ (844ºC), KBO_2 (947ºC), $NaBO_2$ (967ºC)
Silicates	Na_2SiO_3 (1410ºC), K_2SiO_3 (976ºC), Li_2SiO_3 (1201ºC)

Table 2.1: Halide and oxyanionic salts (with their melting points), 1 atm (produced by author) [18] [51].

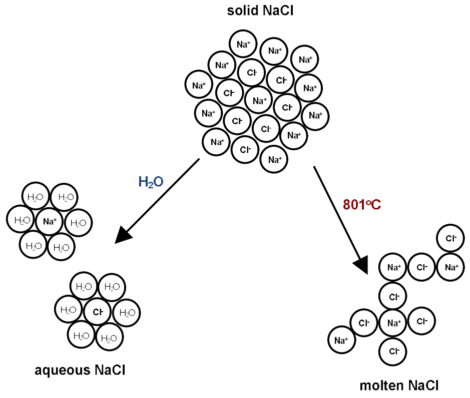

Figure 2.1: Aqueous and molten NaCl (reproduced by author) [52-53].

Figure 2.1 illustrates a molecule of NaCl in its solid, liquid and aqueous states. When a salt dissolves in an aqueous solution (NaCl in H_2O) polar H_2O molecules are attracted to charged ions (Na^+, Cl^-) due to the electric dipole moment of H_2O molecules, thus destroying the lattice arrangement of the solid (often called solvation) [54]. When a salt is heated to its melting temperature (NaCl at 801ºC), the cohesive forces and regular arrangement of the lattice is disturbed by thermal energy, causing the charged ions (Na^+, Cl^-) to become unbound from the rigid lattice, allowing them to become more ionic in character than conventional liquids. These charged ions interact amongst themselves in a mobile state and even combine to form complex ions. This interaction is often caused by coulomb forces between the particles [55].

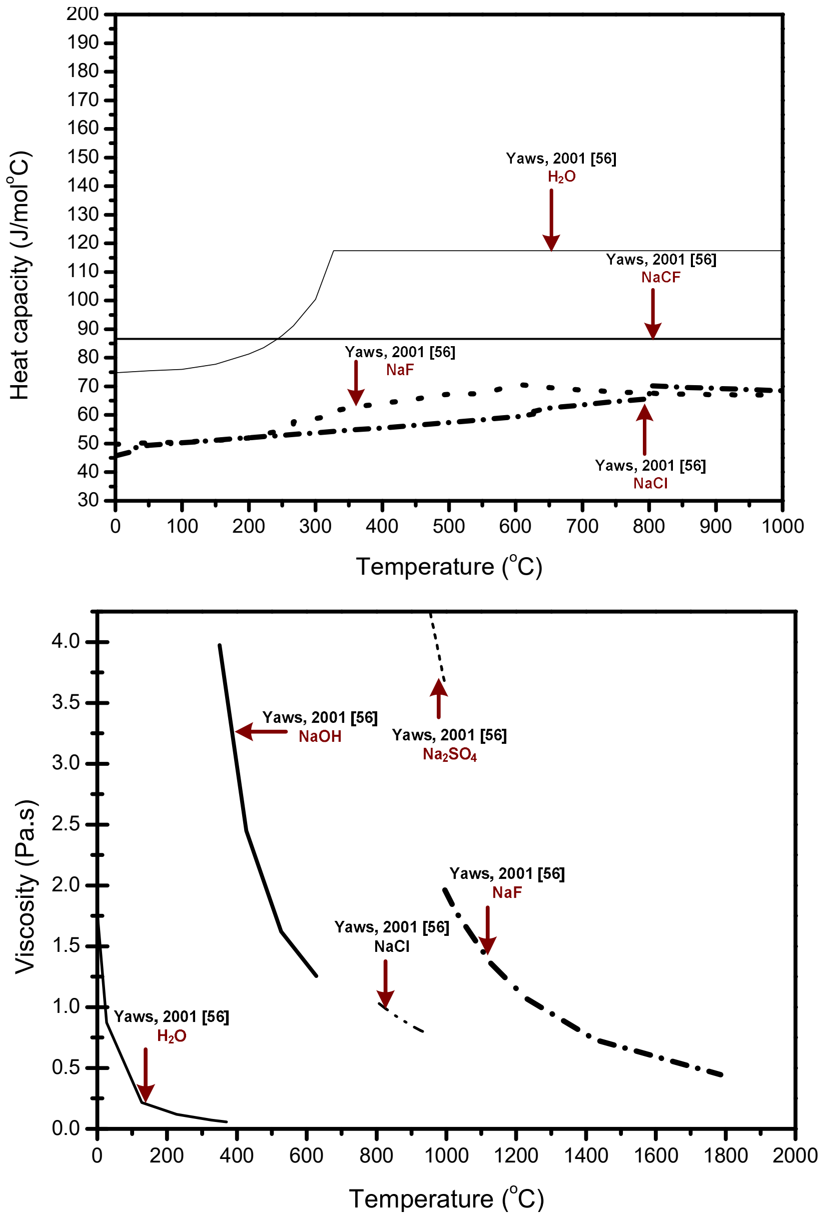

Figure 2.2: ΔC_p (top) and viscosity (bottom) of common salts (with a Na^+ ion), 1 atm (produced by author) [56].

Figure 2.2 illustrates the heat capacities (C_p) and viscosities of molten salts at 1 atm. It can be seen that molten salts have similar C_p values to aqueous media which allows them to store or transfer large quantities of thermal energy. Molten salts also have viscosities similar to aqueous media which allows them to be transported at low pressures [53]. This can be useful for chemical processes as it removes the need for auxiliary equipment (such as pumps).

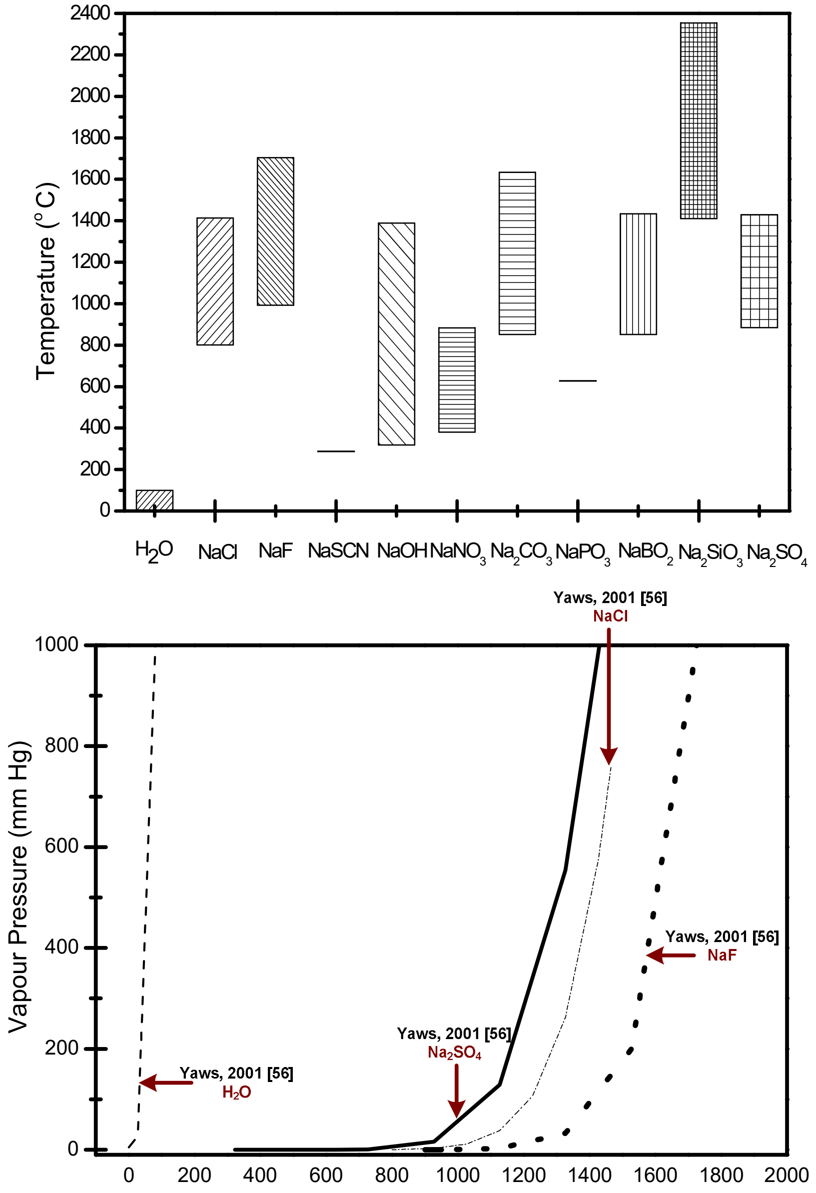

Figure 2.3: Stability ranges (top) and vapour pressures (bottom) of common salts (with Na$^+$ ion), 1 atm (produced by author) [56].

Figure 2.3 shows the stability ranges and vapour pressures of common salts. Molten salts can have large stability ranges (801-1413°C for NaCl), higher than aqueous media, which is useful for high temperature processes. Molten salts also have similar vapour pressures to aqueous media (0.302 mmHg °C^{-1} for NaCl at 801°C, 26.5 mmHg °C^{-1} for H_2O at 25°C) beyond their melting temperatures [18]. This can be useful for chemical processes as it avoids the loss of reactants.

The properties of molten salts are useful for many commercial and conceptual technologies, for example molten beryllium and lithium fluorides are used as primary fuel/coolants in molten salt nuclear reactors [57-64]. These salts dissolve fissile and fertile elements, such as uranium, plutonium and thorium [57-64].The molten salts become critical in the reactor core, generating thermal energy which is then transferred to an external heat exchanger. The thermal energy is then transferred to a secondary molten salt which is pumped to a CCGT to generate electricity [98]. Molten salt nuclear reactors are generally safer than conventional nuclear reactors as in the event of power failures, the salt is drained immediately to a cooled storage facility to terminate the nuclear reaction. The start-up costs are also lower as molten salts have generally low viscosities, thus reducing the cost of auxiliary equipment (such as pumps) [57-64]. Also it has been estimated the thermal to electrical efficiency of molten salt nuclear reactors are ~45%, which is 40% higher than conventional nuclear reactors with similar fuel consumptions [57-64].

Molten salt nuclear reactors were developed in 1954, as part of the U.S. Aircraft Nuclear Propulsion (ANP) program at the Oak Ridge National Laboratory (ORL) in Texas [59-61]. The objective was to create a nuclear propulsion engine for aircraft, to increase their flight range. The project resulted in a 2.5 MWt molten salt nuclear reactor called the Aircraft Reactor Experiment (ARE), containing a molten fluoride mixture as a primary and secondary coolant in conjunction with a solid ceramic fuel [59-61]. Another example was the Molten Salt Experimental Reactor (MSRE), developed in the 1960's, by the United States Atomic Energy Commission (AEC). The project resulted in a 7.4 MWt molten salt nuclear reactor containing a graphite reactor core and tested with uranium dissolved in a molten fluoride mixture [59-61]. Recently there has been a growing interest in advancing the development of molten salt nuclear reactors and in 2011, they were identified by the Generation IV International Forum as one of six possible nuclear reactors candidates to be commercialised by 2030 [64].

Molten salts such as molten bromides, chlorides and fluorides are used as electrolytes in thermal and high temperature rechargeable batteries. Thermal batteries contain solid non-conductive salts at room temperature, which are mobilized by a pyrotechnic heat source. When heated the salt becomes a liquid to provide short bursts of power until the salt is no longer molten [65-72]. High temperature rechargeable batteries contain a conductive molten electrolyte which is powered externally through the mains [65-72]. The "Durathon" battery is an example of a high temperature rechargeable battery, developed by GE Energy Storage [70-72]. The battery contains a molten chloride electrolyte, with a sodium anode and nickel chloride ($NiCl_2$) cathode. The anode and cathode are connected to a β-Al_2O_3 solid electrolyte that is conductive to Na^+ ions. The battery operates between 270-350ºC with an energy density of 115 Wh kg^{-1} [70-72].

Molten salts such as molten lithium and potassium carbonates are used as electrolytes in molten carbonate fuel cells (MCFCs) [73-78]. These operate at higher temperatures (~650ºC) then fuel cells (~90^{o}C), resulting in improved reaction kinetics and greater electrical efficiencies (~50%) [73-78]. A typical molten carbonate fuel cell contains a nickel anode and nickel oxide (NiO) cathode catalyst, coupled with a molten carbonate electrolyte suspended in a porous ceramic membrane. The nickel anode splits H_2 to H^+ ions to release an electron, which travels through an external circuit to generate electricity, and the H^+ ion reacts with CO_3^{2-} ions to form H_2O and CO_2 and an electron. The electron then travels to the cell cathode to complete the reaction and the H_2O and CO_2 is expelled from the system [73-78]. “DFC 300A combined heat and power system”, and “HotModule unit”, are examples of molten carbonate fuel cells developed by FuelCell Energy and MTU Friedrichshafen respectively. These are used as decentralized energy units and provide ~250 kW of power [73-78].

Molten salts such as chlorides are used as reactants and electrolytes in the electrolytic extraction of sodium and lithium. Sodium is produced by placing NaCl in a Downs cell and heating above its melting point [79-81]. A typical Downs cell contains 3 chambers, 4 carbon anodes, surrounded by steel cathodes to split molten NaCl into Cl_2 and sodium. These operate at 590ºC at 7 V, higher than the decomposition potential of NaCl (3.21V), caused by high anodic and cathodic overpotentials [79-81]. Companies such as DuPont are known to produce sodium in a Downs cell [81].

Molten salts such as cryolite (Na_3AlF_6) are used as solvents and electrolytes in the electrolytic extraction of aluminium (Hall-Héroult process) [82-85]. The process involves dissolving Al_2O_3 (~6 wt%) in molten cryolite (Na_3AlF_6) and other additives such as aluminium fluoride (AlF_3), calcium fluoride (CaF_2), magnesium fluoride (MgF_2), lithium fluoride (LiF) and NaCl (~12 wt%), which increases the melt’s electrical conductivity and lowers the reaction temperature in comparison with pure

Na_3AlF_6 [82-85]. In the process, the reactants are placed in a carbon-lined cell and carbon anodes inserted into the molten salt. Then an electrical current is passed through the cell (at ~960ºC) which causes aluminium to deposit, as a liquid, at the bottom of the cell (due to its higher density then Na_3AlF_6). O_2 is also released from Al_2O_3 which combines with the carbon anodes to produce CO_2 and CO, causing them to be consumed [82-85]. A typical Hall-Héroult cell requires 4.5 V of which 2.8 V is taken up by ohmic losses making the process ~40% efficient. A typical aluminium smelter produces 200,000 tonnes of aluminium per annum, and requires between ~100-200 Hall-Héroult cells connected electrically in series. Rio Tinto Alcan is a well-known producer of aluminium via electrolytic extraction.

Molten salts such as chlorides are used as electrolytes in titanium extraction (FFC Cambridge process) [86-90]. Traditionally, titanium is produced in the Kroll process, by reacting impure TiO_2 (Rutile) with coke (at ~1000ºC) and Cl_2 to produce titanium tetrachloride ($TiCl_4$). Then the $TiCl_4$ is reduced by molten magnesium (at ~800ºC), producing titanium and magnesium chloride ($MgCl_2$) which is separated by vacuum distillation [86-90]. In the FFC Cambridge process, a graphite anode and TiO_2 cathode is immersed in a molten chloride (at ~900ºC). Then an electrical current is passed through the molten salt causing TiO_2 to reduce to titanium and O_2. The O_2 reacts with the graphite anode to produce either CO_2 or CO, causing them to be consumed in the process [86-90]. The FFC Cambridge process can produce ~10 tonnes of titanium over several days using 160 kg of TiO_2 to produce 100 kg of titanium. This is an improvement from the Kroll process, which uses 380 kg of $TiCl_4$ and ~100 kg of magnesium to produce 100 kg of titanium and 380 kg of $MgCl_2$ [83-87].The process doesn't involve hazardous materials such as Cl_2, $TiCl_4$ and $MgCl_2$, which is more environmentally friendly [86-90].

Molten salts such as sodium and potassium nitrates are used as thermal energy storage mediums in solar power plants [91-94]. A typical molten salt solar plant contains a central tower receiver, a heliostat and molten salt storage system. The heliostat contains a parabolic mirror which concentrates thermal radiation from the sun (factor of ~80) onto a focal point which is then transferred to a molten salt. The molten salt is then pumped to a power CCGT to generate electricity [91-94]. Often a thermal energy storage system is integrated into the plant which allows it to work on overcast days and at night "Archimede" is a molten salt solar plant in Sicily, by ENEL and Archimede Solar Energy, which generates 5 MW of electrical power (at 550ºC) [91-94].

Molten salts such as nitrates, nitrite, chlorides and cyanides, are used in the heat treatments of metals, to enhance mechanical toughness and surface hardness [95-97]. Molten salts offer more controllable heat transfer rates than heat treatments in air due to a uniform temperature distribution across the alloy [95-97]. A typical heat treatment involves heating iron in steel beyond its phase transformation temperature, to transform the ferrite phase to austenite, followed by quenching to form martensite [95-97].

2.2 Dissolution of compounds in molten salts

Dissolution of compounds in molten salts has been investigated through phase diagrams, ΔH_{mix} and K_{sp} values. These have been useful for many conceptual and commercial applications of molten salts, which can no doubt affect the quality of the final product and/or process.

2.2.1 Heats of mixing of compounds in molten salts

Dissolution of compounds in molten salts has been investigated through ΔH_{mix} values. ΔH_{mix} or "excess enthalpy" is the enthalpy change associated with the dissolution of a compound in a liquid at constant pressure and temperature [98-99].

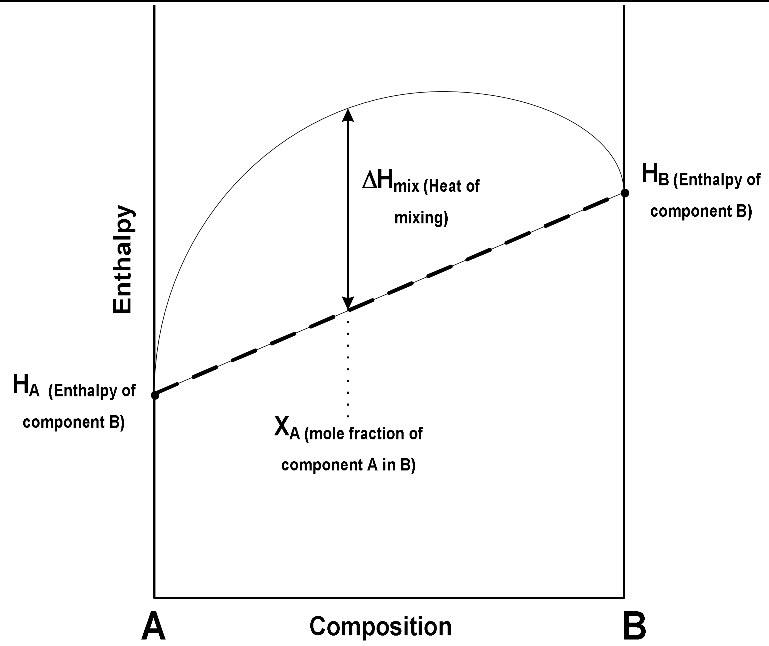

Figure 2.4: ΔH_{mix} of a binary system for components A and B (reproduced by author) [98-99].

Figure 2.4 illustrates the ΔH_{mix} of a binary system for components A and B, where H_A and H_B are the enthalpies of the pure substances (available in thermodynamic tables) and ΔH_{mix} is the heat of mixing (an integral quantity) at mole fraction X_1, obtainable directly from calorimetric measurements [98-99]. Symmetrical representations of the heats of mixing (denoted ideal mixing behaviour) between two components are represented by a regular solution model [98-99].

$$\Delta H_{mix} = x_A(1 - X_A)\ A \qquad \textbf{Equation 2.1}$$

Equation 2.1 describes the regular solution model, where X_A is the composition of component A, ΔH_{mix} is the heat of mixing and A is a constant. Most experimental data do not conform to symmetrical representations (denoted non-ideal mixing behaviour), thus a sub-regular solution model is often used [98-99].

$$\Delta H_{mix} = x_A(1 - X_A)\ (A + Bx_A + C\,x_A(1 - X_A)) \qquad \textbf{Equation 2.2}$$

Equation 2.2 describes the sub-regular solution model, where X_A is the composition of component A, ΔH_{mix} is the heat of mixing, and A, B and C are sub-regular solution coefficients (when B and C approach zero, the regular solution model is obtainable).

There has been considerable interest in the ΔH_{mix} values of various molten salt binary systems, such as molten chlorides, iodides, nitrates and fluorides (including their ternary mixtures) [100-105]. For example, in 1965, Hersh and Kleppa investigated the ΔH_{mix} in molten LiCl-NaCl, LiCl-KCl, LiCl-RbCl, LiCl-CsCl, NaCl-KCl, NaCl-RbCl, NaCl-CsCl, KCl-RbCl, KCl-CsCl, and RbCl-CsCl, between 810-670ºC, using drop calorimetery, under argon. The melts were either used as received or vacuum dried, melted and filtered through quartz wool, before being placed in fused silica (SiO_2) crucibles. It was shown the ΔH_{mix} data for most systems (with the exception of the last three) displayed negative contributions, which increased the larger the size differences between the two cations i.e. the sub-regular solution coefficient; A is -1120 for the LiCl-NaCl binary system and -490 for molten NaCl-KCl [102].

In 1976, Anderson and Kleppa investigated the ΔH_{mix} values of molten Li_2CO_3-Na_2CO_3, Li_2CO_3-K_2CO_3, Li_2CO_3-Rb_2CO_3, Li_2CO_3-Cs_2CO_3, Na_2CO_3-Rb_2CO_3, Na_2CO_3-Cs_2CO_3, K_2CO_3-Rb_2CO_3, K_2CO_3-Cs_2CO_3 and Rb_2CO_3-Cs_2CO_3, between 857-907°C, using drop calorimetery, under CO_2. The purpose of CO_2 was to inhibit the decomposition of the carbonates at the reaction temperatures. The reactants were previously dried under vacuum to remove any residual moisture and placed in a palladium-gold (Pd-Au) alloy crucible. The ΔH_{mix} data showed most systems had negative ΔH_{mix} values, with the minimum value at ~-2.864, ~-8.229, ~-8.326, ~-9.966, ~-1.347, ~-2.141 and ~-2.124 kJ mol^{-1} respectively. For molten K_2CO_3-Rb_2CO_2, K_2CO_3-Cs_2CO_3 and Rb_2CO_3-Cs_2CO_3, the heat effects demonstrated small positive contributions at 0.0002 kJ mol^{-1}, 0.0567 kJ mol^{-1} and 0.0473 kJ mol^{-1} respectively. This was largely attributed to the association reaction between CO_2 and O_2 to the CO_3^{2-} complex ion [103].

In 1990, Dessurealt et al compiled a list of ΔH_{mix} (and phase diagrams) for 24 binary systems (A_2CO_3-AX, A_2SO_4-AX (where A = Li, Na, K and X = F, Cl, OH, NO_3) to create a set of optimized thermodynamic functions. In four of the 24 systems the ΔH_{mix} values in the liquid phase were measured using a drop calorimeter and fitted to an appropriate model. The Gibbs free energies of mixing (ΔG_{mix}) were evaluated, and combined with the calorimetric data to obtain excess liquid entropies. When calorimetric data was not available, the entropy was set to zero and the ΔG_{mix} and ΔH_{mix} values were obtained from phase diagrams [106].

In 1994, Gaune-Escard et al investigated the ΔH_{mix} values in molten NaCl-NdCl$_3$, KCl-NdCl$_3$, RbCl-NdCl$_3$, CsCl-NdCl$_3$, between 792-576ºC, using a drop calorimeter, under argon. The reactants were melted under hydrochloric (HCl) and argon by progressive heating, in an alumina crucible, inside a quartz tube. To remove trace impurities, the authors performed distillation under a reduced pressure. The ΔH_{mix} data displayed negative contributions with minimum values at -5.7, -16.6, -20.2 and -23.4 kJ mol^{-1} respectively. These minimum values were shifted towards the chloride rich compositions, suggesting the existence of Cl_6^{3-} complex ions [107].

In 2005, Rycerz et al investigated the ΔH_{mix} values in molten PrCl$_3$-CaCl$_2$ and NdCl$_3$-CaCl$_2$, at 800ºC, using drop calorimetery, under argon. The reactants were melted under HCl and argon by progressive heating in an alumina crucible, inside a quartz tube. To remove trace impurities, distillation was performed under reduced pressure. The ΔH_{mix} data demonstrated "S" shaped functions (positive for $PrCl_3^-$ and $NdCl_3^-$ rich compositions). This behaviour was attributed to the existence of complex ions, possibly $Pr_2Cl_{11}^{5-}$ and $Nd_2Cl_{11}^{5-}$ which may have existed in the liquid. These ΔH_{mix} values were considered low (between -200-180 J mol^{-1}) thus the systems were assumed to be ideal [108].

Binary system	**Temperature (°C)**	**Sub-regular solution coefficients (ΔH_{mix} in kJ mol^{-1})**		
		A	**B**	**C**
NaCl-KCl	810	-2.05	-0.27	0
NaCl-LiCl	740	-4.69	0	0
NaCl-RbCl	810	-3.22	-0.33	0
NaCl-CsCl	810	-4.31	0.42	0
NaCl-Na$_2$CO$_3$ [8]	-	0.50	0	0
Na$_2$CO$_3$-K$_2$CO$_3$	857	-5.03	1.27	0
Na$_2$CO$_3$-Li$_2$CO$_3$	905	-9.90	-2.59	0
Na$_2$CO$_3$-Rb$_2$CO$_3$	905	-8.26	0.32	5.66
Na$_2$CO$_3$-Cs$_2$CO$_3$	862	-8.89	0.47	0

Table 2.2: ΔH_{mix} in chloride-carbonate, chloride and carbonate binary systems (with a Na^+ ion) (produced by author) [102-106].

---

[8] Calculated from the phase diagram of the Na$_2$CO$_3$-NaCl binary system.

Table 2.2 summaries the sub-regular solution coefficients for chloride, carbonate and chloride-carbonate binary systems, sharing a common Na^+ ion. The effect of temperature upon ΔH_{mix} are assumed to be negligible, therefore these coefficients can be used to calculate the liquidus and solidus points for phase diagrams at any temperature [109].

2.2.2 Phase diagrams of compounds in molten salts

Dissolution of compounds in molten salts has been investigated through phase diagrams [119-128]. Phase diagrams represent thermodynamically stable regions of systems at specific temperatures, pressures and compositions [110-115]. These regions are separated by phase boundaries, marking conditions where multiple phases coexist at equilibrium conditions. They are classified by the different phase behaviours encountered, governed by the number of species in the system, including one component (unary), two component (binary) systems and three component (ternary) systems [110-115]. A one component (unary) system can exist in three different phases (solid, liquid or gas), as a function of pressure and temperature at fixed composition [110-115].

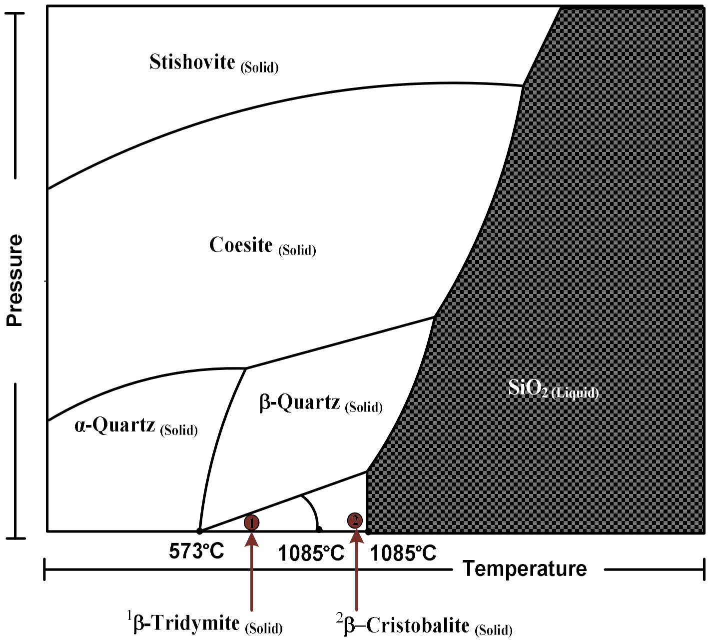

Figure 2.5: One component system; SiO_2 (reproduced by author) [112]

Figure 2.5 illustrates the many crystalline forms of SiO_2, at different temperatures and pressures. The most common form is α-quartz which undergoes a non-reversible phase transition (at 570ºC) to β-quartz [112]. Metastable (non-equilibrium) phases of SiO_2 also occur, at these temperatures but not represented on phase diagrams [116]. A eutectic system represents two solid solutions with miscibility (in some proportion). If comparable differences in atomic radii and crystal structure between the components are present (larger than isomorphous systems), a miscible region arises, extending to the liquid phase [110-115].

A two component (binary) system exists in three different phases (solid, liquid or gas), as a function of pressure, temperature and composition [110-115]. There are four types of binary systems; isomorphous, eutectic, peritectic and monotectic, each resulting in different representations [110-115]. An isomorphous system is the simplest type of binary system, representing two components dissolving into each other in all (or some proportion). This dissolution behaviour arises from both components having similar crystal structures and atomic radii [110-115].

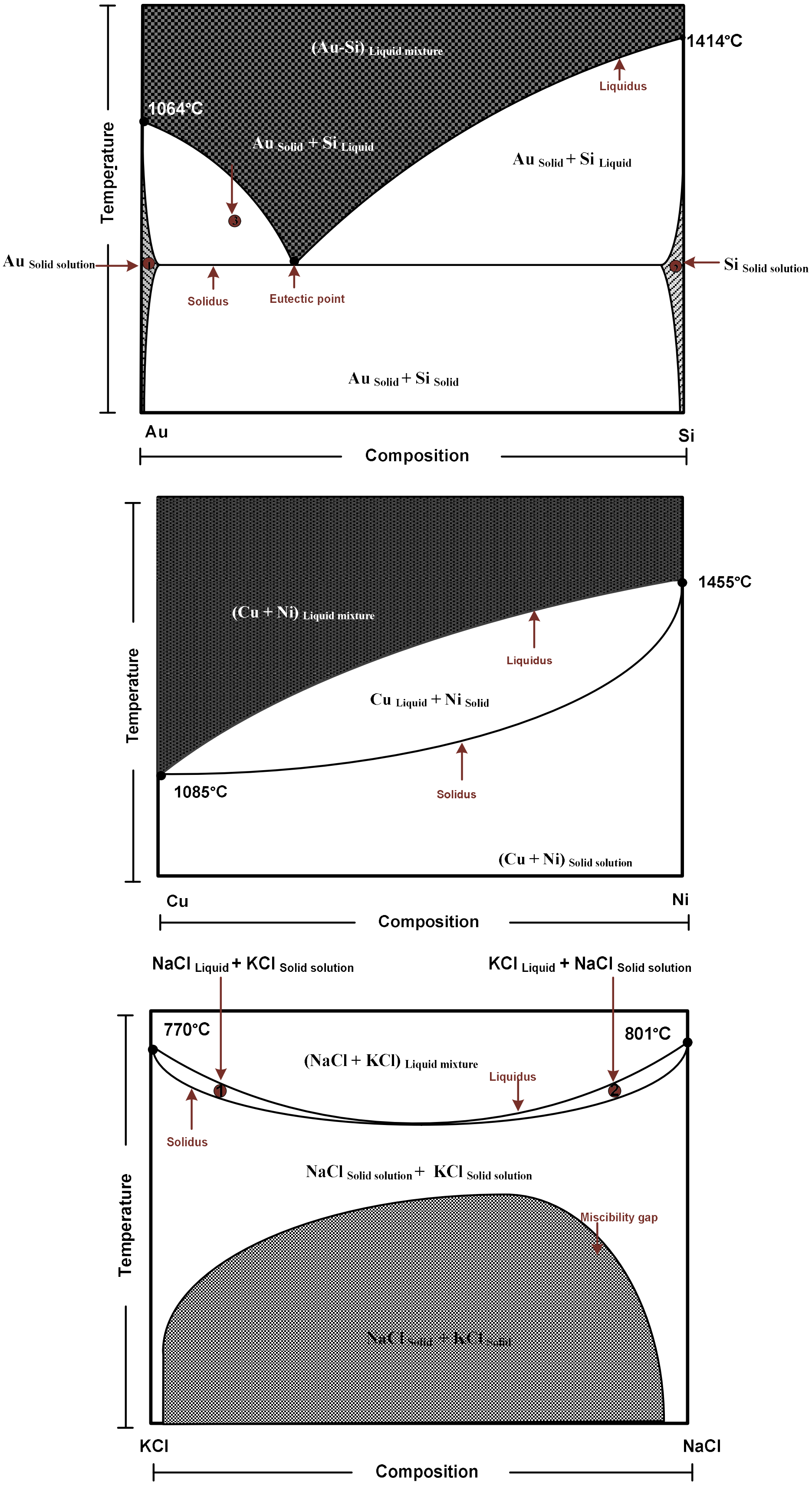

Figure 2.6: Two component isomorphous systems; Cu-Ni (middle), NaCl-KCl (bottom) and eutectic system; Au-Si (top) (reproduced by author) [113] [117-119].

Figure 2.6 illustrates the isomorphous systems for copper-nickel (Cu-Ni), NaCl-KCl binary system and the eutectic system for gold-silicon (Au-Si) [117-119]. The boundary lines between the liquid mixture region and liquid + solid or solid solution regions is denoted the liquidus and between the liquid + solid and solid (or solid solution region) is denoted the solidus. The liquidus and solidus lines meet at the fusion temperatures for copper (at 1085ºC), nickel (at 1085ºC), NaCl (at 801ºC) and KCl (at 770ºC). If comparable differences in atomic radii and crystal structure between the components are present, a miscible region arises (denoted a miscibility gap). Peritectic and monotectic systems consider additional reactions to a phase diagram. During a peritectic reaction, a liquid phase and solid phase react together to form a new solid phase and during a monotectic reaction, a liquid phase cools to form a new liquid phase and solid mixture [113]. Often phase diagrams can involve three (or multiple) components which represent solid, liquid or gas phases as a function of pressure, temperature and composition of multiple components.

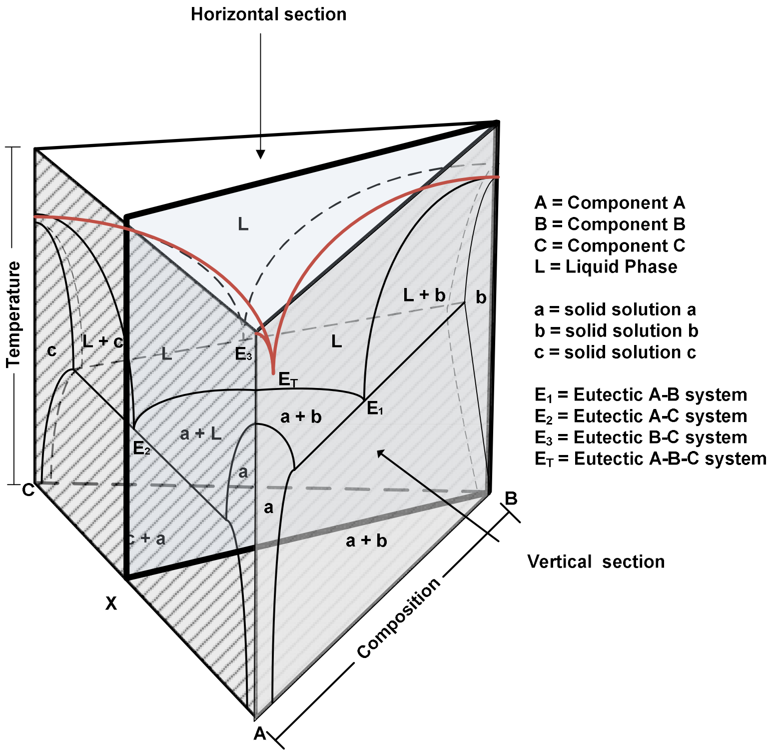

Figure 2.7: Space model of a three component system; A-B-C (reproduced by author) [110-115].

Figure 2.7 illustrates a space model for a ternary eutectic system for components A, B and C, being combinations of binary systems; A and B, B and C and C and A. Space models serve limited practical purpose, thus often represented in two dimensions, as liquidus/solidus or composition triangles (a horizontal section of a space model).

There has been considerable interest in the phase diagrams of various binary systems, such as molten chlorides and carbonates [120-128]. For example, in 1990, Dessureault et al compiled a list of phase diagrams (and ΔH_{mix}) for 24 binary systems (A_2CO_3-AX, A_2SO_4-AX (where A = Li, Na, K and X = F, Cl, OH, NO_3, to create a set of optimized thermodynamic functions to calculate phase diagrams and ΔH_{mix} using the CALPHAD method (CALculation of PHAse Diagrams). All carbonate-chloride mixtures represented a eutectic system, with no solid solubility (assumed to be 0 in most cases). More specifically, the transition temperatures for Na_2CO_3 were 359ºC and 485ºC, and fusion temperature was 858ºC and the phase diagram for molten NaCl-Na_2CO_3 demonstrated a eutectic point at 643°C at 43 mol% Na_2CO_3 [106].

In 2000, Iwasawa and Maeda investigated the phase diagram for molten NaCl-Na_2CO_3, NaCl-Na_2SiO_3, and LiCl-Li_2SiO_3, using a novel hot filament technique, to allow solid, liquid-solid and liquid phases to be visually observed. These mixtures were slowly heated in a hot filament cell, purged with argon to eliminate H_2O. This allowed the fusion temperature of NaCl, Na_2CO_3 and the eutectic point for molten NaCl-Na_2CO_3, to be determined at 801ºC, at 851ºC, and at 643ºC at 43 mol% Na_2CO_3 [124].

In 2007, Yaokawa et al investigated the phase diagram for molten NaCl-Na_2CO_3, NaCl-Na_2SO_4, KCl-K_2SO_4, KCl-K_2CO_3, NaCl-KCl, Na_2SO_4-K_2SO_4, Na_2CO_3-K_2CO_3, Na_2SO_4-Na_2CO_3, K_2SO_4-K_2CO_3, NaCl-Na_2SO_4-Na_2CO_3, KCl-K_2SO_4-K_2CO_3, NaCl-Na_2SO_4-KCl-K_2SO_4, NaCl-Na_2CO_3-KCl-K_2CO_3, and Na_2SO_4-Na_2CO_3-K_2CO_3.K_2SO_4. These were used to calculate the phase diagram for the molten NaCl-Na_2SO_4-KCl-K_2SO_4-K_2CO_3, using a Modified Quasichemical solution model. The phase diagram exhibited no solid solution or intermediate phases and the eutectic point was found (at 631°C, 45 mol% Na_2CO_3) [125].

Also in 2007, Lindberg et al investigated phase diagrams and thermodynamic functions for molten NaCl-Na_2CO_3, KCl-K_2CO_3, Na_2CO_3-K_2CO_3 and NaCl-KCl to calculate the phase diagram for molten KCl-K_2CO_3-NaCl-Na_2CO_3. Initially the phase diagram for molten NaCl-Na_2CO_3 was calculated and compared with previous measured liquidus and solidus points. The melting point of Na_2CO_3 (at 851ºC) was found to be lower than the extrapolated value of the calculated liquidus line (at 858ºC) and the eutectic point was found to be 632ºC, 45 mol% Na_2CO_3 [126].

In 2011, Kochkarov et al investigated the phase diagram for molten NaCl-Na_2CO_3, including the fusion temperatures for NaCl and Na_2CO_3 using DTA. The NaCl and Na_2CO_3 were initially fused and placed inside a platinum crucible. The fusion temperatures were found to be 801ºC and 851ºC respectively, which were used in combination with the phase diagram for molten $NaBO_2$-Na_2CO_3 and NaCl-$NaBO_2$ to calculate the phase diagram for molten $NaBO_2$-NaCl-Na_2CO_3, with a eutectic point, at 612°C, 16 mol% $NaBO_2$, 42 mol% NaCl and 42 mol% Na_2CO_3. A similar approach was used to calculate the phase diagram for molten $NaBO_2$-Na_2CO_3-Na_2WO_4, and $NaBO_2$-NaCl-Na_2WO_4 and the eutectic point were found to be at 568°C, 12 mol%, $NaBO_2$, 28 mol% $NaBO_2$, 60 mol% Na_2MoO_4 and 655°C, 9 mol% $NaBO_2$, 53 mol% NaCl, 38 mol% Na_2WO_4 [127].

In 2014, Longgang et al investigated the density, viscosity, volatilization, decomposition, melting point, eutectic composition and enthalpy of fusion for molten NaCl-Na_2CO_3, using a DTA, rotating-cylinder, horizontal-hammer method, transpiration method, XRD, SEM, and EDS, under argon. The Na_2CO_3 and NaCl were placed in a corundum (Al_2O_3) crucible and heated to melt completely, to remove residual moisture, and then ground in a ball mill. They found the melting point of the mixture was 636ºC, the enthalpy of fusion was 101.12 J g^- and the density was 1.83 g cm^{-3} at 700ºC, and 1.67 g cm^{-3} at 1000ºC, showing that the density decreased linearly with temperature. The viscosity was 17.02 cp at 700ºC and 1.21 cp at 1000ºC, showing that the viscosity had an exponential dependence upon temperature in its liquid state. The vapour pressure was 13.34 Pa at 700ºC and 151.06 Pa at 900ºC, showing that the vapour pressure increased with temperature. The evaporation of NaCl became evident after 804ºC and ~90 wt% was lost at 1000ºC. The weight loss of Na_2CO_3 was slow indicating its decomposition to Na_2O and CO_2. The XRD showed the composition and phase of the mixture remained unchanged after high-temperature treatment. The SEM and EDS showed particles of Na_2CO_3 and NaCl in the mixture were randomly distributed with no uniform phase [128].

2.2.3 Solubility products of compounds in molten salts

Dissolution of compounds in molten salts has been investigated by obtaining K_{sp} values. K_{sp} values describe the activity of “free ions” in a saturated solution, and are often accompanied by dissociation constants (K_d), describing the extent of dissociation of the compound in an unsaturated solution, and formation constants (K_f), describing the formation of a complex ion in solution [129-130]. These terms can be used to describe a compound at equilibrium with its ions/complex ions, at a specific temperature and pressure, and are independent of the initial and final concentration of the reactants and products.

$$K_{sp} = [Me^{2+}][O^{2-}]$$

Equation 2.3

$$K_d = \frac{[Me^{2+}][O^{2-}]}{[MeO]} = \frac{K_{sp}}{[MeO]}$$

Equation 2.4

$$K_f = \frac{[MeO]}{[Me^{2+}][O^{2-}]} = \frac{[MeO]}{[K_{sp}]}$$

Equation 2.5 [9]

Equations 2.3-2.5 describe the K_{sp}, K_d and K_f values for a two-charged metal cation oxide, where $[Me^{2+}]$ is the activity of the metal cation, $[O^{2+}]$ is the activity of the O^{2-} ion and [MeO] is the activity of the dissolved non-dissociated oxide. K_{sp}, $K_{sp,}$ and K_f values in molten salts can be found using techniques such as isothermal saturation, potentiometric titration or the sequential addition method (SAM) [129-131].[10]

---

[9] Only for the case of a two-charged metal cation oxide.

[10] Equilibrium thermodynamic constants units are dimensionless.

- **Isothermal saturation method**

  This method has been employed for studying oxide solubilities over a limited concentration range. The procedure involves the addition of oxides to a molten salt and removing samples at regular intervals to analyse the Me^{2+} or O^{2-} ion activity (using techniques such as radiochemical or complexometric analysis). This is often accompanied by a potentiometry to detect the activity of Me^{2+} or O^{2-} ions in the molten salt (to detect the saturation limit). Upon knowledge of the Me^{2+} or O^{2-} ion activity, $K_{sp,}$ K_d and K_f values of compounds and complexes can be determined [130].

- **Potentiometric titration method**

  This method is employed for studying oxide solubilities over a wide concentration range. The procedure involves the addition of a compound (such as an oxide) to a molten salt (often saturated with a metal chloride (or vice versa)). This is accompanied by a potentiometry to detect the activity of Me^{2+} or O^{2-} ions in the molten salt (to detect the formation of a complex or insoluble compound). The addition of the oxide causes complexes and/ or insoluble compounds to form in a "titration reaction", which can be followed by potentiometry. Upon knowledge of the Me^{2+} or O^{2-} ion activity, $K_{sp,}$ K_d and K_f values of compounds and complexes can be determined [130].

- **Sequential addition method**

  This method is employed for studying oxide solubilities over a wide concentration range. The procedure involves the addition of a compound (such as an oxide) to a molten salt (often saturated with a metal chloride (or vice versa)). This is accompanied by potentiometry to detect the activity of Me^{2+} or O^{2-} ions in the molten salt (to detect the saturation limit). The addition of the compound causes a "dissolution reaction" up to the saturation limit of the molten salt, which can be followed by potentiometry. Upon knowledge of the Me^{2+} or O^{2-} ion activity, K_{sp} values of compounds can be determined [130].

There has been considerable interest in obtaining K_{sp} values in various melts, such as molten chlorides, nitrates and fluorides (and their binary and ternary mixtures) [132-160]. The scale of literature is extensive therefore we will focus upon K_{sp} values in molten NaCl, KCl, LiCl-KCl, NaCl-KCl and $CaCl_2$-NaCl.

2.3.1.1 Solubility products of compounds in molten LiCl-KCl

Molten LiCl-KCl is used as electrolytes in molten salt batteries, molten carbonate fuel cells and as solvents for the pyrochemical reprocessing of nuclear fuel, due to its low melting temperature (at 348ºC) and high proliferation resistance over aqueous solvents [57-58]. These applications are highly dependent upon the O^{2-} ion activity in the molten salt therefore K_{sp} values of oxides in this molten salt are frequently investigated.

One of the first authors to measure K_{sp} values in molten LiCl-KCl was Delarue in 1959, where he qualitatively investigated the solubility of cadmium oxide (CdO), lead oxide (PbO), barium oxide (BaO), CaO, silver oxide (Ag_2O), cobalt oxide (CoO), NiO, zinc oxide (ZnO), magnesium oxide (MgO), beryllium oxide (BeO) and Al_2O_3 in molten LiCl-KCl, at 500ºC, by visual inspection. The molten salt was contained in a Pyrex tube, which was heated to the experimental temperature, followed by the addition of oxide pellets. When no deposit of oxide appeared in the molten salt, they considered it to be soluble, and when a deposit formed, the oxide was considered slightly soluble or insoluble. He found that CdO, PbO, BaO, CaO and Ag_2O were soluble in the molten salt, CoO, NiO, ZnO were slightly soluble and MgO, BeO and Al_2O_3 were insoluble. He also found the solubility of oxides, added as pellets were greater than powders, which can be attributed to its larger surface area [132].

In 1960, Laitinen and Bhatia investigated the K_{sp} values of NiO, palladium oxide (PdO), PtO_2 and copper oxide (Cu_2O) in molten LiCl-KCl, by potentiometry, at 450ºC, under nitrogen (N_2). The technique involved an ISE and reference electrode immersed in the molten salt at the experimental temperature. The ISE was constructed from graphite with a platinum wire in the centre, and the reference electrode was a platinum wire, immersed in molten platinum chloride ($PtCl_2$). They found the behaviour of the reference electrode wasn't reversible which was attributed to the reaction of platinum with molten LiCl-KCl at highly acidic conditions. Therefore the Cl^- ions in the electrode were analysed after each experiment, to determine the amount of $PtCl_2$ present. The reference electrode potential was then corrected for a $PtCl_2$ activity of 1. They found the K_{sp} values for NiO, PdO, PtO_2 and Cu_2O to be -log 1.46, -log 1.95, -log 1.49, -log 1.56 respectively. They also found heavier metal oxides were more soluble than lighter ones in these melts [133].

In 1979, Picard et al investigated the K_{sp} values for Al_2O_3 in molten LiCl-KCl, at 470ºC, by potentiometry, under CO_2. The technique involved a reference electrode and an ISE immersed in the molten salt. The ISE was constructed from Y_2O_3-ZrO_2 (YSZ) and contained a silver wire, immersed in molten LiCl-KCl and Ag_2O, and the reference electrode contained a silver wire immersed in molten LiCl-KCl and Ag_2O. The experimental procedure involved the addition of Na_2CO_3 to the molten salt, containing metal ions. They found a titration curve displaying two equivalence points at 1 and 1.5, which was attributed to the formation of $AlOCl_2^-$ and $AlCl_4^-$ complex ions. The K_{sp} values of Al_2O_3 were reported to be -log 27.4 and K_f values for the AlO^+ complex ion at -log 10.7, and -log 6 respectively [134].

In 1986, Martinot and Fuger investigated the K_{sp} values for thorium oxide (ThO_2), protactinium dioxide (PaO_2), uranium dioxide (UO_2), neptunium dioxide (NpO_2), uranium(IV) oxide (UO_3) and plutonium(III) oxide (Pu_2O_3) in molten LiCl-KCl, at 500ºC, under argon. The technique involved an ISE and reference electrode immersed in the molten salt. The ISE was constructed from calcia-stabilized zirconia (CaO-ZrO_2), which contained a silver wire immersed in molten AgCl, Li_2O and molten LiCl-KCl and the reference electrode contained a silver wire immersed in molten AgCl and molten LiCl-KCl. The experimental procedure involved the addition of Na_2CO_3 to the molten salt, containing thorium chloride ($ThCl_2$), protactinium chloride ($PaCl_2$), uranium chloride (UCl_2), neptunium chloride ($NpCl_2$) and plutonium chloride ($PuCl_2$). They found a titration curve displaying one equivalence point, attributed to the formation of ThO_2, PaO_2, UO_2, NpO_2, UO_3 and Pu_2O_3. The K_{sp} values for ThO_2, PaO_2, UO_2, NpO_2, UO_3 and Pu_2O_3 were reported to be -log 13.3, -log 15.2, -log 14.0, log 5.1, -log 7.12 and -log 25.7 respectively [135].

In 1994, Rouault-Rogez et al investigated the K_{sp} values of ZnO in molten LiCl-KCl, at 450ºC, by potentiometry and electrolysis, under N_2. The technique involved an ISE and reference electrode immersed in the molten salt. The ISE was constructed from YSZ, and contained a silver wire, immersed in molten AgCl, Ag_2O and molten LiCl-KCl, and the reference electrode contained a silver wire immersed in molten AgCl and molten LiCl-KCl. The electrolysis arrangement involved a tungsten wire immersed in the molten salt, serving as an anode, and a tungsten wire in a Pyrex tube, containing molten zinc, Na_2CO_3 and molten LiCl-KCl, serving as a cathode. The experimental procedure involved the addition of Na_2CO_3 to the molten salt; however this was disturbed by the slow reaction kinetics of carbonate decomposition, therefore they precipitated ZnO by the anodic oxidation of zinc chloride ($ZnCl_2$), using electrolysis, under CO_2, The K_{sp} values for ZnO were reported to be -log 5.6 [136].

In 1999, Cherginets investigated the K_{sp} values of CoO, MgO and NiO in molten LiCl-KCl, at 700ºC using potentiometry, under N_2. The technique involved an ISE and reference electrode immersed in the molten salt. The ISE was constructed from YSZ, and contained a platinum wire immersed in molten Ag_2O and molten LiCl-KCl, under O_2, and the reference electrode contained a platinum wire, immersed in molten AgCl, and molten LiCl-KCl. The molten salt was initially melted under N_2 saturated with CCl_4 which was followed by the addition of argon and ammonium chloride (NH_4Cl) to remove any residual O^{2-} impurities. A calibration curve was then realized by additions of Na_2CO_3 to the molten salt, which displayed an inflection point at -log 2.3, attributed to the formation of O_2^{2-} ions on the platinum wire surface (in the ISE). This was followed by the addition of Na_2CO_3 to the molten salt containing $MgCl_2$, $NiCl_2$ or $CoCl_2$. They found a titration curve displaying one equivalence point attributed to the formation of CoO, MgO and NiO. The titration curve for CoO displayed an appreciable non-saturated solution region, suggesting that CoO was soluble. The titration curve for MgO and NiO didn't include a non-saturated solution region, suggesting these were insoluble in the molten salt. The K_{sp} values for MgO, CoO and NiO were reported to be -log 4.43, -log 5.34, and -log 5.87 respectively and the K_d value for CoO at -log 1.18 [137].

In 2001, Caravaca et al investigated the K_{sp} values of cerium oxychloride (CeOCl), lanthanum oxychloride (LaOCl), praseodymium oxychloride (PrOCl) and yttrium(III) oxide (Y_2O_3) in molten LiCl-KCl, at 450ºC, by potentiometry, under argon. The technique involved an ISE and a reference electrode immersed in the molten salt. The ISE was constructed from YSZ, and contained a silver wire, Ag_2O and AgCl with molten $CaCl_2$-NaCl or molten LiCl-KCl, and the reference electrode contained molten AgCl with molten LiCl-KCl. Initially the salt was prepared under vacuum, to remove residual O^{2-} ion impurities. Then a calibration curve was realized by additions of Na_2CO_3 and BaO, which demonstrated good Nernstian behaviour. The experimental procedure involved the addition of Na_2CO_3 or BaO to the molten salt containing $CeCl_3$, $LaCl_3$, praseodymium(III) chloride ($PrCl_3$), yttrium(III) chloride (YCl_3). They found the titration curves displayed one equivalence point at -log 1 and -log 1.5 corresponding to the formation of oxychloride compounds and Y_2O_3 respectively. The K_{sp} values for CeOCl, LaOCl, PrOCl and Y_2O_3 were reported to be -log 7.45, -log 7, -log 7.45 and -log 19.9 respectively [138].

In 2003, Casterillego et al investigated the K_{sp} values of LaOCl, CeOCl, neodymium oxychloride (NdOCl) and PrOCl in molten LiCl-KCl, at 450ºC, by potentiometry, under argon. The technique involved an ISE and a reference electrode immersed in the molten salt. The ISE was constructed from YSZ containing a silver wire immersed in molten AgCl, Na_2CO_3 and molten LiCl-KCl, and the reference electrode contained a silver wire, immersed in molten AgCl and molten LiCl-KCl. Initially the molten salt was calibrated by additions of Na_2CO_3 or BaO, demonstrating good Nernstian behaviour. The experimental procedure involved the addition of Na_2CO_3 or BaO to the molten salt. They found titration curves which demonstrated an equivalence point at -log 1, corresponding to the formation of oxychloride species. The K_{sp} values for CeOCl, LaOCl, NdOCl and PrOCl were reported to be -log 7.45, -log 7, -log 7.45 and -log 7.67 respectively [139].

In 2004, Cherginets et al investigated the K_{sp} values of MgO in molten LiCl-KCl, between 600-800ºC, under argon and CO_2, at 0.1 MPa. The technique involved an ISE and a reference electrode immersed in the molten salt. The ISE was constructed from YSZ, containing a platinum wire under O_2, and the reference electrode, contained a silver wire, immersed in molten AgCl in molten LiCl-KCl. Initially the molten salt was treated with CCl_4 and argon, followed by NH_4Cl to remove residual O^{2-} ion impurities. Then a calibration curve was realized by additions of potassium hydroxide

(KOH), which displayed an inflection point at -log 2, corresponding to the formation of O_2^{2-} ions in the ISE. The experimental procedure involved the addition of MgO to the molten salt up to the saturation limit. The K_{sp} values for MgO were reported to be -log 6.99 at 600ºC, -log 5.87 at 700ºC and -log 5.41 at 800ºC [140].

In 2007, Cordoba and Caravaca investigated the K_{sp} values for SmOCl in molten LiCl-KCl, at 450ºC, under argon. The technique involved an ISE and reference electrode immersed in the molten salt. The ISE was constructed from YSZ, containing a silver wire, molten AgCl, BaO, Li_2CO_3 or Na_2CO_3, and molten LiCl-KCl and the reference electrode contained a silver wire immersed in molten AgCl and molten LiCl-KCl. The salt was prepared by bubbling HCl and argon, to remove residual O^{2-} ion impurities. Initially the molten salt was calibrated by additions of Na_2CO_3, demonstrating good Nernstian behaviour. The experimental procedure involved the addition of Li_2CO_3, Na_2CO_3 and BaO to the molten salt containing samarium(III) chloride ($SmCl_3$). The titration curve displayed one equivalence point at -log 1, corresponding to the formation SmOCl. The K_{sp} values for SmOCl were reported to be ~-log 7.54. In addition, the K_{sp} values for SmOCl and Sm_2O_3 were calculated form thermodynamic data, at -log 7.76 and -15.93 respectively, at the same experimental temperature [141].

In the same year, Kado et al investigated the solubility of Li_2O in molten LiCl-KCl, between 400-650ºC, by CV. The technique involved a three electrode arrangement; an anode, a cathode and a reference electrode immersed in the molten salt. The anode and cathode electrodes were constructed from glassy carbon and the reference electrode contained a silver wire immersed in molten AgCl and molten LiCl-KCl. The experimental procedure involved the addition of Li_2O to the molten salt at 58.5, 75, 90 and 100 mol% LiCl. They found the current of the electrochemical cell increased linearly as the amount of Li_2O increased, up to the saturation limit. The CV curves demonstrated the solubility of Li_2O at 1.12 mol%, 0.708 mol%, 1.14 mol% and 1.32 mol% at 400ºC, 450ºC, 500ºC and 550ºC respectively and the highest solubility of Li_2O was reported to be 12.0 mol% at 650ºC [142].

In 2012, Osipenko et al investigated the K_{sp} values of CmOCl and curium(III) oxide (Cm_2O_3) in molten LiCl-KCl, at 450ºC, by potentiometry, under argon. The ISE electrode was constructed from YSZ, containing a platinum wire under O_2 and the reference electrode, containing a silver wire immersed in molten AgCl and molten LiCl-KCl. Initially the salt was prepared under vacuum, and melted under argon to remove residual O^{2-} ion impurities. The experimental procedure involved the addition of Na_2CO_3 to the molten salt containing curium chloride ($CuCl_3$). The titration curve displayed three equivalence points corresponding to the formation of CmOCl, CmO^+ and Cm_2O_3. The K_{sp} and K_f values for CmOCl, the CmO^+ complex ion and Cm_2O_3 were reported to be -log 2.5, -log 7.5 and -log 15.5 at 450ºC, -log 2.4, -log 5.7 and -log 12.7 at 550ºC and -log 0.8, -log 5.2 and -log 12.5 at 650ºC respectively [143]. A complete list of K_{sp} values for various oxides in molten LiCl-KCl are reported in table 2.3.

Name	Compound	-log K_{sp}	Temperature (ºC)
Nickel oxide	NiO	1.46	450
		5.87	700
Palladium oxide	PdO	1.95	450
Platinum oxide	PtO_2	1.49	450
Copper(II) oxide	Cu_2O	1.56	400
Aluminium(III) oxide	Al_2O_3	27.4	470
Thorium(IV) oxide	ThO_2	13.3	500
Protactinium dioxide	PaO_2	15.2	500
Uranium dioxide	UO_2	14.0	500
Neptunium dioxide	NpO_2	5.1	500
Uranium(IV) oxide	UO_3	7.12	500
Plutonium(IV) oxide	Pu_2O_3	25.7	500
Zinc oxide	ZnO	5.6	450
Magnesium oxide	MgO	4.43	700
		6.99	600
		5.87	700
		5.41	800
Cobalt oxide	CoO	5.34	700
Cerium oxychloride	$CeOCl$	7.45	450
Lanthanum oxychloride	$LaOCl$	7.00	450
Protactinium oxychloride	$PrOCl$	7.45	450
		7.67	450
Yttrium(III) oxide	Y_2O_3	19.9	19.9
Lithium oxide	Li_2O	**1.12 (wt%)**	400
		0.108 (wt%)	450
		1.14 (wt%)	500
		1.32 (wt%)	550
Samarium oxychloride	$SmOCl$	7.54	450
Curium oxychloride	$CmOCl$	2.5	450
		2.4	550
		0.8	650
Curium(III) oxide	Cm_2O_3	15.5	450
		12.7	550
		12.5	650
Indium oxychloride	$NdOCl$	7.45	450

Table 2.3: K_{sp} values of compounds in molten LiCl-KCl (produced by author) [132-143].

2.3.3.2 Solubility products of compounds in molten NaCl, KCl and NaCl-KCl

Molten NaCl, KCl and NaCl-KCl are used as solvents for the growth of crystals, as electrolytes for molten carbonate fuel cells, and as solvents for the pyrochemical reprocessing of nuclear fuel, due to its low melting temperature (at 727ºC), high electrical conductivity and high proliferation resistance over aqueous solvents [57]. These applications are dependent upon the O^{2-} ion activity in the molten salt therefore K_{sp} values of oxides in these melts are frequently investigated.

In 1966, Neumann and Reinhard investigated the K_{sp} values of CaO, strontium oxide (SrO) and BaO in molten NaCl-KCl, molten NaCl and molten KCl, between 727-900ºC, by isothermal saturation, under argon. Initially the molten salt was dried between 160-200ºC for 24 hours, to remove residual O^{2-} ion impurities. The experimental procedure involved the addition of CaO, SrO and BaO to the molten salt, until the saturation limit. The molten salt was then filtered using a nickel frit and analysed by complexometric titration. The K_{sp} values for CaO, SrO and BaO were reported to be -log 1.60, -log 1.77, -log 1.36 in molten NaCl, -1.77, -1.77, -log 1.75 in molten KCl and -log 1.11, -log 0.93, -log 1.08 in molten NaCl-KCl, at 900ºC respectively. They also found the K_{sp} values increased in the sequence CaO > SrO > BaO, with the K_{sp} values for molten KCl-NaCl and molten KCl being similar and those for molten NaCl being higher [144].

In 1975, Combes et al investigated the K_{sp} values for CaO and NiO in molten NaCl-KCl, between 706-800ºC, by potentiometry, under argon. The technique involved an ISE and a reference electrode immersed in the molten salt. The ISE was constructed from CaO-ZrO_2, containing a silver wire, immersed in molten NaCl-KCl and Ag_2O, and the reference electrode, contained a nickel wire immersed in molten NaCl-KCl, and NiO. Initially, the molten salt was dehydrated at 10^{-2} Torr, between 200-500ºC, to remove residual O^{2-} ion impurities. Then the molten salt was calibrated by additions of CaO and the potentiometric plots displayed good Nernstian behaviour. The experimental procedure then involved the addition CaO or Na_2CO_3 to the molten salt, containing $NiCl_2$ and copper chloride ($CuCl_2$) and the K_{sp} values for CaO and NiO were reported to be -log 14.6 at 706ºC and -log 12.4 at 800ºC respectively. The values were also calculated from thermodynamic data and experimental activity coefficients from Me^{2+} ions; Ag_2O, Cu_2O, ZnO, CoO, PdO, FeO, SnO, CuO, NiO, FeO, CrO and ZrO_2 at -log 0.8, -log 5.4, -log 8.3, -log 9.3, -log 9.6, -log 9.8, -log 10, -log 10.1, -log 11.2, -log 21.1, -log 23.1, -log 33.6 respectively [145].

In the same year, Combes et al investigated the K_{sp} values of CaO in molten NaCl-KCl, between 710-820ºC, by potentiometry, under argon. The technique involved an ISE and reference electrode, immersed in the molten salt. The ISE were constructed from CaO-ZrO_2, containing a silver wire, with molten NaCl-KCl and Ag_2O and the reference electrode contained a nickel wire immersed in molten NaCl-KCl and NiO. The experimental procedure involved the addition of CaO to the molten salt, and the partial pressure of H_2O over the molten salt was modified to allow specific Ca^{2+} ion activities to be achieved. The K_{sp} values for CaO in the molten salt were reported at -log 5.4 at 710ºC, -log 5.0 at 727ºC and -4.3 at 820ºC. Then WO_3 was added to the molten salt after an O^{2-} ion activity was imposed and a titration curve was obtained with two equivalence points at -log 0.5 and ~-log 0.6. This corresponded to the formation of WO_4^{2-} and $W_3O_{10}^{2-}$ complex ions and K_d values for WO_4^{2-} and $W_3O_{10}^{2-}$ complex ions were found to be -log 10 and -log 12.7 respectively. The K_{sp} values for CaO and $CaWO_4$ were also calculated from thermodynamic data at -log 7.6 and -log 3.5 respectively [146].

In 1978, Combes et al investigated the K_{sp} values of cerium(III) oxide (Ce_2O_3) in molten NaCl-KCl, at 727ºC, by potentiometry, under CO_2 at 10^{-2} atm. The technique involved a reference electrode and ISE immersed in the molten salt. The reference electrode contained a silver wire, immersed in molten NaCl-KCl and Ag_2O, and the ISE was constructed from CaO-ZrO_2, containing a nickel wire immersed in molten NaCl-KCl and NiO. Initially, the molten salt was heated to 400ºC, under vacuum and melted under HCl, CO_2 and argon to remove residual O^{2-} ion impurities. The molten salt was then calibrated by adding Na_2CO_3 and the potentiometric curve demonstrated good Nernstian behaviour. Then the experimental procedure involved the addition of Na_2CO_3 to the molten salt, containing cerium(III) chloride ($CeCl_3$). The titration curve demonstrated two equivalence points, corresponding to the formation of Ce_2O_3 and CeO^+ complex ions. The K_d values for CeO^+ complex ions and Ce_2O_3 were found to be -log 11 and -log 7.9 respectively, and the K_{sp} values for Ce_2O_3 at -log 30 [147].

In 1979, Combes et al investigated the K_{sp} values of MgO, CaO and BaO in molten NaCl-KCl at 727ºC, by potentiometry, under argon. The technique involved a reference electrode and ISE immersed in the molten salt. The reference electrode contained a silver wire immersed in molten NaCl-KCl and Ag_2O, and the ISE was constructed from CaO-ZrO_2, containing a nickel wire immersed in molten NaCl-KCl and NiO. The first experimental procedure involved the addition of BaO, CaO or MgO to the molten salt, and then measuring the activity of Ba^{2+}, Ca^{2+} or Mg^{2+} ions at the saturation limit. The second experimental procedure involved the addition of BaO to the molten salt, after calibration, containing $MgCl_2$. The titration curve displayed two equivalence points at -log 0.5 and -log 1, corresponding to the formation of Mg_2O^{2+} complex ions and MgO. They also found the K_d for Mg_2O^{2+} complex ions and MgO at -log 9.35, -log 8.5 respectively and K_{sp} values for BaO, CaO and MgO at -log 2.31, -log 9 and -log 5 respectively [148].

In 1981, Stern and Deanhard investigated the K_{sp} values for NiO and CoO in molten NaCl, at 827ºC, by potentiometry, under O_2 at 0.2 atm. The technique involved a reference electrode and ISE immersed in the molten salt. The reference electrode a silver wire immersed in molten NaCl and AgCl, and the ISE, was constructed from YSZ, containing a silver wire immersed in molten NaCl, AgCl and Na_2O. Initially, the salt was dried at 500ºC under vacuum to remove residual O^{2-} ion impurities. Then the molten salt was calibrated by additions of Na_2O, demonstrating good Nernstian behaviour. The experimental procedure involved the addition of Na_2O to the molten salt containing $NiCl_2$ and cobalt chloride ($CoCl_2$). The titration curve demonstrated 2 equivalence points, corresponding to the formation of NiO and nickel(III) sodium oxide ($NaNiO_2$). The titration curve demonstrated 3 equivalence points, corresponding to the formation of cobalt (II, III) oxide (CO_3O_4), CoO and cobalt(III) sodium dioxide ($NaCoO_2$), showing competing equilibrium within the system. The K_{sp} values for NiO and CO_3O_4 were reported to be 2.18 x 10^{-12} and 9.0 x 10^{-12} respectively (in mole fraction scale) [149].

In 1986, Martinot and Fuger investigated the K_{sp} values of ThO_2 and UO_2 in molten NaCl-KCl, at 700ºC, under argon. The technique involved an ISE and reference electrode immersed in the molten salt. The ISE was constructed from CaO-ZrO_2 containing a silver wire, immersed in molten AgCl, Na_2CO_3 and molten NaCl-KCl and the reference electrode contained a silver wire immersed in molten NaCl-KCl and AgCl. The molten salt was calibrated by additions of Na_2CO_3, demonstrating good Nernstian behaviour. The experimental procedure involved the addition of Na_2CO_3 to the molten salt, containing $ThCl_2$ and UCl_2. The titration curve showed one equivalence point, corresponding to the formation of ThO_2 and UO_2 respectively. The K_{sp} values for ThO_2 and UO_2 were reported to be -log 15.5 and -log 18.0 respectively [134].

In 1991, Volovich investigated the K_{sp} values of CaO, Li_2O and BaO in molten NaCl-KCl, between 700-800ºC, by isothermal saturation, under argon. Initially the NaCl was dried between 160-200ºC to remove residual O^{2-} ion impurities. The experimental procedure involved the addition of CaO to the molten salt up to the saturation limit. Then samples of the salt were analysed by complexometric titration. The K_{sp} values for CaO, Li_2O and BaO were reported to be -log 1.84, -log 1.37, -log 0.96 respectively [150].

In the same year, Volovich investigated the K_{sp} values of PbO in molten NaCl-KCl, at 700ºC, under argon. The technique involved an ISE and reference electrode immersed in the molten salt. The ISE was constructed from YSZ, with a platinum wire immersed in molten NaCl-KCl and Ag_2O, and the reference electrode contained a silver wire immersed in molten NaCl-KCl and AgCl. Initially the salt was dried, between 160-200ºC to remove residual O^{2-} ion impurities. The molten salt was calibrated by additions of Na_2CO_3, demonstrating good Nernstian behaviour. The experimental procedure involved the addition of Na_2CO_3 to the molten salt containing $PbCl_2$. The titration curve exhibited one equivalence point at 1, corresponding to the formation of PbO. The K_{sp} value for PbO was reported to be -log 4.72 [129].

In the same year, Watson and Perry investigated the K_{sp} values of ZnO in molten KCl, at 800ºC, by potentiometry, under argon. The technique involved an ISE and reference electrode immersed in the molten salt. The ISE was constructed from YSZ, containing and a platinum wire immersed in molten KCl and NiO and the reference electrode contained a silver wire immersed in molten AgCl and KCl. Initially the salt was prepared by bubbling through HCl to remove residual O^{2-} ion impurities. The molten salt was calibrated by additions of Na_2O, demonstrating good Nernstian behaviour.

The first experimental procedure involved additions of Na_2O to the molten salt containing $ZnCl_2$. The titration curve demonstrated an equivalence point at 1, corresponding to the formation of ZnO. The second experimental procedure involved the addition of $ZnCl_2$ to the molten salt, containing ZnO. The titration curve demonstrated an equivalence point at 0.5, corresponding to the formation of ZnO_2^{2-} complex ions. The K_{sp} values of ZnO was reported to be 2.3 x 10^{-8} mol kg^{-1} (-log 1.18) and the K_f values for the ZnO_2^{2-} complex ion was reported to be 3 x 10^{-12} mol^3 kg^{-3} [151].

In 1999, Koeller and Combes investigated the K_{sp} values of SrO in molten NaCl-KCl, at 727ºC, by potentiometry, under argon. The technique involved an ISE and reference electrode immersed in the molten salt. The ISE was constructed from ZrO_2-ZrO_2 containing a nickel wire, NiO and molten NaCl-KCl, and the reference electrode contained a silver wire, AgCl and molten NaCl-KCl. Initially the salt was dried under vacuum to remove residual O^{2-} ion impurities. Then the molten salt was calibrated by additions of BaO, demonstrating good Nernstian behaviour. The experimental procedure involved the addition of BaO to the molten salt containing strontium chloride ($SrCl_2$). The titration curve demonstrated an equivalence point at 1, corresponding to the formation of SrO. The K_{sp} value for SrO was reported to be -log 4.2 [152].

In the same year, Barbin et al investigated the solubility of Li_2O in molten KCl-NaCl, between 700-800ºC, by isothermal saturation, under argon. Initially the salt was dehydrated under vacuum, and treated with HCl, Cl_2 and helium (to remove residual O^{2-} ion impurities. The experimental procedure involved the addition of a sintered Li_2O pellet to the molten salt. Samples of the salt was analysed at regular intervals, and the solubility of Li_2O determined using an alkalinity test. The solubility of Li_2O was reported to be -log 0.107 (in mole fraction) [153].

In 2002, Koeller and Combes investigated the K_{sp} values of CaO in molten NaCl, between 827-927ºC, using potentiometry, under argon. The technique involved an ISE and reference electrode immersed in the molten salt. The ISE was constructed from CaO-ZrO_2, containing a nickel wire, Na_2CO_3 and molten NaCl, and the reference electrode contained a nickel wire immersed in molten NaCl. Then the molten salt was calibrated by additions of Na_2CO_3, demonstrating good Nernstian behaviour. The experimental procedure involved the addition of CaO to the molten salt up to the saturation limit. The K_{sp} values for CaO are reported to be -log 4.3 at 827ºC, -log 4.1 at 877ºC and -log 3.9 at 927ºC [154].

In the same year, Cherginets investigated the K_{sp} values of CaO in molten NaCl-KCl at 830ºC, under argon. The technique involved an ISE and reference electrode immersed in the molten salt. The ISE was constructed from YSZ, containing a platinum wire under O_2, and the reference electrode contained a platinum wire immersed in molten NaCl-KCl and AgCl. Then the molten salt was calibrated by additions of NaOH, demonstrating two linear sections with an inflection point at -log 2 corresponding to the formation of O_2^{2-} ions. The experimental procedure involved adding CaO to the molten salt up to the saturation limit. The K_{sp} values of CaO was reported to be -log 3.77, K_d value at -log 2.59, amount of non-dissociated oxide at 0.066 mol kg^{-1} and Ca^{2+} ion activity at 0.013 mol kg^{-1} [156]. A complete list of K_{sp} values for various oxides in molten NaCl, KCl and NaCl-KCl are reported in table 2.4.

Name	Compound	-log K_{sp}	Temperature (ºC)	Melt
Calcium oxide	CaO	1.60	900	NaCl
		1.11	900	NaCl-KCl
		1.77	900	KCl
		14.6	706	NaCl-KCl
		15.4	710	NaCl-KCl
		5	727	NaCl-KCl
		4.3	820	NaCl-KCl
		9	727	NaCl-KCl
		9.0 x 10^{-12} (mole fraction)	827	NaCl-KCl
		1.84	727	NaCl-KCl
		4.3	827	NaCl-KCl
		4.1	827	NaCl-KCl
		3.77	827	NaCl-KCl
Strontium oxide	SrO	1.77	900	NaCl
		0.93	900	NaCl-KCl
		1.77	900	KCl
		4.2	800	NaCl-KCl
Barium oxide	BaO	1.36	900	NaCl
		1.09	900	NaCl-KCl
		1.75	900	KCl
Cerium(III) oxide	Ce_2O_3	30	727	NaCl-KCl
Magnesium oxide	MgO	2.31	727	NaCl-KCl
Nickel oxide	NiO	12.4	827	NaCl-KCl
		2.18 x 10^{-12} (mole fraction)	827	NaCl
Thorium oxide	ThO_2	15.5	727	NaCl-KCl
Uranium oxide	UO_2	18	727	NaCl-KCl
Lithium oxide	Li_2O	**0.107 (mole fraction)**	727	NaCl-KCl
Lead oxide	PbO	4.72	700	NaCl-KCl
Zinc oxide	ZnO	**2.3 x 10^{-8} (mole fraction)**	800	NaCl-KCl

Table 2.4: K_{sp} values of compounds in molten NaCl-KCl, NaCl and KCl (produced by author) [144-155].

2.3.3.3 Solubility products of compounds in molten $CaCl_2$-NaCl

Molten $CaCl_2$-NaCl is used as a solvent for the pyrochemical reprocessing of nuclear fuel, due to its low eutectic point (at 504ºC) [156]. This application is dependent upon the O^{2-} ion activity in the molten salt, which can have a detrimental influence upon the preferred reactions therefore K_{sp} values in this molten salt are frequently investigated.

In 1997, Castrillego et al investigated the K_{sp} values of MgO in molten $CaCl_2$-NaCl, at 575ºC, using potentiometry, under argon. The technique involved an ISE and reference electrode immersed in the molten salt. The ISE was constructed from YSZ, containing a silver wire immersed in molten $CaCl_2$-NaCl and Ag_2O and the reference electrode contained a silver wire immersed in molten $CaCl_2$-NaCl and AgCl. Initially, the molten salt was treated under vacuum and HCl and argon to remove residual O^{2-} impurities. The experimental procedure then involved the addition of Na_2CO_3 to the molten salt containing $MgCl_2$. The molten salt was calibrated with additions of Na_2CO_3, demonstrating a Nernstian response. The titration curve displayed one equivalence point corresponding to the formation of MgO. The K_{sp} value for MgO was reported to be -log 5.3 [157].

In 1998, Martinez et al investigated the K_{sp} values for titanium oxide (TiO) and titanium(III) oxide (Ti_2O_3) in molten $CaCl_2$-NaCl, at 550ºC, under argon. The technique involved an ISE and reference electrode immersed in the molten salt. The ISE was constructed from YSZ, containing a silver wire immersed in molten $CaCl_2$-NaCl, AgCl and Ag_2O, and the reference electrode contained a silver wire immersed in molten $CaCl_2$-NaCl and AgCl. The experimental procedure involved the addition of Na_2CO_3 to the molten salt, containing titanium tetrachloride ($TiCl_3$) or titanium dichloride ($TiCl_2$) solution. The titration curve demonstrated one equivalence point at 1 and 1.5 corresponding to the formation of TiO and Ti_2O_3. The K_{sp} values for TiO and Ti_2O_3 were reported to be -log 9.01 and -log 25.7 respectively [158].

In 2002, Lambertin et al investigated the K_{sp} values of Pu_2O_3 in molten $CaCl_2$-NaCl, at 550ºC, by potentiometry, under argon. The technique involved an ISE and reference electrode immersed in the molten salt. The ISE was constructed from YSZ, containing a silver wire immersed in molten NaCl-$CaCl_2$, AgCl and Na_2CO_3, and the reference electrode contained a silver wire immersed in molten NaCl-$CaCl_2$ and AgCl. Initially, the salt was fused under argon, followed by the addition of graphite powder and bubbling Cl_2 to remove residual O^{2-} ion impurities. The molten salt was then calibrated by additions of Na_2CO_3, demonstrating good Nernstian behaviour. The experimental procedure involved the addition of Na_2CO_3 to the molten salt containing $PuCl_3$. The titration curve displayed one equivalence point at 1, corresponding to the formation of Pu_2O_3. The K_{sp} value for Pu_2O_3 was reported to be -log 17.5 [159].

In 2008, Wang et al investigated the solubility of CaO in molten $CaCl_2$-NaCl, $CaCl_2$-KCl, $CaCl_2$-$SrCl_2$, $CaCl_2$-$BaCl_2$, $CaCl_2$-LiCl, between 600-950ºC, by isothermal saturation. The salts were dried at between 100-200ºC to remove residual O^{2-} ion impurities. The experimental procedure involved the addition of CaO to the molten salt and then removing samples at regular intervals. These samples were analysed by NaOH solution and then titrated with dibutyl orthophthalate, NaOH, and HCl solution. They found the K_{sp} values for CaO to be at 15 wt% ($CaCl_2$ at 877ºC), 5 wt% ($CaCl_2$-NaCl at 727ºC), 4 wt% ($CaCl_2$-KCl at 877ºC), 6 wt% at ($CaCl_2$-$SrCl_2$ at 877ºC), 6 wt% ($CaCl_2$-$BaCl_2$ at 877ºC) and 7 wt% ($CaCl_2$-LiCl at 627ºC) [160]. A complete list of K_{sp} values for various oxides in molten $CaCl_2$-NaCl are reported in table 2.5.

Name	**Compound**	**-log K_{sp}**	**Temperature (ºC)**
Magnesium oxide	MgO	5.3	575
Calcium oxide	CaO	**5 (wt%)**	600-950
Titanium oxide	TiO	9.01	550
Titanium(III) oxide	Ti_2O_3	25.7	550
Plutonium(III) oxide	Pu_2O_3	17.5	550

Table 2.5: K_{sp} values of compounds in molten $CaCl_2$-NaCl (produced by author) [157-160].

2.3 Molten salt synthesis of compounds

MSS of compounds involve mixing reactant (s) with an excess of salt, in a crucible, under a modified atmosphere or under air. The crucibles are made from either alumina (Al_2O_3), zirconia (ZrO_2) or SiO_2, depending upon the selection of the molten salt, to avoid any interaction with the container materials [50] [161]. The crucible is then heated in a furnace above the melting point of the salt, where the reactants dissolve and react with in solution. During this process, the salt behaves as a solvent and/or as a reactant and upon completion, the molten salt is cooled and washed with H_2O, alcohol, or mechanically separated to obtain the final product [50]. When using hydroscopic salts (such as nitrates), the salt is pre-treated (such as drying under vacuum) to eliminate any H_2O attached to the salt [215]. The product is then analysed using thermo gravimetric analysis (TGA), XRD, infrared (IR) spectroscopy, gas chromatography (GC), or transmission electron microscopy (TEM) [161-188].

There have been many investigations into the MSS of compounds in molten chlorides, nitrates and fluorides [161-188]. The scale of materials synthesised are extensive therefore the author has selected the compounds; ZrO_2, Al_2O_3, and titanium dioxide (TiO_2) and previous studies for the MSS of cement compounds. These are examples of oxides and silicates due to the assimilation of the O^{2-} and Si^{4+} ions into the crystal structure, similar to the cementitious compounds being synthesised.

2.3.1 Molten salt synthesis of ZrO_2

ZrO_2 is used in gas sensors, fuel cells, coatings and catalytic agents, advanced metal oxide semiconductors (MOS) and dynamic random-access memory (DRAM) devices due to its wide band gap and high dielectric constant ($\varepsilon \sim 25$) [161]. It also exhibits several polymorphic transitions including a monoclinic polymorph (m-ZrO_2), below 1170ºC, a tetragonal polymorph (t-ZrO_2), between 1170-2370ºC, and a cubic polymorph (c-ZrO_2) between 2370-2706ºC [162]. This makes the synthesis of ZrO_2 complicated and doping with additives is required to stabilize the phases, making the MSS of ZrO_2 attractive to many scientists/technologists.

The first authors to produce crystals of ZrO_2 in molten salts were Kerridge and Rey, in 1975, using thermo gravimetric analysis (TGA), XRD, infrared spectroscopy (IR) and gas chromatography (GC). They produced crystals of m-ZrO_2 by reacting zirconium(IV) sulphate ($Zr(SO_4)_2$) in molten $LiNO_3$-KNO_3 at ~200ºC. They also increased the basicity of the molten salt, by adding sodium peroxide (Na_2O_2), sodium oxide (Na_2O) or sodium hydroxide (NaOH), which was found to reduce reaction temperatures, to 150ºC. In all cases, they found a soluble intermediate forming, before the formation of m-ZrO_2, deduced to be zirconium nitrate ($Zr(NO_3)_4$). They also found m-ZrO_2 depleted slowly after being formed, probably due to the formation of a zirconate, which was stronger as the basicity of the molten salt increased [163].

In 1994, Raihani et al investigated the MSS of ZrO_2 using TGA, XRD and transmission electron microscopy (TEM), by reacting $Zr(SO_4)_2$ in molten sodium nitrate ($NaNO_3$), $LiNO_3$-KNO_3, $NaNO_3$-KNO_3, $NaNO_2$-KNO_2, between 300-500ºC. They found that multi-stage reactions occurred in molten $NaNO_3$ at 500ºC, which didn’t go to completion. They also increased the molten salt basicity, by adding NaCl and Na_2CO_3. In both cases, the reactions went to completion but for different reasons. In molten NaCl-$NaNO_3$, this was probably due to the complexing effect of Cl^- ions. In molten Na_2CO_3-$NaNO_3$, this was probably due to the formation of sodium zirconate (Na_2ZrO_3), forming at a lower reaction temperature (at ~440ºC). Upon adding KNO_2 to molten $LiNO_3$-KNO_3, both m-ZrO_2 and t-ZrO_2 crystals were formed by multi-stage reactions. When using molten $NaNO_2$-KNO_2, only t-ZrO_2 crystals were formed a single reaction occurred (below 200ºC). The t-ZrO_2 crystals obtained at 450ºC in molten $NaNO_2$-KNO_2 were agglomerates; with spherical grains ~6 nm in diameter and a specific surface area greater than 150 m^2 g. The t-ZrO_2 crystals obtained at 300ºC in molten $NaNO_2$-KNO_2 were agglomerates with smaller grains ~3 nm in diameter and a specific surface area of ~250 m^2 g [164].

In 1995, Afanasiev and Geantet investigated the MSS of ZrO_2, using XRD and TEM, by reacting zirconyl(IV) chloride, octahydrate ($ZrOCl_2.8H_2O$) or zirconyl nitrate dihydrate ($ZrO(NO_3)_2.2H_2O$) in molten $NaNO_3$-KNO_3, $LiNO_3$, $NaNO_3$ or molten potassium nitrate (KNO_3), between 300-500ºC. They found poor or amorphous crystalline phases were produced (at ~370ºC) and, crystalline phases of m-ZrO_2 and t-ZrO_2 were produced (between 400-500ºC). They also found the surface area of the crystals varied according to the reaction temperatures and molten salt, which ranged between 50-220m^2 g^{-1}. The crystallite sizes of the final products also ranged for the different salts and temperatures; between 300-370ºC, (from highest to lowest) was $LiNO_3$ > $NaNO_3$ > KNO_3, between 400-430ºC, was $NaNO_3$ > $LiNO_3$ > KNO_3, and between 430-500ºC, was $LiNO_3$ > $NaNO_3$ > KNO_3. Above 430ºC, the crystallite sizes were small in all melts, probably due to the increasing growth of nuclei and division of crystals. In all cases, the product purities were high as the residual element activity was low, at ~0.2 wt% [165].

In the same year, Du and lnman investigated the MSS of ZrO_2, using XRD, TG, DTG and DTA, by reacting $Zr(SO_4)_2$ in molten $NaNO_3$, $LiNO_3$-KNO_3, $NaNO_3$-KNO_3 and $NaNO_2$-KNO_2, between 170-460ºC. They found a single reaction occurred in molten $NaNO_2$-KNO_2, between 170-250ºC, and multiple reactions occurred in molten $NaNO_3$-KNO_3, $LiNO_3$-KNO_3 and molten $NaNO_3$, between 200-460ºC. In general, m-ZrO_2 and t-ZrO_2 crystals were produced in the nitrate melts, and only t-ZrO_2 crystals in the nitrite melt. Also in the nitrate melts, the crystallite sizes were between 1-20 nm and lower than 10 nm in the nitrite melts, probably due to the increase of reactivity of the melt. They also found the reaction in the nitrite melt to be second order with activation energy of ~183 kJ mol^{-1} [166].

In 1996, Du and Inman investigated the MSS of ZrO_2, using TGA and XRD, by reacting α-$Zr(SO_4)_2$ or β-$Zr(SO_4)_2$ in molten $NaNO_2$-KNO_2, $LiNO_3$-KNO_3 and $NaNO_3$-KNO_3, between 300-450ºC. They found t-ZrO_2 crystals were produced in molten $NaNO_2$-KNO_2 below 270ºC, producing crystallite sizes of ~3.8 nm. Upon increasing the temperature to 450ºC, the crystallite sizes became smaller (at ~3.5 nm) and reducing the temperature to 320ºC, caused the crystallite sizes to become larger (at ~4.6 nm), probably due to faster reaction times. In the $LiNO_3$-KNO_3 binary system and molten $NaNO_3$-KNO_3, both t-ZrO_2 and m-ZrO_2 crystals were produced with crystallite sizes between 10-20 nm, probably due to multiple or side reactions. In all cases, an increase in temperature (higher than 400ºC) favoured the formation of crystalline phases, and reducing the temperature (to ~350ºC) favoured non-crystalline or amorphous phases. This was probably caused by a slow reaction rate, leading to fewer nuclei, but larger crystal sizes. In all cases, the product purities were high as the residual element activity was low, at ~1.5 wt% [167].

In the same year, Du et al investigated the MSS of ZrO_2, using XRD and TEM, by reacting $Zr(SO_4)_2$ in molten $NaNO_3$-KNO_3, between 200-450ºC. They found that m-ZrO_2 and t-ZrO_2 crystals were produced via two reactions in molten $NaNO_3$-KNO_3, at ~200ºC. Also by increasing the melt basicity, through the addition of Na_2O_2 and Na_2CO_3 and using molten $NaNO_2$-KNO_2, the reaction temperature was lowered to ~130ºC. This was probably caused by the increase of O^{2-} ions in the molten salt, causing multiple or side reactions to take place. A direct relationship was found between the proportion of the t-ZrO_2 phase in the final product, and basicity of the molten salt (reaching 100% at 20 mol% of Na_2O_2, 20 mol% of Na_2CO_3, and 40% mol of $NaNO_2$-KNO_2). The crystallite sizes were also found to decrease according to the same relationship [168].

In 1997, Afanasiev investigated the MSS of ZrO_2, using XRD, atomic emission spectroscopy (AES) and N_2 gas adsorption, by reacting $ZrOCl_2.8H_2O$ in molten $NaNO_3$-KNO_3, at 500ºC. They also investigated the effect of adding fluoride ions to the molten salt, by adding ammonium hydrogen fluoride (NH_4HF_2). They found that NH_4HF_2 promoted the formation of m-ZrO_2 crystals, with mean radiuses, surface areas and pore volumes increasing up to 0.05 wt% NH_4HF_2 and decreasing up to 1 wt% NH_4HF_2. The amount of residual Na^+ and F^- ions in the final product were also low and irregular, between 0.1-0.2 wt%. This was probably caused by F^- ions becoming partially bound to the final precipitate [169].

In 2002, Maroto et al investigated the MSS of ZrO_2, using XRD DTA, TGA and SEM, by reacting $ZrOCl_2.8H_2O$ or zirconium dichloride ($ZrCl_2$) in molten lithium nitrate ($LiNO_3$) or $NaNO_3$, at 450ºC. They found that in molten $LiNO_3$ and $NaNO_3$, $ZrOCl_2.8H_2O$ promoted the formation of the m-ZrO_2 crystals with t-ZrO_2 only present lower than 10 wt%. In molten $LiNO_3$ and $NaNO_3$, $ZrOCl_2.8H_2O$ promoted the formation of the t-ZrO_2 crystals, with only the t-ZrO_2 crystals present lower than 70 wt%. Also, in molten $LiNO_3$ and $NaNO_3$, $ZrOCl_2.8H_2O$ promoted larger crystallite sizes of m-ZrO_2, of ~10 nm and ~8 nm respectively, and t-ZrO_2, of ~13 nm and ~8 nm respectively. When using $ZrCl_2$ in the same melts, crystallite sizes of t-ZrO_2 and m-ZrO_2 were much larger and more dispersed, between 12-20 nm and 8-16 nm respectively. The crystal surface areas were also larger when using $ZrOCl_2.8H_2O$, between 104-204 $m^2.g^{-1}$ than using $ZrCl_2$, between 63-91 $m^2.g^{-1}$. In all cases, the product purities were high as the residual element activity was low, between 0.3-3.4 wt% [170].

The MSS of ZrO_2 are not limited to nitrate and nitrite melts. In 1982, Finch and Belcher investigated the MSS of m-ZrO_2 using atomic emission spectroscopy (AES), by passing H_2O through molten LiF-NaF, between 650-800ºC and adding zirconium fluoride (ZrF_4). The final product formed crystallite sizes up to ~3 mm, with an etched appearance, probably caused by the low solubility of ZrO_2 in the molten salt. The impurity levels of the residual elements were also low, with the highest element detected being nickel (at 0.5 wt%) [171].

2.3.2 Molten salt synthesis of Al_2O_3

Al_2O_3 has been used as a catalyst, catalyst carrier and adsorbent, due to its high catalytic activity and high surface area [50]. In addition, its main mineral form, bauxite, is used as a reactant in aluminium smelting [57]. However the synthesis of Al_2O_3 is complicated, due to its many metastable polymorphs (γ, η, κ, θ, α, ι, δ, ε, χ), besides its main stable alpha-alumina (α-Al_2O_3) form. These polymorphs are dependent upon the choice of starting materials and conditions. The most common method of producing Al_2O_3 is by precipitation or sol-gel methods, however more recently, MSS has proven to be successful route [172-178].

The first MSS study of Al_2O_3 was by Kerridge and Shakir in 1990, where they investigated the MSS of Al_2O_3 by reacting aluminium(III) chloride ($AlCl_3$) or aluminium sulphate ($Al_2(SO_4)_3$) in molten $LiNO_3$-KNO_3, between 140-450ºC. When using $AlCl_3$, a yellow suspension initially formed, at 200ºC, which led to the formation of α-Al_2O_3, and evolution of NO_2 and O_2. When using $Al_2(SO_4)_3$ at 320ºC, the reactants were incompletely soluble, with evidence of a yellow-white suspension, forming γ-Al_2O_3 along with the evolution of NO_2 and O_2 [172].

In 1996, Du and Inman investigated the MSS of Al_2O_3, using XRD, atomic adsorption spectroscopy (AAS) and TEM, by reacting $Al_2(SO_4)_3$ or $AlCl_3$ in molten $NaNO_3$, the $NaNO_3$-KNO_3 binary system, molten $LiNO_3$-KNO_3, and the $NaNO_2$-KNO_2 binary system at ~400ºC. They also investigated the effects of increasing the basicity of the molten salt, by adding Na_2O_2 and Na_2CO_3. They found that in molten $NaNO_2$-KNO_2, reaction temperatures were lower than molten nitrates. Also when using $AlCl_3$ in molten $NaNO_2$-KNO_2, reaction temperatures were lower at ~160ºC, than using $Al_2(SO_4)_3$, at ~210ºC. This probably occurred due to the rise of O^{2-} ions in the salt, accelerating the reaction between Al^{3+} and O^{2-} ions to form Al_2O_3. In all cases, fine or poorly crystallite powders of α-Al_2O_3 were produced. Also, when using $AlCl_3$ in molten $NaNO_2$-KNO_2, the crystallite sizes were below 10 nm, in comparison to when using $Al_2(SO_4)_3$, causing crystallite between 1-2 nm. The total impurity levels of the elements; sodium and potassium were also low (at ~0.5 wt%) indicating a high product purity [173].

In 1998, Hashimoto and Yamaguchi investigated the MSS of Al_2O_3, using SEM, XRD, DTA and TG, by reacting $Al_2(SO_4)_3$ in molten potassium sulphate (K_2SO_4), between 1000-1300ºC. The final product was washed with hydrochloric acid (HCl), between 70-80ºC, to produce porous aggregations of α-Al_2O_3 platelets, with crystallite sizes of ~10 μm. They found the surface area of the crystals reached a maximum of 5.2 m^2 g^{-1} at 1000ºC, and minimum of 0.7 m^2 g^{-1} at 1100ºC. They also found increasing the amount of K_2SO_4, increased the Al_2O_3 crystallite sizes [174].

In 1999, Hashimoto and Yamaguchi investigated the MSS of Al_2O_3, using SEM, XRD, DTA and TG, by reacting $Al_2(SO_4)_3$ or γ-Al_2O_3 in molten sodium sulphate (Na_2SO_4) at 1100ºC. The final product was then washed with HCl, between 70-80ºC, to produce porous aggregations of α-Al_2O_3 platelets, with crystallite sizes of ~5 μm. They found that increasing the amount of Na_2SO_4, caused hexagonal α-Al_2O_3 platelets to form, which increased in size up to 120 μm. They also found when using γ-Al_2O_3, platelets of α-Al_2O_3 were produced with average diameters of 3.7 μm and thickness of 0.3 μm. Upon increasing the amount of Na_2SO_4, hexagonal α-Al_2O_3 platelets with crystallite sizes of 5 μm were produced [175].

In 2008, Li-Hui et al investigated the MSS of Al_2O_3, using SEM and XRD, by reacting aluminium hydroxide ($Al(OH)_3$), amorphous Al_2O_3 or α-Al_2O_3 in the NaCl-KCl binary system, between 900-1000ºC. They found when using $Al(OH)_3$, both γ-Al_2O_3 and κ-Al_2O_3 platelets were produced, at 900ºC and only α-Al_2O_3, at 1100ºC. The surface area of the platelets decreased at higher temperatures, from 62 m^2 g^{-1} at 900ºC, to 16 $m^2 g^{-1}$at 1100ºC. When amorphous α-Al_2O_3 was used, only α-Al_2O_3

platelets were produced, between 900-1100ºC. There was no significant difference, between increasing temperature and the surface area of the platelets, shown by sizes of 1.7 m^2 g^{-1} at 900ºC, and 1.6 m^2g^{-1} at 1100ºC. When using molten NaCl-KCl and amorphous Al_2O_3 crystals as reactants, the formation of α-Al_2O_3 crystals was favoured, probably because the salt would remain inside the crystal, increasing the interfacial area [176].

In 2011, Li-Hui and Huang investigated the MSS of Al_2O_3, using SEM and XRD, by reacting aluminium sulphate octadecahydrate (($Al_2(SO_4)_3.18H_2O$)) in molten Na_2SO_4-K_2SO_4 or NaCl-KCl, between 1100-1300ºC. They also investigated the effect of using Na_2CO_3, trisodium phosphate dodecahydrate ($Na_3PO_4.12H_2O$), titanium(IV) oxysulfate ($TiOSO_4$) and α-Al_2O_3 as additives. They found most α-Al_2O_3 platelets were hexagonal, with some overlapping and upon increasing the amount of salt, caused their diameters and number of crystals to increase. This was probably because more space was available inside the molten salt, allowing a higher diffusivity of the reactants. Upon the addition of $Na_3PO_4.12H_2O$, α-Al_2O_3 platelets of irregular shapes were obtained whilst the addition of $TiOSO_4$, allowed thick α-Al_2O_3 particles of hexagonal shapes to be produced. When both $Na_3PO_4.12H_2O$ and titanium(IV) oxysulfate ($TiOSO_4$) were used, thin α-Al_2O_3 platelets of discal shapes would form. The addition of α-Al_2O_3 increased the size of α-Al_2O_3 platelets, but caused overlapping and abnormal crystal growth [177].

In 2011, Li-Hui et al investigated the MSS of Al_2O_3, using SEM and XRD, by reacting $NaAlO_2$ in molten Na_2SO_4-K_2SO_4 and molten NaCl-KCl, between 900-1400ºC. They also investigated the effect of using $TiOSO_4$, $Na_3PO_4.12H_2O$ and α-Al_2O_3 as additives. They found as the temperature increased (up to 1200ºC), and amount of salt increased, the size distribution of α-Al_2O_3 platelets also increased, with minimal overlapping. They also found in molten Na_2SO_4-K_2SO_4 at 1200ºC, platelets with diameters of 7.5 μm were produced and platelets with diameters of 5.8 μm in molten NaCl-KCl. Upon the addition of α-Al_2O_3, the diameter of platelets decreased in both molten Na_2SO_4-K_2SO_4 and molten NaCl-KCl, to 5.8 μm and 1.5 μm respectively. When both $Na_3PO_4.12H_2O$ and $TiOSO_4$ were added, thinner platelets of discal shapes were obtained [178].

2.3.3 Molten salt synthesis of TiO_2

TiO_2 has been used in environmental remediation, solar cells, lithium ion batteries, gas sensors, photonic crystals and self cleaning coatings, due to its chemical stability, environmental friendless and low cost [50]. The production of TiO_2 is complicated due to its several polymorphs; including rutile, antase (which is metastable) and brookite phases. In addition, up to five polymorphs also exist at high pressures [50]. TiO_2 is currently produced by flame aerosol synthesis, hydrothermal synthesis, sol-gel synthesis, and more recently, MSS has proven to be successful route [179-184].

One of the first MSS studies of TiO_2 was by Kerridge and Rey, in 1977 using TGA, where they produced antase crystals of TiO_2 and other titanates by reacting potassium(IV) hexafluorotitanate (K_2TiF_6) in molten $LiNO_3$-KNO_3, between 130-320ºC. They also investigated the effects of increasing the basicity of the salt, by adding Na_2O_2, Na_2O or NaOH. They found reactions in molten $LiNO_3$-KNO_3 were rapid, at 320ºC, producing TiO_2 along with NO_2 and O_2 and slower at lower temperatures. Upon increasing the melt basicity, different reactions were observed, for example, upon the addition of Na_2O_2, antase TiO_2 was produced, with only the evolution of O_2, at lower temperatures. When using excess quantities of Na_2O_2, at 230ºC, Na_2O_2 decomposed to Na_2O to produce a titanate, instead of TiO_2. Upon the addition of Na_2O and excess quantities of K_2TiF_6, antase TiO_2 was produced, at 200ºC, without the evolution of a gas. When Na_2O was used in excess, various titanates were produced instead of TiO_2. Upon the addition of NaOH, antase TiO_2 was produced, at 180ºC, with the evolution of H_2. When using excess quantities of NaOH, titanates were produced instead of TiO_2 and finally when using excess quantities of K_2TiF_6, with Na_2O, a mixture of antase TiO_2 and titanates were produced [179].

In 2006, Afanasiev investigated the MSS of TiO_2 using mass spectroscopy (MS) and SEM, by reacting titanium oxysulfate ($TiOSO_4$) or TiO_2 in molten lithium nitrate ($LiNO_3$), molten KNO_3 or molten $NaNO_3$, between 400-550ºC. They also investigated the effect of increasing the basicity of the melt by adding potassium hydroxide (KOH), NaOH, Na_2CO_3, and potassium carbonate (K_2CO_3). They found shorter reaction times at temperatures below 500ºC were insufficient to produce pure titanates, leading to mixtures of TiO_2 and titanates to be produced. As the temperature or basicity of the salt decreased, the sequence of compounds obtained were; $TiOSO_4$,

TiO_2, $Alk_2Ti_6O_{13}$, $Alk_2Ti_4O_9$, $Alk_2Ti_2O_5$ and Alk_2TiO_3. When salts were used in excess quantities, a single phase TiO_2 was produced over a wide temperature range. They also found the morphology and composition varied as a function of the reaction conditions, for example when potassium based preparations were used, particles formed rods, whiskers, lamellae and when using sodium based preparations, fine dispersions were used. This was probably because the rod-like particles were intermediate phases, due to reactants not being fully dissolved in the salt, which underwent pseudomorphic transformations or the ionic salt promoted the selective growth of specific crystallographic planes. The final products produced were rod-like dispersions of TiO_2 and other titanates, with crystallite sizes, between 1-10 μm [180].

In 2011, Kozakova et al investigated the MSS of TiO_2 nanorods, using XRD and SEM, by reacting TiO_2 in molten $NaCl$-$Na_2HPO_4.12H_2O$, above 735ºC, after exposure to 750W microwaves. They found that samples prepared by dry homogenization produced pure rutile TiO_2 whilst wet homogenisation resulted in mixture of antase and rutile TiO_2 or the formation of elongated particles. This was probably due to the encompassment of TiO_2 particles, forming of diffusion barrier, causing the reactants to coalesce into complex structures. The final products produced were nanorods of antase TiO_2 with crystallite sizes between 2-10 μm [181].

In 2012, Han et al investigated the MSS of rutile TiO_2, using XRD and SEM, by reacting TiO_2 slag in molten NaOH, at 500ºC. The final product was washed and treated with H_2SO_4 (at 50ºC) and hydrolyzed to sodium metatitanate (Na_2TiO_3), which was then calcined, at 940ºC, and doped to produce dispersed rutile TiO_2. They found impurities in the initial slag, such as chromium, aluminium, manganese and silicon could be separated during the washing process, and impurities such as iron, calcium and magnesium could be separated in the acid dissolution process. They also found at lower temperatures (at ~350ºC), the crystallinity of the final product was low, with a titanium conversion rate of 67.6%. As the temperature increased, to 500ºC, the crystallinity improved with a titanium conversion rate of 92.3%. After treating with Na_2TiO_3, coating and crushing, the TiO_2 content in the final product was 98.6 wt%. The final product had crystallite sizes between 0.1-0.4 μm [182].

Also in 2012, Wu et al investigated the MSS of rutile TiO_2 microrods, using XRD, SEM, photoluminescence (PL) and UV-visible spectroscopy (UV-vis), by reacting $TiOSO_4.H_2SO_4$ in molten hydrogen fluoride (HF), hydrogen peroxide (H_2O_2) and NaCl, at 810ºC. They found the transformation process of TiO_2 microrods was rapid, achieving a length of 100 μm and diameters between 1-5 μm. After 4 hours, the quantity of microrods increased and micro-particles decreased, and after 8 hours, ultra-long microrods were produced of lengths, between 200-500 μm and ~2 μm in diameter [183].

Also in 2012, Peining et al investigated the MSS of antase TiO_2 nanorods, using SEM and XRD, by reacting $TiOSO_4.H_2SO_4$ in molten $LiNO_3$ and molten LiCl at 280ºC. They found agglomerated nanostructures of diameters between 100-300 nm were produced, with aggregate sizes between 40-60 nm in diameter. These were each composed of smaller particles with an average diameter of ~5 nm with a surface area of ~200 $m^2 g^{-1}$ [184].

2.3.4 Molten salt synthesis of cement compounds

The effects of global warming and the rise of CO_2 emissions from the cement process led to the EPSRC funded project ULECES: Ultra low energy cement synthesis: A radical process change to achieve green and sustainable technologies project grant (EP/FO144499/1) in 2008 [185]. The objective of the project was to reduce reaction temperatures, energy consumption and hence CO_2 emissions by synthesising individual phases of cement in molten salts. The results of the project were reported in the following publications [185-188].

In 2011, Photiadis et al investigated the MSS of the cement compounds; β-Ca_2SiO_4 and Ca_3SiO_5, using SEM, XRD and Raman scattering, by reacting $CaCO_3$ and SiO_2 in molten NaCl, at 908ºC. They found that β-Ca_2SiO_4 was successfully synthesised, however the synthesis of Ca_3SiO_5 led to the formation of β-Ca_2SiO_4 and CaO, suggesting higher reaction temperatures were required. These observations also suggested that β-Ca_2SiO_4 was an intermediate compound during the formation of Ca_3SiO_5 [185].

In 2012, Maries et al investigated the resource efficiency (energy consumption and waste output), supply chain influences and management of a molten salt cement production process in comparison with the cement process, using a riskbased model. It was suggested a molten salt cement process would have lower reaction temperatures, lower fossil fuel consumption and lower CO_2 emissions than the conventional process. Also the possibility of using renewable sources of electricity to power the process and sequestering CO_2 into the molten salt were highlighted [186].

In 2014, Photiadis et al investigated the MSS of the cement compound; β-Ca_2SiO_4, by reacting $CaCO_3$ with SiO_2 in molten NaCl-$CaCl_2$ and $CaCl_2$, using Raman scattering and XRD at 900°C. However it was found the reaction in molten $CaCl_2$ produced calcium chlorosilicate ($Ca_2SiO_4 \cdot CaCl_2$) and the reaction in molten $CaCl_2$-NaCl produced mixtures of β-Ca_2SiO_4 and $Ca_2SiO_4 \cdot CaCl_2$ [187].

In 2015, Photiadis et al investigated the MSS of the cement compound; $Ca_3Al_2O_4$ by reacting $CaCO_3$ with Al_2O_3 in molten NaCl and $CaCl_2$ between 900-1100°C. However it was found the reaction in molten NaCl produced dodecacalcium heptaaluminate ($Ca_{12}Al_{14}O_{33}$) and the reaction in molten $CaCl_2$ produced $11CaO.7Al_2O_3.CaCl_2$ [188].

2.4 Diagrammatic representation of molten salt reactions

Molten salt reactions (including K_{sp} and K_f values) have been depicted on predominance diagrams [189-191]. These diagrams show the stability areas of dissolved or precipitated compounds at a specific molten salt activity and temperature [189-191]. These are analogous to Pourbaix diagrams (potential-pH diagrams), used to represent stability areas of species in aqueous solutions, where the specific ion activity is the H^+ ion [192]. The construction of predominance diagrams requires plotting the equilibrium potential (or redox potentials) of electrochemical reactions against the negative logarithm of a specific ion activity, often selected to be the O^{2-} ion for molten salts.

$$pO^{2-} = -\log [O^{2-}]$$ **Equation 2.5**

Equation 2.5 describes the definition for O^{2-} ion activity in molten salts, where $[O^{2-}]$ is the O^{2-} ion activity in the electrolyte and pO^{2-} is its negative logarithm and it is for this reason that predominance diagrams are often denoted potential-pO^{2-} diagrams. The equilibrium potentials are often equated to the standard redox potentials of electrochemical reactions, by neglecting the activity coefficient of the species in the electrolyte. The equilibrium (or standard redox potentials) and O^{2-} ion activity can be calculated using decomposition potentials of electrolytes, equilibrium potentials (by voltammatery), K_{sp} values (by potentiometry) and thermodynamic data [189-191]. Predominance diagrams can be used to describe the following processes.

- **Corrosion reactions of metals in molten salts;**
  These diagrams show stability domains of chemical species, where metals are immune to corrosion, where metals corrode, and where passivity of metals occur, at a specific temperature, pressure, O^{2-} ion and Me^{2+} ion activity.

- **Electrowinning of metals from molten salts;**
  The diagrams show the electrowinning pathways of metals and alloys from their ores (metal oxides) in molten salts. This can be obtained by following the equilibrium potential at a specific temperature, pressure, O^{2-} ion and Me^{2+} ion activity.

- **Precipitation of oxides from molten salts;**
  The diagrams show the K_{sp} and K_f values of oxides in molten salts (on the x-axis) which can be used to precipitate or dissolve compounds such as metal oxides, by knowledge of temperature, pressure, O^{2-} ion and Me^{2+} ion activity.

The construction of predominance diagrams is based upon representing chemical and electrochemical equilibria in molten salts in three combinations (according to Trémillon and Littlewood) [189-191].

- Chemical reactions (involving no electron transfer) are represented as vertical lines (on the x-axis) on predominance diagrams and independent of equilibrium potential (on the y-axis).

$$\Delta G^\circ = -RT\ln K \qquad \textbf{Equation 2.6}$$

Equation 2.6 describe the equilibria of a chemical reaction where ΔG° is the Gibbs free energy of the chemical reaction and K is the equilibrium constant of the chemical reaction. These can be substituted into each other to provide the following relationship.

$$\Delta G^\circ = -RTpO^{2-}$$ **Equation 2.7**

Equation 2.7 describes the equilibria of a chemical reaction involving O^{2-} ions, where ΔG° is the Gibbs free energy of the chemical reaction, pO^{2-} is the negative logarithm of the oxide ion activity, R is the universal gas constant and T is the temperature of the chemical reaction.

- Electrochemical reactions (involving electron transfer) are represented as horizontal lines (on the x-axis) on predominance diagrams and are independent of pO^{2-} (on the x-axis).

$$\Delta G^\circ = -nFE^\circ$$ **Equation 2.8**

Equation 2.8 describes the equilibria of an electrochemical reaction, where E_o is the equilribium potential of the electrochemical reaction, n is the number of electrons, ΔGo is the Gibbs free energy of the electrochemical reaction and F is the Faradays constant.

- Electrochemical and chemical equilibria (with electron transfer) are represented by straight lines on predominance diagrams and are dependent upon equilibrium potential (on the y-axis) and pO^{2-} (on the x-axis).

$$E = E^o + \frac{RT}{nF}K$$ **Equation 2.9**

$$E = E^o + \frac{RT}{nF}pO^{2-}$$ **Equation 2.10**

Equation 2.9-10 describes the equilibria for chemical and electrochemical reactions in molten salts, where E^o is the equilibrium potential of the electrochemical reaction, n is the number of electrons, R is the universal gas constant and K is the equilibrium constant of the electrochemical/chemical reaction.

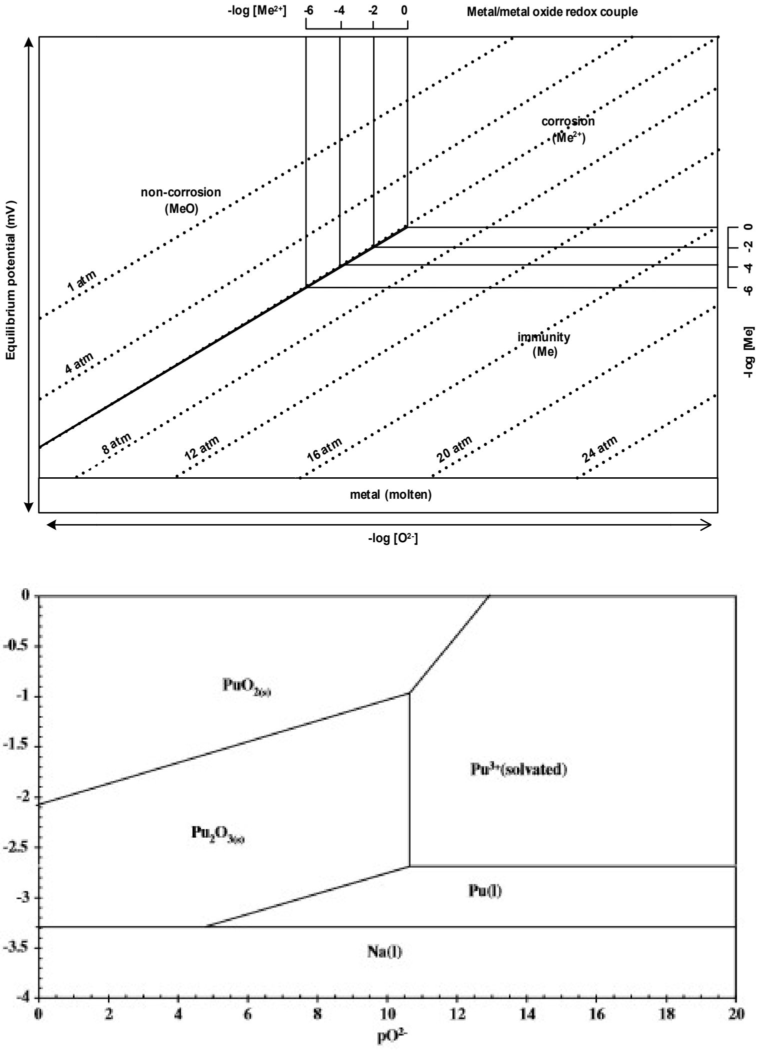

Figure 2.8: Predominance diagram for a metal in a molten chloride (produced by author) and plutonium in molten NaCl-KCl at 800°C, metal ion activity = 0.01 (in mole fraction) [189-191] [196].

Figure 2.8 shows a fundamental predominance diagram for a metal in a molten chloride, at a specific temperature and pressure, relative to a metal/metal chloride reduction potential and a preominance diagram for plutonum compounds in molten NaCl-KCl. The O^{2-} ion activity in a molten salt can be obtained by knowledge of the equilibrium potential (on the vertical axis), pressure (the dotted lines), Me^{2+} ion activity (on the horizontal [Me^{2+}] axis) and temperature, therefore Pu_2O_3 dissociates in molten NaCl-KCl at -log 10.2. Alternatively, the activity of a metal ion (on the vertical log [Me] axis) can be determined by knowledge of the O^{2-} ion activity.

Predominance diagrams have been constructed for molten chlorides, sulphates, carbonates and hydroxides (including their binary mixtures) [189-208]. The literature is extensive, thus predominance diagrams for metals in molten $CaCl_2$-NaCl, NaCl-KCl, KCl, NaCl and $CaCl_2$ will be investigated.

2.4.1 Diagrammatic representation of reactions in molten NaCl, KCl and NaCl-KCl

As described earlier, molten NaCl, KCl and NaCl-KCl have been used as electrolytes in molten carbonate fuel cells, and as solvents for the pyrochemical reprocessing of nuclear fuel, due to their low melting temperatures (at 801ºC and 770ºC and 727ºC), high electrical conductivity and high proliferation resistance over aqueous solvents [57]. These applications are dependent upon the O^{2-} ion activity in the molten salt; therefore predominance diagrams in these molten salts are frequently constructed.

The construction of predominance diagrams in molten salts initiated in 1962 when Littlewood, constructed the diagrams for magnesium, zirconium, nickel and titanium in molten $MgCl_2$, LiCl, potassium chloride (KCl) and NaCl, at 800ºC, relative to the Cl^-/Cl_2 reduction potential, at metal ion activities of 1, 10^{-2}, 10^{-4} and 10^{-6}. These diagrams showed the stability domains for Li_2O, potassium oxide (K_2O), Na_2O, NiO, MgO, ZrO_2, TiO, TiO_2, titanium(III) carbonate (Ti_2CO_3) and Mg^{2+}, Ni^{2+}, Zr^{2+}, Zr^{3+}, Zr^{4+}, Ti^{2+}, Ti^{3+}, Ti^{4+} ions in the molten salt. These were used to describe O^{2-} ion and metal ion activity in molten salts and applied to corrosion processes of metals in molten salts, electrowinning processes of metals from molten salts and reduction processes of molten salt by reactive metals. The diagrams also depicted the K_{sp} values for MgO in molten KCl, NiO in molten KCl, NiO in molten LiCl, ZrO_2 in molten KCl and titanium in molten $MgCl_2$, NaCl and KCl at -log 23, -log 19, -log 8, -log 19, and ~-log 22 respectively [189].

In 1974, Trémillon constructed predominance diagrams for nickel in molten NaCl and zirconium in molten KCl, at 800ºC, relative to the Na^+/Na reduction potential at metal ion activities of 10^{-2}, 10^{-4} and 10^{-6}. These diagrams were used to show the stability domains for NiO, ZrO_2, K_2O and Ni^{2+}, Zr^{3+}, Zr^{2+}, Zr^{4+} ions in the molten salt. The diagrams also showed the K_{sp} values for NiO and ZrO_2 in molten NaCl at -log 17 and -log 20 respectively [190].

In 1991, Nishikata et al constructed the predominance diagrams for nickel, magnesium zirconium and titanium in molten KCl, at 800ºC, relative to the Cl^-/ Cl_2 reduction potential, at metal ion activities of 10^{-2} and 10^{-6}. These diagrams showed the stability domains for NiO, MgO, ZrO_2, TiO_2, TiO, titanium(V) oxide (Ti_3O_4), titanium(III) oxide (Ti_2O_3) and Ni^{2+}, Zr^{2+}, Ti^{4+} ions in the molten salt and were used to describe the corrosion of metals in the molten salt. They suggested that although the diagrams illustrated the existence of oxide layers at high O^{2-} ion activities, these were most likely broken down by reactions with Cl^- ions in the molten salt. Also the K_{sp} values for NiO, MgO, ZrO_2 and TiO_2 in molten KCl were shown at -log19, -log 21, -log 20 and -log 25 respectively [194].

In 2000, Ishitsuka and Nose constructed the predominance diagram for chromium in molten NaCl-KCl. These were plotted at 727ºC, relative to the Cl^-/Cl_2 reduction potential, at metal ion activities of 10^{-2}, 10^{-4} and 10^{-6}. These diagrams showed the stability domains for the chromium(II) oxide (Cr_2O_3), Cr^{2+}, Cr^{3+}, Cr^{6+} ions and $Cr_2O_7^{2-}$, CrO_4^{2-} complex ions in the molten salt. These were used to describe the behaviour of Cr_2O_3 film in the molten salt, suggesting that these dissolve at high O^{2-} ion activities, forming CrO_4^{2-} complex ions. Also the K_{sp} values for Cr_2O_3 in molten NaCl-KCl were shown at -log 12 [195].

In 2005, Lambertin et al constructed the predominance diagrams for plutonium in molten NaCl-KCl and $CaCl_2$. These were plotted at 900ºC, relative to the Cl^-/Cl_2 reduction potential at metal ion activities of 10^{-2}. These diagrams showed the stability domains for Pu_2O_3, plutonium(IV) oxide (PuO_2) and the Pu^{2+} ion in the molten salt. It was shown that the stability domain for the Pu^{2+} ion was higher in molten $CaCl_2$ than NaCl-KCl. Also the K_{sp} values for Pu_2O_3 in molten NaCl-KCl and $CaCl_2$ were shown to be -log 10 and -log 6 respectively [196].

2.4.2 Diagrammatic representation of reactions in molten LiCl-KCl

As described earlier, molten LiCl-KCl is used as electrolytes in molten salt batteries, molten carbonate fuel cells and solvents for the pyrochemical reprocessing of nuclear fuel, due to its low melting temperature (at 348ºC) and high proliferation resistance over aqueous solvents [57-58]. These applications are dependent upon the O^{2-} ion activity in the molten salt; therefore predominance diagrams in this molten salt are frequently constructed.

In 1975, Takahashi et al constructed the predominance diagram for platinum in molten LiCl-KCl, at 450ºC, relative to the Ag^+/Ag and Cl^-/Cl_2 reduction potential, at metal ion activities of 10^{-2}, 10^{-4}, 10^{-6} and 10^{-8}. This diagram showed the stability domains for platinum oxide (PtO_2) and Pt^{2+} ion in the molten salt. It was shown how platinum was probably passivated by a PtO_2 film at high O^{2-} ion activities and a $PtCl_2$, lithium tetrachloroplatinate ($LiPtCl_4$) or potassium tetrachloroplatinate (K_2PtCl_4) film at low O^{2-} ion activities. The passivation characteristics of platinum were shown to be independent of temperature within the range of 400-450ºC [197].

In the same year, Uchida et al constructed the predominance diagram for uranium in molten LiCl-KCl, at 450ºC, relative to the Pt^{2+}/Pt reduction potential at a metal ion activity of 10^{-2}. These diagrams showed the stability domains for UO_3, UO_2 compounds, U^{4+}, U^{3+} ions and $UO_2{}^{2+}$ complex ions in the molten salt. Also the stability constants for $UO_2{}^{2+}$ complex ions and the U^{4+} ion in molten LiCl-KCl was shown to be -log 4.6 and -log 9 respectively [198].

In 1973, Landresse constructed the predominance diagram for uranium in molten LiCl-KCl, at 450ºC, relative to the Cl^-/Cl_2 reduction potential at a metal ion activity of 10^{-2}. These showed the stability domains for UO_3, UO_2, UO^{2+}, $UO_2{}^{2+}$ complex ions and U^{4+}, U^{3+} ions in the molten salt. Also the K_{sp} values for UO_2 and UO_3 in molten LiCl-KCl was shown to be -log 3.5 and -log 2.6 respectively [199].

In 1982, Seon et al constructed the predominance diagram for iron in molten LiCl-KCl at 470ºC, relative to the Cl^-/Cl_2 reduction potential at metal ion activities of 1, 6.18×10^{-2}, 1.68×10^{-2} and 0.108. This showed the stability domains for iron oxide (FeO), iron (II, III) oxide (Fe_3O_4), iron(III) oxide (Fe_2O_3), Fe-Li_2O compounds, FeO^{2-} complex ions and Fe^{2+} ions in the molten salt. Also the stability constants for the FeO^{2-} ion in molten LiCl-KCl was shown to be -log 1.7 [200].

In 2004, Rouquette-Sanches and Picard constructed the predominance diagrams for selenium in molten LiCl-KCl at 450ºC, 500ºC, 550ºC and 600ºC, relative to the Cl^-/Cl_2 reduction potential at a metal ion activity of 1. These showed the stability domains for lithium(II) sulphide (Li_2S_3), selenium chloride ($SeCl_2$) and SeO_2 compounds, and $Se_2O_7{}^{6-}$, $SeO_3{}^{2-}$ complex ions in the molten salt. Also the K_{sp} values for $Se_2O_7^{6-}$ complex ions at 450ºC, 500ºC and 600ºC were shown to be -log 6, -log 4 and -log 3 respectively [201].

In 2005, Hayashi and Minato constructed the predominance diagrams for lanthanide, gadolinium and neodymium in molten LiCl-KCl, at 450ºC, relative to the Cl^-/Cl_2 reduction potential at metal ion activities of 10^{-2}, 5 x 10^{-3} and 10^{-3}. These showed the stability domains for LaOCl, lanthanum chloride ($LaCl_3$), neodymium(III) oxide (Nd_2O_3), neodymium oxychloride (NdOCl), $NdCl_3$, gadolinium(III) oxide (Gd_2O_3), gadolinium oxychloride (GdOCl) and gadolinium chloride ($GdCl_3$) compounds in the molten salt. Also K_{sp} values for neodymium oxychloride (LaOCl), neodymium(III) oxide (Nd_2O_3) and gadolinium oxychloride (GdCOCl) in molten LiCl-KCl were shown to be -log 6, -log 4 and -log 9.37 respectively [202].

In 2007, Cordoba and Caravaca constructed the predominance diagram for samarium in molten LiCl-KCl, at 450ºC, relative to the Cl^-/Cl_2 reduction potential, at a metal ion activity of 0.1. This showed the stability domains for samarium oxide (Sm_2O_3), samarium oxychloride (SmOCl) and Sm^{3+}, Sm^{2+} ions in the molten salt. It was stated how Sm^{3+} ions could not removed due to their equilibrium potential being more electronegative than the molten salt. Also the K_{sp} values for SmOCl in molten LiCl-KCl was shown to be -log 7.54 [203].

In 2008, Caravaca et al constructed the predominance diagram for plutonium in molten LiCl-KCl, at 550ºC, relative to the Cl^-/Cl_2 reduction potential at a metal ion activity of 10^{-2}. This showed the stability domains for Pu_2O_3, plutonium chloride ($PuCl_3$), plutonium(IV) oxide (PuO_2) in the molten salt. It was suggested the diagram could be used to predict the precipitation of PuOCl from the molten salt, although this wasn't observed during the experiment. This could have been due to Pu^{3+} ions becoming stabilized by complexation which could shift its stability domain to higher O^{2-} ion activities. Also the K_{sp} values for Pu_2O_3 in molten LiCl-KCl were shown to be -log 22.1 [137].

In 2013, Brown et al constructed the predominance diagram for uranium in molten LiCl-KCl, at 500ºC, relative to the Cl^-/Cl_2 reduction potential at a metal ion activity of 1. This showed the stability domains for lithium uranium oxide (Li_2UO_3), UO_2, uranium (IV, V) oxide (U_4O_9), uranium (V, VI) oxide (U_3O_8), uranium (VI) oxide), uranium oxydichloride (UCl_2O), uranium pentaoxychloride ($U_2Cl_5O_2$), uranium (III) chloride (UCl_3), uranium tetrachloride (UCl_4) compounds in the molten salt. They suggested the reduction of UO_2 to uranium was easier at higher temperatures, as it required less control over the O^{2-} ion activity. Also the K_{sp} values for Pu_2O_3 in molten LiCl-KCl was shown to be -log 16 [204].

2.4.3 Diagrammatic representation of reactions in molten $CaCl_2$-NaCl

As described earlier, molten $CaCl_2$-NaCl is used as a solvent for the pyrochemical reprocessing of nuclear fuel, due to its low eutectic point (at 504ºC) [156]. This application is dependent upon the O^{2-} ion activity in the molten salt, which can have a detrimental influence upon the preferred reactions; therefore predominance diagrams in this molten salt are frequently constructed.

In 2000, Martinez et al constructed the predominance diagram for chromium in molten $CaCl_2$-NaCl, at 550ºC, relative to the Cl^-/Cl_2 reduction potential, at metal ion activities of 1 and 10^{-1}. The diagram showed the stability areas for Cr_2O_3 and Cr_2O^{2+}, Cr^{2+}, Cr^{3+} complex ions in the molten salt. They suggested how these diagrams could be used in conjunction with a predominance diagram of chlorinating gaseous mixtures to predict the operating conditions for chlorinating chromium oxides. These operating conditions include the chlorination of the sample and electrowinning to obtain the final metal. Also the stability constants for the Cr_2O^{2+} complex ion, and K_{sp} values for CrO and Cr_2O_3 in molten $CaCl_2$-NaCl was shown to be -log 1.23, -log 7.75 and -log 26.5 respectively [158].

2.4.4 Diagrammatic representation of reactions in molten $CaCl_2$

Molten $CaCl_2$ has been used as a solvent for the extraction of metals, such as titanium [87]. This application is dependent upon the O^{2-} ion activity in the molten salt, which can have a detrimental influence upon the preferred reactions; therefore predominance diagrams in this molten salt are frequently constructed.

In 2005, Dring et al constructed the predominance diagram for titanium in molten $CaCl_2$ at 800ºC, 900ºC and 1100ºC, relative to the Cl^-/Cl_2 reduction potential, at a metal ion activity of 1. This showed the stability domains for calcium titanate ($CaTiO_2$), Ti_3O_5, trititanium dioxide (Ti_3O_2), titanium oxide (TiO), titanium(III) oxide (Ti_2O_3), TiO_2, titanium(III) oxychloride (TiClO) compounds and Ti^{3+}, Ti^{2+} ion activity in the molten salt. This diagram was used to describe the electrolytic reduction pathway to producing titanium from rutile. It was suggested this could only occur at high O^{2-} activities there is a high probability that rutile would react with Ca^{2+} ions to form calcium titanate ($CaTiO_3$). This could have a delirious effect upon the deoxidation process of rutile as the O^{2-} ions may have to diffuse through a solid phase. $CaTiO_3$ could however been further reduced to titanium, but may also increase the CaO activity in the molten salt. Also the K_{sp} values for TiO_2 in molten $CaCl_2$ was shown to be -log 12.5 and -log 10 at 1100ºC and 800ºC respectively [206].

In 2006, Dring et al constructed the predominance diagram for titanium in molten $CaCl_2$ and superimposed the predominance diagram for tungsten at 900ºC, relative to the Cl^-/Cl_2 reduction potential at a metal ion activity of 1. These diagrams demonstrated the stability domains for calcium titanate ($CaTiO_3$), calcium tetraoxotungstate ($CaWO_4$), Ti_3O_2, titanium(II) oxide (TiO), Ti_2O_3, trititanium pentoxide (Ti_3O_5), TiO_2, tungsten(VI) oxide (WO_3), tungsten dioxychloride (WCl_2O), tungsten trioxychloride (WO_2Cl_3) and titanium oxychloride (TiClO) compounds in the molten salt. These were used to describe the electrolytic reduction pathway of WO_3 and TiO_2 to W-Ti alloys. It was suggested that tungsten was produced prior to titanium upon reducing the potential at the cathode. At less negative potentials than those required for the electrolytic reduction of TiO_2, tungsten oxide (WO_2) could be reduced to tungsten before the onset of TiO_2. Also the K_{sp} values for TiO_2 in molten $CaCl_2$ was shown to be -log 12.5 and -log 10 at 1100ºC and 800ºC respectively [207].

In 2007, Yasuda et al constructed the predominance diagram for silicon in molten $CaCl_2$ at 850ºC, relative to the Ca^{2+}/Ca reduction potential at a metal ion activity of 1. This diagram demonstrated the existence of stability domains for β-Ca_2SiO_4, calcium silicate ($Ca_3Si_2O_7$), calcium metasilicate ($CaSiO_3$), SiO_2, silicon tetrachloride ($SiCl_4$) and calcium silicide ($CaSi_2$) in the molten salt. The electrolytic reduction pathway of SiO_2 to silicon was shown and was suggested an intermediate $CaSiO_3$ phase was formed. SiO_2 was stable at positive potentials, between -log 5.2 and -log 10.7 and reduced to silicon at negative potentials. Also the K_{sp} values for CaO in molten $CaCl_2$ was shown to be -log 0.1 [208].

2.6 Summary of literature review

This chapter introduced previous literature describing the **dissolution of compounds in molten salts**, through **phase diagrams, ΔH_{mix} and K_{sp} values, MSS of compounds** and the **diagrammatic representation of molten salt reactions** (predominance diagrams).

Phase diagrams in molten salts have been obtained by measuring liquidus and solidus values of unary/binary/ternary/quaternary systems, using a DSC, under different atmospheres and/or calculated directly from thermodynamic data using computer programs (such as FactSage and MTDATA and many others) [270] [209-210]. These programs use mathematical models to represent the thermodynamic potentials ((Gibbs free energy (ΔG), enthalpy (ΔH), entropy (ΔS) and heat capacity (ΔC_p)) for each phase within the phase diagram. These potentials are used in an optimization method (CALPHAD coupled with a Gibbs free energy minimization routine) to obtain the equilibrium compositions of mixtures of phases to plot liquidus and solidus points of unary/binary/ternary/quaternary systems as a function of temperature [208-210]. Often the potentials include ΔH_{mix} values from drop calorimetery experiments which have proven to affect the liquidus lines on a phase diagram. Phase diagrams in molten salts will be useful for our investigation as they can help describe dissolution reactions and hence suggest whether the MSS of cementitious compounds are possible in industry.

ΔH_{mix} values in molten salts have been obtained from drop calorimetry experiments or existing phase diagrams in literature using FactSage or MTDATA and many others [270] [209-210]. These values can either be positive or negative, depending upon choice of cations and anions in the system [53]. The author has found values reported as high as ± 20 kJ mol^{-1} which have suggugested the formation of complex ions or or as low as ± 200-180 J mol^{-1} for ideal systems. ΔH_{mix} values in molten salts will be useful for our investigation as they can help describe dissolution reactions and hence suggest whether the MSS of cementitious compounds are possible in industry.

K_{sp} values in molten salts have been obtained from using potentiometry or isothermal saturation experiments. These values are dependent upon dependent upon the cation and anion activity in the molten salt and the author has found values as high as -log 1.1 or as low as 25.7 in molten salts. A wide range of molten salt systems have been investigated, and been proven that values in molten chlorides are lower in comparison to other molten salts (where precipitation generally occurs) [209-210]. K_{sp} values in molten salts will be useful for our investigation as they can help describe dissolution reactions and hence suggest whether the MSS of cementitious compounds are possible in industry.

MSS is a proven alternative route to the synthesis of a wide range of compounds (such as TiO_2, ZrO_2 and Al_2O_3). To the authors knowledge, TiO_2 has been produced from the reactants; $TiOSO_4.H_2SO_4$, K_2TiF_6, $TiOSO_4$ in molten $LiNO_3$-KNO_3, LiCl, KNO_3, $LiNO_3$, $NaNO_3$, HF, NaOH, NaCl, H_2O_2 and NaCl-Na_2HPO. m-ZrO_2 and t-ZrO_2 has been produced from the reactants; $Zr(SO_4)_2$, $ZrOCl_2.8H_2O$ and $ZrO(NO_3)_2.2H_2O$ in molten $NaNO_3$, $LiNO_3$-KNO_3, $NaNO_3$-KNO_3, $NaNO_2$-KNO_2 and LiF-NaF. α-Al_2O_3 and γ-Al_2O_3 has been produced from the reactants; $AlCl_3$, $Al(OH)_3$, $Al_2(SO_4)_3$, $NaAlO_2$ and additives; $TiOSO_4$, $Na_3PO_4.12H_2O$, α-Al_2O_3 in molten $LiNO_3$-KNO_3, $NaNO_3$, $NaNO_3$-KNO_3, $NaNO_2$-KNO_2, Na_2SO_4, NaCl-KCl, Na_2SO_4-K_2SO_4 and K_2SO_4 [161-184]. The final crystallites sizes of these compounds were a function of various heating and cooling rates and the basicity of the molten salt. Upon increasing this basicity, reaction temperatures have been lowered and in some cases produced undesirable products (such as titanates instead of TiO_2) [183-184]. MSS will be useful for our investigation as they can be used to obtain the cementitious compounds considered in this thesis.

Predominance diagrams are a useful tool to depict molten salt reactions, K_f and K_{sp} values and stability areas for ions, complex ions and precipitated compounds in molten salts [189-208]. These are plotted mainly relative to the Cl^-/Cl_2 reduction potential, at metal ion activities between 1-10^{-8} at reaction temperatures. Their calculation requires reduction potentials of electrochemical reactions, thermodynamic data and stability constants of the species considered. The uses of these diagrams are limited to the choice of thermodynamic data as often compounds dissolved in molten salts are subjected to the effects of complexation and thus requires an activity coefficient term. They also require knowledge of the species and molten salt reactions, which can only be confirmed using other analytical techniques. Predominance diagrams will be useful to our investigation as they can help determine molten salt conditions required for the MSS of cementitious compounds.

Chapter 3

Characterization, electroanalytical, calorimetric techniques & experimental setup

3.1 Introduction

This chapter describes the **characterization, electroanalytical and calorimetric techniques** used in this thesis, to investigate the **structures and purities of the reactants in the molten salt, behaviour of the molten salt at the reaction conditions, dissolution of the reactants in the molten salt** and the **MSS of cementitious compounds,** which includes XRD, SEM, potentiometry, CV, drop calorimetry and DSC. It also provides a description of the setup for each experiment.

3.2 X-ray diffraction

XRD was used to investigate the **structures and purities of the reactants in the molten salt, dissolution of the reactants in the molten salt** and **MSS of cementitious compounds.** The equipment used was a STOE STADI-P and a PANalytical X'pert PRO powder diffractometer (figure 3.1).

Figure 3.1: Image of the STOE STADI-P (top) and a PANalytical, X'pert PRO powder diffractometer system (bottom) [211].

Each system was equipped with a cobalt X-ray tube to provide cobalt X-rays. A typical operating condition was a 2θ scan range of 5-110° with 150 seconds per steps. XRD involved illuminating a crystalline sample with X-rays, between wavelengths of 0.5-22 Å, which caused radiation to be diffracted by adjacent planes in the sample. When path differences between the diffracted waves are equal to an integer number of wavelengths (γ), constructive interference occurs [212-214]. i.e. if AB + BC are equal to γ, a wave with a larger amplitude is produced (figure 3.2).

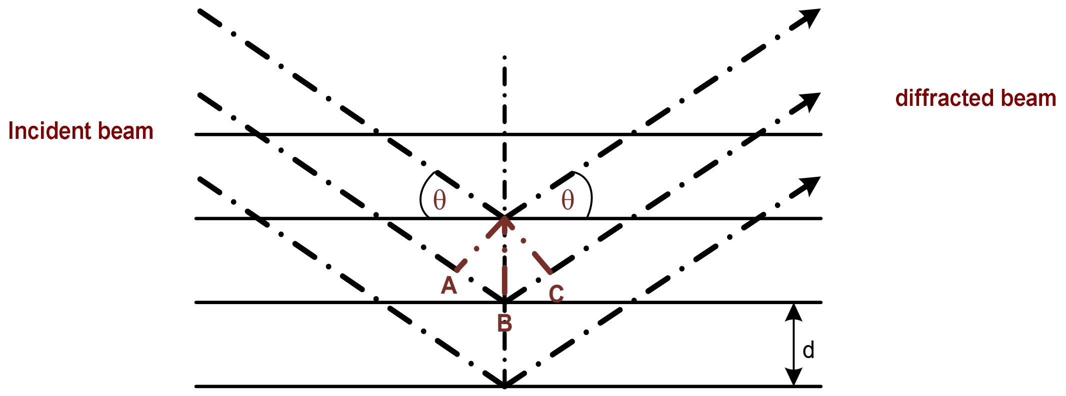

Figure 3.2: Diffraction by crystals (reproduced by author) [211].

The intensity of the diffracted radiation was recorded at various detector angles, between 0-180° which were plotted as a function of the scattering angle to provide an XRD pattern. Each XRD pattern was indicative of a crystalline sample's inter-atomic spacing and used to identify phase(s) of a particular material, after comparing the patterns against a database for possible matches. In these studies, the phases were identified using "The International Centre for Diffraction Data database (ICDD)" [215].

$$\lambda = 2d\sin\theta \qquad \textbf{Equation 3.1}$$

Equation 3.1 expresses Bragg's law, used to relate the X-ray scattering angle with the X-ray wavelength, where λ is the X-ray wavelength, θ is the scattering angle and d is the d-spacing between the adjacent planes in the crystalline sample [212]. From this equation, it was possible to determine peak positions on an XRD pattern theoretically (on a 2θ scale) providing the X-ray wavelength and lattice parameters are known (i.e. 1.78 Å for cobalt, $K\alpha1$ radiation).

X-rays were produced by passing a current through a tungsten (cathode) filament causing electrons to be released. These electrons are accelerated over a voltage and attracted to a cobalt target (anode), generating cobalt X-rays of wavelength $K\alpha1$ (6930.3 eV), $K\alpha2$ (6915.3 eV) and $K\beta$ (7649.4 eV). These were then passed through an iron or germanium filter to remove unwanted $K\alpha2$ and $K\beta$ radiation, which would cause unwanted peaks in an XRD pattern (figure 3.3) [212-214].

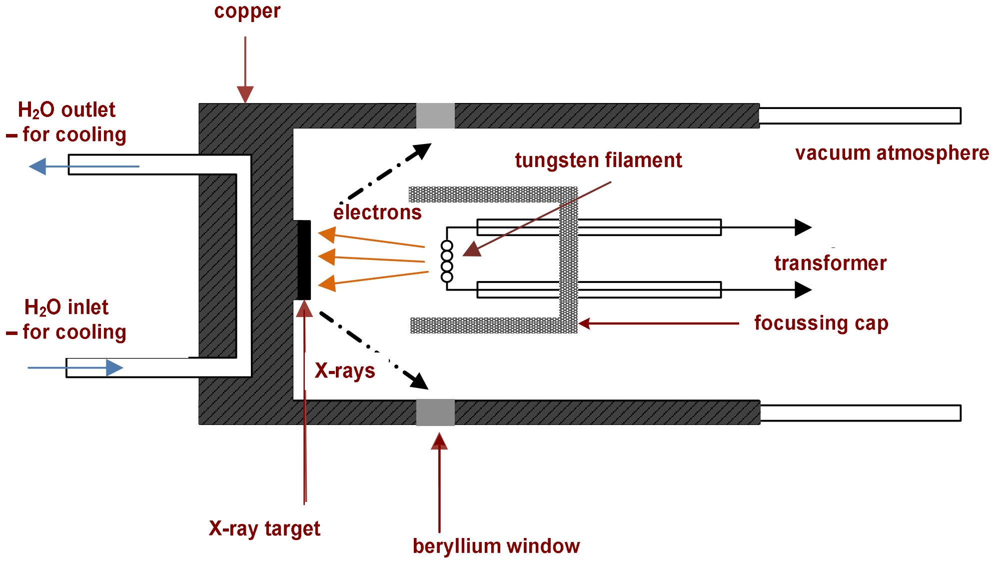

Figure 3.3: Tungsten (cathode) filament for XRD (reproduced by author) [212].

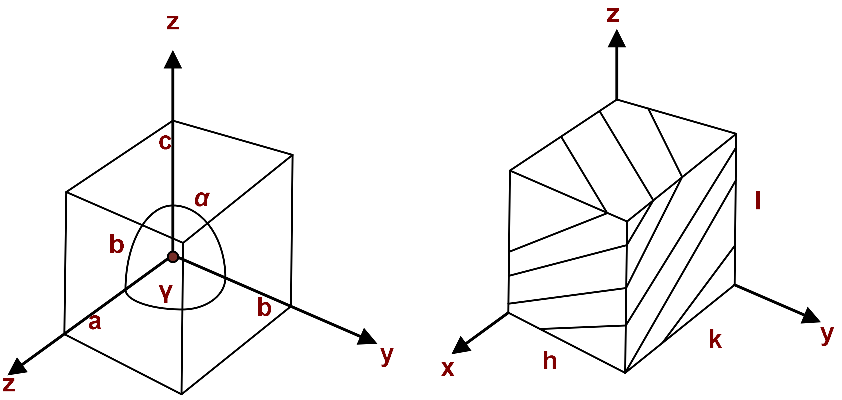

Figure 3.4: Lattice parameters: a, b, c – axis length, α,β, γ – axis angle and h, k, l – planes of direction (reproduced by author) [214].

The analysis of the XRD patterns was performed upon the principle that the inter-atomic spacings of crystalline samples can be described in terms of a unit cell (figure 3.4) [212]. These unit cells are stacked in three dimensional spaces and represented by the lattice parameters; x, y and z, describing the dimensions of the unit cell, a, b and c, describing the axis length, α, β, and γ, describing the angles between the axes and h, k and l, describing the planes of direction. The perpendicular spacing between the planes is the d-spacing [214]. These parameters are determined directly from an XRD pattern, and provide information upon the axis system of the crystalline sample, and ultimately its crystal structure (table 3.1).

Crystal structure	Axis system	
Cubic	$a = b = c$	$\alpha = \beta = \gamma = 90°$
Tetragonal	$a = b \neq c$	$\alpha = \beta = \gamma = 90°$
Hexagonal	$a = b \neq c$	$\alpha = \beta = 90°, \gamma = 120°$
Rhombohedral	$a = b = c$	$\alpha = \beta = \gamma \neq 90°$
Orthorhombic	$a = b \neq c$	$\alpha = \beta = \gamma = 90°$
Monoclinic	$a = b \neq c$	$\alpha = \beta = 90°\ \beta \neq 90°$
Triclinic	$a = b \neq c$	$\alpha \neq \beta \neq \gamma \neq 90°$

Table 3.1: Crystal structure and axis system, a, b and α,β, γ cell parameters (reproduced by author) [214].

3.3 Scanning Electron Microscopy

An SEM was used to investigate the **dissolution of the reactants in the molten salt** and **MSS of cementitious compounds.** The SEM equipment was a Jeol JSM 6480LV and Jeol JSM 35CF SEM, each with secondary electron imaging (SEI) and back scattered electron analysis (BSE) detection modes (figure 3.5).

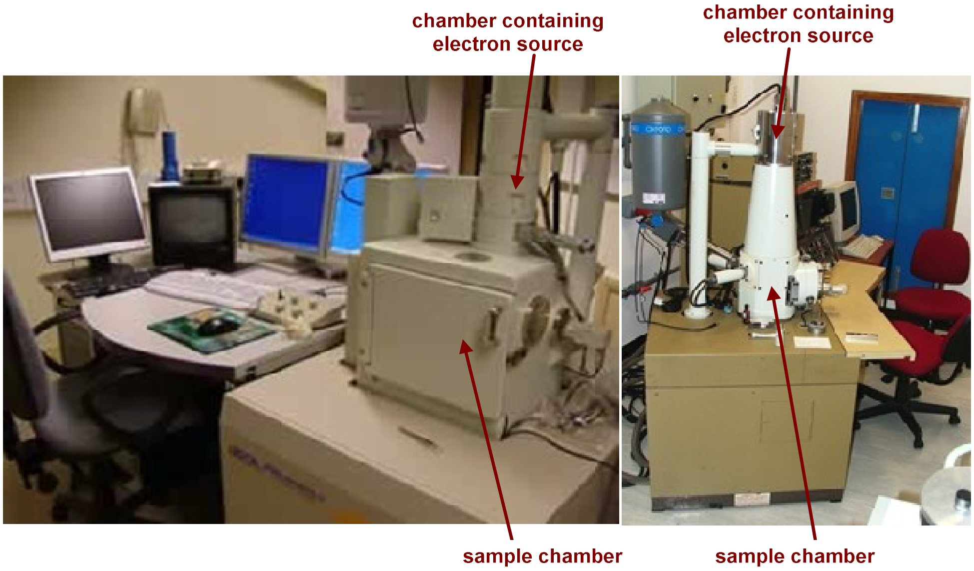

Figure 3.5: Image of the Jeol JSM 6480LV (left) and Jeol JSM 35CF (right) SEM systems.

SEM involved illuminating a sample with high energy electrons which interacted with its surface, to produce secondary electrons or X-ray's depending upon the choice of detection mode. These signals were used to determine a sample's topography, morphology, composition and size which use both SEI and BSE detection modes [216-218].

During the SEI detection mode, secondary electrons (with energies < 50 eV) in valence orbitals of a sample's surface are released by inelastic scattering. The number of electrons and projection angle was dependent upon the angle of the incoming beam and sample surface topography, therefore steeper surfaces appeared brighter than flatter surfaces. This resulted in a variation of electron intensity and image contrast, which was used to produce high-resolution images of a samples surface (between ~1-5 nm) [216-218].

During the BSE detection mode, a fraction of electrons from the incident beam entered a sample (up to 20 nm below the surface) and became scattered by the electromagnetic field of the nucleus. If the scattering angle was greater than 180°, backscattered electrons (with energies > 50eV) were diffracted out of valence orbitals from the surface by elastic scattering. This caused higher energy electrons to fill the valence orbitals, causing X-rays to be released. The X-ray wavelength was then related to the energy level differences in different orbitals for a given element, and used for EDS analysis. The higher the atomic number of the sample, the more electrons are scattered, leading to a sharper image contrast (up to ~5.5 nm) [216-218].

SEM electrons are produced (~0.0025 nm in wavelength) by passing a current through a tungsten (cathode) filament and accelerating it across a voltage (between 1-300 kV), similar to X-ray production (figure 3.6). The electron beam is passed through a grid cap (an electrostatic lens) and magnetic plate (anode) which focuses the electrons onto a small area (between 50-100 Å in diameter), causing electrons to be produced [218].

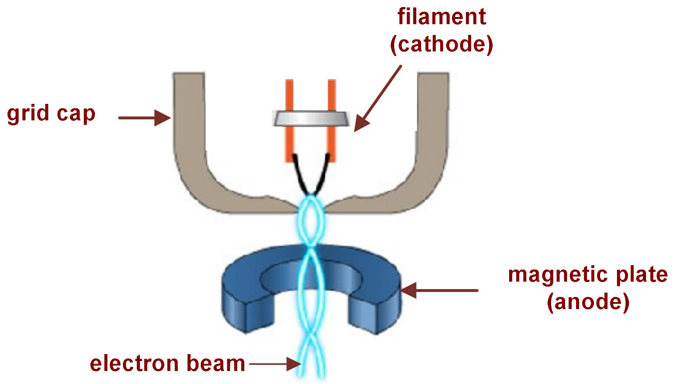

Figure 3.6: Tungsten (cathode) filament for SEM [219].

The interaction of the incident beam within a sample forms a limiting interaction volume, dependent upon the energy of the electron incident beam and density of the sample. This limiting interaction volume varies throughout the sample, being greatest at the beam impact point [218].

$$R = \frac{0.0276A\ {}_{o}^{1.67}}{Z^{0.9}\rho} \qquad \textbf{Equation 3.2}$$

Equation 3.2 expresses the radius of the limiting interaction volume of a sample, where Z is the atomic number of the sample, ρ is the density of the sample (in g cm^{-3}), E_o is the incident beam energy (in kV) and A is the atomic weight (in g mol^{-1}) [218]. This demonstrates the interaction volume increases with increasing incident beam energy and decreases as the atomic number of the sample rises.

3.4 Drop calorimetry

An isoperobolic drop calorimeter was used to investigate the **dissolution of the reactants in the molten salt**. The calorimeter was constructed in-house with a temperature range up to 930ºC however the author used reaction tempereatures of 830ºC. This temperature was selected previously by the author and the drop calorimeter was allowed to stabilze for at least 3 days prior to measurements. A schematic of the drop calorimeter is shown in figure 3.7 [220].

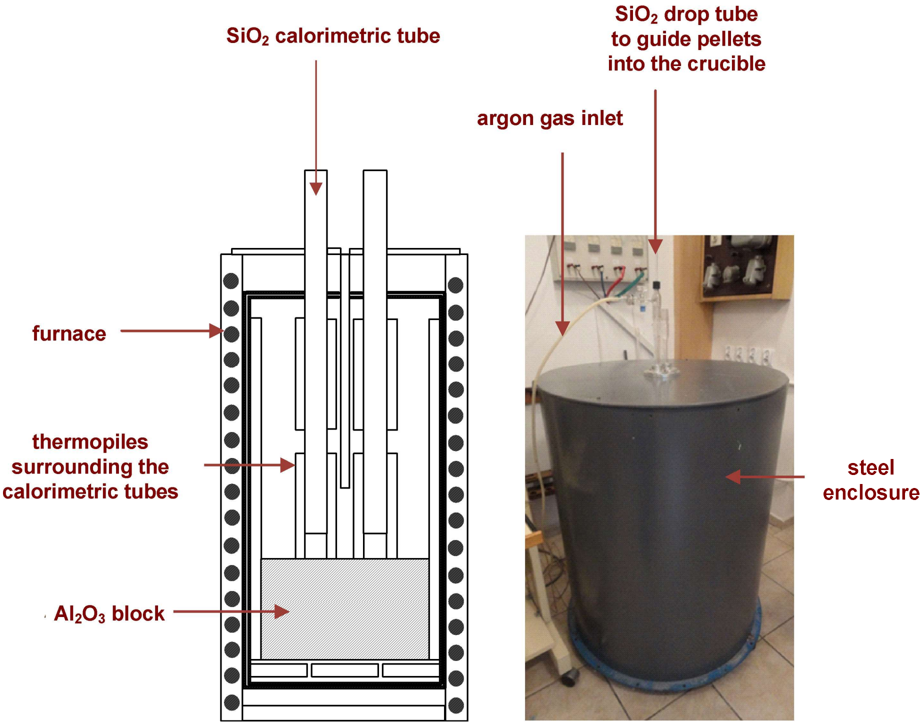

Figure 3.7: Drop calorimeter schematic (left) and image of the drop calorimeter (right).

The drop calorimeter contained an Al_2O_3 block, in a cylindrical furnace, surrounded by a steel enclosure. The Al_2O_3 block contained two cylindrical wells placed in parallel to each other, surrounded by thermopiles [220]. A thermopile is a series of thermocouples connected together in a radial arrangement, their purpose being to measure the temperature at a specific location within a tube. The radial arrangement of the thermopiles ensured the complete integration of heat within the tube, allowing the signal to be independent of localised temperature distributions [221]. Each thermopile was constructed from a platinum-rhodium (Pt-Rd) alloy, ~17 mm in diameter, ~80 mm in height containing 22 hollow alumina support discs. These were connected electrically in opposition to compensate for any irregular heat effects. The temperature of the calorimeter was controlled by an electronic thermostat, connected to a thermocouple in the centre of the Al_2O_3 block [221-223].

Before the experiments, a sample and reference closed-ended calorimetric tube, constructed from SiO_2, was inserted into each well, under argon gas. The sample calorimetric tube contained a glassy carbon crucible, containing the sample under study and the reference calorimetric tube remained empty. These materials were selected due to their high melting temperatures (SiO_2 at 1600ºC, glassy carbon at 3550ºC) thus suitable for the operational temperatures and conditions required [18]. The purpose of the reference calorimetric tube was to provide a stable and reproducible signal to obtain potential readings from, by closing off the entrance to the drop calorimeter, thus avoiding the interference of gases (such as air).

Drop calorimetry involved measuring the differential temperature between the sample and reference calorimetric tube. During an experiment, pellets and crystals of the sample was dropped into the glassy carbon crucible, at steady-state conditions, causing the temperature of the sample calorimetric tube to lag behind (or ahead) of the reference, and then decay exponentially [221-223]. [11] The potential difference between the thermopiles was recorded as a function of time, to produce a heat flow signal (in mV s^{-1}). This potential difference was interpreted by FlukeView Basic 3.0 and OriginPro 8 Peak Analyzer tool [224-225].

---

[11] The procedure for making crystals and pellets is stated in the experimental setup section.

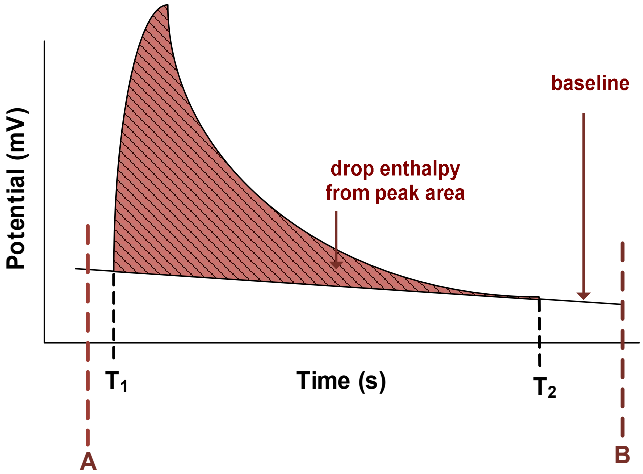

Figure 3.8: Drop calorimeter heat flow signal (reproduced by author) [226].

Figure 3.8 shows a typical heat flow signal obtained from the drop calorimeter. The fusion, transitional and mixing enthalpies of the sample were evident as peak areas. To calibrate the peak areas, a calibration was performed on the heat flow signal prior to measurements, using a standard material (such as Al_2O_3, NIST-720), at the reaction conditions [220].

$$\Delta H_{Total} = \Delta H_{(298-T_{Reaction})} + \Delta H_{mix} + \Delta H_{fusion} \qquad \textbf{Equation 3.5}$$

Equation 3.5 expresses the total drop enthalpy, where ΔH_{Total} is the total drop enthalpy (in kJ mol^{-1}), ΔH_{mix} is the heat of mixing of a mixture of components A in B (in kJ mol^{-1}), ΔH_{fusion} is the enthalpy of fusion (in kJ mol^{-1}) and $\Delta H_{(298\text{-}Treaction)}$ is the enthalpy change of the sample from 298K to the reaction temperature (in kJ mol^{-1}) [220-222]. Both ΔH_{fusion} and $\Delta H_{(298\text{-}Treaction)}$ quantities are available from thermodynamic data [18]. Often a drift of the potential base-line was encountered therefore a separate base-line was taken for each peak (this was probably due to reactions between the calorimetric and sample calorimetric tube).

3.5 Differential Scanning Calorimetry

Two DSCs were used to investigate the **behaviour of the molten salt at the reaction conditions** and **dissolution of the reactants in the molten salt.** The equipment used was a Setaram DSC 121 and a Netzsch DSC STA 449 Jupiter, capable of reaching temperatures up to 827ºC and 2400ºC respectively depending upon the furnace type (figure 3.9) [220] [226-227].

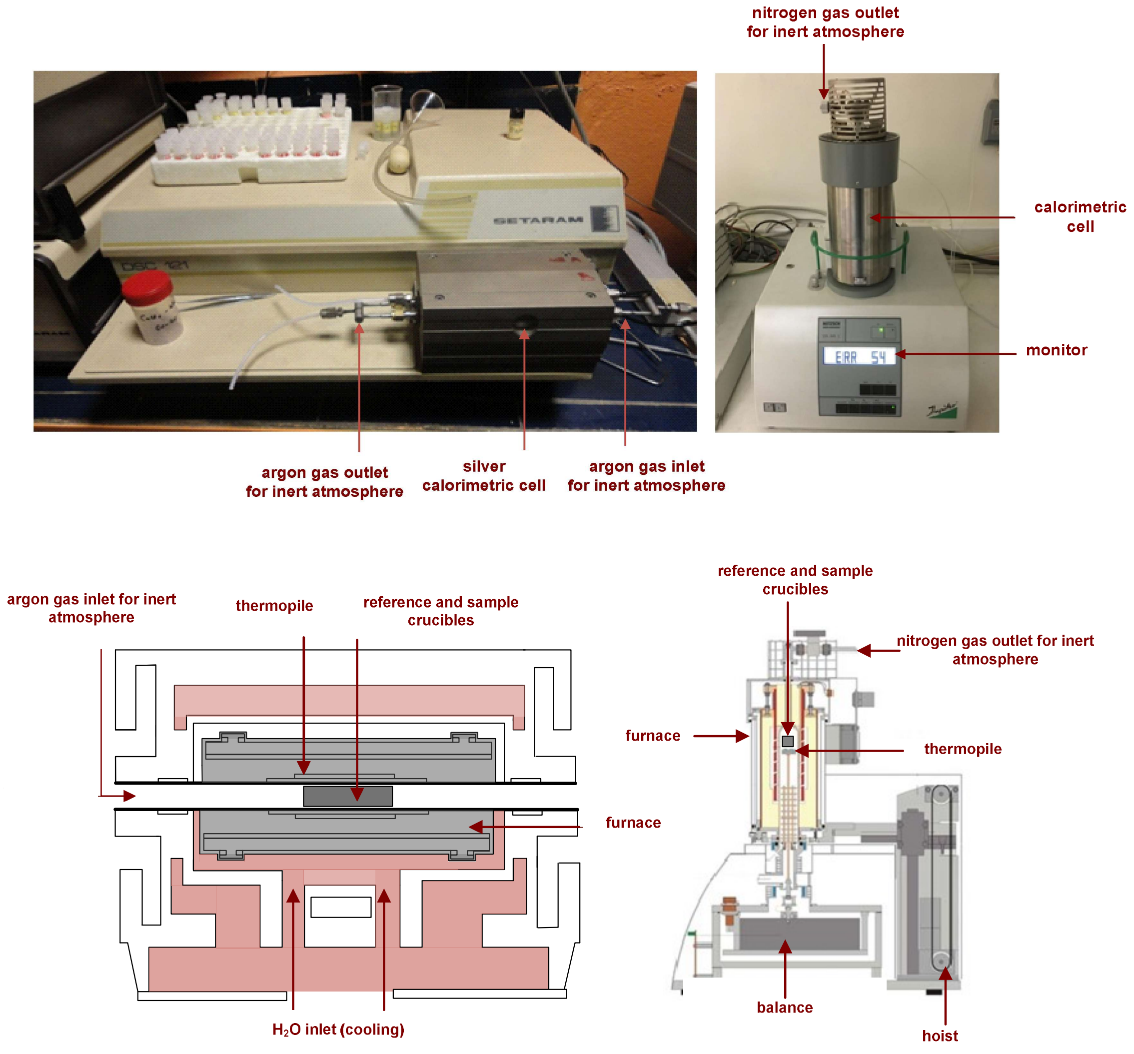

Figure 3.9: Image of the Setaram DSC 121 (left) and Netzsch DSC STA 449 Jupiter (right) and their schematics (bottom) [220].

The Setaram DSC 121 consisted of two ceramic tubes tubes mounted in parallel, embedded with heating elements. Both tubes had Inconel™ 600 internal liners preinstalled from Setaram to protect the heating elements from molten salt leakages [220] [227-228]. These heating elements had a thermal resistivity of 100 Ω each and generated up to 200 mW every 200 seconds. The heat flow signal was measured by thermopiles, made from a Pt-Rd alloy which was placed around each tube. Each thermopile was connected electrically in opposition to compensate for any irregular heat effects [220]. The integration of the peaks was performed by Calisto Thermal Analysis software provided by Setaram [227-228].

The Netzsch DSC STA 449 Jupiter consisted of two ceramic tubes mounted in parallel, embedded with heating elements, with a DSC resolution of 1 μW. The heat flow signal was measured by thermopiles, made from a Pt-Rd alloy which was placed around each tube. The machine had a mass balance to measure differences in weight of the sample as a function of time, with a TG resolution of 0.1 μg. The integration of the peaks was performed by Proteus Thermal Analysis software provided by Netzsch [226] [229].

The procedure involved placing identical sample and reference crucibles in the DSC in calorimetric tubes, connected electrically in the furnace. The differential temperature between the containers was recorded by the thermopiles as a function of time. This arrangement produced a heat flow signal (in mW) and was dependent upon the heat flow path within the unit [220]. When both crucibles were subjected to similar heating/cooling rates, the temperature of the sample crucible lagged behind (or ahead) of the reference and then decayed exponentially. To eliminate any heat effects from the surroundings to the sample, a high thermal resistance (ceramic) was placed between the container and surrounding enclosure to allow heat effects associated solely from the sample to be measured [220-223].

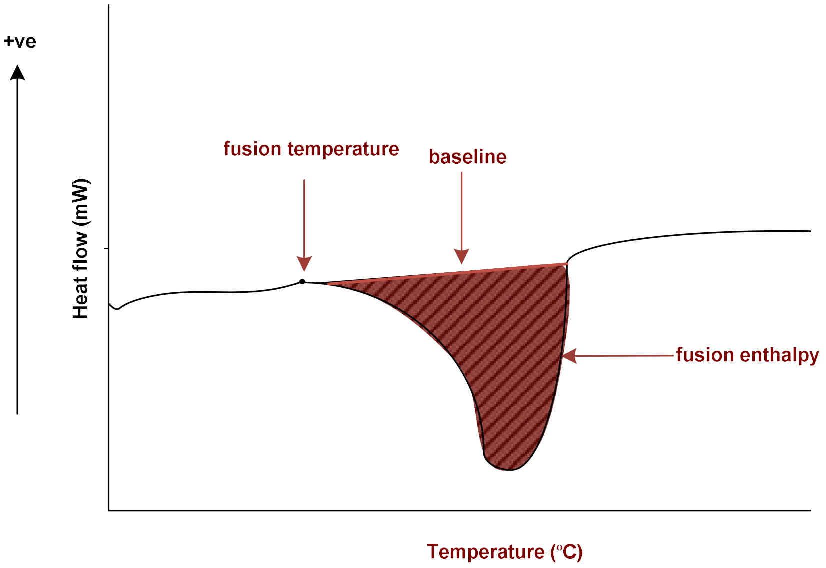

Figure 3.10: DSC heat flow signal (reproduced by author) [220].

Figure 3.10 shows a typical heat flow signal obtained from the DSC's. Heat effects associated with fusion/transitional enthalpies are evident as peaks areas and peak onsets can be used to obtain fusion/transitional temperatures, providing a temperature and calorimetric calibration is performed.

$$\Delta T_C = k\Delta T_D$$ **Equation 3.3**

Equation 3.3 expresses the relationship used for the temperature calibration, where T_C is the differential temperature between the containers (in ºC), ΔT_D is the differential temperature of the sample (in ºC) and k is a constant [224]. The temperature calibration was performed at specific scan rates, prior to measurements, using a standard material (such as Al_2O_3, NIST-720) over the temperature range of the DSC [224]. This resulted in a differential temperature between the crucibles which was related to the actual differential temperature of the DSC.

$$K = \frac{m\Delta H}{A}$$ **Equation 3.4**

Equation 3.4 expresses the relationship used to calibrate the DSC, where K is a constant (in $J\ cm^{-2}$), A is the peak area (in cm^2), ΔH is the enthalpy change of the sample (in $J\ g^{-1}$) and m is the mass of the sample (in g) [224]. The calibration was performed at a specific scan rate, prior to measurements, using a standard material (such as Al_2O_3, NIST-720) over the temperature range of the DSC. This allowed the peak area to be related to the ΔH_f or ΔC_p of the sample.

3.6 Potentiometry

Potentiometry was used to investigate the **dissolution of the reactants in the molten salt**. The technique required the construction of a galvanic cell capable of achieving 830°C. [12] The galvanic cell contained an ISE and reference electrode immersed in the molten salt. These electrodes were connected to a high-resistance voltmeter/potentiostat (Uni-trend), and connected together with leads of similar

---

[12] The construction of the cell underwent at the Centre for CO_2 Technology, University College London.

materials. This ensured no unwanted junction potentials were present from other thermoelectric forces. The electrode designs were based upon previous versions reported by Gale and Lovering, 1991, which have demonstrated a stable and reproducible signal [230]. A schematic of the galvanic cell is shown in figure 3.11.

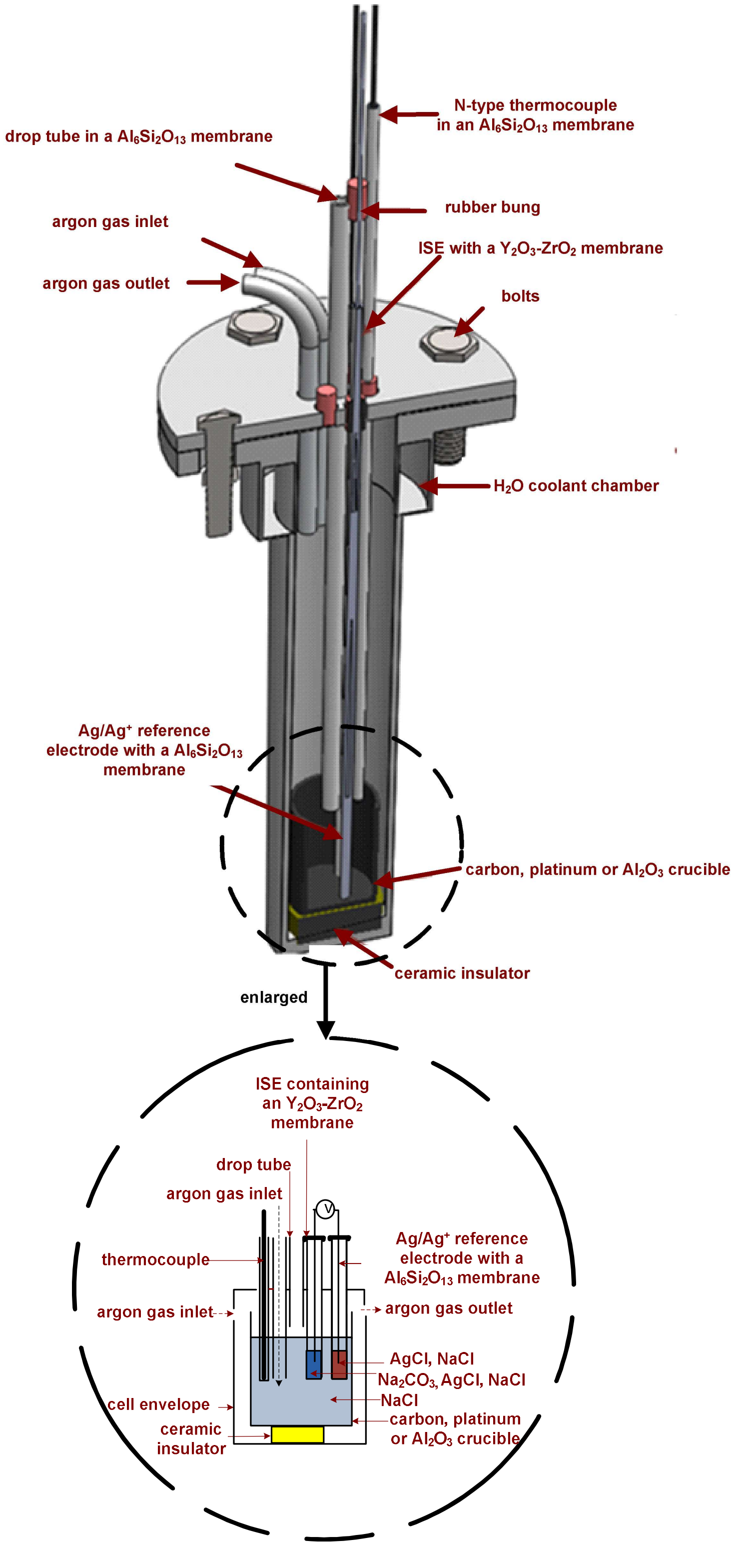

Figure 3.11: Galvanic cell schematic.

The reference electrode contained an aluminium silicate ($Al_6Si_2O_{13}$) membrane, denoted “mullite”. This material was selected due to its high melting temperature (at 1840ºC) and sodium ion (Na^+) conductive properties [18] [51]. [13] The membrane contained a silver wire immersed in molten NaCl-AgCl and capped with a silicon cap. [14] This allowed the reference electrode potential to be a function of the silver wire in contact with Ag^+ ions in molten AgCl-NaCl (Ag/AgCl redox couple) and the Na^+ ions in the molten salt on both sides of the $Al_6Si_2O_{13}$ membrane (junction potential).

The ISE contained an YSZ membrane, containing a silver wire, immersed in molten NaCl-AgCl-Na_2CO_3 and capped with a silicon cap. This material was selected due to it containing oxygen vacancies within its lattice structure, which arose when Zr^{4+} ions of ZrO_2 were substituted with slightly larger Y^{3+} ions (ionic radius of 0.82 Å to 0.96 Å) [231]. These oxygen vacancies allow O^{2-} ions in to pass through, thus allowing the ISE electrode potential to be a function of the boundary between the silver wire in contact Ag^+ ions in molten AgCl-NaCl-Na_2CO_3 (Ag/AgCl redox couple), and O^{2-} ions in the molten salt on both sides of the YSZ membrane [51] [230-233]. The arrangement produced a signal which was a function of one sole variable; the O^{2-} ion activity in the molten salt. ZrO_2 was not used as a membrane material as it undergoes a phase transition, from monoclinic to tetragonal (at ~1000ºC), which results in a 5% volume change. This induces stresses upon ZrO_2, during heating/cooling cycles, causing it to crack. However when ZrO_2 is stabilized with Y_2O_3 (at 8 mol %), the cubic polymorph is stabilized and phase transitions can be avoided, and consequently also increases its ionic conduction capabilities [232].

The melt was placed in platinum, Al_2O_3 or glassy carbon crucibles. These materials were selected due to their high melting temperatures (Al_2O_3 at ~ 2072ºC, platinum at ~1769ºC, glassy carbon at ~3500ºC) and virtually no solubility in molten chlorides which is the general consensus in literature [18] [133]. [15] It has also been reported that platinum reacts with molten chlorides (such as LiCl) to form platinate species (such as lithium platinate (Li_2PtO_3)) at low O^{2-} ion activities, therefore it was expected that similar species could also form in other melts (such as disodium hexachloroplatinate

---

[13] NaCl was selected as a suitable salt for MSS, thus a suitable material for the mullite membrane.

[14] The mixtures are named according to **A-B-C** where **A** is the initial salt, **B** is the secondary compound in A and **C** is the tertiary compound in A.

[15] The salt selected for this investigation was NaCl due to it being a liquid at the reaction conditions.

(Na_2PtCl_6)) in molten NaCl) [234-235]. It was also reported that platinum reacts with O_2 to produce a thin transparent film on its surface (probably PtO_2), and platinum oxide (Pt_3O_4) however at higher temperatures exceeding ~600ºC the film disappears, probably due to the high vapour pressure of these species [234-235]. However as platinum is a frequently used material by previous authors, it was selected for use in our experiments [133].

The cell envelope was constructed from two types of alloys; Stainless steel 316L and Inconel^{TM} 600, selected due to their high operational service, (Stainless steel 316L at ~800ºC, Inconel^{TM} 600 at ~1100ºC) and high melting temperatures (Stainless steel 316L at ~1400ºC, Inconel^{TM} 600 at ~1370ºC) [18] [236-239]. These alloys have a have a high resistance to oxidation due to the presence of chromium, nickel and iron (table 3.2). These elements oxidise to chromium(III) oxide (Cr_2O_3), chromium (IV) oxide (CrO_2), iron(II) oxide (FeO), iron(III) oxide (Fe_2O_3) and NiO at elevated temperatures, which provide a barrier to further oxidation [238]. However at elevated temperatures (816^{o}C for Stainless Steel 316L), the CrO_3 Ce_2O_3 compounds are selectively removed, thus exposing Fe_2O_3 and FeO, which results in their removal. This can be greatly improved by increasing the nickel content in the alloy, using Inconel^{TM} 600, as reported by Davis, 1954 [238]. This particular alloy has been reported to have a lower thermal expansion differential between the base metal and oxide film during heating and cooling, which greatly improves its corrosion resistance [238].

Alloy	**Element (mol%)**				
	Chromium	**Nickel**	**Iron**	**Molybdenum**	**Other**
Stainless steel 316L	16-18.5	10-14	Balance	2-3	<4
Inconel^{TM} 600	15.5	72	8	-	<4.5

Table 3.2: Composition of Inconel^{TM} 600 and Stainless Steel 316L (reproduced by author) [234-235].

The cell envelope was filled with argon, to remove O_2 and moisture which could have detrimental effects to compounds sensitive to humidity. It has been reported that O_2 and moisture interact with molten salts to produce O^{2-} and OH^- ions in the melt. These ionic species have proven to accelerate the corrosion of metals in contact with the molten salt and cause hydrolysis of the molten salt [51] [240]. It has also been reported that O_2 and moisture greatly accelerate the oxidation of Stainless Steel 316L and Inconel^{TM} 600 due to the higher diffusion rates of the ionic species (Fe^{2+}, Ni^{2+} and Cr^{2+}), therefore should be avoided [238-239]. An Al_2O_3 disc was also placed between the crucible and cell envelope to reduce stray potentials that could affect the potential between the ISE and reference electrode. The temperature of the molten salt was also recorded by an N-type thermocouple inserted into the molten salt, sheathed by an $Al_6Si_2O_{13}$ membrane to avoid any reaction between the alloy and the molten salt. A mullite drop tube was also inserted into the cell, to guide pellets of samples into the molten salt. The galvanic cell was connected to a H_2O bath (at 2ºC) to cool the top portion of the cell below 100ºC, for ease of user handling.

The potentiometric method involved measuring the potential difference (in mV), between the ISE and reference electrode, immersed in the molten salt [230]. At steady-state conditions, the potential difference was ~0, which increased/decreased upon changes to the O^{2-} activity in the molten salt and temperature. These changes were shown on a potentiometric plot (figure 3.12).

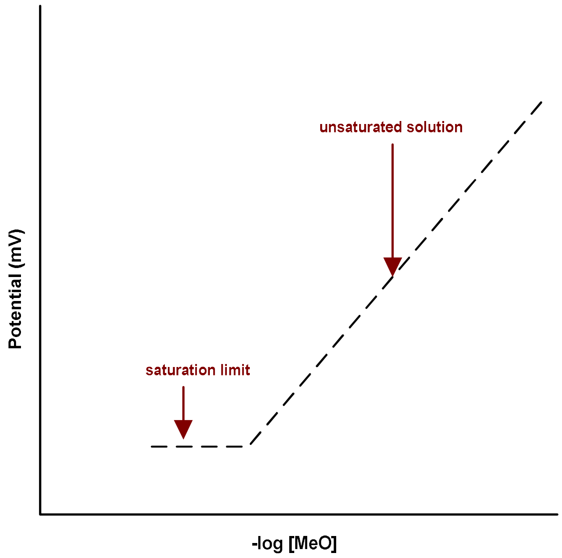

Figure 3.12: Potentiometric plot (reproduced by author).

Figure 3.12 shows a typical potentiometric plot from the galvanic cell. The incline section was created due to the dissolution of compounds (with an O^{2-} ion) below the saturation limit of the molten salt. This section was used to deduce the number of electrons taking part in the electrochemical reactions, at the YSZ membrane surface, using the Nernst relationship [230] [232].

$$\Delta E = E^o + \frac{2.3RT}{nF} pO^{2-}$$ **Equation 3.6**

Equation 3.6 expresses the Nernst relationship, where E^o is the standard redox potential of the electrochemical reaction, R is the universal gas constant, F is the Faradays constant and T is the temperature. The horizontal section is due to the saturation limit of the molten salt, which often results in the precipitation of compounds. The K_{sp} values for compounds (such as oxides) can be deduced using the following relationships [130] [241].

$$\sum S_{MeO} = [Me^{2+}][O^{2-}] = K_{sp}{}^{1/2}$$ **Equation 3.7**

or $$\sum S_{Me_2O} = [2Me^{2+}]^2[O^{2-}] = \frac{1}{4}K_{sp}{}^{1/3}$$ **Equation 3.8**

Equation 3.7-3.8 expresses the relationships between the K_{sp} value and complete oxide solubility, neglecting the non-dissociated oxide term, where $\sum S_{MeO}$ and $\sum S_{Me_2O}$ is the complete oxide solubility. Often the horizontal section has shown to contain a bend towards the -log[O^{2-}] axis, caused by the partial dissolution and existence of a non-dissociated compounds [130].

3.7 Cyclic voltammetery

CV was used to investigate the **structures and purities of the reactants in the molten salt**. This required the construction of an electrolytic cell, with an operational temperature up to 830ºC. The cell consisted of working, counter and reference electrodes immersed in the molten salt, connected to a potentiostat. The reference electrode was made from an $Al_6Si_2O_{13}$ membrane, containing a silver wire immersed in molten AgCl-NaCl and capped with a silicon cap (similar to the galvanic cell). The working and counter electrodes were made from a platinum wire, selected due to their high melting temperature (at ~1769ºC) and high electrical conductivity, as described by Gale and Lovering, 1991 [18] [230]. The Al_2O_3 crucible was selected due to its high melting temperature (at ~ 2072ºC) and limited solubility in molten chlorides, as shown by previous authors [18] [50]. A schematic of the electrolytic cell is shown in figure 3.13.

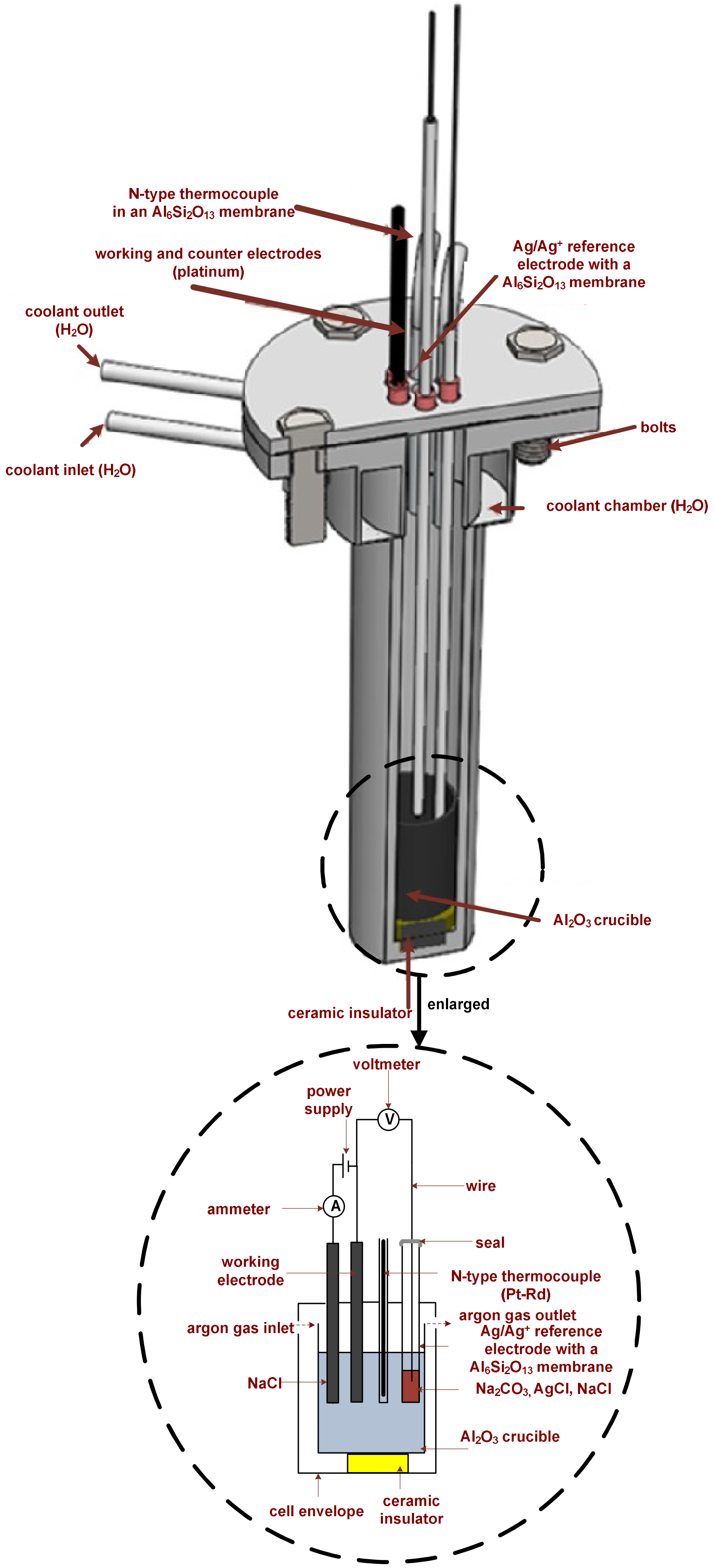

Figure 3.13: Electrolytic cell schematic.

The electrolytic cell was filled with argon to remove significant quantities of O_2 and moisture and an Al_2O_3 disc was placed between the crucible and cell envelope due to the same reasons described previously (in the potentiometry section). The temperature of the molten salt was recorded by an N-type thermocouple, sheathed by an $Al_6Si_2O_{13}$ tube before inserting into the molten salt to avoid the interaction of the molten salt. The electrolytic cell was connected a H_2O bath (Huber), which cooled the top portion of the cell to temperatures below 100ºC, with running water at 2ºC, for ease of user handling.

Voltammatery involved measuring the potential difference (in mV) and current (in mA) between the working, counter and reference electrode whilst immersed in the molten salt [242]. The working and counter electrodes coupled with the power supply/potentiostat provided electrical energy to the molten salt to facilitate electrochemical reactions using cyclic voltammatery sweeps. These sweeps were both cathodic or anodic depending upon their connection to the working, counter and reference electrode, and power supply/potentiostat. The potential changes of the working electrode and current produced across the electrodes were plotted on a voltammogram (figure 3.14).

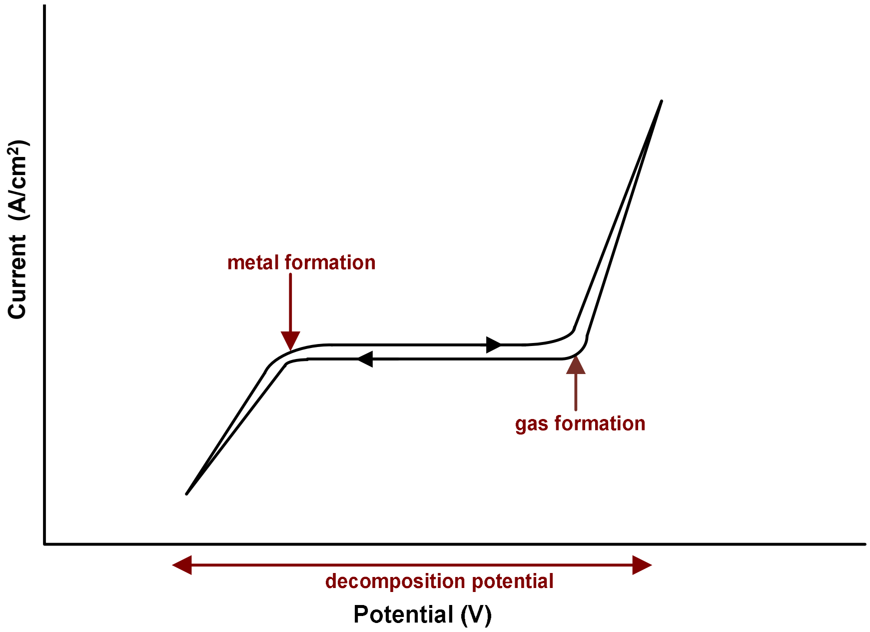

Figure 3.14: Voltammogram (reproduced by author).

Figure 3.14 shows a voltammogram illustrating a typical CV curve from the electrolytic cell containing a molten salt (such as a molten chloride). The decomposition potential (E_d) of the molten salt can be obtained between the difference between the oxidation and reduction potential. This is evident when the current begins to increase exponentially upon increasing the potential. The theoretical E_d of the molten salt can also be determined using thermodynamic data, using the following reaction [208].

$$\Delta G^{\circ} = -nFE_d \qquad \textbf{Equation 3.9}$$

Equation 3.9 expresses the relationship between decomposition potential and Gibbs free energy of the dissociation reaction of the molten salt, where E_d is the decomposition potential, F is the Faradays constant, n is the number of electrons in the dissociation reaction and ΔG° is the Gibbs free energy of the dissociation reaction of the molten salt [256].

3.8 Experimental setup

This section describes the experimental setup for the **feasibility of the synthesis of cementitious compounds**, **structures and purities of the reactants in the molten salt, behaviour of the molten salt at the reaction conditions, dissolution of the reactants in the molten salt** and the **MSS of cementitious compounds.**

3.8.1 Feasibility of the synthesis of cementitious compounds

The first stage of the investigation determined the **feasibility of the synthesis of cementitious compounds**; β-Ca_2SiO_4, Ca_3SiO_5, α-Na_2SiO_3 and β-Na_4SiO_4, using thermodynamic data. This was performed using the reaction equation and chemical equilibrium module in HSC-Chemistry 6.1, developed by Outec [18]. The reaction equation module contains a list of mathematical functions for thermodynamic data, compiled by Barin et al, 2008 [19]. The chemical equilibrium module uses the Gibbs free energy optimization method, developed by Eriksson et al, to generate chemical equilibrium calculations for multi-component systems [19]. This method works upon the principle that reactions proceed spontaneously if changes in the total Gibbs free energy (ΔG) of the system is negative, at constant temperature and pressure [210].

3.8.2 Structures and purities of the reactants in the molten salt

The second stage of the investigation determined the **structures and purities of the reactants;** $CaCO_3$ (≥ 99%), SiO_2 (≥ 99%) and NaCl (≥ 99%) (Sigma-Aldrich) using XRD, CV and thermodynamic data. [16] These studies were performed using the H, S, C and G, Diagrams module in HSC-Chemistry 6.1, developed by Outec which is described earlier [18]. A list of selected experiments that were performed by the author is shown in table 3.4. Prior to all these experiments, the reactants were dried at ~200ºC at atmospheric pressure for ~72 hours in an evaporating furnace (Carbolite).

Experiment	Description	Temperature (°C)	Reactant (s)	Composition (mol%)
1	Structure and purity of $CaCO_3$	25	$CaCO_3$	100
2	Structure and purity of NaCl	25	NaCl	100
3	Structure and purity of SiO_2	25	SiO_2	100
4	Purity of NaCl	25	NaCl	100

Table 3.3: Structures and purities of the reactants in the molten salt experiments.

Experiments 1-3 were taken directly to an XRD machine (STOE, PANalytical).

Experiment 4 was placed in a round bottom sintered Al_2O_3 crucible (Dynamic ceramic) of dimensions 50 mm OD x 44 mm ID x 75 mm high, 110 ml capacity, previously dried for ~72 hours [18]. The crucible was placed inside a high-temperature tubular furnace (Vecstar) under argon (≥ 99.9%) (at 0.010 l/s) (BOC). The furnace temperature was controlled by a temperature programmer (Eurotherm 315) (± 2ºC) and the internal cell temperature was measured by an N-type thermocouple (RS Components). The furnace was then heated (at 2ºC min^{-1}) to 830ºC, and two platinum wires (serving as anodes and cathodes) in $Al_6Si_2O_{13}$ tubes (Dynamic ceramic) and a reference electrode was immersed in the molten salt, at a depth of 1 cm. Then cyclic voltammetry sweeps were performed using a potentiostat (Autolab) controlled by GPES 4.9 software [243].

---

[16] The salt was NaCl.

3.8.3 Behaviour of the molten salt at the reaction conditions

The third stage of the investigation determined the **behaviour of the molten salt at the reaction conditions** using a DSC and thermodynamic data. These studies were performed using NaCl (≥ 99%) (Sigma-Aldrich), and $CaCl_2$ (from calcium chloride hexahydrate (($CaCl_2.6H_2O$)) (≥ 99%) (Sigma-Aldrich)). A list of selected experiments performed by the author is shown in table 3.5. Prior to all experiments, NaCl was dried at ~200ºC at atmospheric pressure for ~72 hours in an evaporating furnace (Carbolite) and $CaCl_2.6H_2O$ was taken directly as received.

Experiment	Description	Temperature (°C)	Reactant (s)	Composition (mol%)
5	Melting point (open crucible)	25-850	NaCl	100
6	Melting point (closed crucible)	25-850	NaCl	100
7	Melting point (closed crucible)	25-850	$CaCl_2$	100

Table 3.4: Behaviour of the molten salt at the reaction conditions experiments.

Experiment 5 involved placing NaCl (Sigma-Aldrich) in an open Al_2O_3 crucible (Dynamic ceramic) alongside an empty reference crucible, in a DSC (Setaram) [227].

Experiment 6 involved placing NaCl (Sigma-Aldrich) in an Inconel^{TM} 600 crucible. This was hermitically sealed and heated in a furnace (Vecstar Ltd) to ~860ºC, to ensure the container was airtight. The Inconel^{TM} 600 crucible was then placed alongside an empty reference crucible, in a DSC (Setaram) [227].

Experiment 7 involved placing $CaCl_2.6H_2O$ in an Al_2O_3 crucible (Dynamic ceramic) of dimensions 50 mm OD x 48 mm ID x 50 mm height and fusing under argon (≥ 99.9%) in a furnace (Vecstar) to ~860ºC, at atmospheric pressure (BOC), to dehydrate the $CaCl_2.6H_2O$ to $CaCl_2$. The mixture was then broken into several pieces in a glove box under argon (≥ 99.9%) and placed in an empty Inconel^{TM} 600 crucible. The crucible was then hermitically sealed and heated in a furnace (Vecstar) for 15 minutes and placed alongside an empty reference crucible, in a DSC (Setaram) [227]. All samples were then subjected to a heating rate of 2°C min^{-1} between 25-850ºC.

3.8.4 Dissolution of the reactants in the molten salt

The fourth stage of the investigation determined the **dissolution of the reactants**; Na_2CO_3, (≥ 99%), $CaCO_3$ (≥ 99%) and SiO_2 (≥ 99%) in molten NaCl (≥ 99%) (Sigma-Aldrich) at 830ºC, using XRD, SEM, drop calorimetry, predominance diagrams, thermodynamic data and a DSC, which subsequently led to obtaining the phase diagram for molten NaCl-Na_2CO_3, ΔH_{mix} values for molten NaCl-Na_2CO_3 and K_{sp} values for CaO and Na_2O in NaCl at 830ºC. The solubilities of $CaCO_3$ and SiO_2 are well-known to be low, as described by Yasuda, 2007 and Cherginets, 2005, therefore it was not possible to investigate these at this stage [130] [208]. A list of selected experiments performed by the author is shown in tables 3.6-3.9. Prior to these experiments, the reactants were dried at ~200ºC at atmospheric pressure for ~72 hours in an evaporating furnace (Carbolite).

3.8.4.1 Phases of the reactants in the molten salt

Experiment	Description	Temperature (°C)	Reactant (s)	Composition (mol%)
8	Phases of $CaCO_3$ in NaCl	830	$CaCO_3$, NaCl	20, 80
9	Phases of Na_2CO_3 in NaCl	830	Na_2CO_3, NaCl	20, 80
10	Phases of $CaCO_3$ in NaCl	830	$CaCO_3$, NaCl	20, 80
11	Phases of $CaCO_3$ in NaCl	830	$CaCO_3$, NaCl	20, 80
12	Phases of $CaCO_3$ in NaCl	830	$CaCO_3$, NaCl	20, 80
13	Phases of $CaCO_3$ in NaCl	830	$CaCO_3$, NaCl	20, 80
14	Phases of Na_2CO_3 in NaCl	830	Na_2CO_3, NaCl	20, 80
15	Phases of SiO_2 in NaCl	830	SiO_2, NaCl	20, 80

Table 3.5: Phases of the reactants in the molten salt experiments.

Experiments 8-15 involved placing the reactants in a round bottom sintered Al_2O_3 crucible (Dynamic ceramic) of dimensions 50 mm OD x 44 mm ID x 75 mm high, 110 ml capacity, also previously dried for ~72 hours. The crucible and contents were then placed in a muffle furnace (Vecstar) with an air atmosphere and open exhaust, and temperature was raised over ~5 hours to 830°C. After ~3 hours, the furnace was switched off and allowed to cool naturally for ~24 hours. The final product was fused to the crucible, and required a screwdriver and hammer to remove the pieces. These pieces were then taken to an XRD machine (STOE, PANalytical) and an SEM machine (Jeol). The experimental layout for these experiments is shown in figure 3.15.

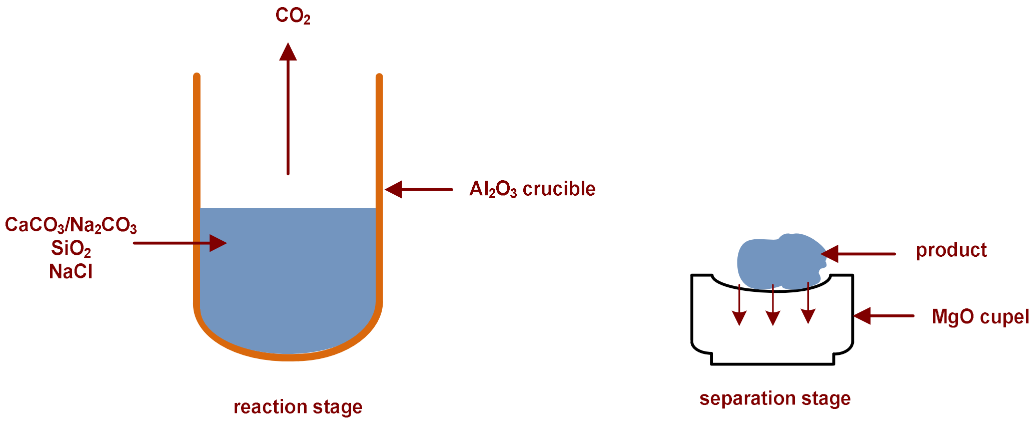

Figure 3.15: Phases of the reactants in the molten salt experimental layout.

3.8.4.2 Phase diagrams of the reactants in the molten salt

Experiment	Description	Temperature (°C)	Reactant (s)	Composition (mol%)
16	Molten NaCl-Na_2CO_3	830	Na_2CO_3, NaCl	-
17	Molten NaCl-Na_2CO_3	830	Na_2CO_3, NaCl	-
18	Molten NaCl-Na_2CO_3	830	Na_2CO_3, NaCl	-
19	Molten NaCl-Na_2CO_3	830	Na_2CO_3, NaCl	-
20	Molten NaCl-Na_2CO_3	830	Na_2CO_3, NaCl	-

Table 3.6: Phase diagrams of the reactants in the molten salt experiments.

Experiments 16-20 involved placing the reactants in an Inconel^{TM} 600 crucible which was hermitically sealed and heated in a muffle furnace (Vecstar) to ~860ºC to ensure the container was airtight. The crucible was then placed alongside an empty reference crucible, in a DSC (Setaram) [227]. All samples were subjected to a heating rate of 2°C min^{-1} between 25-850ºC and all peaks on the heat flow curves were analyzed from heating curves, to avoid any effects of super cooling which can cause shifts in peak temperature. The experimental layout for these experiments is shown in figure 3.16.

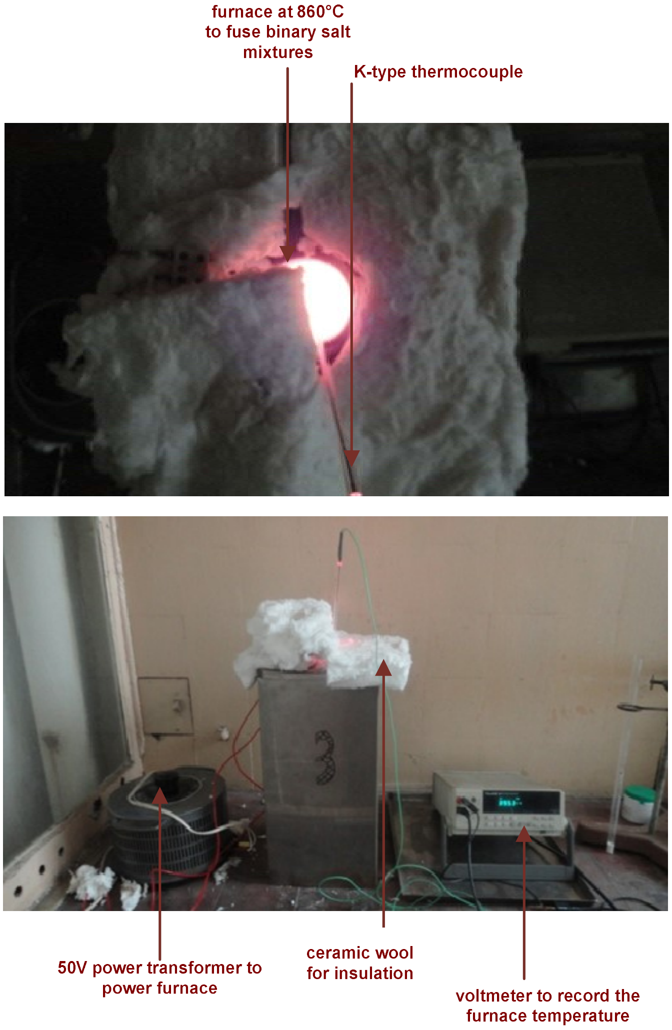

Figure 3.16: Phase diagrams for the reactants in the molten salt experimental layout.

3.8.4.3 Heats of mixing of the reactants in the molten salt

Experiment	Description	Temperature (˚C)	Reactant (s)	Composition (mol%)
21	Signal stabilization	830	NaCl	100
22	Signal stabilization	830	NaCl	100
23	ΔH_f of Na_2CO_3 (pellets)	830	Na_2CO_3	100
24	ΔH_f of Na_2CO_3 (pellets)	830	Na_2CO_3	100
25	ΔH_f of Na_2CO_3 (crystals)	830	Na_2CO_3	100
26	ΔH_f of Na_2CO_3 (crystals)	830	Na_2CO_3	100
27	ΔH_f of NaCl (pellets)	830	NaCl	100
28	ΔH_{mix} of molten NaCl-Na_2CO_3 (pellets)	830	Na_2CO_3, NaCl	-
29	ΔH_{mix} of molten NaCl-Na_2CO_3 (pellets)	830	Na_2CO_3, NaCl	-
30	ΔH_{mix} of molten NaCl-Na_2CO_3 (crystals)	830	Na_2CO_3, NaCl	-

Table 3.7: ΔH_{mix} and ΔH_f values of the reactants in the molten salt experiments.

Experiments 21-22 involved filling a glassy carbon crucible (Alfa Aesar) with NaCl and then placing inside a SiO_2 calorimetric tube. The tube was then inserted into the drop calorimeter well at ~830ºC under argon (≥ 99.9%), (BOC) at a flowrate of 0.1 l min^{-1} to prevent its oxidation, along with a reference tube tube for 15 minutes.

Experiments 23-26 involved placing Na_2CO_3 in an Al_2O_3 crucible (Dynamic ceramic) of dimensions; 50 mm OD x 48 mm ID x 50 mm high, in a furnace at 860ºC at atmospheric pressure, and fusing under argon (≥ 99.9%) for 15 minutes (BOC). The crucible was then broken into several pieces in a glove box to produce crystals of Na_2CO_3. Then Na_2CO_3 and NaCl were placed into an evacuable pellet die (Specac) and a 5 mm plunger (Specac) placed ontop of the pellet die. These materials were then placed into a manual press, where a pressure was applied by the user for ~10 minutes to produce pellets of Na_2CO_3 and NaCl (figure 3.17). The exact pressure quantity was unknown due to the limitations of the press.

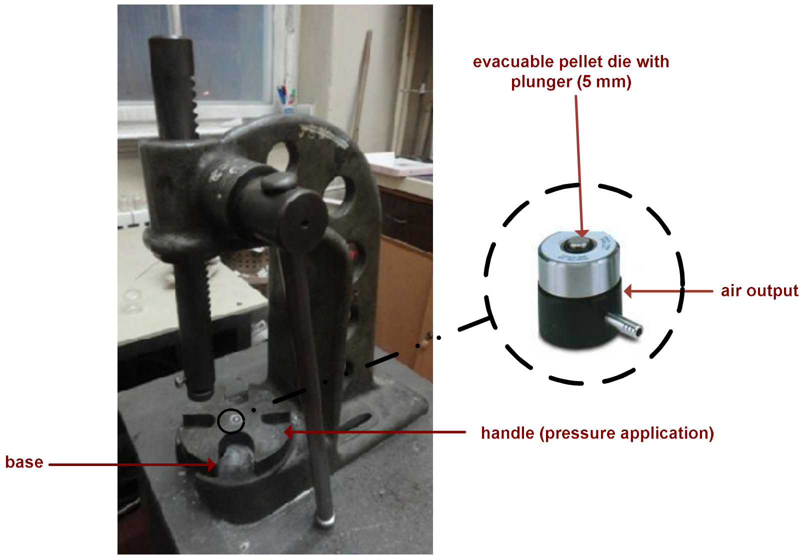

Figure 3.17: Manual press with pellet die.

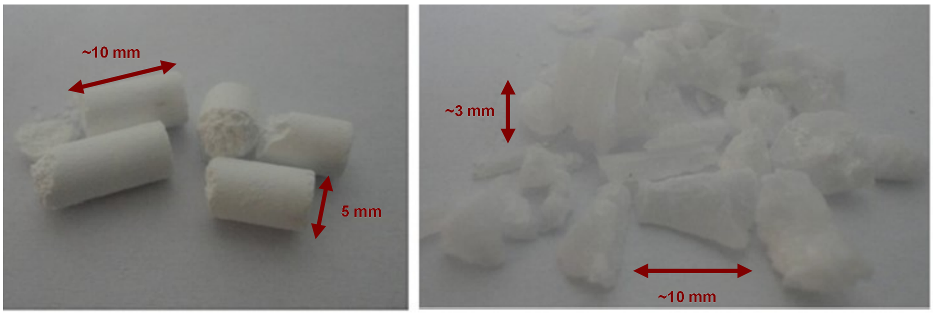

Figure 3.18: Pellets (left) and crystals (right) of Na_2CO_3.

Figure 3.18 shows the pellets and crystals of Na_2CO_3 which were ~5 mm in diameter and of irregular shape. The pellets of Na_2CO_3 were reasonably held together however it was suspected each pellet contained irregular voids due to the limitations of the press. This may have resulted in a slightly different surface area exposed to the atmosphere, which may cause the effects of moisture to play a role (forming sodium carbonate hydate ($Na_2CO_3.nH_2O$)). It is for this reason that crystals of Na_2CO_3 were also produced for purposes of comparison. This should result in voids being within the tens to hundreds of nanometres, corresponding to a minute and consistent porosity. These crystals and pellets were both kept in an evaporating oven prior to the experiments to minimize the effects of moisture in the atmosphere. Then an empty crucible was placed into the sample calorimetric tube, which was placed into the drop calorimeter well, at ~830ºC, under an argon flowrate of 0.1 l min^{-1}. The drop calorimeter was then stabilized for ~3 hours before each experiment before the addition of pellets or crystals of Na_2CO_3 and pellets of platinum (between 0.7-1.4 g) for calibration.

Experiments 27-30 involved placing Na_2CO_3 in an Al_2O_3 crucible (Dynamic ceramic) of dimensions; 50 mm OD x 48 mm ID x 50 mm high, in a furnace at 860ºC, at atmospheric pressure and fusing under argon (≥ 99.9%) (BOC) for ~15 minutes. The crucible was then broken into several pieces in a glove box under argon (≥ 99.9%), prior to the experiments to produce crystals of Na_2CO_3. Then Na_2CO_3 and NaCl were placed into an evacuable pellet die (Specac) and a 5 mm plunger (Specac) placed ontop of the die. These materials were placed into the manual press, where a pressure was applied by the user for ~15 minutes, to produce pellets of Na_2CO_3 and NaCl. Then a glassy carbon crucible (Alfa Aesar) was filled with NaCl and placed inside a SiO_2 calorimetric tube. This tube was then inserted into the drop calorimeter well at ~830ºC under argon at a flowrate of 0.1 l min^{-1} (BOC). The drop calorimeter was stabilized for ~3 hours before each measurement before the addition of pellets or crystals Na_2CO_3, pellets of NaCl and pellets of platinum (between 0.7-1.4 g) for calibration.

3.8.4.4 Solubility products of the reactants in the molten salt

Experiment	Description	Temperature (°C)	Reactant (s)	Composition (mol%)
31	Signal stabilization (Al_2O_3 crucible)	830	NaCl	100
32	Signal stabilization (Al_2O_3 crucible)	830	NaCl	100
33	Signal stabilization (Al_2O_3 crucible)	830	NaCl	100
34	$CaCO_3$ in NaCl (Al_2O_3 crucible)	830	$CaCO_3$, NaCl	-
35	Na_2CO_3 in NaCl (Al_2O_3 crucible)	830	Na_2CO_3, NaCl	-
36	Na_2CO_3 in NaCl (glassy carbon crucible)	830	Na_2CO_3, NaCl	-
37	Na_2CO_3 in NaCl (glassy carbon crucible)	830	Na_2CO_3, NaCl	-
38	$CaCO_3$ in NaCl (glassy carbon crucible)	830	$CaCO_3$, NaCl	-
39	Na_2CO_3 in NaCl (glassy carbon crucible)	830	Na_2CO_3, NaCl	-
40	Na_2CO_3 in NaCl (platinum crucible)	830	Na_2CO_3, NaCl	-
41	Na_2CO_3 in NaCl (platinum crucible)	830	Na_2CO_3, NaCl	-
42	NaCl	830	NaCl	-

Table 3.8: K_{sp} values of the reactants in the molten salt experiments.

Potentiometry involved constructing a cell envelope, an ISE and a Ag/Ag^+ reference electrode. The ISE was constructed from a closed ended YSZ (8 mol% Y_2O_3, 92 mol% ZrO_2) membrane of dimensions 6 mm OD, 4 mm ID containing Na_2CO_3 (0.1 mol kg^{-1}), molten AgCl-NaCl (0.75 mol kg^{-1}) and NaCl (0.1 mol kg^{-1}) with a silver wire (≥ 99.9%, 2 mm OD) and silicon cap. The Ag/Ag^+ reference electrode was constructed from a closed-ended mullite ($Al_6Si_2O_{13}$) membrane of dimensions 6 mm OD, 4 mm ID, containing molten AgCl-NaCl (0.75 mol kg^{-1}) with a silver wire (≥ 99.9%, 2 mm OD) and silicon cap. The cell envelope was constructed from Inconel^{TM} 600 or Stainless Steel 316L (Philip Cornes, Berkley Stainless Steel).

Experiments 31-33 involved placing NaCl inside an Al_2O_3, platinum and glassy or carbon crucible (Dynamic Ceramic, Alfa Aesar, Johnson Matthew) and placing inside a cell. The cell was then placed inside a high-temperature tubular furnace (Vecstar) under an argon atmosphere (≥ 99.9%) (BOC) at 0.010 l/s. The furnace temperature was controlled by a Eurotherm 315 programmer (± 2ºC) and the internal cell temperature measured with an N-type thermocouple (RS Components). The electrodes were inserted into the cell and connected electrically using a voltmeter (Uni-trend) and a drop tube constructed from an $Al_6Si_2O_{13}$ membrane was also inserted. The furnace temperature was then heated to 830ºC at 2ºC min^{-1} for ~8 hours prior to the experiments and both the Ag/Ag^+ reference electrode and ISE were immersed in the molten salt, at a 1 cm depth.

Experiments 34-41 involved placing NaCl inside an Al_2O_3, platinum and glassy carbon crucible (Alfa Aesar) and placing inside a cell, constructed from Inconel^{TM} 600 or Stainless Steel 316L. The cell was then placed inside a high-temperature tubular furnace (Vecstar) under argon (≥ 99.9%) at 0.010 l/s. The electrodes were inserted into the cell and connected electrically using a voltmeter (Uni-trend) and a drop tube constructed from $Al_6Si_2O_{13}$ was also inserted. The furnace temperature was heated to 830ºC at 2ºC min^{-1} for ~8 hours prior to the experiments, when both reference electrode and ISE were immersed in the molten salt, at a depth of 1 cm. Then pellets of Na_2CO_3 and $CaCO_3$ were added to the molten salt, using the drop tube and the potentiometric signal recorded using Uni-Trend software. The pellets of Na_2CO_3 and $CaCO_3$ were produced using a similar procedure to that described previously in the ΔH_{mix} and ΔH_f experiments however in this case an exact pressure of ~2 tonnes was applied to the pellet press (Specac). Upon the addition of pellets, time frames of between 10 minutes to 5 hours were allowed between each experiment and an argon gas bubbler inserted into the molten salt to ensure the complete dissolution and decomposition of the pellet.

Experiment 42 involved removing a sample of evaporated powder on the cell envelope walls and taking to an SEM (Joel) machine. The experimental layout for the potentiometric cell and the cell envelope materials are shown in figure 3.19-3.20.

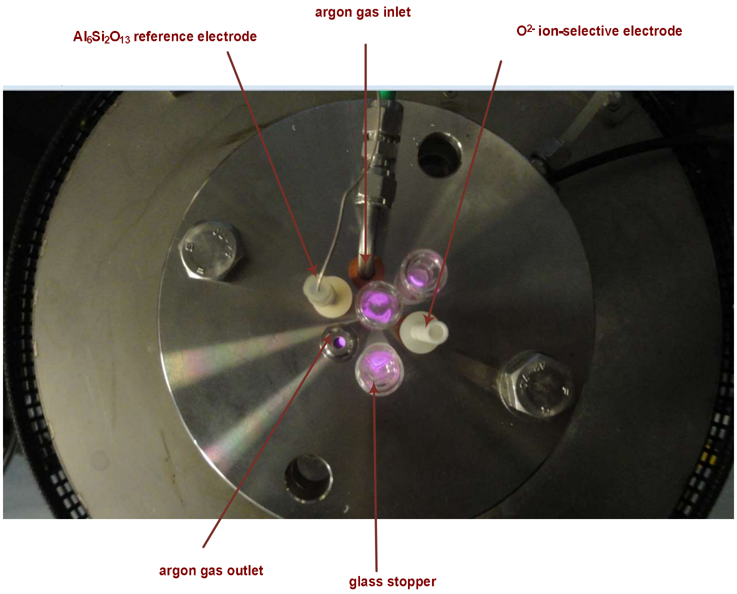

Figure 3.19 Image of the galvanic cell layout (top view).

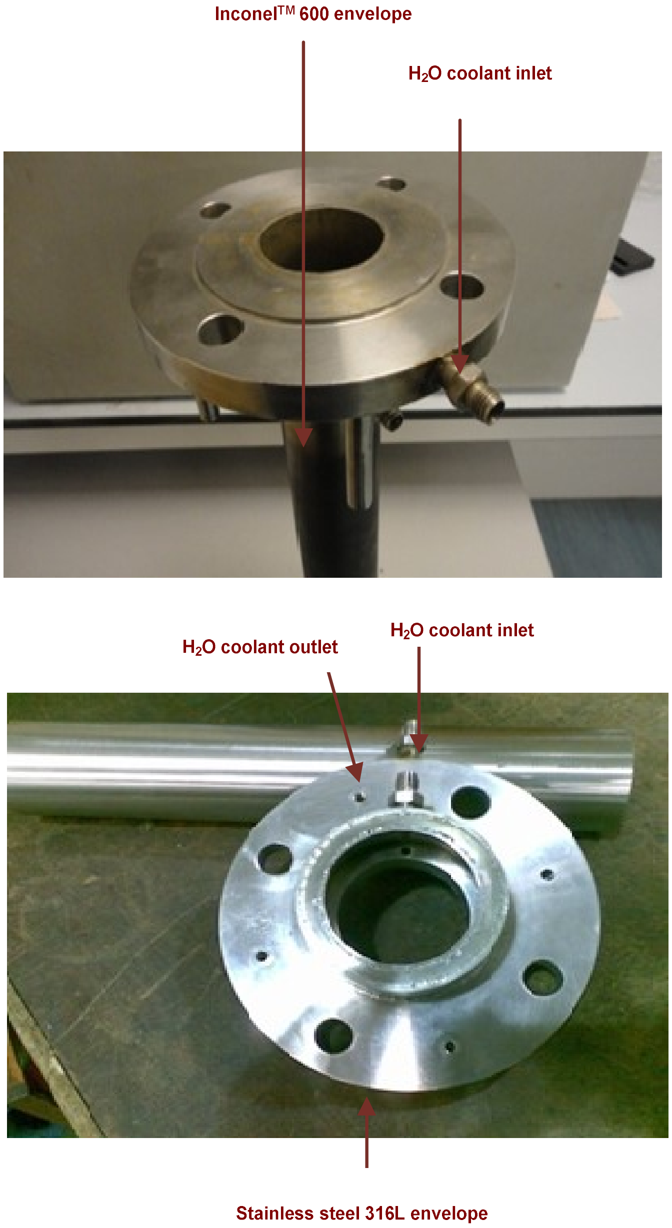

Figure 3.20: Image of cell envelope materials; Inconel^{TM} 600 (top) and Stainless Steel 316L (bottom).

3.3.5 Molten salt synthesis of cementitious compounds

The fifth stage of the investigation investigated the **MSS for cementitious compounds**; α-Na_2SiO_3, β-Na_4SiO_4, Ca_3SiO_5 and β-Ca_2SiO_4, from the reactants; SiO_2 (≥ 99%) $CaCO_3$ (≥ 99%) Na_2CO_3 (≥ 99%), to 830ºC and 1100ºC, using XRD and SEM. The cementitious compounds were also depicted on predominance diagrams for the molten salt systems considered. A list of selected experiments that were performed by the author is shown in table 3.10. Prior to all experiments the reactants were dried at ~200ºC at atmospheric pressure for ~72 hours in an evaporating furnace (Carbolite).

Experiment	Description	Temperature (s)	Reactant (s)	Composition (mol%)
43	MSS of Ca_2SiO_4 (Al_2O_3 crucible)	830	$CaCO_3$, SiO_2, NaCl	10, 5, 85
44	MSS of Ca_2SiO_4 (Al_2O_3 crucible)	830	$CaCO_3$, SiO_2, NaCl	10, 5, 85
45	MSS of Ca_2SiO_4 (Al_2O_3 crucible)	830	$CaCO_3$, SiO_2, NaCl	10, 5, 85
46	MSS of Ca_3SiO_5 (Al_2O_3 crucible)	1100	$CaCO_3$, SiO_2, NaCl	11.25, 3.75, 85
47	Separation of Ca_2SiO_4 (MgO cupel)	830	$CaCO_3$, SiO_2, NaCl	-
48	Separation of Ca_2SiO_4 (MgO cupel)	830	$CaCO_3$, SiO_2, NaCl	-
49	Separation of Ca_3SiO_5 (MgO cupel)	1100	$CaCO_3$, SiO_2, NaCl	-
50	MSS of Na_2SiO_3 (Al_2O_3 crucible)	830	Na_2CO_3, SiO_2, NaCl	1.25, 3.75, 85
51	MSS of Na_4SiO_4 (Al_2O_3 crucible)	830	Na_2CO_3, SiO_2, NaCl	1.25, 3.75, 85
52	MSS of Na_2SiO_3 (Al_2O_3 crucible)	830	Na_2CO_3, SiO_2, NaCl	10, 5, 85
53	MSS of Ca_2SiO_4 (Al_2O_3 crucible)	830	$CaCO_3$, SiO_2, NaCl	10, 5, 85
54	MSS of Na_2SiO_3 (Al_2O_3 crucible)	830	$CaCO_3$, SiO_2, NaCl	10, 5, 85
55	Separation of Ca_2SiO_4 (MgO cupel)	830	$CaCO_3$, SiO_2, NaCl	-
56	MSS of Na_2SiO_3 (Al_2O_3 crucible)	830	Na_2CO_3, SiO_2, NaCl	10, 5, 85
57	Separation of Na_2SiO_3 (MgO cupel)	830	Na_2CO_3, SiO_2, NaCl	-

Table 3.9: MSS of cementitious compounds experiments.

Experiments 43-46 involved placing the reactants in an Al_2O_3 crucible (Dynamic ceramic). The crucible and contents were then placed in a muffle furnace (Vecstar) in an air atmosphere and open exhaust, and furnace temperature raised over ~5 hours to 830ºC and 1100ºC. After ~3 hours, the furnace was switched off and allowed to cool naturally for ~24 hours. The final samples were fused to the crucible, therefore a screwdriver and hammer was used to remove the pieces, before being taken for XRD (STOE, PANalytical).

Experiments 47-49 involved placing the products from Experiment 42, 43 and 45 and in an MgO cupel (Cerex Ltd) also previously dried at ~200ºC. This was selected due to its high melting temperature (at 1800ºC) and porosity to liquids. The cupel and contents were placed in a muffle furnace and the furnace temperature raised to ~1000ºC for ~6 hours. During this period, molten NaCl was absorbed by the cupel and a small quantity lost by evaporation. The furnace was then switched off and allowed to cool for ~1 hour. The samples were then removed using a screwdriver and hammer and taken for XRD (STOE, PANalytical).

Experiments 50-54 and 56 involved placing the reactants in an Al_2O_3 crucible (Dynamic ceramic). The crucible and contents were then placed in a muffle furnace with an air atmosphere and open exhaust, and temperature was raised over ~5 hours to 830ºC and 1100ºC. After ~3 hours, the furnace was switched off and allowed to cool naturally for ~24 hours. The samples were then removed using a screwdriver and hammer and taken for XRD (STOE, PANalytical).

Experiments 55 and 57 involved taking the products from Experiment 54 and 56 in an Al_2O_3 crucible (Dynamic Ceramic) and placing the contents in an MgO cupel (Cerex Ltd) - also previously dried at ~200ºC. The cupel and contents were placed in a muffle furnace (Vecstar) and the temperature was raised to ~1000ºC for ~6 hours. During this period, molten NaCl was absorbed by the cupel and a small quantity lost by evaporation. The furnace was then switched off and allowed to cool for ~1 hour and samples removed using a screwdriver and hammer and taken to an SEM (Joel). The experimental layout for these experiments is shown in figure 3.21.

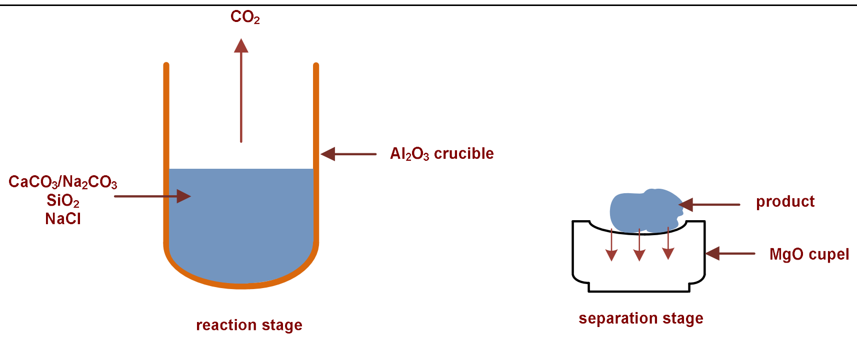

Figure 3.21: MSS of cementitious compounds experimental layout.

Chapter 4

Results & discussion

4.1 Introduction

This chapter describes an investigation into the MSS of cementitious compounds. Initially the **feasibility of the synthesis of cementitious compounds** will be investigated using thermodynamic data. This will be used to suggest the reaction temperatures required to produce cementitious compounds, useful for the selection of a salt for MSS. Then the **structures and purities of the reactants in the molten salt** will be investigated using XRD and CV. This will used to suggest the purity and phase transitions of the reactants at the reaction conditions, useful for analyzing XRD and SEM patterns. Then, the **behaviour of the molten salt at the reaction conditions** will be investigated using a DSC and the chemical equilibrium module in HSC-Chemistry 6.1, useful for describing the effects of vapour pressure upon the salt, and reaction conditions required for the experiments. Then, the **dissolution of the reactants in the molten salt** will be investigated, using a DSC, drop calorimetery, potentiometry and thermodynamic data, and will subsequently lead to obtaining K_{sp}, ΔH_{mix} values and phase diagrams, useful for determining whether MSS of cementitious compounds are possible. Then the **MSS of cementitious compounds** will be investigated using XRD and SEM and depicted on predominance diagrams, useful for determining which other compounds can be produced in this manner.

4.2 Feasibility of the synthesis of cementitious compounds

The initial stage of the investigation was to determine the **feasibility of the synthesis of cementitious compounds**; β-Ca_2SiO_4, Ca_3SiO_5, α-Na_2SiO_3 and β-Na_4SiO_4 from the reactants; $CaCO_3$, Na_2CO_3 and SiO_2, using thermodynamic data. This information will be used to select a salt for investigation.

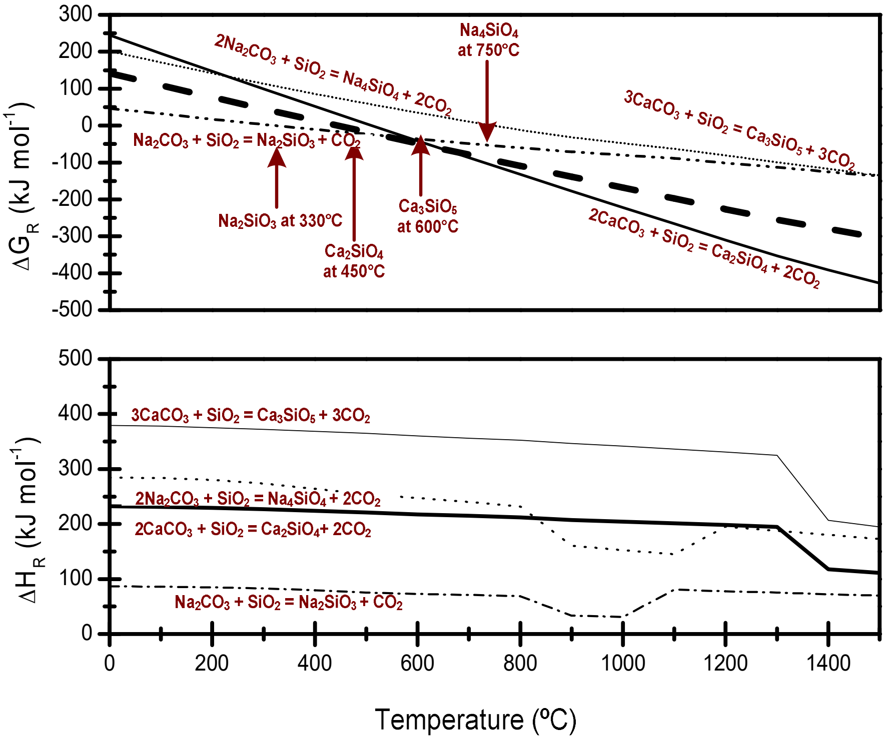

Figure 4.1: ΔH_R (bottom) and ΔG_R (top) data for the synthesis as a function of temperature, 1 atm (HSC-Chemistry 6.1) [18-19].

The reaction temperatures for the synthesis of β-Ca_2SiO_4, Ca_3SiO_5, α-Na_2SiO_3 and β-Na_4SiO_4 was investigated using the reaction equation module in HSC-Chemistry 6.1 [18]. This module plotted the Gibbs free energies (ΔG_R) and enthalpies of reaction (H_R) data for α-Na_2SiO_3, β-Na_4SiO_4, β-Ca_2SiO_4 and Ca_3SiO_5 from the reactants; $CaCO_3$, Na_2CO_3 and SiO_2, as a function of temperature respectively (figure 4.1).

The ΔH_R data shows these reactions are highly exothermic, producing between ~100-400 kJ mol^{-1} of energy over this temperature range. The ΔG_R data shows these reactions occur at 330ºC, 450ºC, 600ºC and 750ºC respectively (shown by negative ΔG_R values above these temperatures). This information is similar to previous reviews by Taylor, 1990 and synthesis studies by Wesselsky and Jensen, 2009, and the Na_2O-

SiO_2 phase diagram generated by Ryś and Müller, 2010 and Halter et al, 2004, whom state that β-Ca_2SiO_4, α-Na_2SiO_3 and β-Na_4SiO_4 require reaction temperatures exceeding 680ºC, 577.8ºC and 750ºC to be produced [14] [49] [246-247]. However the synthesis studies performed by Wesselsky and Jensen, 2009 state that Ca_3SiO_5 requires reaction temperatures exceeding 1250ºC to be produced, and below which CaO and β-Ca_2SiO_4 is produced [14] [49]. This difference of ~500ºC suggests there maybe an intermediate reaction which takes place before this compound is produced, probably β-Ca_2SiO_4. This intermediate reaction has also been reported on the CaO-SiO_2 phase diagram generated in the Bale et al, 2002, FactSage thermochemical database [209].

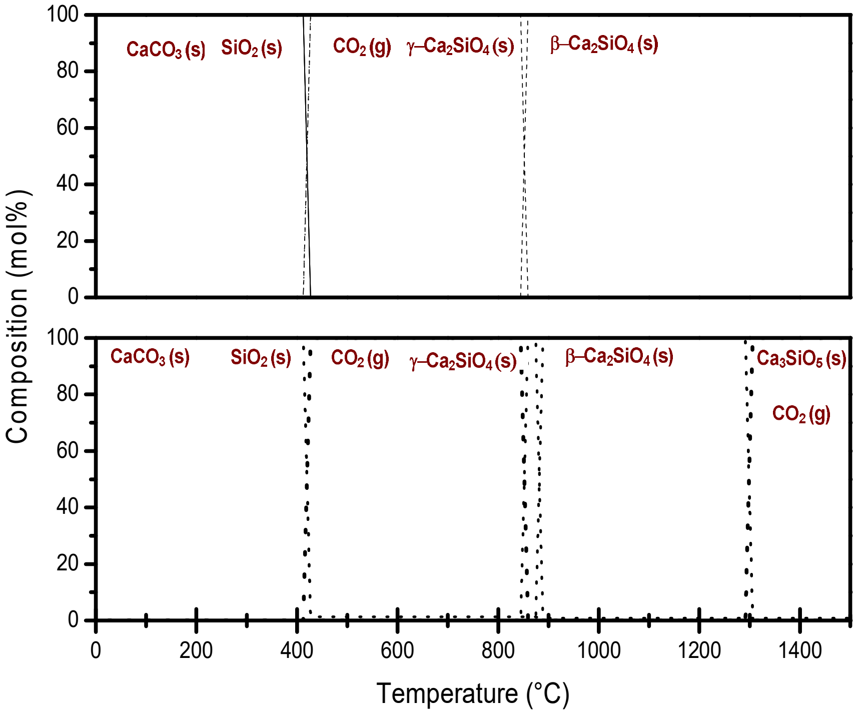

Figure 4.2: Chemical equilibrium calculations for the synthesis of β-Ca_2SiO_4 (top) and Ca_3SiO_5 (bottom) as a function of temperature, 1 atm (HSC-Chemistry 6.1) [18-19].

The reaction temperatures for the synthesis of β-Ca_2SiO_4 and Ca_3SiO_5 were also obtained using the chemical equilibrium module in HSC-Chemistry 6.1 [18]. This module plotted the equilibrium conditions for these reactions as a function of temperature (figure 4.2).

The diagram shows the synthesis of β-Ca_2SiO_4 and Ca_3SiO_5 occurs at ~820ºC and ~1250ºC. The information supports previous experimental studies by Wesselsky and Jensen, 2009, the ΔG_R data for β-Ca_2SiO_4 in the reaction equation module in HSC-

Chemistry 6.1, however disagrees with the ΔG_R data for Ca_3SiO_5 [14] [49]. This also supports the conclusion that β-Ca_2SiO_4 is an intermediate compound which forms before the formation of Ca_3SiO_5, and can be supported by the previous experimental synthesis studies by Wesselsky and Jensen, 2009 [49]. These authors also produced β-Ca_2SiO_4 and Ca_3SiO_5 in solid-state reactions at 680ºC, which required quenching and stabilization with foreign ions and at 1250ºC respectively [49]. It is the authors opinion however that these solid-state reactions are difficult to incorporate in an industrial process as this requires the presence of a liquid flux (melting the reactant with the lowest melting temperature (i.e. $CaCO_3$ (at 1339ºC))), making such reactions extremely energy-intensive [18]. MSS could potentially lower these reaction temperatures, and hence the energy requirement as suggested by Kimura, 1991 [50].

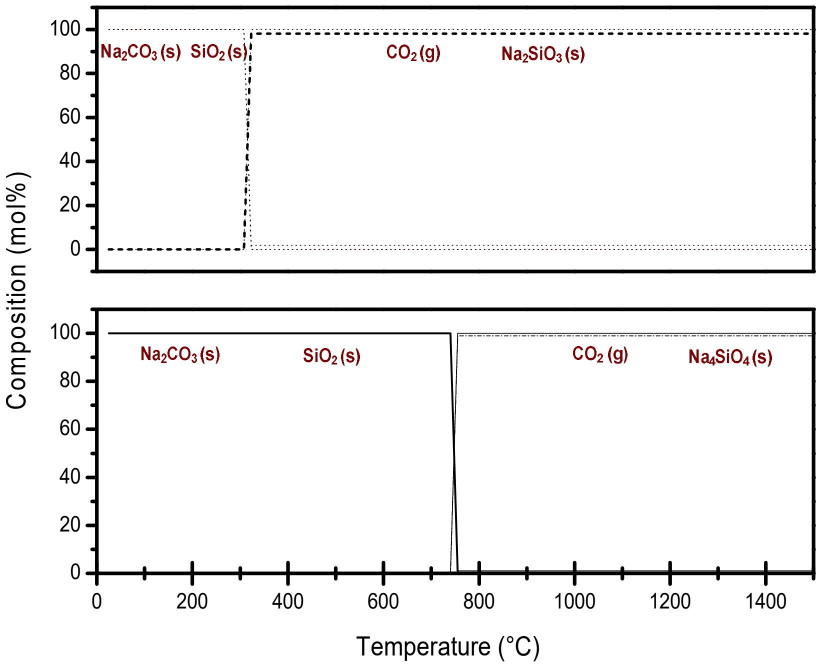

Figure 4.3: Chemical equilibrium calculations for the synthesis of β-Na_4SiO_4 (bottom) and α-Na_2SiO_3 (top) as a function of temperature, 1 atm (HSC-Chemistry 6.1) [18-19].

The reaction temperatures for the synthesis of β-Na_4SiO_4 and α-Na_2SiO_3 were obtained using the chemical equilibrium module in HSC-Chemistry 6.1 [18]. This module plotted the equilibrium conditions of the reactions considered as a function of temperature (figure 4.3).

The diagram shows the synthesis of α-Na_2SiO_3 and β-Na_4SiO_4 occurs at ~200ºC and ~750ºC respectively. This information agrees with the previous ΔG_R data shown earlier and demonstrates the synthesis of these compounds do not have an intermediate compound. The information also supports the Na_2O-SiO_2 phase diagrams generated by authors such as Halter et al, 2004, Ryś and Müller, 2010 that β-Na_4SiO_4 and α-Na_2SiO_3 require reaction temperatures of ~800ºC to be produced (using Na_2O instead of Na_2CO_3) [245-249]. This information also coupled with previous reports from Mersen Group, 2016 that state that these compounds are produced at reaction temperatures exceeding ~900ºC, in a solid-liquid reaction (by melting Na_2CO_3 and reacting with SiO_2) [264]. This information suggests there is potential to lower the reaction temperatures in industry using MSS, and hence the overall energy requirement.

Compounds	Reaction temperature (ºC)		
	ΔG_R data	**Chemical equilibrium module**	**Solid-state synthesis studies**
Na_2SiO_3 (s)	330	200	900
Na_4SiO_4 (s)	450	750	900
Ca_2SiO_4 (s)	600	820	680
Ca_3SiO_5 (s)	750	1250	1250

Table 4.1: Reaction temperatures for the synthesis of cementitious compounnds; β-Na_4SiO_4 (s), Na_2SiO_3 (s), β-Ca_2SiO_4 (s) and Ca_3SiO_5 (s) [18-19].

The reaction temperatures from various sources were tabulated for comparison (table 4.1). It can be noted the reaction temperatures from ΔG_R data are often lower than the chemical equilibrium module in HSC-Chemistry 6.1, which can be attributed to the possible presence of intermediate compounds before the reaction which affects the calculation. The reaction temperatures from ΔG_R data and chemical equilibrium module were also different from previous synthesis studies, which can be attributed to differences in reaction conditions (such as the flow of gases affecting the pressure of the system).

This section has shown it maybe possible to synthesise α-Na_2SiO_3, β-Ca_2SiO_4, Ca_3SiO_5 and β-Na_4SiO_4 at reaction temperatures between 200-1250ºC and hence MSS. This suggests a suitable molten salt for this investigation could be NaCl, which has a stability range between ~801-1413ºC (the same range as the reactions investigated in this thesis) [56]. Also the viscosity of NaCl (1.03 Pa.s at 810ºC) is in the same magnitude of H_2O (0.874 Pa.s at 25ºC) which allows for a reasonable separation from an insoluble product and the vapour pressure of NaCl (0.302 mmHg $ºC^{-1}$ at 801ºC) was lower than H_2O (26.5 mmHg $^{\circ}C^{-1}$ at 25ºC) indicating minimal loss of the reactants at 830°C [56].

4.3 Structures and purities of the reactants in the molten salt

The second stage of this investigation was to investigate the **structures and purities of the reactants**; Na_2CO_3, SiO_2, $CaCO_3$ and NaCl, using XRD and CV. This will be used to deduce any phase transitional temperatures at room temperature and pressure (25ºC, 1 atm) and at 830ºC, useful for analysing XRD and SEM data at a later stage.

.

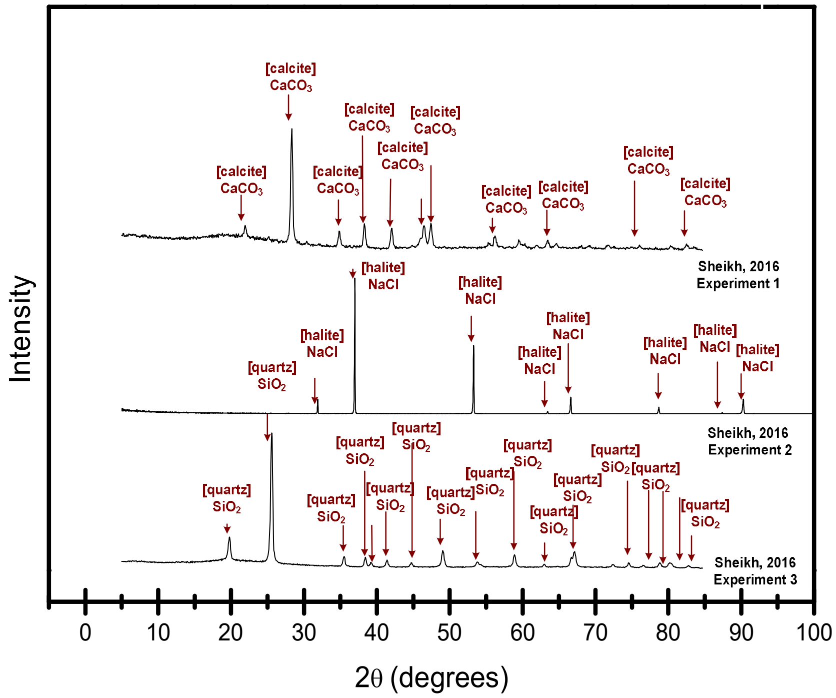

Figure 4.4: XRD pattern for $CaCO_3$, NaCl and SiO_2 powders (as received) at room temperature and pressure (25ºC, 1 atm), typical operating conditions; 2θ scan range of 5-110° with 150 seconds per steps.

The purities of the reactants were investigated by taking samples of SiO_2, $CaCO_3$ and NaCl directly from their containers (as received) at room temperature and pressure (25ºC, 1 atm) and recording their XRD patterns (figure 4.4).

The structure for Na_2CO_3 was stated as λ-Na_2CO_3 (a monoclinic structure) on the packet, therefore no XRD studies were performed. However previous structural studies for λ-Na_2CO_3 have shown it undergoes polymorphic phase transitions at ~332ºC and ~478ºC to β-Na_2CO_3 (monoclinic structure) and α-Na_2CO_3 (hexagonal structure) respectively, which is stable up to its melting temperature of 851ºC [246]. This suggests that Na_2CO_3 will be in its β-Na_2CO_3 phase (hexagonal structure) at 830ºC and 1100ºC. There is also evidence of the $Na_2CO_3.nH_2O$ compound in literature, suggesting one should dry this reactant prior to experiments [215].

The XRD pattern for SiO_2 demonstrates the existence of α-quartz (silica) its most natural form found in nature. There was no significant interaction with air/O_2 or H_2O vapour under these conditions, shown by the absence of $SiO_2.nH_2O$ phases (hydrates) which can exist under these conditions, however previous reports by Monroe et al, 1969 suggests one should dry this reactant prior to experiments [253]. Previous structural studies by Kuskov and Fabrichnaya, 1987 and information stored on the ICCD suggest for α-quartz (monoclinic structure) suggests it exhibits four polymorphic transitions at 573ºC, 870ºC and 1470ºC to β-quartz (hexagonal structure), β-tridymite (monoclinic structure) and β-cristobalite (cubic structure) up to its melting point of 1607ºC (including many other metastable structures still under investigation) [116] [215]. This suggests that SiO_2 (α-quartz) is likely to exist in its β-quartz (hexagonal structure) at 830ºC and 1100ºC.

The XRD pattern for NaCl shows the existence of halite. The XRD pattern demonstrates no significant interaction with air/O_2 or H_2O vapour which can exist under these conditions and has been reported by Kotiranta and Roine 2009 [18]. Previous structural studies for NaCl by Stern 2001 and information stored on the ICCD have shown it exhibits a single cubic structure up to its melting temperature of 801ºC, which is its most natural phase found in nature [215] [254]. This suggests that halite is most likely to be found at 830ºC and 1100ºC.

The XRD pattern for $CaCO_3$ shows the existence of calcite. Previous structural studies for $CaCO_3$ by Clifford and Chen, 1998 have shown it exhibits three anhydrous polymorphs namely; Vaterite (hexagonal structure), Aragonite (orthorhombic structure) and calcite (monoclinic structure) [255]. These polymorphic transitions occur at ~60ºC and ~400ºC of which the last two are metastable structures as shown on the Na_2O-SiO_2 phase diagram [247]. This suggests that $CaCO_3$ will probably remain in its calcite phase (monoclinic structure) at 830ºC and 1100ºC. There is also evidence of the $CaCO_3.nH_2O$ compound in literature and on the ICCD which suggests one should dry this reactant prior to experiments [215] [255].

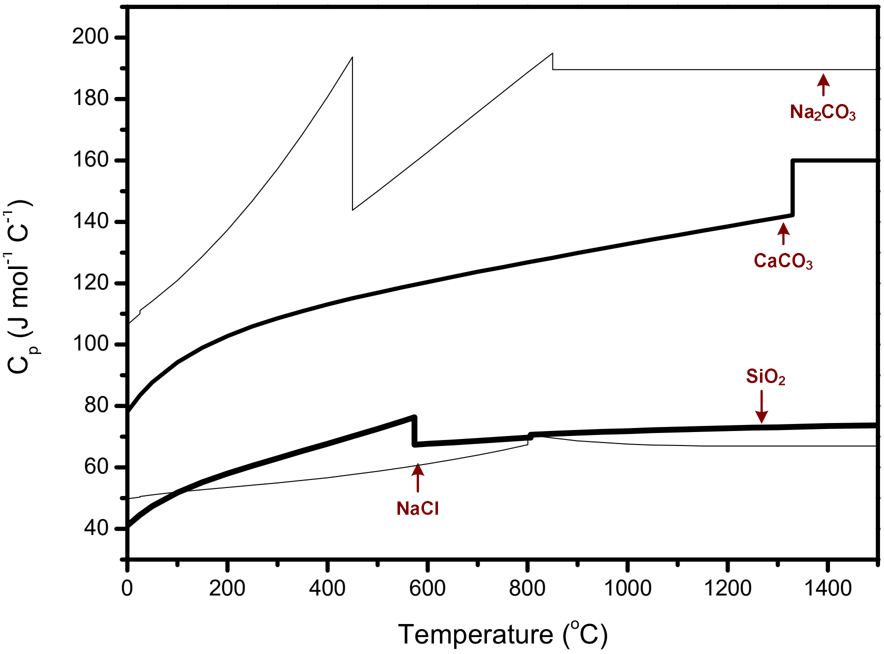

Figure 4.5: ΔC_p data for the reactants; Na_2CO_3, $CaCO_3$, SiO_2 and NaCl as a function of temperature, 1 atm (HSC Chemistry 6.1) [18-19].

The temperatures of the phase transitions of the reactants were shown by plotting the ΔC_p data for Na_2CO_3, $CaCO_3$, SiO_2 and NaCl, as a function of temperature respectively at 1 atm. This was plotted using the "H, S, C and G, Diagrams" module in HSC-Chemistry 6.1, which contains a list of mathematical functions for the thermodynamic data, compiled by Barin et al, 2008 (figure 4.5) [18-19].

The ΔC_p data for SiO_2 lies between 40-60 J mol^{-1} ºC^{-1}, exhibiting a directional change at ~570ºC, which can be attributed to its phase transitional temperature from α-quartz (monoclinic structure) to β-quartz (hexagonal structure). It also shows that the other transitional temperatures are not that significant in terms of energy being released from the bonds. This agrees with previous structural studies for SiO_2 by Kuskov and Fabrichnaya, confirming that it is most likely to be found in its β-quartz phase at 830ºC and 1100ºC [18-19] [116].

The ΔC_p data for NaCl lies between 40-55 J mol^{-1} ºC^{-1}, exhibiting a directional change at ~800ºC which can be attributed to its melting temperature at 801ºC. This can be attributed to being a single halite phase (monoclinic structure) throughout the temperature range. This agrees with previous structural studies for NaCl, stored on the ICCD and thermodynamic tables, confirming that it is most likely to remain in this state at 830ºC and 1100ºC [18-19] [215].

The ΔC_p data for $CaCO_3$ lies between 80-150 J mol^{-1} C^{-1}, exhibiting a directional change at 1300ºC, which can be attributed to its melting temperature at 1336ºC. This shows that the transitional temperatures are not that significant in terms of energy being released from the bonds. This agrees with previous structural studies for $CaCO_3$ by Clifford and Chen, 1998 and thermodynamic tables, confirming that it is most likely to remain in its calcite phase at 830ºC and 1100ºC [18-19] [215].

The ΔC_p data for Na_2CO_3 lies between 50-190 J mol^{-1} C^{-1}, exhibiting two directional changes at 470ºC and 851ºC, which can be attributed to its phase transitional temperature from β-Na_2CO_3 (monoclinic structure) to α-Na_2CO_3 (hexagonal structure) and its melting temperature of 851ºC. It also shows the other transitional temperatures are not that significant in terms of energy being released from the bonds. This agrees with previous structural studies for Na_2CO_3, thermodynamic tables and the ICCD, confirming it is most likely to remain as α-Na_2CO_3 (monoclinic structure) at 830ºC and 1100ºC [18-19] [215].

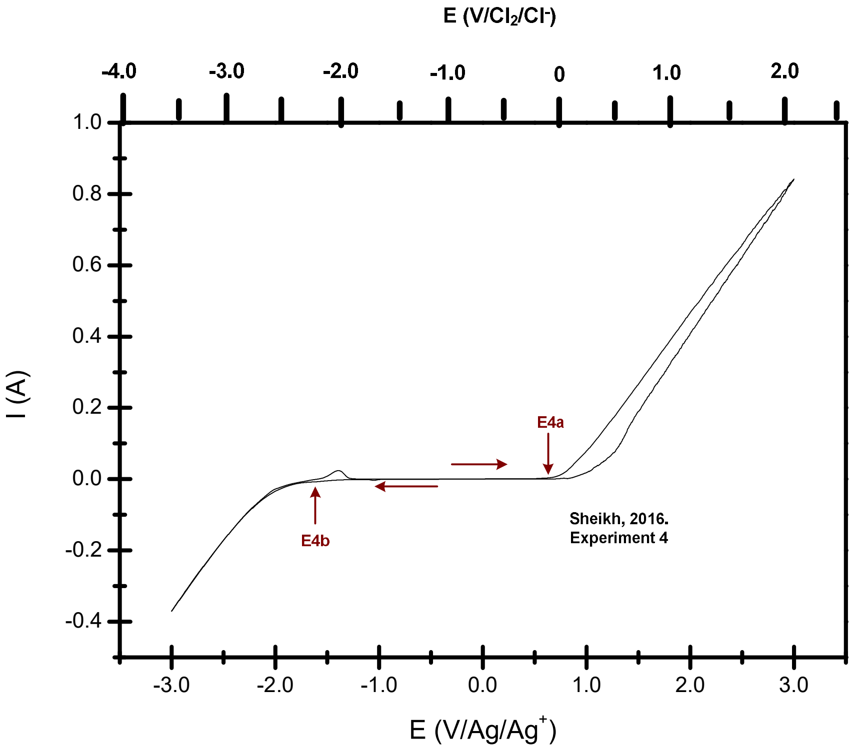

Figure 4.6: CV curve using platinum working and counter electrodes and Ag/Ag$^+$ reference electrode in NaCl at 830ºC (scan rate 0.1 V s^{-1}, electrode surface area 0.05 cm^2).

The purity of NaCl at the reaction conditions, was also investigated by immersing two platinum wires (sheathed in hollow $Al_6Si_2O_{13}$ tubes) in molten NaCl and connecting to a silver-silver chloride (Ag/Ag$^+$) reference electrode and potentiostat. These wires behaved as counter and working electrodes, and the potentiostat supplied electrical charge (electrons) for the facilitation of non-spontaneous electrochemical reactions in the molten salt (and measure the current across the electrodes). The electrodes were immersed in molten NaCl, at a depth of 1 cm, at 830ºC and the CV curve recorded (figure 4.6).

The CV curve shows an increase in current at 0.7 V/Ag/Ag$^+$ (E4a) which is presumed to be due to a compound forming at the anode (probably sodium ions (Na$^+$) converting to sodium liquid (Na (l)) and a decrease in current at -1.8 V/Ag/Ag$^+$ (E4b) which is presumed to be due to a gas forming at the cathode (probably chlorine ions (Cl$^-$) converting to chlorine (Cl_2 (g)). These are shown by the following electrochemical reactions.

$$Na^+ + e = Na\ (l) \qquad \textbf{Equation 4.1}$$

$$2Cl^- + e = Cl_2\ (g)$$ **Equation 4.2**

The difference between these values is presumed to be the decomposition potential (ΔV_d) of NaCl at ~3.1 V, which is in good agreement with values calculated using the Gibbs energy of the dissociation reaction (ΔG°);

$$E_{Na/Na^+} = -\frac{\Delta G^\circ}{F} = -3.2\ V$$ **Equation 4.3** [17]

Equation 4.3 describes the reduction potential for the Na/Na$^+$ reduction potential where ΔG^o is the Gibbs free energy for the dissociation reaction and F is the Faradays constant [256]. There is a difference of 0.1 V between the theoretical and actual value which can be attributed towards reaction inefficiencies (common for reactions involving gases) or a temperature gradient across the molten salt. The shape of the CV curve at the cathode is characteristic of a substance dissolving in the molten salt, which suggests good solubility of the presumed compound (Na (l)). This CV curve also confirms the high purity of molten NaCl shown by no further reduction peaks for electrochemical reactions, such as O^{2-} ions.

---

[17] $\Delta G^o_{\text{NaCl at 830}^o\text{C}} = 312.4\ \text{kJ mol}^{-1}$.

Faradays constant = 96485.3 C mol^{-1}.

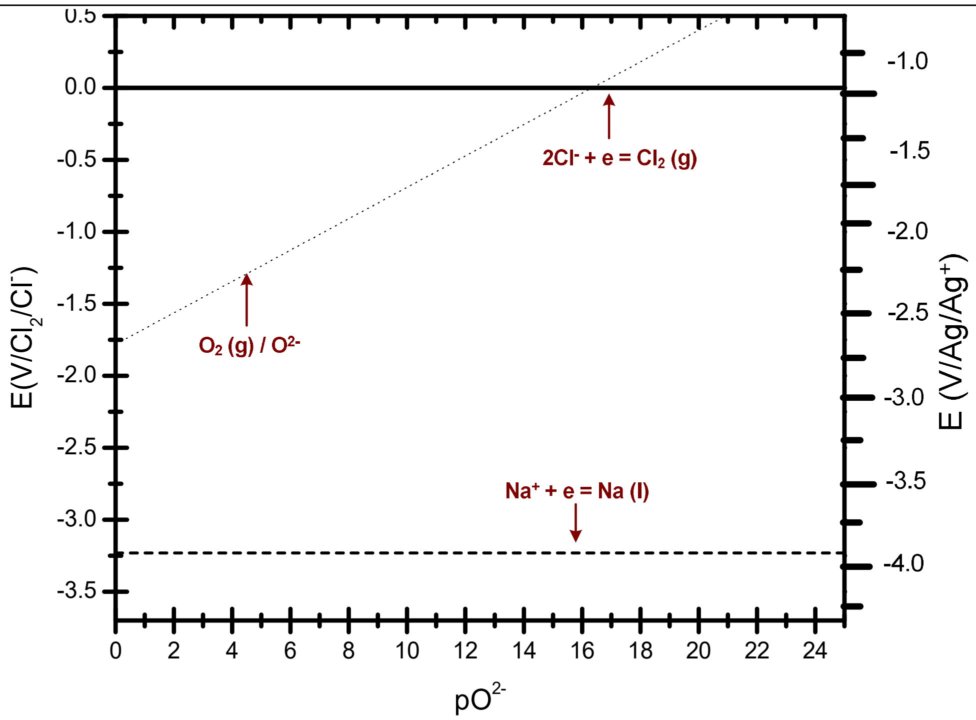

Figure 4.7: Predominance diagram for the Na-O-Cl system at 830℃, 1 atm, metal ion activity 1.

The decomposition potential of NaCl can be represented on a fundamental predominance diagram for the Na-O-Cl system at 830ºC, 1 atm (figure 4.7). This diagram utilizes the calculation method described by Littlewood and Trémillon [189-191]. The diagram displays O^{2-} ion activity (in logarithmic scale) on the x-axis and reduction potentials for electrochemical reactions on the y-axis, relative to the Cl_2/Cl^- reduction potential and reduction potentials on the z-axis, relative to the Ag^+/Ag reduction potential for comparison. The Cl_2/Cl^- reduction potential is frequently set as zero in a pure halide melt which has a difference of ~0.8 V relative to the Ag^+/Ag reduction potential, which has also been confirmed by experimental measurements by Plambeck (molten NaCl-KCl at 800ºC) [257]. The reduction potential for O_2/O^{2-} was calculated using the ΔG_f of the O^{2-} ion, which was calculated using ΔG_f for Na_2O (l) from HSC-Chemistry 6.1 using the following equations [18];

$$\mathrm{Na^+ + e = Na\ (l)}$$ **Equation 4.4** [18]

$$\mathrm{2Na + \tfrac{1}{2}O_2(g) = 2Na^+ + O^{2-}}$$ **Equation 4.5** [19]

$$\mathrm{2e + \tfrac{1}{2}O_2(g) = O^{2-}}$$ **Equation 4.6** [20]

---

[18] $\Delta G^\circ_{\mathrm{NaCl\ at\ 830^\circ C}}$ = 312.5 kJ mol^{-1} [18-19]

[19] $\Delta G_{f\ \mathrm{Na_2O\ (l)\ at\ 830^\circ C}}$ = -255.4 kJ mol^{-1} [18-19]

Equations 4.4-4.6 describe the relationships used to obtain the ΔG_f of the O^{2-} ion in molten NaCl. This allows the ΔG_f of the O^{2-} ion to be different according to the electrolyte chosen. The reduction potential for the O_2/O^{2-} redox system is shown by the broken line at -1.8 V for infinite O^{2-} activities which then decreases for low O^{2-} activities. The ΔV_d for molten NaCl was obtained using the relationship described previously (equation 4.3). At the anodic and cathodic limits, sodium liquid (Na (l)) and Cl_2 are produced which is in agreement with the CV curve of molten NaCl. A difference of 3.2 V exists between these limits, which is the ΔV_d of NaCl [190]. Between these limits, molten NaCl is partially dissociated into Na^+ and Cl^- ions. This diagram provides a framework to superimpose further electrochemical and chemical reactions occurring in the molten salt. The molten salt reactions depicted on this diagram can be found in table A5 (Appendix).

This section has shown the reactants were pure with no significant interaction with air or moisture. Also these compounds are expected to exhibit phase transitions at the reaction temperatures, therefore all phases should be considered upon examining XRD patterns.

4.4 Behaviour of the molten salt at the reaction conditions

The third stage of this investigation was to investigate the **behaviour of the molten salt at the reaction conditions** to determine the effects of vapour pressure of NaCl at 830ºC, using thermodynamic data and a DSC. This was to select suitable reaction conditions required for the dissolution of the reactants and MSS of cementitious compounds.

---

[20] ΔG_f O^{2-} at 830ºC = 365.6 kJ mol^{-1}

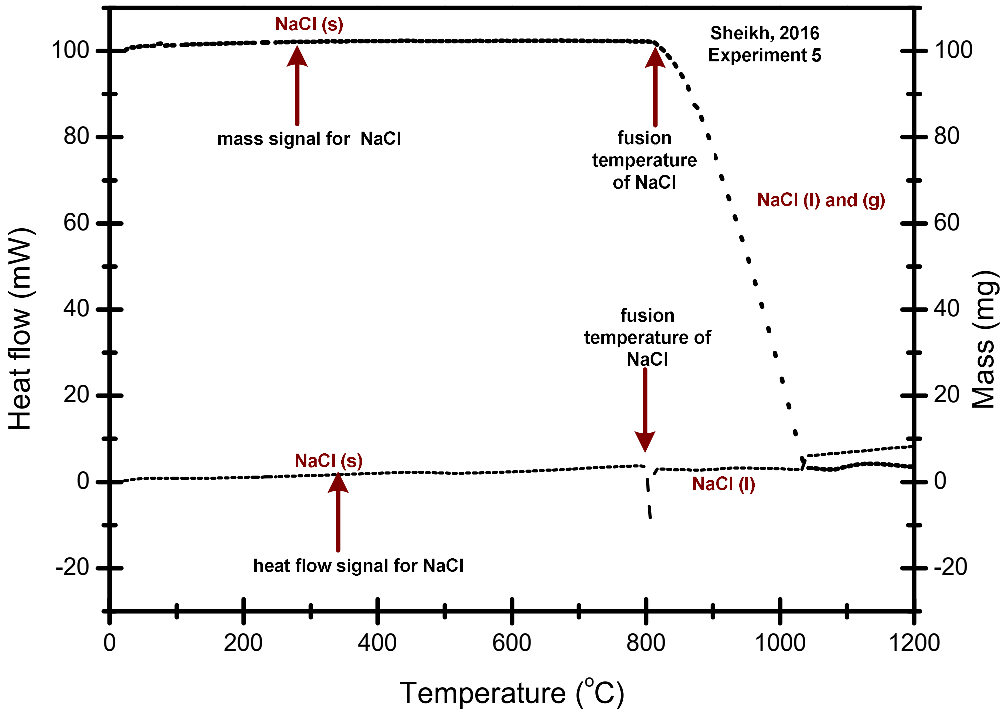

Figure 4.8: DSC heat flow and mass signal for NaCl under N_2 in open crucible,

The behaviour of molten NaCl exposed to the atmosphere at the reaction conditions (830ºC, 1100ºC) was investigated by filling an Al_2O_3 crucible with NaCl and placing in a DSC under N_2 (experiment 5). The crucible was then heated at 5ºC min^{-1} to 1200ºC and the heat flow and mass signal was recorded (figure 4.8).

The diagram shows a strong endothermic peak (at ~801ºC), which can be attributed towards the fusion temperature of NaCl. This agrees with previous experimental studies by Ye et al, 2014 on the melting point of NaCl (at 801ºC) [128]. A sharp decrease in mass was observed after 801ºC, which can be attributed towards the effects of increasing vapour pressure of the molten salt and the effect of a flow of gas coupled with colder surfaces in the DSC equipment. There is also sufficient evidence to suggest that pressurized vessels cause increase of partial pressure of gases inside the cell, however these results suggest this probably wouldn't affect the outcome of the melting temperatures.

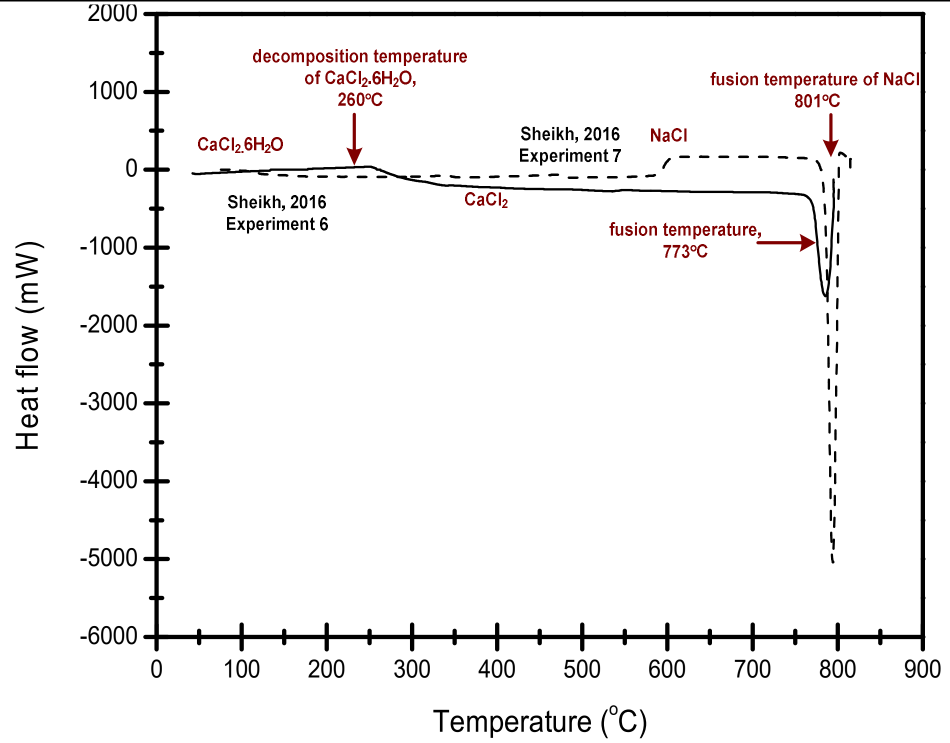

Figure 4.9: DSC heat flow signal for NaCl and $CaCl_2$ under argon in sealed Inconel^{TM} 600 crucibles.

The behaviour of NaCl in a closed environment at 830ºC and 1100ºC, was investigated using a DSC. The procedure involved filling an Inconel^{TM} 600 crucible with NaCl and $CaCl_2$ and hermetically sealing it. The Inconel^{TM} 600 crucibles were selected due to their proven stability in molten chlorides [220]. To serve as a suitable comparison, $CaCl_2$ was prepared from $CaCl_2.6H_2O$, which was dehydrated according to the procedure described earlier. The crucible was then placed in a DSC under argon and the heat flow signal recorded (figure 4.9).

The diagram shows strong exothermic peaks at 801ºC and 770°C which can be attributed towards the fusion temperatures of NaCl and $CaCl_2$ respectively. These are in agreement with the previous studies by Ye et al, 2014 and thermodynamic tables for the melting temperatures of NaCl and $CaCl_2$ (at 801ºC and 772ºC respectively) [18] [220]. The shape of the peaks can be attributed to the liquidus temperatures for high purity substances as reported by Brown and Gallagher, 2008 [222]. The heat flow signal for $CaCl_2$ showed a gradient change at 260ºC, which can be attributed to the decomposition of $CaCl_2.6H_2O$ to $CaCl_2$, suggesting the purification procedures could be improved and/or the atmosphere of the glove box may have had minute amounts of moisture.

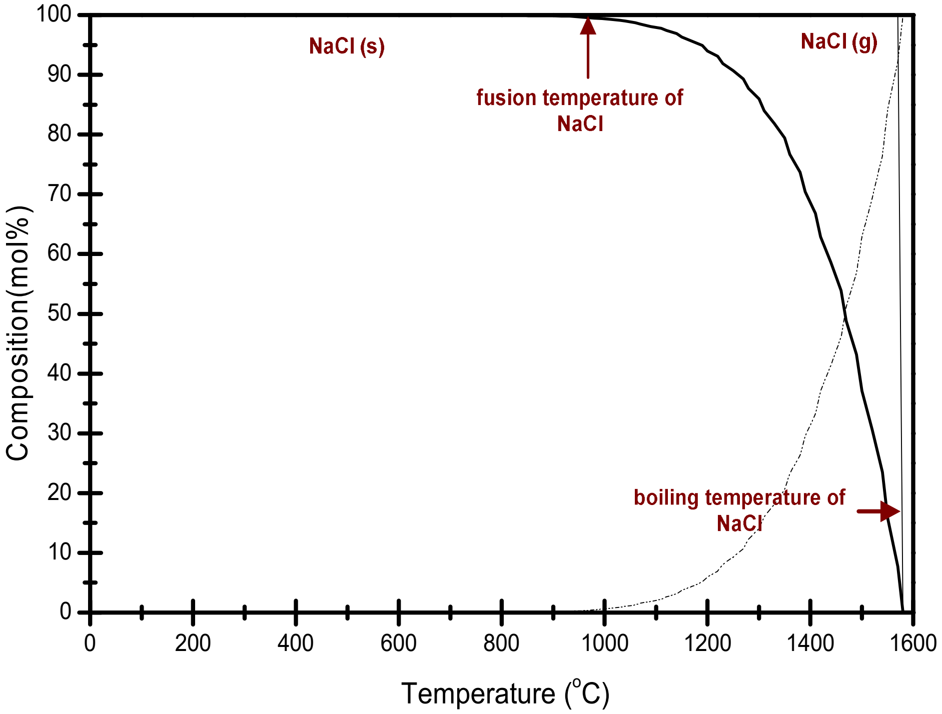

Figure 4.10: Chemical equilibrium calculations for NaCl as a function of temperature, 1 atm (HSC-Chemistry 6.1).

The behaviour of molten NaCl was also investigated using the chemical equilibrium module in HSC-Chemistry 6.1, by plotting the equilibrium conditions for NaCl as a function of temperature (figure 4.10) [18]. The diagram shows these compounds are subjected to the increasing effects of vapour pressure as shown by the changes in composition below the boiling temperature. It is expected the flow of gases above the molten salt coupled with temperature gradients in reaction vessels can cause the evaporation of the molten salt, therefore it is expected that some mass loss may be present during the experiments.

This section has shown it is possible to utilize molten NaCl at these reaction temperatures; however the thermodynamic data suggests the salt is likely to evaporate beyond its melting temperature, probably due to the increasing effects of vapour pressure. This could also in turn have delirious effects upon the experiments performed, such as in the presence of a temperature gradient across the reaction vessel will likely drive the evaporation process. It is the author’s opinion that the reaction vessels that will be used should be sealed where possible to minimize this occurring.

4.5 Dissolution of the reactants in the molten salt

The fourth stage of this investigation was to investigate the **dissolution of the reactants**; Na_2CO_3, $CaCO_3$ and SiO_2 in NaCl at 830ºC, using XRD, SEM, drop calorimetry and a DSC (which will subsequently lead to obtaining K_{sp}, ΔH_{mix} values and phase diagrams). This was to determine whether the MSS of cementitious compounds are possible.

4.5.1 Phases of the reactants in the molten salt

This section investigates the **dissolution reactions of the reactants**; Na_2CO_3, $CaCO_3$ and SiO_2 in molten NaCl at the reaction conditions (830 ºC, 1 atm), using XRD and SEM.

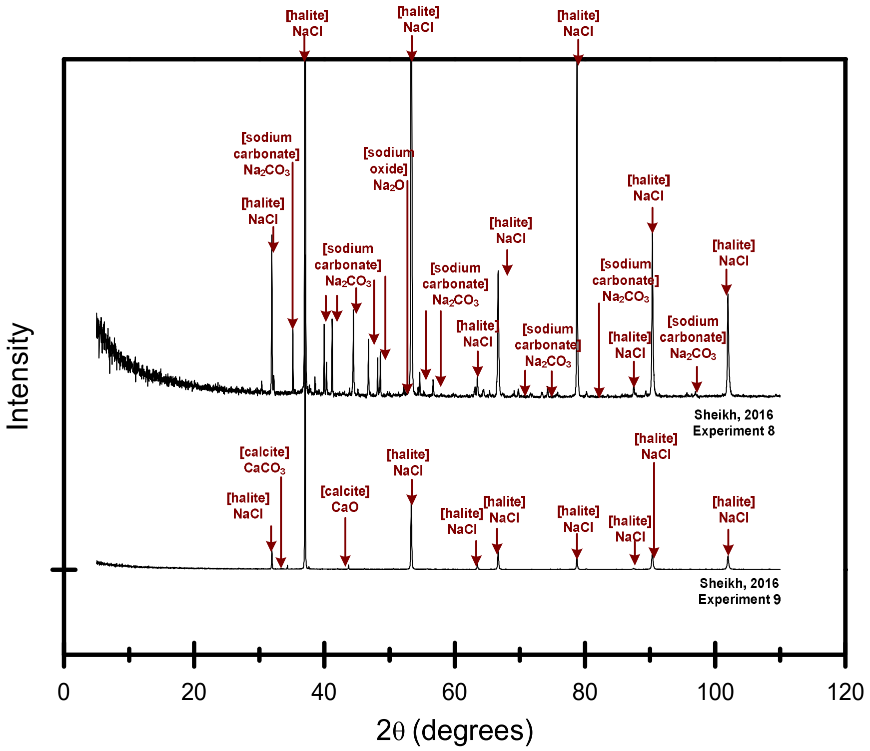

Figure 4.11: XRD pattern for $CaCO_3$ (bottom) and Na_2CO_3 (top) in NaCl at 830ºC, for 3 hours; typical operating condition; 2θ scan range of 5-110° with 150 seconds per step, Cu-Kα radiation.

Initally, the **dissolution of the reactants:** Na_2CO_3 and $CaCO_3$ in NaCl were investigated at 830ºC, using XRD and SEM, by filling an Al_2O_3 crucible with the reactants and raising the temperature to 830ºC for ~3 hours (experiment 8-9). The

Al_2O_3 crucible was then cooled and samples removed (using the procedure described earlier) and taken to record their XRD patterns (figure 4.11).

The XRD pattern shows multiple low intensity peaks of Na_2O probably produced during the decomposition of Na_2CO_3. The XRD pattern shows multiple peaks for Na_2CO_3, indicating the extent of the decomposition reaction for Na_2CO_3 was low. It is suspected this decomposition reaction occurred at the melting temperature of NaCl (at 801ºC) which can be probably attributed to a lower eutectic melting temperature of the mixture [258].

The XRD pattern also shows strong multiple peaks of CaO, which were probably produced due to the decomposition of $CaCO_3$. This suggests a ~3 hour reaction time was sufficient to complete the reaction and the reaction kinetics for the decomposition of $CaCO_3$ were sufficiently high, in comparison to other carbonates such as Na_2CO_3, as reported by Hills, 1968 and Kim and Lee. 2001 [259-260]. This also confirms that reactions in molten salts can occur more rapidly in comparison to solid-state reactions (probably due to the dissolution of the compounds in the molten salt), as reported by Kimura, 1991 and Trémillon and Inman, 1997 [50-51]. In both cases, no other significant peaks for additional compounds were observed ($CaCl_2$ or Al_2O_3) before separation stage, which indicates the dissolution of the Al_2O_3 crucible or interaction of molten NaCl with the reactants were not that significant.

The decomposition temperatures for $CaCO_3$ and Na_2CO_3 were lower than those reported by previous solid-state reactions (at 900°C and 851°C respectively), reported by Motzfeldt 1955 and Hills, 1968, from thermodynamic data (825ºC for $CaCO_3$) and the chemical equilibrium module (860ºC for $CaCO_3$) [18-19] [258-259]. This was probably attributed to the exhaust above our muffle furnace, which drove the decomposition reactions to completion.

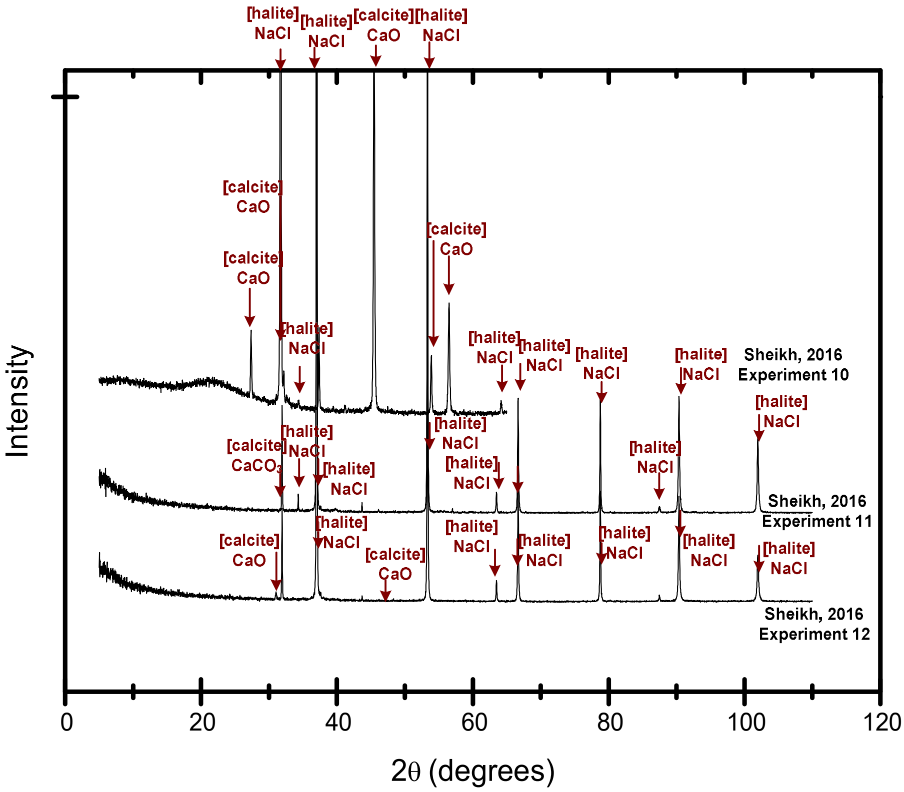

Figure 4.12: XRD pattern for CaCO$_3$ in NaCl at 830°C, for 2-3 hours; typical operating condition; 2θ scan range of 5-110° with 150 seconds per step, Cu-Kα radiation.

The effect of reaction time upon the dissolution of CaCO$_3$ in molten NaCl was investigated by filling an Al$_2$O$_3$ crucible with the reactants and heating to 830ºC, for ~2 hours (experiment 11) and ~3 hours (experiment 10, 12). Then samples were removed from the crucible using the procedure described earlier and their XRD patterns recorded (figure 4.12).

The XRD pattern shows strong multiple peaks for CaCO$_3$ (experiment 11) after a reaction time of ~2 hours. This suggests this molten salt reaction did not go to completion. Strong multiple peaks for CaO were observed after ~3 hours (experiment 10, 12) which indicates a high extent of reaction for the decomposition of CaCO$_3$ in molten NaCl and demonstrates good data reproducibility. In both cases, no other peaks were observed for additional compounds (CaCl$_2$ or Al$_2$O$_3$), indicating no significant dissolution of the Al$_2$O$_3$ crucible or the molten salt itself with the reactants.

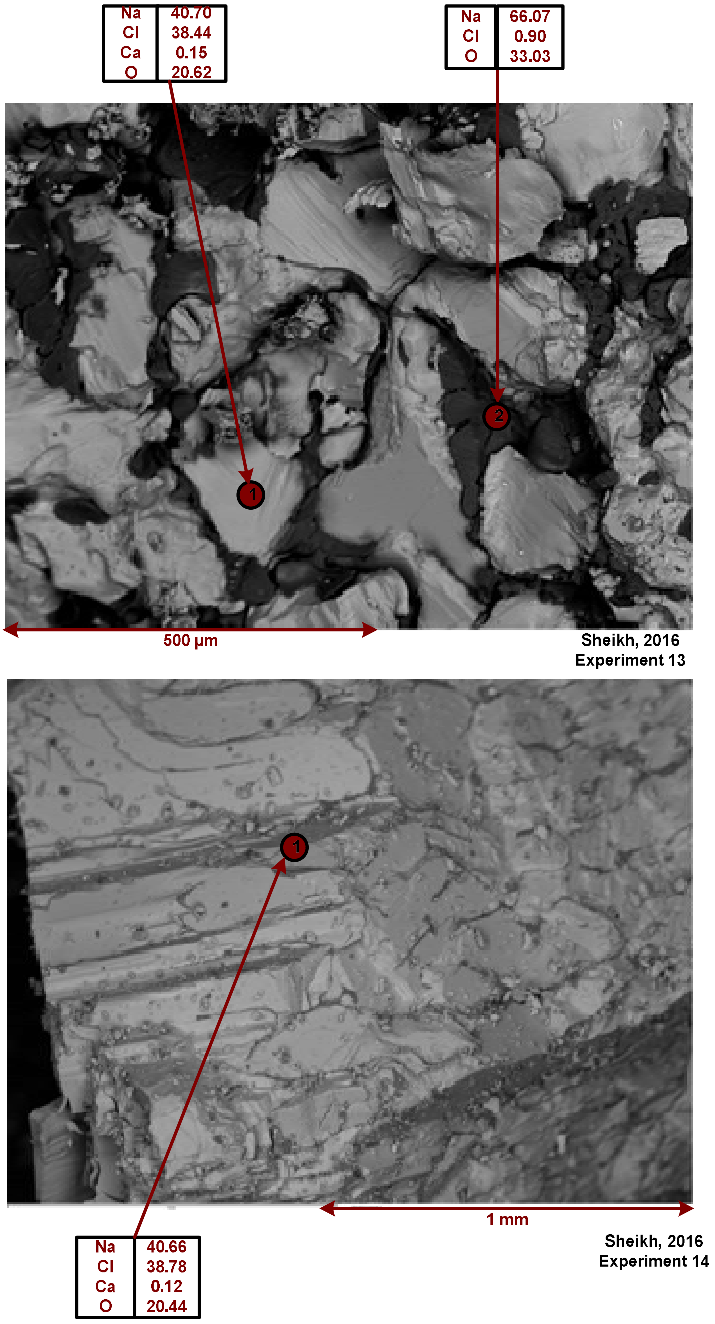

Sheikh, 2016
Experiment 13

Sheikh, 2016
Experiment 14

Figure 4.13: SEM image and EDS analysis for Na_2CO_3 *(top) and* $CaCO_3$ *(bottom) in NaCl at 830°C for 3 hours.*

The phases produced during the dissolution of $CaCO_3$ and Na_2CO_3 in molten NaCl (experiments 13-14), were investigated by removing samples from the Al_2O_3 crucible, using the procedure described earlier and taking to an SEM for particle size and EDS analysis (figure 4.13).

The EDS analysis suggested the phases; Na_2O (experiment 13), CaO (experiment 14) NaCl and/or their constituent ions (O^{2-} and CO_3^{2-} ions) were possibly present. Na_2O was probably produced during the decomposition of Na_2CO_3 and CaO during the decomposition of $CaCO_3$. The O^{2-} ion could also have been caused by the dissolution of O_2 from the atmosphere in molten NaCl however the solubility of this gas has been reported to be generally low, as shown by Hefter and Tomkins, 2004 [261].

The amount of calcium (experiment 14) was also reported to be extremely low, which can be attributed to a low K_{sp} value of CaO in molten NaCl. No other elements were observed such as glassy carbon or aluminium, indicating no significant dissolution of the Al_2O_3 crucible in molten NaCl and in agreement with previous authors whom used similar crucibles [50]. It also demonstrates the decomposition of $CaCO_3$ was driven to completion in both cases, due to presence of CO_2. The agglomerated particle sizes for experiment 14 (~200 µm) was lower than experiment 13 (~2 mm) which also suggests that Na_2O has higher physical solubility in molten NaCl than CaO and/or K_d value which can correspond to higher particle sizes. No hydrolysis of NaCl was observed, at the reaction conditions which can be attributed to low humidity levels in the atmosphere.

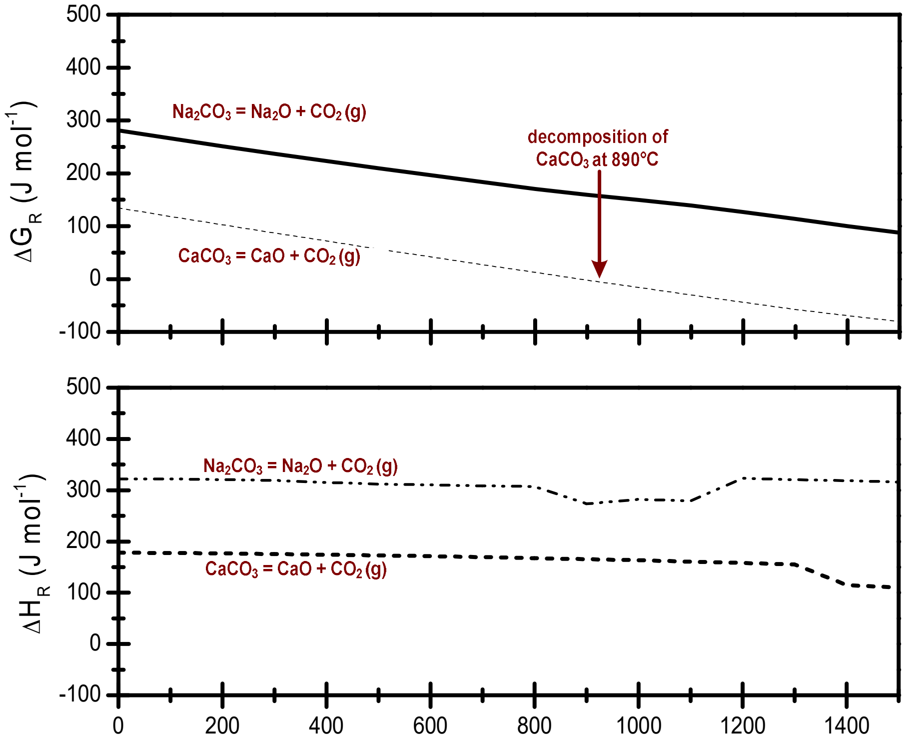

Figure 4.14: ΔH_R (bottom) and ΔG_R (top) data for the decomposition of Na_2CO_3 and $CaCO_3$ as a function of temperature, 1 atm (HSC-Chemistry 6.1).

The decomposition of Na_2CO_3 and $CaCO_3$ was also investigated using the reaction equation module in HSC-Chemistry 6.1 [18]. This module contained a list of mathematical functions of thermodynamic data, compiled by Barin et al, 2008 [19]. The ΔG_R and H_R were plotted as a function of temperature respectively (figure 4.14).

The ΔH_R data for the decomposition of Na_2CO_3 and $CaCO_3$ indicates these reactions are highly endothermic, and require between ~200-300 kJ mol^{-1} of energy over this temperature range. This indicates these reactions won't proceed unless an external source of energy is applied.

The ΔG_R data for the decomposition of $CaCO_3$ shows this reaction occurs above ~890ºC, shown by negative ΔG_R values above this temperature. This supports previous decomposition studies by Motzfeldt, 1955 and Hills, 1968 whom show that $CaCO_3$ decomposes at ~840ºC [258-259]. This reaction has also proven to be reversible and upon cooling will react with CO_2 in the atmosphere to revert back to $CaCO_3$.

The ΔG_R data for the decomposition of Na_2CO_3 shows this reaction is unfeasible up to 1500ºC, due to positive ΔG_R values throughout this temperature range. However, this doesn't agree with previous decomposition studies by Kim and Lee, 2001, and Motzfeldt, 1955, whom show that Na_2CO_3 decomposes slowly upon melting at 851ºC, however the amount of Na_2O produced is ~1 mass % in comparison to Na_2CO_3 [258] [260]. This was probably due to different reaction conditions being used, such as the presence of an inert gas to increase the partial pressure of CO_2 or the fact that ΔG_R data can only serve as a useful "guide" to solving reaction feasibility problems and requires improved thermodynamic data (ΔG_f function) for Na_2CO_3 (s).

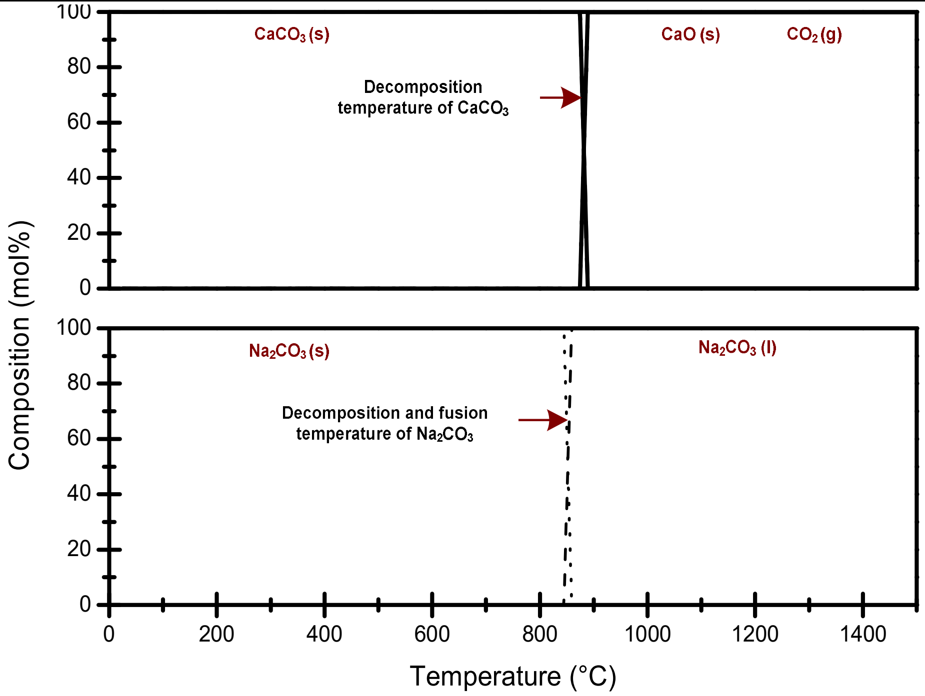

Figure 4.15: Chemical equilibrium calculations for $CaCO_3$ (top) and Na_2CO_3 (bottom) as a function of temperature, 1 atm (HSC-Chemistry 6.1).

The decomposition of $CaCO_3$ and Na_2CO_3 was also investigated using the chemical equilibrium module in HSC-Chemistry 6.1 [18]. The module plotted the equilibrium conditions of species as a function of temperature respectively (figure 4.15).

The chemical equilibrium module shows that $CaCO_3$ (s) decomposes to CaO (s) and CO_2 (g) at ~840ºC, which supports previous decomposition studies by Motzfeldt, 1955 and Hills, 1968 and our dissolution experiments [259-260]. The diagram also shows that Na_2CO_3 (s) only transforms to Na_2CO_3 (l) and doesn’t decompose, which doesn’t agree with the current dissolution results or literature, probably due to the pressure of the system being different to 1 atm which could have been caused by the flow of argon gas over molten NaCl.

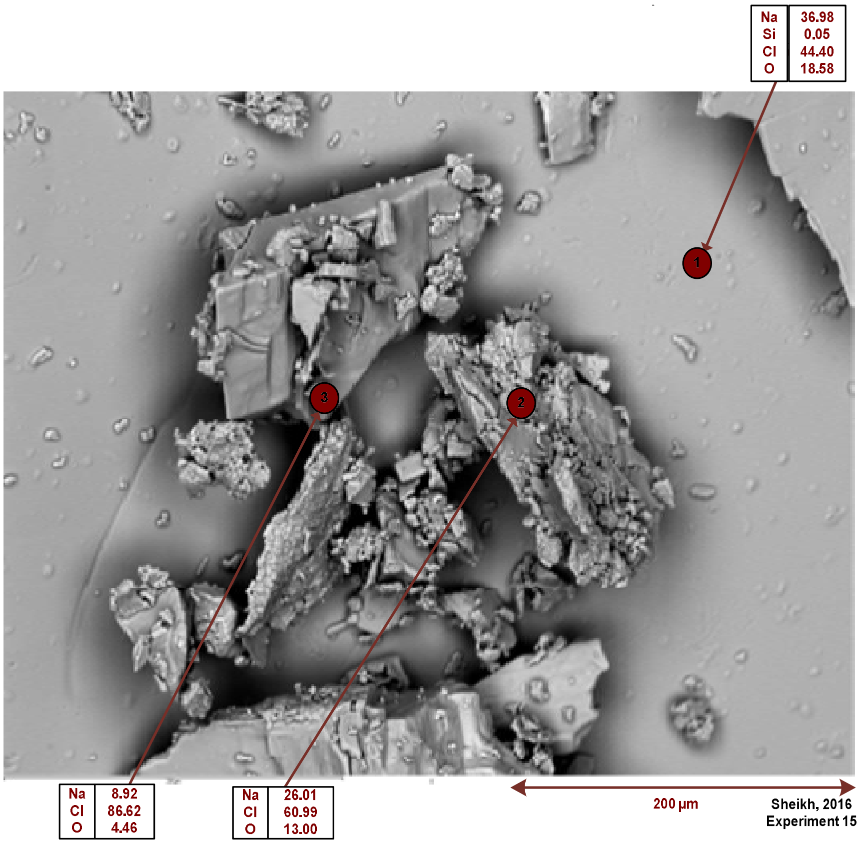

Figure 4.16: SEM image and EDS analysis of SiO_2 in NaCl at 830ºC, for 3 hours.

The **dissolution of the reactant**; SiO_2 in NaCl at 830ºC was investigated by filling an Al_2O_3 crucible with SiO_2 and NaCl and heating to 830ºC over ~3 hours and leaving at the reaction temperature for ~3 hours. Upon cooling to room temperature, a sample was removed from the crucible using the procedure described earlier, and taken to an SEM for particle size and EDS analysis (figure 4.16).

The EDS analysis suggested the phases; SiO_2, Na_2O, NaCl and/or their constituent ions (O^{2-} or Si^{4+} ions) were possibly present (experiment 15). This could have been either caused by the solubility of SiO_2 in molten NaCl or the dissolution of O_2 in molten NaCl from the atmosphere, however as the solubility of O_2 in molten NaCl has been reported to be low, it was deemed to be the latter [261]. Solid particles were evident in molten NaCl which were visually evident, which also suggested a low solubility in the melt. No other elements were present, such as glassy carbon or aluminium indicating no significant dissolution of the Al_2O_3 crucible.

This section has shown that Na_2CO_3 and $CaCO_3$ decompose in molten NaCl to Na_2O, CaO and CO_2 and have some solubility in the melt. This is in agreement with previous decomposition studies by Motzfeldt, 1955, Hills, 1968 and Kim and Lee. 2001.and the ΔG_R data for the decomposition of $CaCO_3$ [258-260]. These compounds probably form CO_3^{2-} and O^{2-} ions in molten NaCl, and produce CO_2 in the process. SiO_2 also dissolves in molten NaCl but with a limited solubility in comparison to other oxides (such as CaO) and no other phases were detected. In all cases, the Al_2O_3 crucible had a limited interaction with the reactants, as no compounds containing the Al^{3+} ion were detected on the XRD patterns. The next stage is to attempt to describe the dissolution reactions that probably take place. This can be performed using previous dissolution and decomposition studies of carbonates by Cherginets, 2005 and Combes et al, 1977 [130] [263]. Using the same analogy, the dissolution and decomposition of Na_2CO_3 in molten NaCl can be described using the following equations;

$$Na_2CO_3\ (s) = Na_2CO_3\ (l)$$ **Equation 4.7**

$$Na_2CO_3\ (l) = 2Na^+ + {CO_3}^{2-}$$ **Equation 4.8**

$${CO_3}^{2-} = CO_2(g) + O^{2-}$$ **Equation 4.9**

$$2Na^+ + O^{2-} = Na_2O\ (l)$$ **Equation 4.10**

$$Na_2O\ (l) = Na_2O\ (s)$$ **Equation 4.11**

Equation 4.7-4.11 describes the dissolution and decomposition of Na_2CO_3 (s) in molten NaCl, to produce Na^+, CO_3^{2-}, O^{2-} ions and CO_2. The O^{2-} ions then react with Na^+ ions in molten NaCl to form Na_2O (l), which possibly precipitates out of the molten salt. These reactions can be summarised using the following equation;

$$Na_2CO_3\ (l) = Na_2O\ (l) + CO_2\ (g)$$ **Equation 4.12**

Equation 4.12 describes the dissolution and decomposition of Na_2CO_3 (s) in molten NaCl, to produce Na_2O (l) and CO_2 (g). Using a similar analogy, the dissolution and decomposition of $CaCO_3$ in molten NaCl can be described using the following equations;

$$CaCO_3\ (s) = CaCO_3\ (l)$$ **Equation 4.13**

$$CaCO_3\ (l) = Ca^{2+} + {CO_3}^{2-}$$ **Equation 4.14**

$CO_3^{2-} = CO_2(g) + O^{2-}$ **Equation 4.15**

$Ca^{2+} + O^{2-} = CaO\ (l)$ **Equation 4.16**

$CaO\ (l) = CaO\ (s)$ **Equation 4.17**

Equation 4.13-4.17 describes the dissolution and decomposition of $CaCO_3$ (s) in molten NaCl to produce Ca^{2+}, CO_3^{2-}, O^{2-} ions and CO_2. The O^{2-} ions then react with Ca^{2+} ions to form CaO (l), which possibly precipitates out of the molten salt. These reactions can also be summarised using the following equation;

$CaCO_3\ (s) = CaO\ (s) + CO_2(g)$ **Equation 4.18**

Equation 4.18 describes the dissolution and decomposition of $CaCO_3$ (s) in molten NaCl, to produce CaO (l) and CO_2 (g). Using a similar analogy, the dissolution of SiO_2 in molten NaCl can be written in the following equation.

$SiO_2\ (s) = Si^{4+} + 2O^{2-}$ **Equation 4.19**

Equation 4.19 describes the dissolution of SiO_2 (s) in the molten salt, to produce Si^{4+} and O^{2-} ions. As the solubility of SiO_2 (s) in molten NaCl was deemed to be low in our case, only the solid phase was considered. However the author didn't consider the possibility of SiO_3^{2-} complex ions which can also form when SiO_2 (s) reacts with O^{2-} ions in molten NaCl, as described by Yasuda 2007, and further experimental studies should be performed to investigate this [208]. The agglomerated particle sizes for SiO_2 (~100 µm) suggests a low solubility in molten NaCl and/or K_d value which can correspond with higher particle sizes. No hydrolysis of NaCl was observed at 830ºC, as described by Hanf and Sole, 1970, which can be attributed to low humidity levels in the atmosphere [240].

4.5.2 Phase diagrams of the reactants in the molten salt

The **dissolution of the reactant;** Na_2CO_3 in molten NaCl was investigated by obtaining the liquidus and solidus points of molten NaCl-Na_2CO_3, using a DSC.[21] However the dissolution of the reactants; SiO_2 and $CaCO_3$ in molten NaCl were not investigated however due to their low solubilities in the melt, which have been described previously by Yasuda, 2007 and Cherginets, 2005 [130] [208].

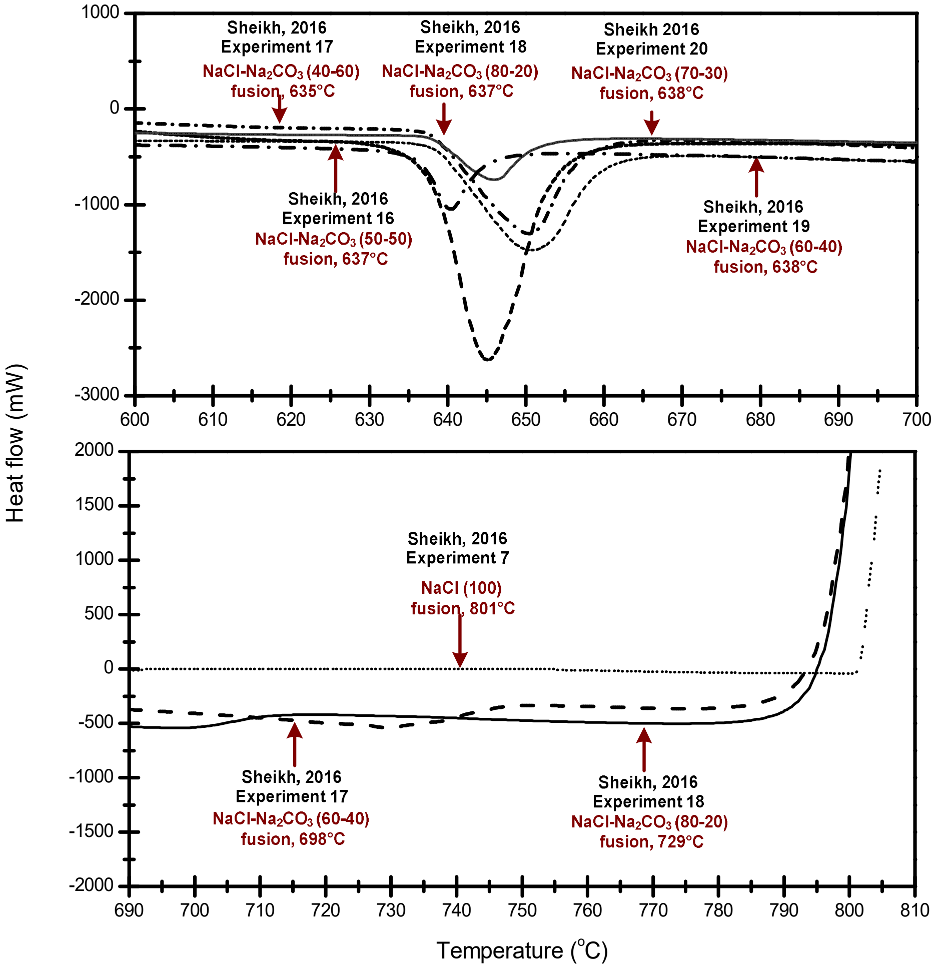

Figure 4.17: DSC heat flow signal for molten NaCl-Na_2CO_3, liquidus (bottom), solidus (top), under argon.

Initially, an Al_2O_3 crucible was filled with Na_2CO_3 and NaCl and heated in a furnace to ~900ºC and leaving at the reaction temperature for ~30 minutes. Then samples were removed from the crucible, using the procedure described earlier and placed in an Inconel™ 600 crucible. This material was selected due to its high melting temperature

---

[21] These experiments were performed at the Wrocław University of Technology, in Poland with the support of Dr. J. Kapala and Dr. L. Rycerz.

(~1100ºC) and proven stability in molten chlorides [220]. The Inconel™ 600 crucible was then placed in a DSC, alongside an empty reference crucible (experiment 16-20). The DSC was then heated at a temperature ramp rate of 5ºC min^{-1} over ~5 hours and the heat flow signal recorded (figure 4.17).

The diagram shows shows multiple peaks occurring in the same experiment, which are characteristic of liquidus and solidus points of mixtures [222]. This confirms that heat effects associated with fusion/transitional temperatures of our samples were greater than any interaction of the sample with the Inconel™ 600 crucible, which is good for our investigation. The onset temperatures for the peaks from the cooling curves were used to plot the phase diagram for molten NaCl-Na_2CO_3. The enthalpies of fusion for the samples were determined by integrating the peaks and using the Calisto Thermal Analysis Software by Setaram [228]. The values were; -88.3 J g^{-1} (20 mol% of Na_2CO_3), -488.51 J g^{-1} (50 mol% of Na_2CO_3) -255.6 J g^{-1} (30 mol% of Na_2CO_3) and -144.1 J g^{-1} (60 mol% of Na_2CO_3). This information suggests the mixture had a eutectic point between 40-60 mol% of Na_2CO_3.

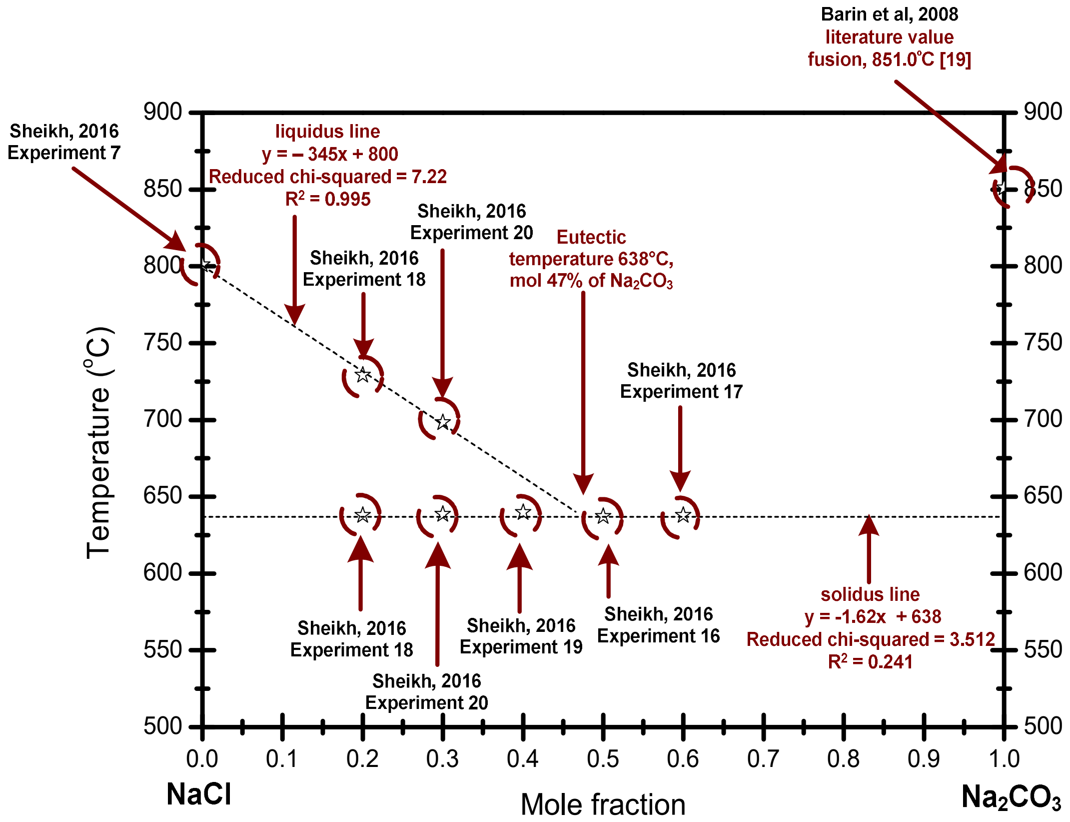

Figure 4.18: Phase diagram for molten NaCl-Na_2CO_3, under argon.

The liquidus and solidus points from the DSC heat flow signal were plotted as a function of composition, also described as the phase diagram for the NaCl-Na_2CO_3 binary system (figure 4.18). The literature value for Na_2CO_3 was obtained from thermodynamic tables compiled by Barin et al, 2008 [19].

This diagram is characteristic of a eutectic phase diagram with a eutectic point at 47 mol% Na_2CO_3. This point was determined by extrapolating the liquidus lines on the NaCl-rich side. A complete solid phase was also reported below 638°C which was lower than previously thermodynamic calculations performed by Yaokawa et al, 2007, Lindberg et al, 2006 and Iwasawa and Maeda, 2000, whom illustrated a solidus temperature of 634°C [106] [124]. This was attributed to the effects of the decomposition of Na_2CO_3 to Na_2O and CO_2 under these conditions. The diagram also confirms that Na_2CO_3 decomposes in molten NaCl at elevated temperatures, which is in agreement with previous decomposition studies by Motzfeldt, 1955 and Kim and Lee, 2001 [258] [260].

The author couldn't locate any transitional points for Na_2CO_3, probably due to the mixture being heated to 860ºC prior to measurements to produce β-Na_2CO_3 (hexagonal structure) from its original α-Na_2CO_3 (monoclinic structure). There was also no evidence of mutual solubility of phases, which are often evident by additional peaks on the NaCl or Na_2CO_3 rich-side, which can also be described by thermodynamic calculations performed by Dessureault, 1990 [106].

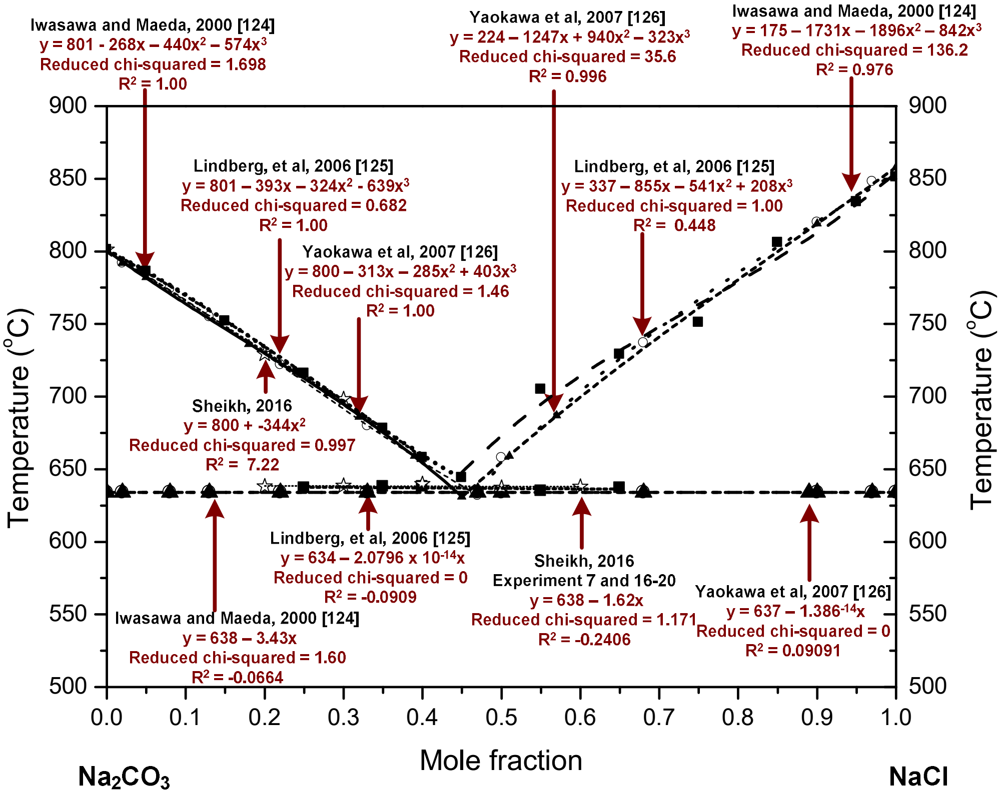

Figure 4.19: Phase diagrams of the NaCl-Na_2CO_3 binary system by previous authors and DSC measurements [124-126].

The liquidus and solidus points from previous phase diagrams for molten NaCl-Na_2CO_3 were obtained using Plot Digitizer 2.6.3, and superimposed onto the current experimental phase diagram for analysis (figure 4.19) [125-126]. The liquidus and solidus lines (functions) were obtained by linear extrapolation using Origin Pro 8 [225]. The values for the liquidus and solidus points (experiment 7 and 16-20) can be found in tables A3-A4 (Appendix).

The diagram shows Na_2CO_3 is soluble in molten NaCl with a eutectic point between 40-50 mol% and confirms that Na_2CO_3 is not stable under these conditions. These results are slightly different to those reported in literature, which can be attributed to the decomposition of Na_2CO_3 and evaporation of NaCl occurring in the melt. This was probably due to the presence of argon over our experimental setup in comparison to CO_2 used by Lindberg et al, 2006 and Yaokawa et al, 2007 and/or the use of faster heating times [124-126]. There are also differences in the fusion temperatures of Na_2CO_3 (at 851ºC or 858ºC) which can be attributed to confusions over the phase transitional temperatures of Na_2CO_3 [106].

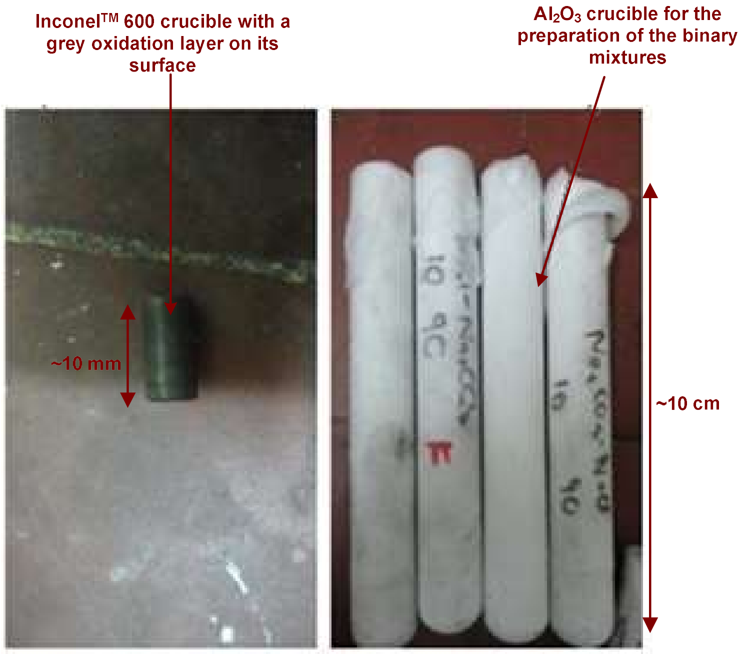

Figure 4.20: Image of the Inconel^{TM} *600 (left) and* Al_2O_3 *(right) crucibles after phase diagram experiments.*

Images were taken of the Al_2O_3 crucibles that were used in the preparation of the NaCl-Na_2CO_3 binary mixtures, and the Inconel^{TM} 600 crucible that was used for obtaining the liquidus and solidus points. The inages for the Al_2O_3 crucibles were taken after ~1 hour at 900ºC and the image of the Inconel^{TM} 600 was taken after ~6 hours reaction temperaturers between 25-850ºC (figure 4.20).

The diagram shows the surface of the Inconel^{TM} 600 crucible exhibiting a slight discoloration, from silver to grey. These colour changes can be attributed to the oxidation of the crucible at the reaction temperatures with O_2 gas that was possibly present. This suggests O_2 could have entered the atmosphere within the DSC and reacted with the crucible. A slight expansion of the Inconel^{TM} 600 crucible was also observed, which can be attributed to CO_2 being released during the decomposition of Na_2CO_3 and modifying the shape of the crucible. Therefore to avoid any breakages of the DSC from their expansion, each Inconel^{TM} 600 crucible was heated to ~900ºC in a furnace for 15 minute, prior to our experiments as a safety measure. After heating, the author found that molten NaCl-Na_2CO_3 had condensed upon the inner walls of the Al_2O_3 crucible. This was attributed to the walls of the crucible being cooler than the temperature of the mixture (at 830ºC). The final mixture was stuck to the sides of crucible and required a chisel to remove the salt. This suggests there was a slight solubility of the Al_2O_3 crucible in molten NaCl otherwise the mixture would have easily been removed. Both Inconel^{TM} 600 and Al_2O_3 crucibles were disused after each experiment.

This section has shown that Na_2CO_3 is not stable in molten NaCl and decomposes to produce CO_2 and Na_2O in a reaction with slow kinetics. These observations support previous experimental studies by Kim and Lee, 2001, and ΔG_R data for the decomposition of Na_2CO_3 [260]. The diagram is also different to previous calculated phase diagram studies by Yaokawa et al, 2007 and Lindberg et al, 2006, which can be attributed to the presence of an inert argon gas over molten NaCl and slower heating times [125-126].

4.5.3 Heats of mixing of the reactant in the molten salt

The **dissolution of the reactant;** Na_2CO_3 in NaCl at 830ºC was investigated by obtaining the ΔH_{mix} values for molten NaCl-Na_2CO_3 and ΔH_f values for Na_2CO_3 and NaCl, using drop calorimetery. [22] However the dissolution of $CaCO_3$ and SiO_2 in molten NaCl was not obtained due to their low solubilities, as described by Yasuda, 2007 and Cherginets, 2005 [130] [208]. These experiments were performed using a glassy carbon crucible, selected due to its slow oxidation rate at high temperatures than conventional carbon [264]. Initially, the procedure involved placing an empty glassy carbon crucible in two locations in a calorimetric tube; Position A (experiment 21) and B (experiment 22) (figure 4.22).

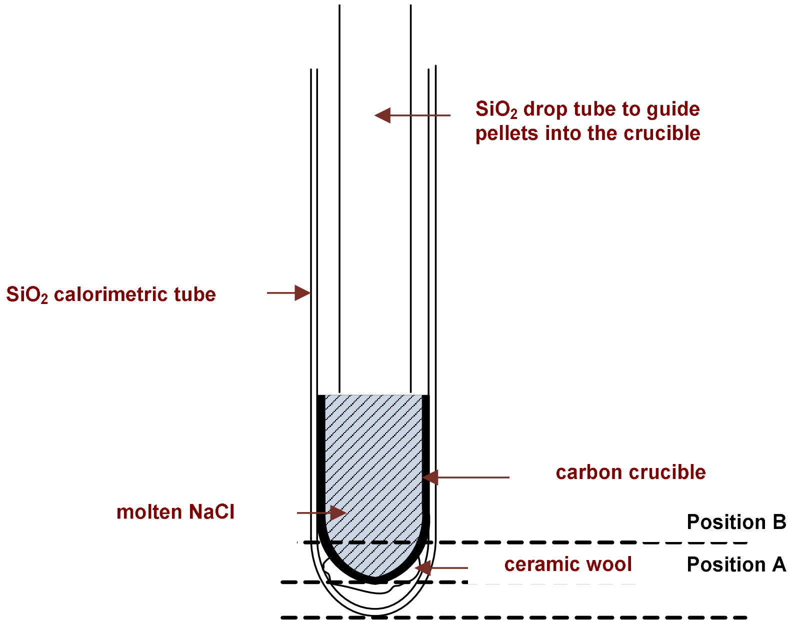

Figure 4.21: Position of the crucible in the calorimetric tube in the drop calorimeter.

---

[22] The experiments were performed at the Wrocław University of Technology, in Poland with the support of Dr. J. Kapala and Dr. L. Rycerz.

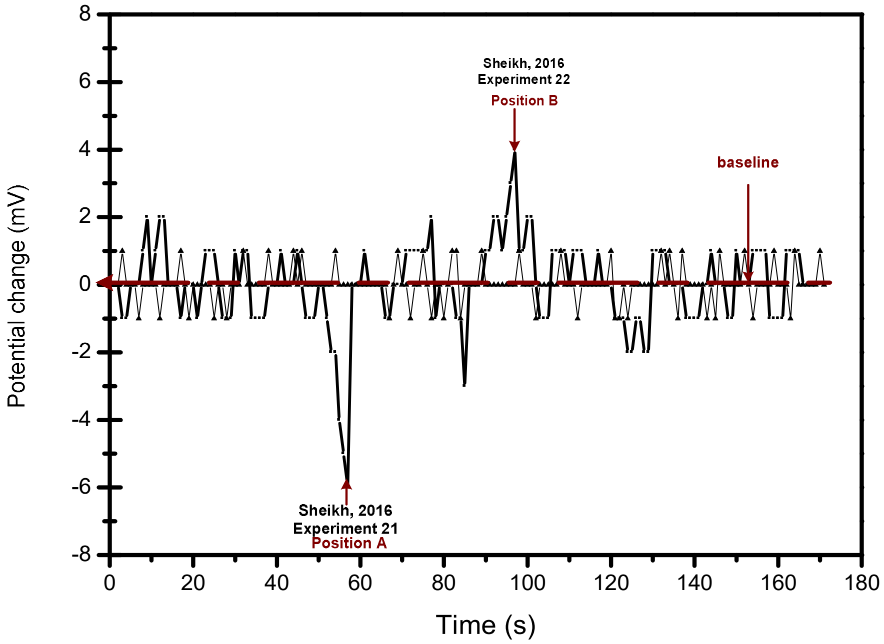

Figure 4.22: Drop calorimeter heat flow signal in Position A and B at 830℃, under argon.

The calorimetric tube was then placed into the well of the drop calorimeter alongside an additional empty reference tube. Then the heat flow signal was recorded between these two tubes for ~15 minutes until the temperature stabilized to its set point value (figure 4.22).

The diagram illustrates that Position B had the lowest potential change (~1 mV) in comparison to Position A (~6 mV). This can be attributed to the glassy carbon crucible being a shorter distance away from the thermopiles (temperature sensors) and therefore selected for every experiment. The relatively long time duration for the heat flow signal to stabilize was attributed to the large mass of the drop calorimeter.

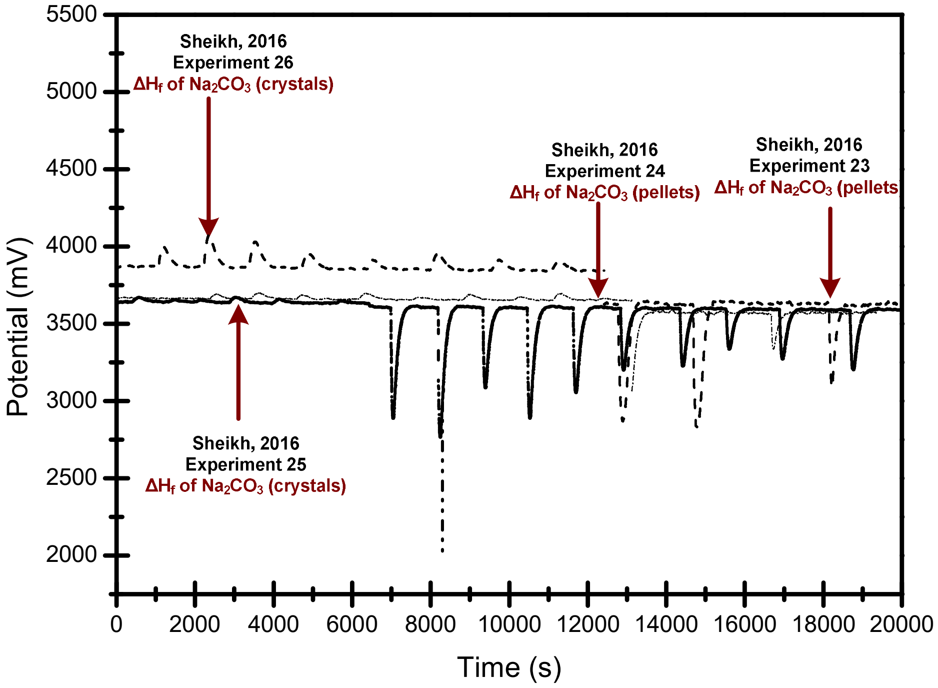

Figure 4.23: Drop calorimeterheat flow signal for Na_2CO_3 at 830℃, under argon.

Then an empty glassy carbon crucible was filled with NaCl and placed at Position B in the calorimetric tube. The calorimetric tube was then placed inside the drop calorimeter and the heat flow signal recorded for ~15 minutes until the temperature of the calorimeter stabilized. Then pellets and crystals of Na_2CO_3 were added to the empty glassy carbon crucible and ~30 minutes allowed for the temperature of the calorimeter to reach its initial set point (experiment 23-26), as evident from the heat flow data. Upon every few additions, a pellet of platinum was added to the glassy carbon acrucible to provide a suitable calibration point for calculating the ΔH_f values (figure 4.23).

The diagram shows the heat flow signal for both crystals and pellets of Na_2CO_3 rising and falling slowly, which can be attributed to the thermal energy from the drop calorimeter being used to heat the compounds to the reaction temperature. The ΔH_f values for both crystals and pellets of Na_2CO_3 were obtained from the heat flow signal by integrating each peak and subtracting the base-line using OriginPro 8 Peak Analyzer tool.

	Experiment 23-26 (left to right)							
	Na_2CO_3 of ΔH_f (kJ mol^{-1})				% Difference			
	Pellets		Crystals		Pellets		Crystals	
Theoretical	-127				-			
Drop 1	-108	-108	-123	-150	15.0	14.9	3.15	18.1
Drop 2	-89.3	-95.2	-114	-139	29.7	25.0	10.2	9.45
Drop 3	-68.7	-71.8	-126	-119	45.9	43.5	0.787	6.30
Drop 4	-64.7	-67.6	-91.9	-122	49.1	46.8	27.6	3.94
Drop 5	-43.2	-117	-88.2	-85.1	66.0	7.87	30.6	32.3
Drop 6	-28.2	-	-81.2	-87.4	77.8	-	36.1	32.2

Table 4.2: ΔH_f data for pellets and crystals of Na_2CO_3 at 830°C.

The typical ΔH_f values for both pellets and crystals of Na_2CO_3 with the least scatter were compared against its theoretical ΔH_f value of -127 kJ mol^{-1} at 830ºC (table 4.2). The average ΔH_f value for the pellets of Na_2CO_3 was ~90.2 kJ mol^{-1} over three pellet drops, which was ~30% lower than its theoretical value. The average ΔH_f value for crystals of Na_2CO_3 was ~129 kJ mol^{-1} over three pellet drops, which was 1.57% higher than its theoretical value. In both cases, these values were fairly consistent over the experiments. However the ΔH_f value for pellets of Na_2CO_3 beyond the third drop was ~46.8% lower than expected and the ΔH_f value for crystals of Na_2CO_3 beyond the fourth drop was ~31% lower than expected.

This data suggests Na_2CO_3 was probably decomposing under these conditions to produce Na_2O and CO_2, as described by Motzfeldt, 1955 and Kim and Lee, 2001 [258] [260]. However, the decomposition temperature was lower than at 851°C, which is probably caused by the lowering of partial pressure of CO_2 due to the flow of argon gas over the melt. This was confirmed by Trémillon and Inman, 1997, whom state that the dissociation constant of the carbonate ion is large enough that lowering the partial pressure of CO_2 leads to its complete dissociation [190]. The data also suggests the ΔH_f values for pellets and crystals of Na_2CO_3 were fairly consistent over the first three drops. There were however small discrepancies between the pellets and crystals of Na_2CO_3, probably due to their geometry, which could affect their distance away from the thermopiles.

The ΔH_f data also suggests the decomposition was more significant at the later stages of the experiment, probably due to the flow of gas over the melt. It was unlikely that additional reactions of the platinum pellets with O_2 to produce PtO_2 or Pt_3O_4 films affected the calibration of the drop calorimeter as the mass of pellets of platinum remained consistent throughout the experiments [234-235]. It was also unlikely the effects of moisture played a role as this would have contributed to higher ΔH_f values. It is the author's recommendation that if one performs these experiments again, a CO_2 gas above the melt should be utilized, to avoid the decomposition of Na_2CO_3 and thus yield closer ΔH_f values to the theoretical.

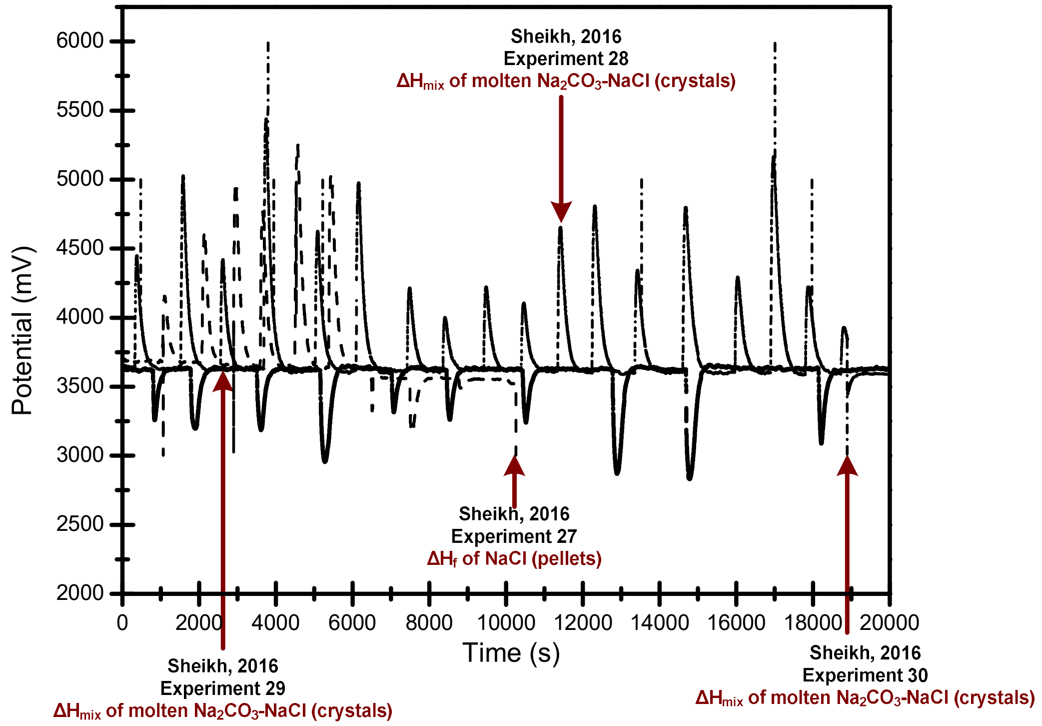

Figure 4.24: Drop calorimeter heat flow signal for NaCl, molten NaCl-Na_2CO_3 at 830°C, under argon.

Then an empty glassy carbon crucible was filled with NaCl and placed at Position B in the calorimetric tube. The calorimetric tube was then placed inside the drop calorimeter and the heat flow signal recorded for ~15 minutes until the temperature of the calorimeter stabilized. Then pellets of NaCl and Na_2CO_3 were added to the empty glassy carbon crucible and a time period of ~30 minutes was allowed between each drop, to allow the temperature of the calorimeter to stabilize to its initial set point, as evident from the heat flow signal. Upon every third addition, a pellet of platinum was added to the glassy carbon crucible to provide a suitable calibration point for calculating the heat of formation (ΔH_f) and ΔH_{mix} values (figure 4.24).

The diagram shows the heat flow signal for NaCl and molten NaCl-Na_2CO_3 rising and falling slowly, which can be attributed to the thermal energy from the drop calorimeter used to heat the compounds to the reaction temperature. In all cases, a minimum base-line of ±1 mV was observed, which can be attributed to the decomposition of Na_2CO_3, as suggested by Kim and Lee, 2001, evaporation of NaCl, and corrosion reactions of the calorimetric tube with NaCl [18] [260]. For this reason, no more than ~6 hours was allowed for each experiment to avoid the deterioration of the drop calorimeter. The ΔH_f values for NaCl and ΔH_{mix} for molten NaCl-Na_2CO_3, was obtained by integrating each peak and subtracting the base-line using OriginPro 8 Peak Analyzer tool.

	Experiment 27		**Experiment 28-30 (left to right)**		
	ΔH_f of NaCl (kJ mol^{-1})	**% Difference**	**ΔH_{mix} of NaCl-Na_2CO_3 (kJ mol^{-1})**		
	Pellets		**Pellets**		**Crystals**
Theoretical	-74.7	-	-		
Drop 1	-73.2	-0.471	0.364	1.55	-0.471
Drop 2	-74.9	0.524	2.10	2.85	0.524
Drop 3	-71.8	0.331	1.72	-2.39	0.331
Drop 4	-72.2	-0.637	0.631	-1.60	-0.637
Drop 5	-69.9	-0.676	-0.099	-1.98	-0.68
Drop 6	-69.4	-0.899	-1.11	-3.15	-0.899

Table 4.3: ΔH_f data for NaCl and ΔH_{mix} data for molten NaCl-Na_2CO_3, at 830ºC.

The typical ΔH_f values for both pellets of NaCl were compared against its theoretical value of ~74.7 kJ mol^{-1}, and typical ΔH_{mix} values for both crystals and pellets of molten NaCl-Na_2CO_3, with the least scattering (R^2 values) were compared against each other at 830ºC (table 4.3). The average ΔH_f value for the pellets of NaCl was ~72.9 kJ mol^{-1} over three pellet additions, which was ~0.4% lower than expected. The average ΔH_{mix} values for molten NaCl-Na_2CO_3, were ~2 kJ mol^{-1}, which were in the same range as other ΔH_{mix} values in literature, with the differences between crystals and pellets of Na_2CO_3 being ~1%.

The table suggests Na_2CO_3 was probably decomposing under these conditions to produce Na_2O and CO_2 as described by Motzfeldt, 1955 and Kim and Lee, 2001, and NaCl was probably evaporating under these conditions [258] [260]. This decomposition temperature was higher than at 851°C, as reported previously, which was also contributed by the lowering of the partial pressure of CO_2, due to a flow of argon gas over molten NaCl. It was unlikely the corrosion of the SiO_2 calorimetric tube with NaCl contributed to these results as the base-line was omitted before analysis. There was also no significant difference between the shape of the pellets and crystals of Na_2CO_3, which suggests the effects of moisture in the atmosphere, can be neglected. However the author cannot confirm whether the pellets and crystals had completely dissolved in the melt due to the limitations of the experiment, however when the calorimetric tube was removed and the molten salt was cooled, the molten NaCl-Na_2CO_3 mixture appeared to be a consistent white solution. Also the ΔH_{mix} values were obtained below the saturation limit of the melt and at least ~30 minutes had been allowed between each drop.

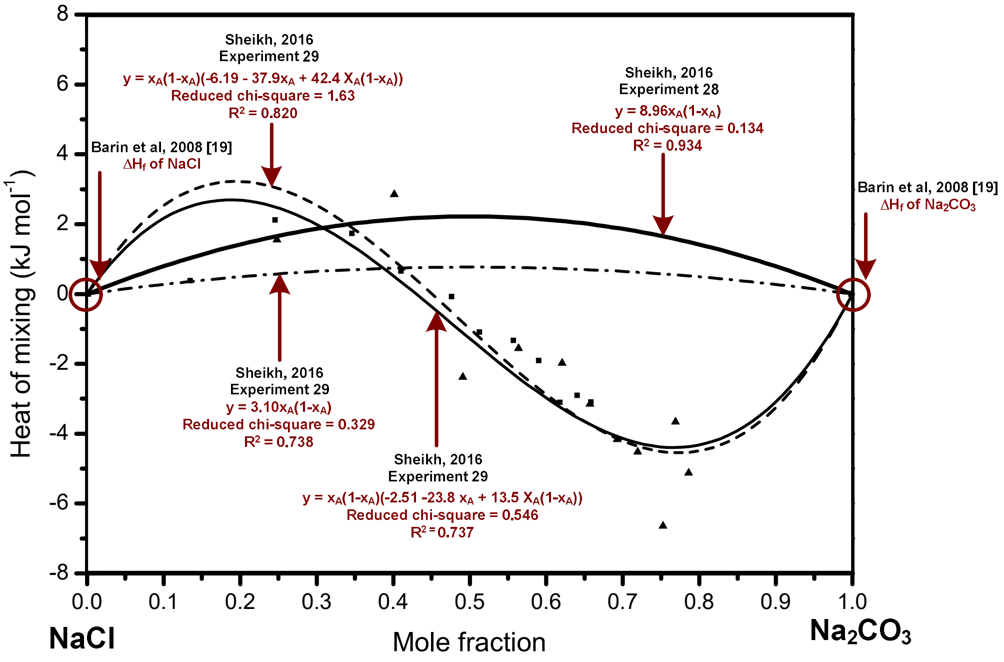

Figure 4.25 ΔH_{mix} data for molten NaCl-Na_2CO_3, at 830°C under argon.

The ΔH_{mix} data for crystals and pellets of molten NaCl-Na_2CO_3 at 830ºC were plotted as a function of composition, and the sub-regular solution model was fitted (experiment 28-30). The ΔH_{mix} data for the crystals of molten NaCl-Na_2CO_3 at 830ºC were then fitted to the regular solution model over initial three drops, and extrapolated over the entire composition range, under the assumption that the decomposition of Na_2CO_3 was less significant at the initial stages of the experiment (figure 4.25).

The diagram represents two S-shaped curves, with a positive contribution ≤50 mol% Na_2CO_3 and a negative contribution ≥50 mol% Na_2CO_3. The positive contribution can be attributed towards the intermolecular interactions of Na_2CO_3 and NaCl, being greater than the energy required for the dissolution of Na_2CO_3. The negative contribution can be attributed towards the decomposition of Na_2CO_3 to CO_2 and Na_2O, coupled with its slow reaction kinetics. This probably arose due to the fact that as the concentration of Na_2CO_3 increases in the molten salt, the amount of CO_2 evolved also increases, which could have contributed towards the evaporation rate of NaCl. It was unlikely the corrosion reactions of the calorimetric tube didn't affect these functions, as the base-line had been substracted.

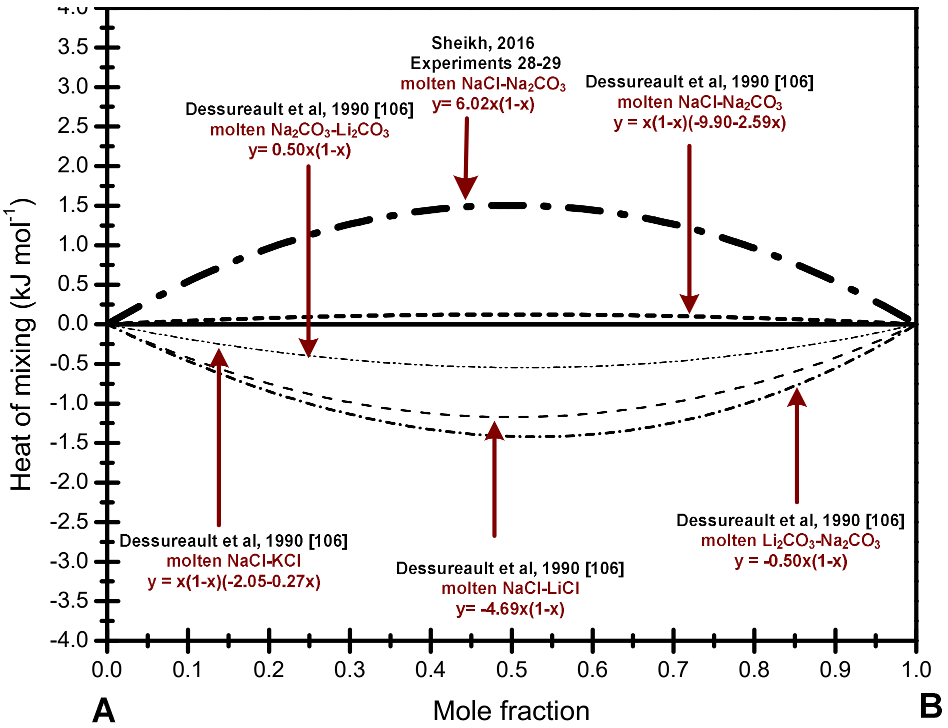

Figure 4.26: Literature and experimental ΔH_{mix} data for binary chloride, carbonate and their mixtures. [23]

The average ΔH_{mix} regular solution model for crystals of molten NaCl-Na_2CO_3 was plotted against previous chloride, carbonate and chloride-carbonate binary systems in literature. The general consensus in literature is the dependence of the ΔH_{mix} functions

---

[23] **A** is the initial salt and B is the secondary compound that dissolves in **A**
i.e. for NaCl = **A** and Na_2CO_3 = **B**

upon temperature is minimal at high temperatures, therefore values taken at different temperatures can be compared (figure 4.26) [120-128].

The diagram demonstrates the ΔH_{mix} functions can be positive or negative, and become larger as the size difference between the solute and solvent ions increases. The relatively large positive ΔH_{mix} function for molten NaCl-Na_2CO_3 (~2 kJ mol^{-1}) at 830ºC was attributed to the decomposition of Na_2CO_3 to CO_2 and Na_2O, as described by Kim and Lee, 2001, and agrees with the previous phase diagram studies by the author [260]. If the experiment was performed again, the author would use a CO_2 above the molten salt to avoid the decomposition of Na_2CO_3 and yield the true values of ΔH_{mix} function for molten NaCl-Na_2CO_3. Also, the author would also use a different NIST calibration material, such as Al_2O_3, as this would confirm that the effect of PtO_2 or Pt_3O_4 layers had no affect upon the ΔH_{mix} or ΔH_f values. An Inconel^{TM} 600 calorimetric tube could also be used to avoid the deterioration of the calorimetric tube and ensure the duration of the experiments can be extended.

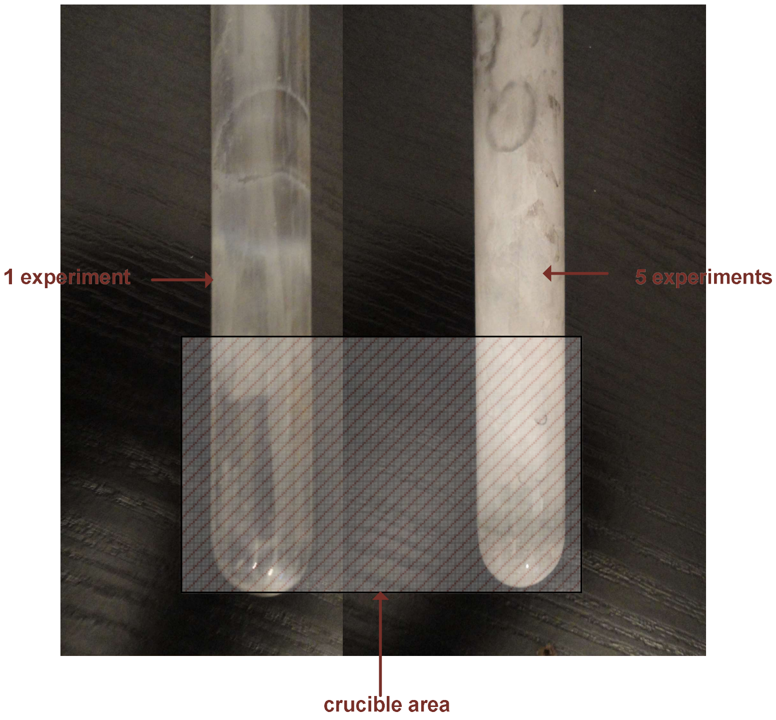

Figure 4.27: Image of the calorimetric tube after 1 (left) and 5 (right) ΔH_f and ΔH_{mix} experiments at 830°C.

The calorimetric tubes were removed from the drop calorimeter and examined after 1 and 5 experiments and images were taken (figure 4.27). The diagram shows a significant colour change was evident upon the inner walls. This colour change was attributed towards the formation of sodium silicates such as α-Na_2SiO_3 or β-Na_4SiO_4 as described by Kracek, 1930, Ryś and Müller, 2010, Halter et al, 2004 and Kracek, 1930 and Zhang et al, 2013 [240-249]. It is likely the decomposition of Na_2CO_3 to Na_2O and CO_2 coupled with the evaporation of NaCl, caused sufficient contact with the inner walls for these reactions to occur. The author also found the strength of the calorimetric tubes weakened over the course of the experiments, which can be attributed to changes in its composition. Therefore each tube was replaced after ~5 experiments and the time frame of a single experiment was shortened to less than 6 hours. It is the author's recommendation if these experiments were performed again, the calorimetric tubes should be constructed from Inconel^{TM} 600, due to its proven stability in molten chlorides, and a CO_2 gas above the molten salt to inhibit the decomposition of Na_2CO_3 [261-262].

This section has shown that Na_2CO_3 is not stable in NaCl at 830ºC, and decomposes to CO_2 and Na_2O, with slow reaction kinetics, as described by Kim and Lee, 2001 [254]. This was confirmed by a positive (endothermic) ΔH_{mix} contribution and lower ΔH_f values for Na_2CO_3, thus supporting the dissolution studies described earlier.

4.5.4 Solubility products of the reactants in the molten salt

The **dissolution of the reactants**; $CaCO_3$ and Na_2CO_3 in NaCl at 830°C was investigated using potentiometry, which subsequently led to obtaining K_{sp} values of CaO and Na_2O in NaCl, using an argon gas bubbler ($Al_6Si_2O_{13}$). The K_{sp} value for SiO_2 in molten NaCl however was not obtained, due to its low solubility, as shown by Yasuda, 2007 [208]. The potentiometric technique required the construction of an electrochemical cell, consisting of a tubular cell envelope (Stainless Steel 316L and/or Inconel^{TM} 600), a circular lid (Stainless Steel 316L) containing several apertures for the insertion of electrodes, a drop tube ($Al_6Si_2O_{13}$), argon gas bubbler ($Al_6Si_2O_{13}$) and inert gas inlet and outlet tubes (Stainless steel 316L) [195-198]. The electrodes consisted of an Ag^+/Ag reference electrode ($Al_6Si_2O_{13}$), and ISE (YSZ), based upon the design by Cherginets, 2005 [130] (figure 4.28)

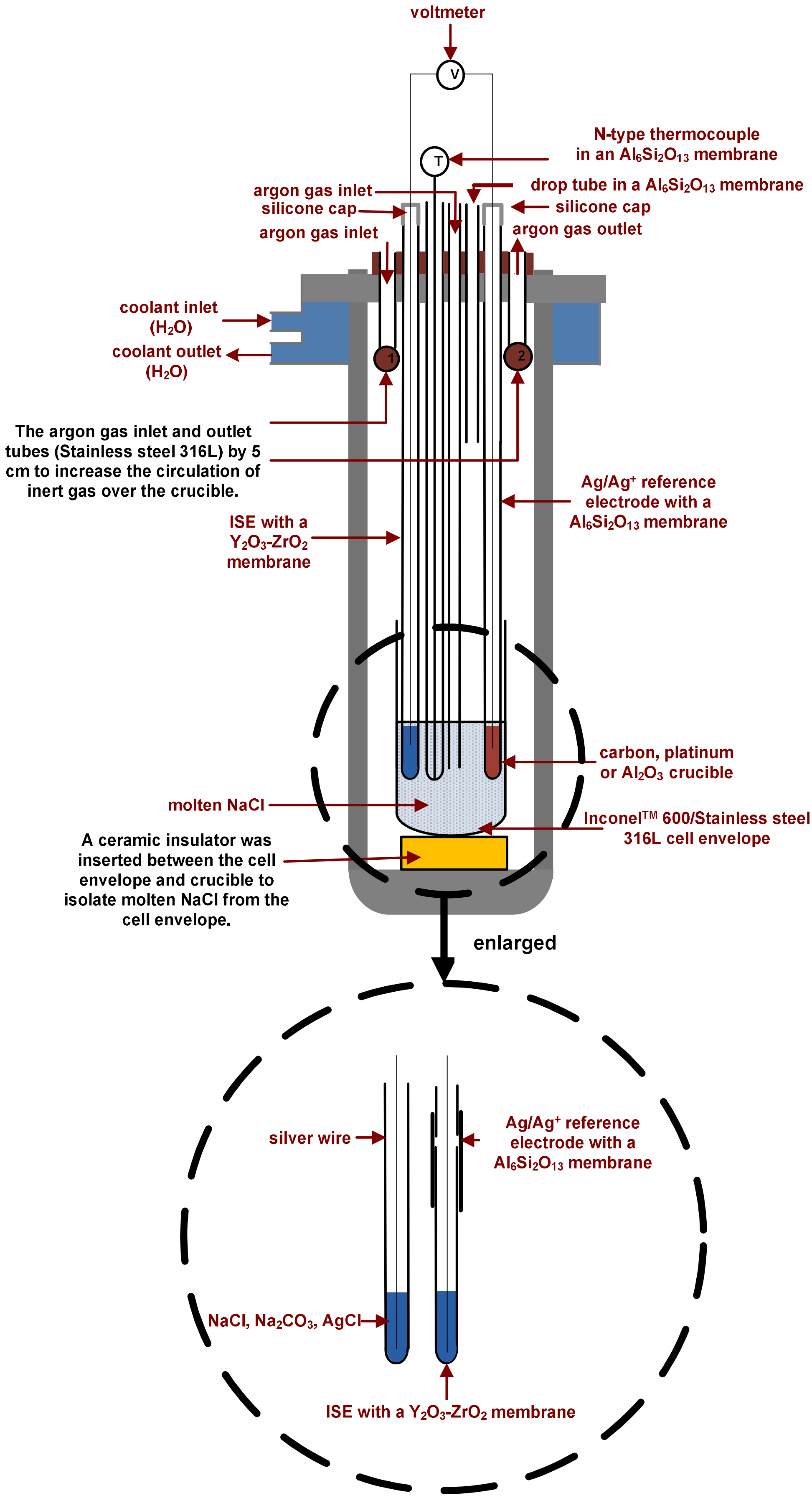

The argon gas inlet and outlet tubes (Stainless steel 316L) by 5 cm to increase the circulation of inert gas over the crucible.

A ceramic insulator was inserted between the cell envelope and crucible to isolate molten NaCl from the cell envelope.

Figure 4.28: Diagram of electrochemical cell (left) and electrodes (right).

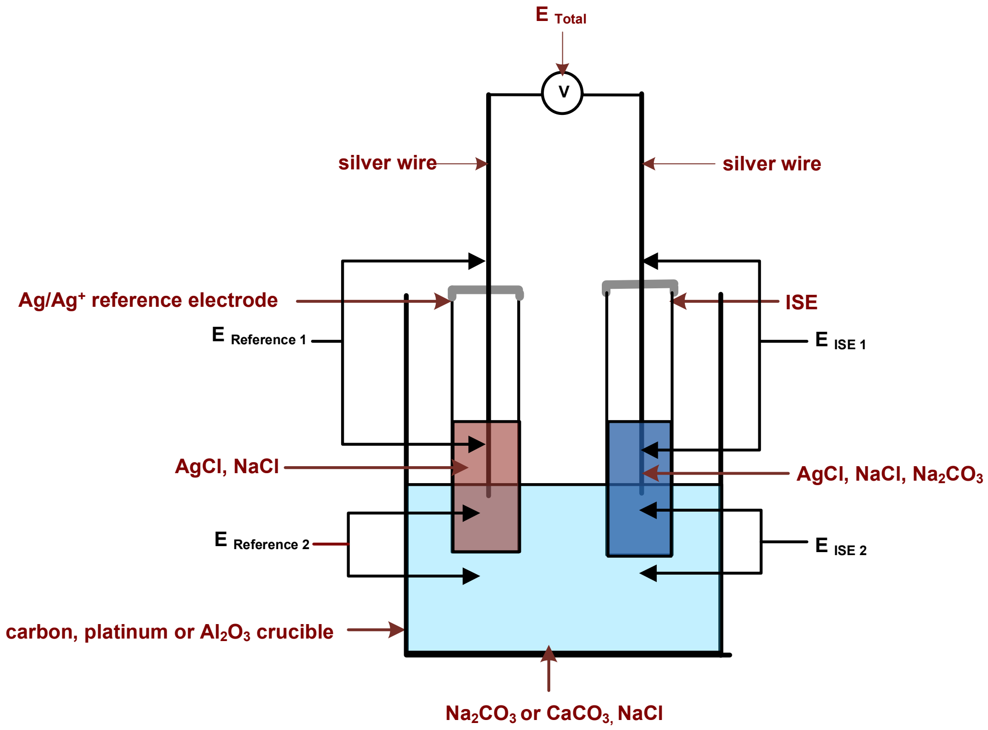

Figure 4.29 Diagram of junction and interface potentials in the electrochemical cell.

Initally, the ISE and Ag/Ag^+ reference electrode were immersed in molten NaCl, to produce a potentiometric signal (E_{Total}) (figure 4.29). This signal was the sum of several junction and interface potentials within the cell, which arose due to the separation of charge. This allowed the potentiometric signal (E_{Total}) to be dependent upon changes in O^{2-} activity in molten NaCl within the crucible, thus suitable for our solubility measurements and following molten salt reactions.Upon the addition of Na_2CO_3 or $CaCO_3$ to the melt, produced CO_3^{2-} and Na^+ ions which dissociated to O^{2-} ions (as the dissociation constant of CO_3^{2-} is extremely large) and CO_2.

The diagram shows junction potentials were present between the silver wires in contact with Ag^+ ions in molten NaCl (the Ag/Ag^+ redox couple) in the ISE and reference electrodes ($E_{Reference\ 1}$, $E_{ISE\ 1}$). It also shows a membrane potential was present between O^{2-} ions in molten NaCl in the ISE ($E_{ISE\ 2}$) and crucible, introduced from the dissolution of $Na_2CO_{3.}$ This potential existed due to the YSZ membrane containing oxygen vacancies within its lattice structure [231]. Such vacancies arose when Zr^{4+} ions of ZrO_2 were substituted with slightly larger Y^{3+} ions (ionic radius of 0.82 Å to 0.96 Å), therefore when O^{2-} ions were present upon both sides of the YSZ membrane, a concentration gradient was established. This concentration gradient would cause O^{2-} ions to selectively migrate through the oxygen vacancies and establish a charge separation [231-233]. Finally it shows a membrane potential ($E_{Reference\ 2}$) was present between Na^+ ions in molten NaCl in the Ag/Ag^+ reference electrode and crucible, due to the $Al_6Si_2O_{13}$ membrane containing vacancies for Na^+ ions. As Na^+ ions were present in molten NaCl in the crucible and the reference electrode in excess quantities, a constant and reproducible potential was established [230].

The author made several modifications to the electrochemical cell to produce the potentiometric signal, for example an Al_2O_3 disc was placed between the crucible and cell envelope and place the crucible away from the inner walls of the cell envelope. This removed electrical contact between the crucible and cell envelope and ensured changes in the potentiometric signal were solely due to the dissolution of the reactants in molten NaCl. This is because when dissimilar metals are exposed to electrolytes such as molten salts, junction potentials are created between metals and metal ions in molten NaCl (denoted redox couples) which contribute towards producing a potentiometric signal, as described by Back, 2001 and Ray, 2006 [53] [265]. Also, when dissimilar metals are in contact with one another at elevated temperatures, junction potentials are created due to a phenomenon called the thermoelectric effect [53]. The author also increased the length of the inert gas inlet and outlet tubes (to at least ~5 cm) into the cell to improve the circulation of inert gas over the molten NaCl to remove unwanted moisture in the cell.

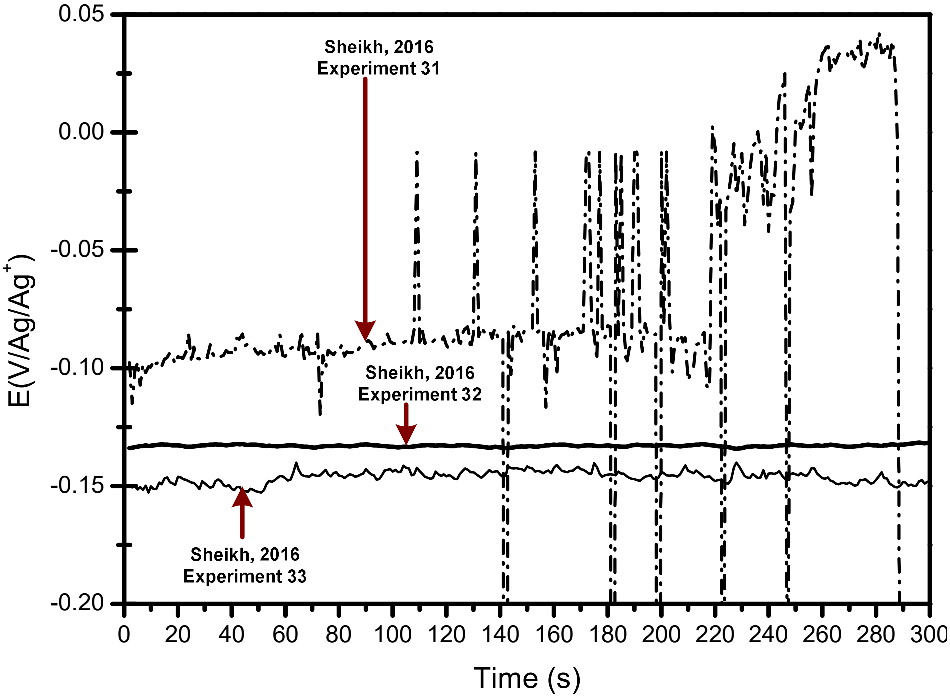

Figure 4.30: Potentiometric signal improvements.

The author also made several improvements to improve the stability and reproducibility of the potentiometric signal (figure 4.30). The author found that the signal often becoming sensitive to changes in the environment instead of O^{2-} ions in molten NaCl (experiment 31). This was attributed to the silver wire in the ISE breaking into two pieces, thus causing the membrane potential between the silver wire and Ag^+ ions in molten NaCl in the ISE to be lost. To reproduce this signal, the author replaced the silver wire in the ISE in-situ and restarted the experiment.

The author also found the potentiometric signal often became unresponsive to O^{2-} ions in molten NaCl, which was due to the YSZ membrane breaking into two separate pieces. This phenomena occured during heating and cooling cycles of the furnace thus attributed to the expansion in volume of the YSZ membrane from its tetragonal phase to monoclinic. It was the author's opinion this phenomena shouldn't have occurred due to the composition of YSZ (8 mol% Y_2O_3, 92 mol% Y_2O_3). This was attributed to insufficient doping from the manufacturer or the effects of thermal shock. [24] To avoid the YSZ membrane breaking again, the heating and cooling cycles were reduced from 10°C to 2°C min^{-1} thus extending the experimental time to ~24 hours. This lead to

---

[24] Thermal shock is when thermal gradients cause various parts of an object to expand by different amounts.

safety concerns by our department, as 24 hour experiments weren't part of the health and regulations. To meet these safety regulations, a switch was incorporated into the furnace to cut the power supply if the temperature rose above a set point value (950°C).

The author also produced a secondary ISE design, using pieces of the broken YSZ membrane (experiment 31). This produced an unstable potentiometric signal (experiment 32) which was attributed to air and moisture entering the ISE which could have interacted with molten NaCl and affect the dissociation of the CO_3^{2-} complex ion to CO_2 and O^{2-} ions.

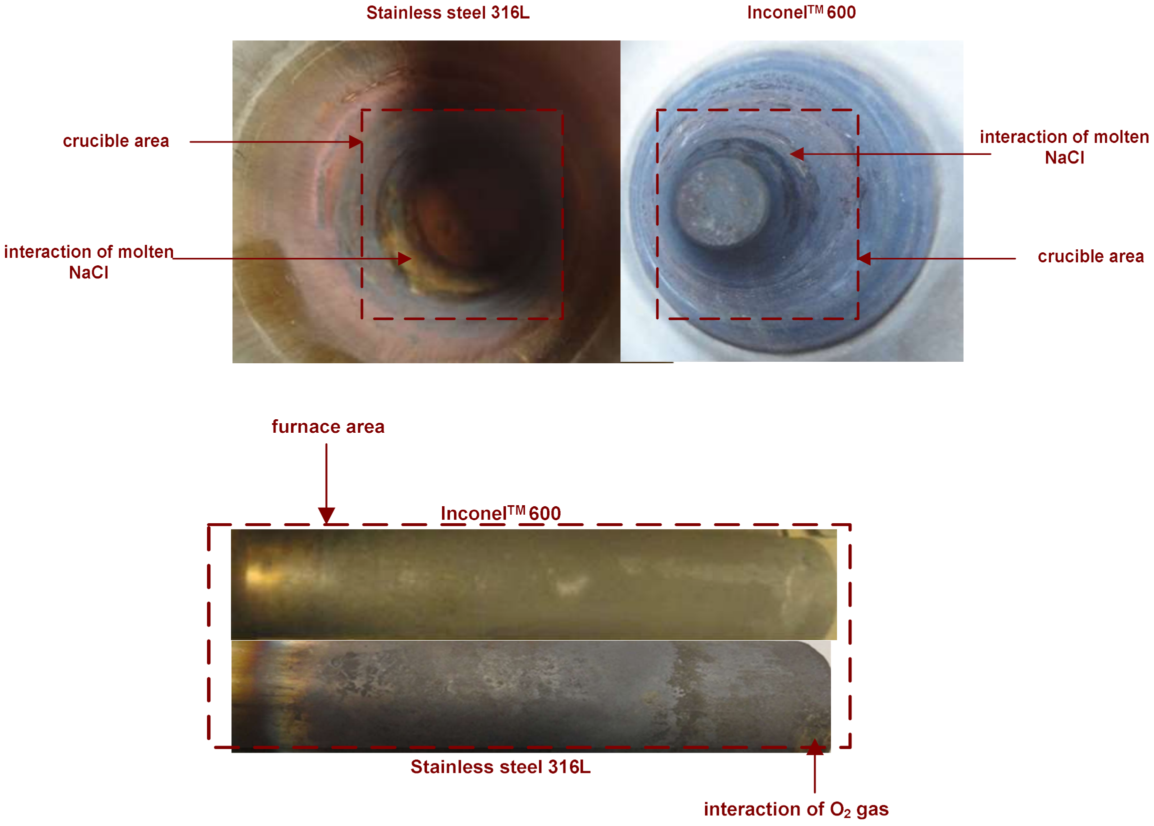

Figure 4.31: Images of Stainless steel 316L and Inconel^{TM} 600 cell envelopes at 830℃ (top) and 900℃ (bottom).

Images of the internal and external surfaces of the Stainless Steel 316L and Inconel^{TM} 600 cell envelopes were taken after exposure to ~900ºC and molten NaCl (figure 4.31). These images illustrate a change in colour and surface finish of the Stainless Steel 316L which was attributed to changes in the composition of the alloy. This probably occurred due to CrO_3 Ce_2O_3 compounds selectively removed (above 816ºC) to expose Fe_2O_3 and FeO to the effects of oxygen and moisture and produce their hydrated forms [238-239].

These compounds were probably produced due to Intergranular Attack (IGA), which occurs when carbon and chromium in the alloy react to form chromium carbides, as described by Davis, 1954 and Indacochea et al, 2000 [238-239]. [25] These chromium carbide compounds precipitate out at grain boundaries which result in chromium depleted zones adjacent to the grain boundaries and a discontinuous oxide layer. This discontinuous oxide layer exposes iron to O_2 and moisture in the air to produce Fe_2O_3 and FeO compounds before disintegrating. [26] The chromium depleted zones also allow the molten salt to enter the alloy to produce produce galvanic couples between the interface of the salt and alloy to cause corrosion reactions. The author found the performance of Inconel^{TM} 600 was found to be better than Stainless Steel 316L which has probably due to the higher nickel content of Inconel^{TM} 600 [237-238]. The higher nickel content probably causes a lower thermal expansion differential between iron and the oxide layer during heating and cooling cycles, thus greatly improving its corrosion resistance.

---

[25] A grain boundary is the interface between two grains (crystallites) in a polycrystalline material.

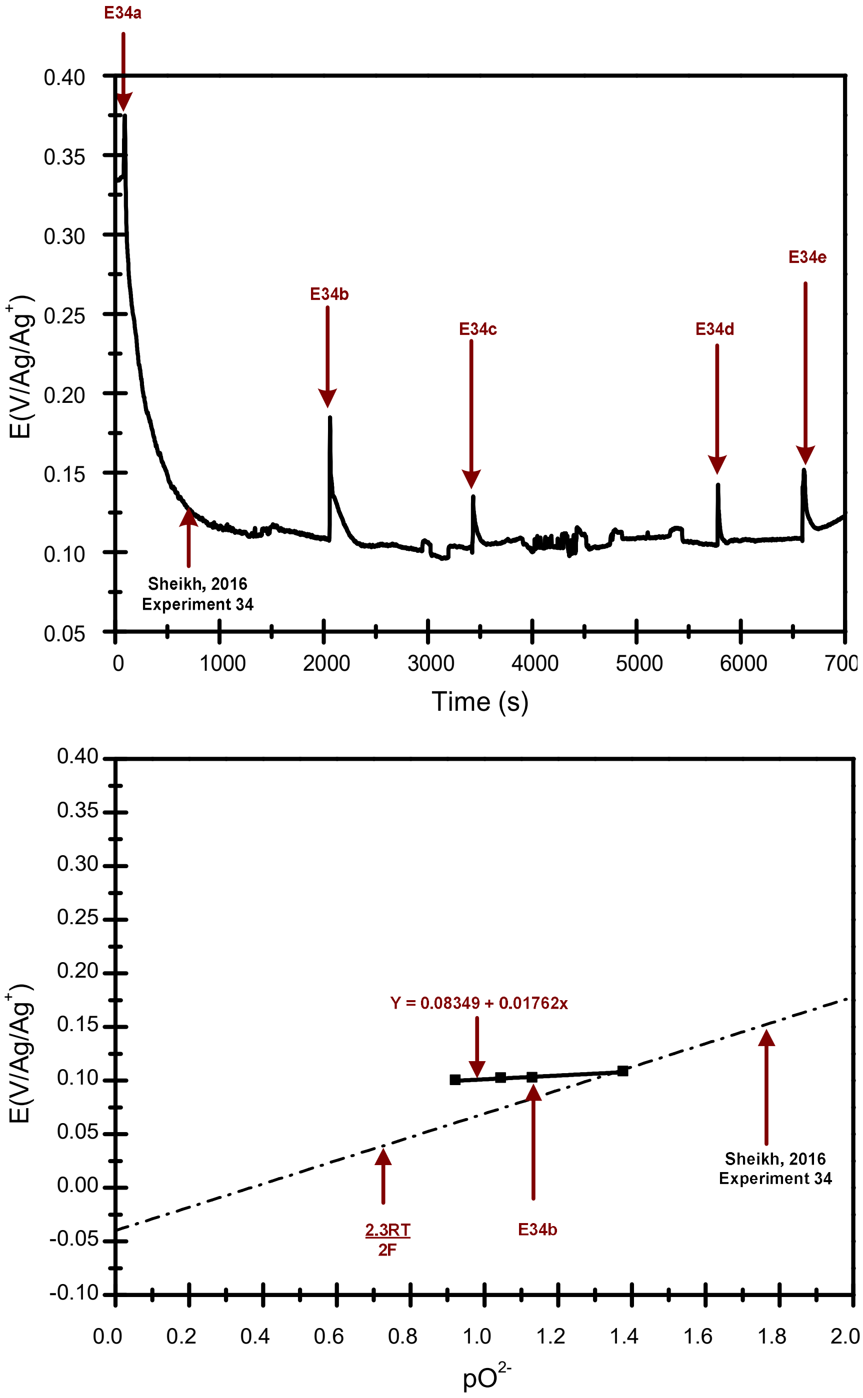

Figure 4.32: Potentiometric signal and O^{2-} ion activity of $CaCO_3$ in NaCl at 830°C, under argon.

The **dissolution of the reactant;** $CaCO_3$ in NaCl was investigated by filling an Al_2O_3 crucible with NaCl, and heating to 830°C over ~10 hours at 2°C min^{-1}. The Ag/Ag^+ reference electrode and ISE were then immersed in molten NaCl in the crucible and the potentiometric signal was recorded. Then ~5 pellets of $CaCO_3$ were added to molten NaCl and at least 10 minutes allowed between each drop. This time period was selected to allow the dissolution and decomposition of $CaCO_3$ in molten NaCl to occur. The experiment was then discontinued by removing the Ag/Ag^+ reference electrode and ISE from the molten NaCl and cooling the furnace to ~50ºC over ~18 hours. Then the potential values when pellets of $CaCO_3$ equilibrated in the melt were obtained directly from the signal using Uni-trend software and plotted as a function of the negative logarithm of O^{2-} ion activity (-log [O^2]) in molten NaCl. The O^{2-} activity in molten NaCl was calculated from the weighed amounts of $CaCO_3$ added to molten NaCl under the assumption that $CaCO_3$ completely dissociated and dissolved to produce CO_2 and CaO, CaO completely dissolved to produce O^{2-} and Ca^{2+} ions and the O^{2-} ion had no deviations from ideality. The total amount of O^{2-} ions in molten NaCl were assumed to have accumulated from previous additions and no additional reactions had occurred (figure 4.32).

The diagram shows the potentiometric signal was initially sensitive to changes in O^{2-} ion activity in molten NaCl, prior to the addition of pellets of $CaCO_3$. This was attributed to minute quantities of O^{2-} ions being present in molten NaCl, probably due to small quantities of O_2 dissolved in molten NaCl. The signal also didn't stabilize over ~2 hours upon immersion of the electrodes, which was attributed to changes in the partial pressure of O_2 and its dissolution in molten NaCl. It was unlikely the solubility of the Al_2O_3 crucible and $Al_6Si_2O_{13}$ membrane in molten NaCl affected this to a large degree, as these were probably extremely small [266]. Upon the addition of pellets of $CaCO_3$ to molten NaCl, the potentiometric signal changed from its initial base-line before reverting back (E34 a-c). This was attributed to the decomposition of $CaCO_3$ to CaO and CO_2, and the dissolution of O^{2-} ions in molten NaCl. It was found that additional pellets (E34 b) didn't affect the potentiometric signal in the same way as previous pellets, which were attributed to molten NaCl becoming saturated from previous additions. The regression line through the potential values and -log [O^2] in molten NaCl didn't match a complete electron value (n, 1, 2, 3) from the Nernst equation. This suggests other processes were taking place that could have affected the potentiometric signal or O^{2-} ion activity. These could have been the pellets not dissolving completely and/or the evaporation of molten NaCl which was probably aided by CO_2 leaving the cell and/or its incomplete decomposition to CO_2. The evaporation of molten NaCl was also supported by a mass change of ~5 wt% of the crucible. These observations however support the fact that $CaCO_3$ decomposes at 830ºC to produce O^{2-} ions and CO_2.

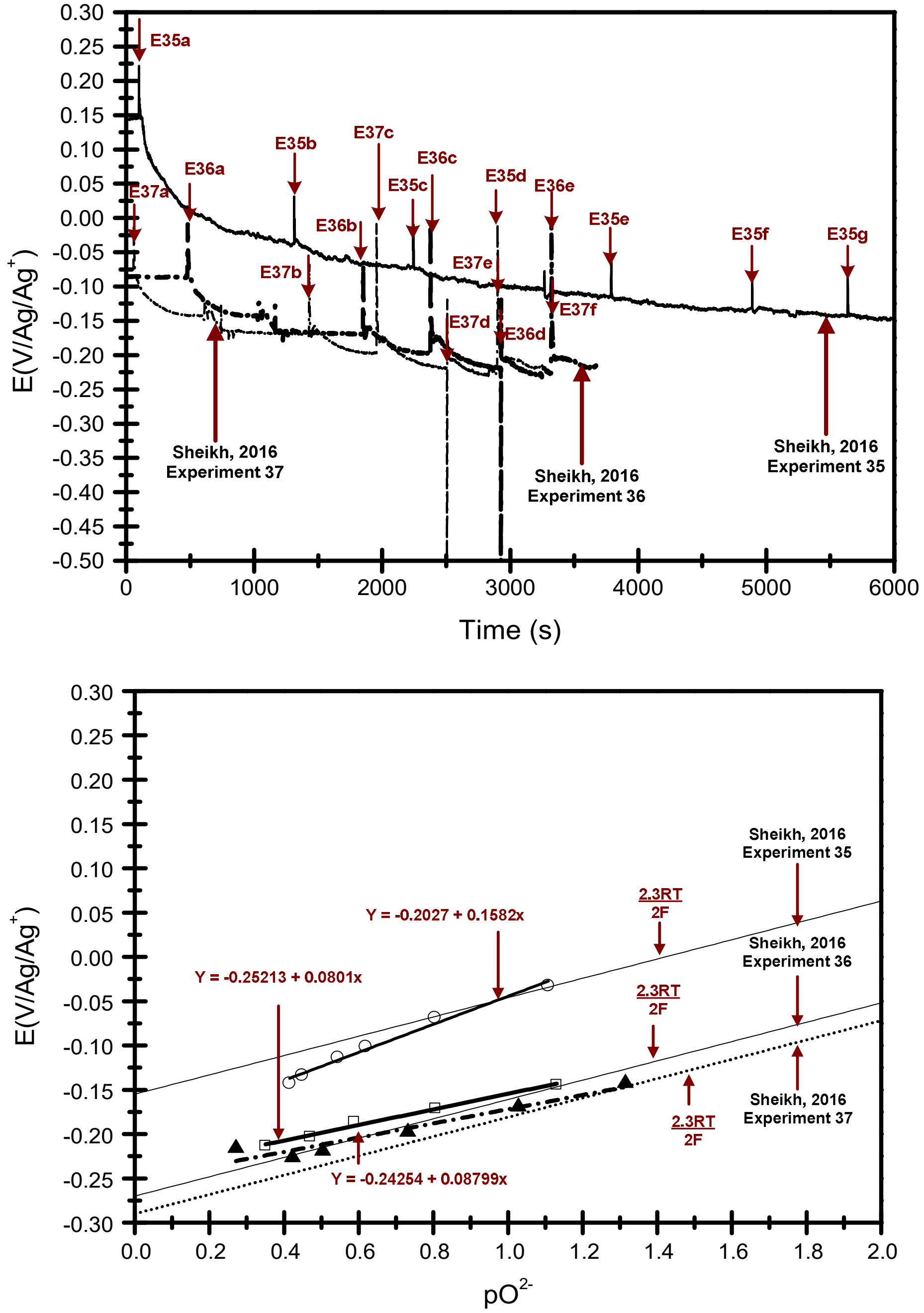

Figure 4.33: Potentiometric signal and and O^{2-} ion activity of Na_2CO_3 in NaCl at 830°C, under argon, with an argon gas bubbler.

The **dissolution of the reactant**; Na_2CO_3 in NaCl was investigated by filling an Al_2O_3 crucible and glassy carbon crucible with NaCl and heating to 830°C over ~10 hours at 2°C min^{-1}. Then the Ag/Ag^+ reference electrode and ISE were immersed into the molten NaCl and the potentiometric signal recorded. Then ~11 pellets of Na_2CO_3 were added to molten NaCl and at least ~30 minutes allowed between each drop. The experiment was then discontinued by removing the Ag/Ag^+ reference electrode and ISE from the molten NaCl in the crucible and cooling the furnace to ~50°C over ~18 hours. The potential values when pellets of Na_2CO_3 equilibrated in molten NaCl were obtained directly from the potentiometric signal, using Uni-trend software and plotted as a function of the negative logarithm of O^{2-} ion activity (-log $[O^2]$) in molten NaCl. The O^{2-} activity in molten NaCl was calculated from the weighed amounts of Na_2CO_3 added to molten NaCl under the assumption that Na_2CO_3 completely dissociated and dissolved to produce CO_2 and Na_2O, Na_2O completely dissolved to produce O^{2-} and Na^+ ions and the O^{2-} ion had no deviations from ideality. The total amount of O^{2-} ions in molten NaCl were assumed to have accumulated from previous additions and no additional reactions had occurred (figure 4.33).

The diagram shows the potentiometric signal was initially sensitive to changes in O^{2-} ion activity in molten NaCl, before the addition of pellets of Na_2CO_3. This can be attributed to minute quantities of O^{2-} ions being present in molten NaCl, probably due to small quantities of O_2 dissolved in the melt. The potentiometric signal didn't stabilize over ~2 hours, upon immersion of the electrodes, which can be attributed to changes in the partial pressure of O_2 and its dissolution in molten NaCl. It was unlikely this was affected by the solubility of the Al_2O_3 crucible and $Al_6Si_2O_{13}$ membrane, which was probably extremely small [266] [269]. Upon the addition of pellets of Na_2CO_3 to molten NaCl, the potentiometric signal changed from its initial base-line before reverting back (E35-37 a-f). This was attributed to their decomposition to Na_2O and CO_2 and the dissolution of O^{2-} and Na^+ ions in molten NaCl. It was found that additional pellets affected the potentiometric signal in similar ways to previous additions, which suggested that molten NaCl was not saturated The regression line through the potential values and -log $[O^2]$ in molten NaCl didn't match a complete electron value (n, 1, 2, 3) from the Nernst equation. This suggests other processes were taking place that affected the potentiometric signal or O^{2-} ion activity. These could have been the pellets not dissolving completely and/or evaporation of molten NaCl which was probably aided by CO_2 leaving the cell and/or its incomplete decomposition to CO_2. The evaporation of molten NaCl was also supported by a mass change of ~5 wt% of the crucible. These observations however support the fact that Na_2CO_3 decomposes at 830ºC to produce O^{2-} ions and CO_2.

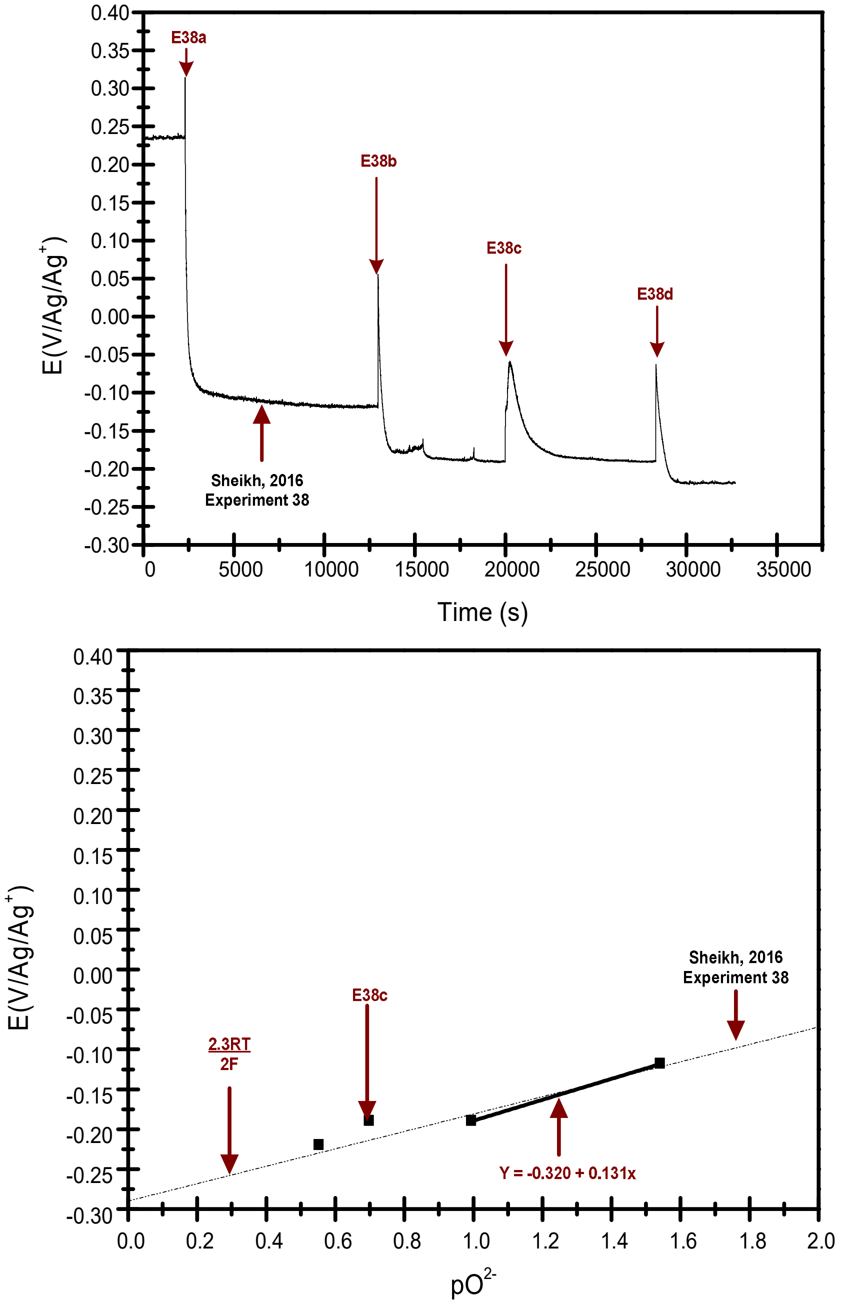

Figure 4.34: Potentiometric signal and O^{2-} ion activity of $CaCO_3$ in NaCl, at 830℃, under argon, with an argon gas bubbler.

The **dissolution of the reactant;** CaO in NaCl was investigated by filling an glassy carbon crucible with NaCl and heating to 830°C over ~10 hours at 2°C min^{-1}. Then the Ag/Ag^{+} reference electrode, ISE and argon gas bubbler ($Al_6Si_2O_{13}$) immersed into molten NaCl in the crucible and the potentiometric signal recorded. Then ~4 pellets of $CaCO_3$ were added to molten NaCl in the crucible and ~5 hours allowed between each drop. This time period was selected to ensure the complete decomposition and dissolution of $CaCO_3$ which was aided by the argon gas bubbler. The experiment was then discontinued by removing the Ag/Ag^{+} reference electrode and ISE from the molten NaCl in the crucible and cooling the furnace to ~50ºC over ~18 hours occurred The potential values when pellets of $CaCO_3$ equilibrated in molten NaCl were obtained directly from the potentiometric signal using Uni-trend software and plotted as a function of the negative logarithm of O^{2-} ion activity (-log $[O^2]$) in molten NaCl. The O^{2-} activity in molten NaCl was calculated from the weighed amounts of $CaCO_3$ added to molten NaCl, assuming $CaCO_3$ completely dissociated and dissolved to produce CO_2 and CaO, CaO completely dissolved to produce O^{2-} and Ca^{2+} ions and the O^{2-} ion had no deviations from ideality. The total amount of O^{2-} ions in molten NaCl were assumed to have accumulated from previous additions and no additional reactions had occurred (figure 4.34).

The diagram shows the potentiometric signal was initially sensitive to changes in O^{2-} ion activity in molten NaCl, before the addition of pellets of $CaCO_3$. This can be attributed to minute quantities of O^{2-} ions being present in molten NaCl, probably from minute quantities of O_2 dissolved in the melt. It was found the signal didn't stabilize over ~2 hours upon immersing the electrodes, which can be attributed to changes in partial pressure of O_2 and its dissolution in molten NaCl. The signal did however stabilize over ~5 hours, which can be attributed to a consistent partial pressure of O_2 being achieved. It was unlikely this was affected by the solubility of the $Al_6Si_2O_{13}$ membrane, which was probably extremely small. Upon the addition of pellets of $CaCO_3$, the potentiometric signal changed from its initial base-line before reverting back (E38 a-f). This was attributed to their decomposition to CaO and CO_2, and the dissolution of O^{2-} and Ca^{2+} ions in molten NaCl. It was found that additional pellets (E38 b) didn't affect the potentiometric signal in the same way as previous pellets. This was attributed to molten NaCl being saturated from previous additions. The regression line through the potential values and -log $[O^2]$ in molten NaCl didn't match a complete electron value (n, 1, 2, 3) from the Nernst equation, which suggests other processes were taking place that affected the potentiometric signal or O^{2-} ion activity. These could have been attributed to the evaporation of molten NaCl which was probably aided by CO_2 leaving the cell. It was also most likely the pellets of $CaCO_3$ had completely decomposed, due to the effects of the argon gas bubbler. The evaporation of molten NaCl was supported by a mass change of ~25 wt% of the crucible. This increase in weight loss from previous experiments was attributed to the argon gas bubbler aiding the evaporation process. The K_{sp} value for CaO in molten

NaCl was calculated from the saturation limit on the potentiometric signal and the calculated amounts of CaO in molten NaCl to be ~1.1 mol kg^{-1}.

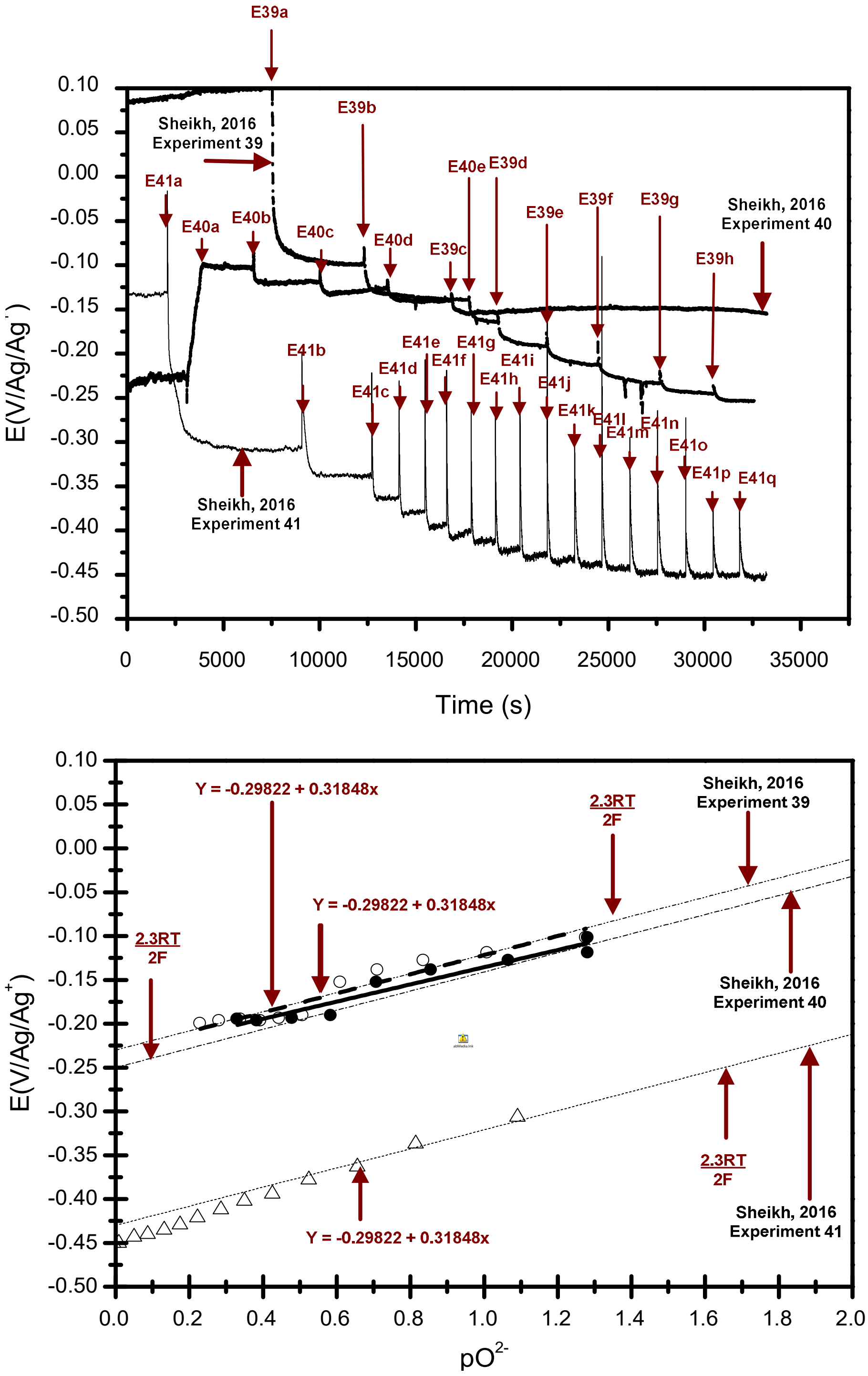

Figure 4.35: Potentiometric signal and O^{2-} ion activity of Na_2CO_3 ini NaCl at 830°C, under argon, with an argon gas bubbler.

The **dissolution of the reactant**; Na_2O in molten NaCl was investigated by filling a glassy carbon and platinum crucible with NaCl and heating to 830°C at 2°C min^{-1} over ~10 hours. Then the Ag/Ag$^+$ reference electrode and ISE were immersed in molten

NaCl in the crucible and the potentiometric signal was recorded. Then ~13 pellets of Na_2CO_3 were added to molten NaCl in the crucible and ~5 hours allowed between each drop. This time period was selected to allow the complete dissolution and decomposition of Na_2CO_3 in molten NaCl which was aided by the argon gas bubbler. The potential values when pellets of Na_2CO_3 equilibrated in molten NaCl were obtained directly from the potentiometric signal using Uni-trend software and plotted as a function of the negative logarithm of O^{2-} ion activity (-log [O^{2}]) in molten NaCl. The O^{2-} activity in molten NaCl in the crucible was calculated from the weighed amounts of Na_2CO_3 added to molten NaCl, assuming Na_2CO_3 had completely dissociated and dissolved to produce CO_2 and Na_2O, Na_2O had completely dissolved to produce O^{2-} and Na^+ ions and and the O^{2-} ion had no deviations from ideality. The total amount of O^{2-} ions in molten NaCl were assumed to have accumulated from previous additions and no additional reactions had occurred. Upon the addition of pellets of Na_2CO_3, the potentiometric signal changed from its initial base-line before reverting back (E39-41 a-f). This was attributed to their decomposition to Na_2O and CO_2, and the dissolution of O^{2-} ions in molten NaCl. It was found that additional pellets (E40 p) didn't affect the potentiometric signal in the same way as previous pellets. This was attributed to molten NaCl being saturated with the previous additions (figure 4.35).

The diagram shows the potentiometric signal was initially sensitive to changes in O^{2-} ion activity in molten NaCl, before the addition of pellets of Na_2CO_3. This can be attributed to minute quantities of O^{2-} ions being present in molten NaCl, probably from quantities of O_2 dissolved in the melt. It was found the signal didn't stabilize over ~2 hours upon immersion of the electrodes, which can be attributed to changes in partial pressure of O_2 and its dissolution in molten NaCl. The signal did however stabilize over ~5 hours, which can be attributed to a consistent partial pressure of O_2 being achieved. It was unlikely this was affected by the solubility of the $Al_6Si_2O_{13}$ membrane which was probably extremely small. The regression line through the potential values and -log [O^{2}] in molten NaCl didn't match a complete electron value (n, 1, 2, 3) from the Nernst equation, which suggests other processes were taking place that affected the potentiometric signal or O^{2-} ion activity. These could have been attributed the evaporation of molten NaCl which was probably aided by CO_2 leaving the cell. The evaporation of molten NaCl was also supported by a mass change of ~25 wt% of the crucible. This increase in weight loss from previous experiments was attributed to the argon gas bubbler aiding the evaporation process. There was no evidence of Na_2O_2 compounds forming on the platinum crucible as evident by no point of inflection on the potentiometric signal, as described by Cherginets, 2005 [130]. Also it was most likely the pellets of Na_2CO_3 had completely decomposed, due to the effects of the argon gas bubbler. The author was able to dissolve 0.337 moles of Na_2O in 0.966 moles of NaCl therefore the K_{sp} value for Na_2O in molten NaCl was calculated to be -log 1.58 (using equation 3.8).

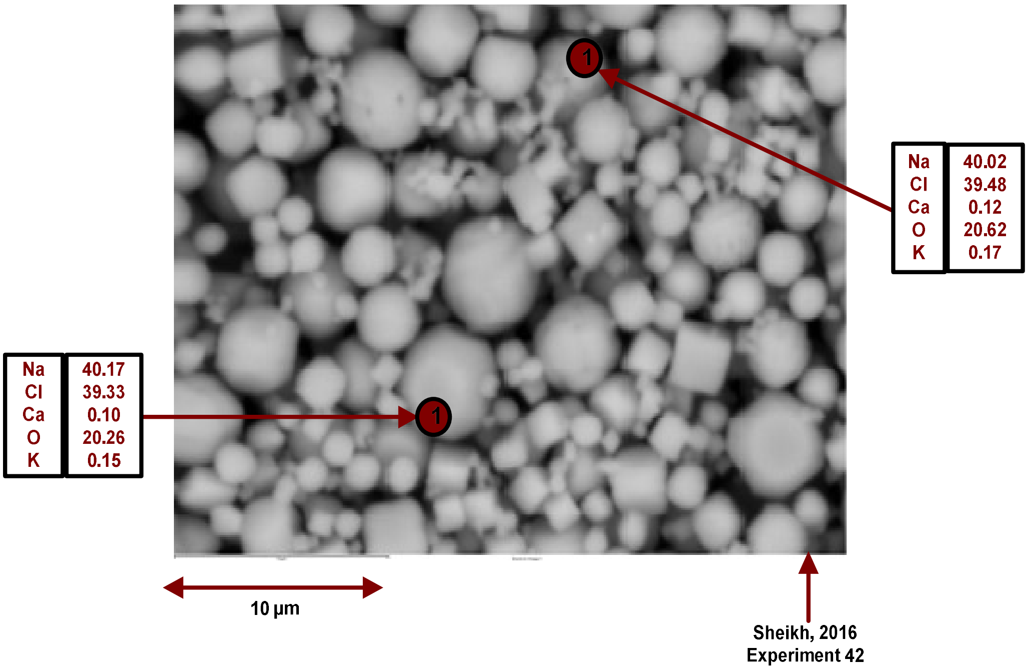

Figure 4.36: SEM image and EDS analysis of NaCl at 830°C.

During the investigation, condensed particles were observed ~2 thirds of the way up the cell, which appeared to have risen from molten NaCl. These condensed particles were taken to an SEM for particle size and EDS analysis (figure 4.36). The EDS analysis suggested the phases; Na_2O, NaCl, K_2O and CaO and/or their constituent ions (O^{2-} ions) were possibly present (experiment 42), in molten NaCl. The presence of Na_2O appeared in large quantities, possibly from the decomposition of Na_2CO_3, coupled with the high vapour pressure of NaCl and release of CO_2. The presence of potassium and calcium appeared in minute quantities, suggesting these were present as impurities. The particles were of various shapes (between 2-10 µm) suggesting the molten salt condensed at various cooling rates across the cell envelope (attributed to the temperature gradient across the cell). The EDS analysis also suggested there was no interaction of the Inconel^{TM} 600 cell envelope with the melt.

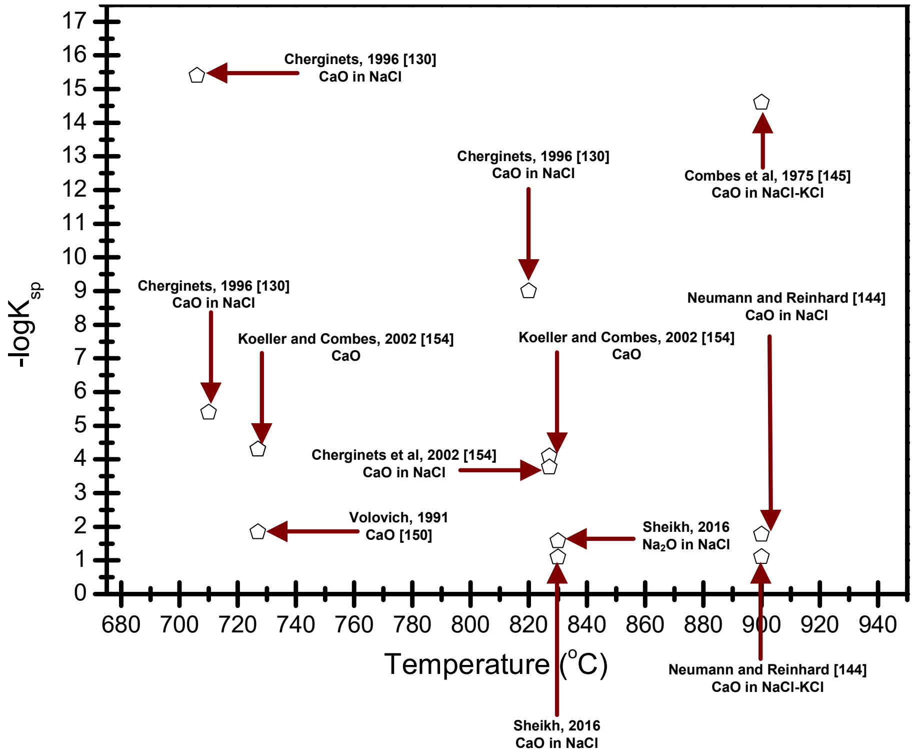

Figure 4.37: K_{sp} values for CaO and Na_2O as a function of temperature [130] [144-145] [150] [154]

The K_{sp} values for Na_2O (~-log 1.58) and CaO (~-log 1.1) in molten NaCl at 830ºC, obtained from potentiometry, were compared with previous reported K_{sp} values in literature (figure 4.37) [130] [144-145] [150] [154]. The K_{sp} value for CaO was found to be higher than those previously reported in literature (-log 3.77) at similar temperatures. This was probably due to the use of the potentiometric titration method over SAM, which is deemed to provide more accurate readings due to the detection of minute O^{2-} ion activities (in the 10^{-3} range). The K_{sp} value for Na_2O was the first reported value according to the author's knowledge, however cannot yet be published due to the significant evaporation of NaCl during the experiments. If these experiments were performed again, the author would insert pellets of Na_2CO_3 and $CaCO_3$ into the cell without opening, which would probably avoid the evaporation of molten NaCl.

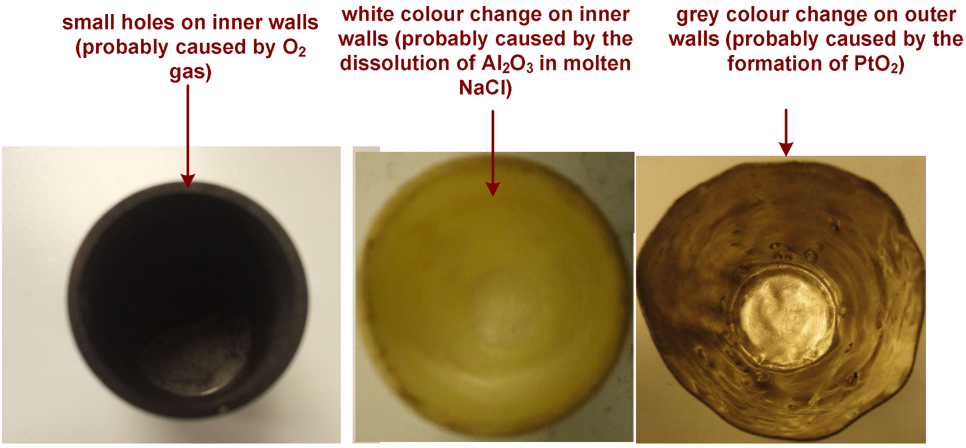

Figure 4.38: Image of the carbon (left), Al_2O_3 (middle) and platinum (right) crucibles after potentiometric measurements at 830 ℃.

Images of the platinum, carbon and Al_2O_3 crucibles were taken after being exposed to NaCl at 830°C from the potentiometric measurements (figure 4.38). Upon examination of the Al_2O_3 crucible, the inner surface walls were white instead of its original yellow colour. This was probably attributed to the dissolution of the Al_2O_3 crucible and the formation of CaO. The Al_2O_3 crucible was also slightly attached to molten NaCl, probably due to the same reason.

$$Al_2O_3(s) = 2Al^{3+} + 3O^{2-}$$ **Equation 4.20**

Equation 4.20 describes the dissolution of Al_2O_3 in molten NaCl, to produce Al^{3+} and O^{2-} ions. As this compound has a low reported solubility in molten chlorides, as described by Inman et al, 1978 thus not expected to cause significant changes to the potentiometric signal or K_{sp} values. The possibility of aluminate compounds, such as sodium aluminate ($NaAlO_2$) was also considered, as described by Kotz, 2009, there was no evidence on the Al_2O_3 crucible or potentiometric signal [266-269].

Upon examination of the glassy carbon crucible, small holes (~1 mm) were seen on the walls, which were not evident on the original design. This could have been attributed to the oxidation of the glassy carbon to CO_2 and CO, which has been reported to occur above ~600°C. As these experiments were done under an inert atmosphere, it can be concluded that this was caused by O_2 leaking into the cell. The oxidation of carbon can be described via the following reaction;

$$C + O_2\,(g) = CO_2(g)$$ **Equation 4.21**

Equation 4.21 describes the oxidation of carbon to CO_2, as described by Kotz et al, 2009 [268]. As the solubility of CO_2 is low in molten chlorides, it is expected this probably wouldn't cause significant changes to the potentiometric signal and K_{sp} values [261-262]. The contents of the crucible were easily removed, which suggested no other side reactions occurred between the crucible and molten salt.

Upon examination of the platinum crucible, the surface of the external walls was grey in colour, which was different from its original silver colour from the manufacturer. This was probably attributed to platinum reacting with O_2 in the atmosphere caused by O_2 leaking into the cell to form PtO_2 or Pt_3O_4 which has been reported to occur above ~600ºC. The oxidation of platinum can be described via the following reaction;

$$\mathrm{Pt} + \mathrm{O_2}\ (\mathrm{g}) = \mathrm{PtO_2} \qquad \textbf{Equation 4.22}$$

Equation 4.22 describes the oxidation of platinum to produce PtO_2, as described by Chaston, 1975 and Jehn, 1984 [234-235]. The contents within the crucible were slightly attached to the melt however easily removed by hand which suggested a slight interaction between the crucible and molten salt. This was probably attributed to the PtO_2 film dissolving in molten NaCl, however was just a speculation.

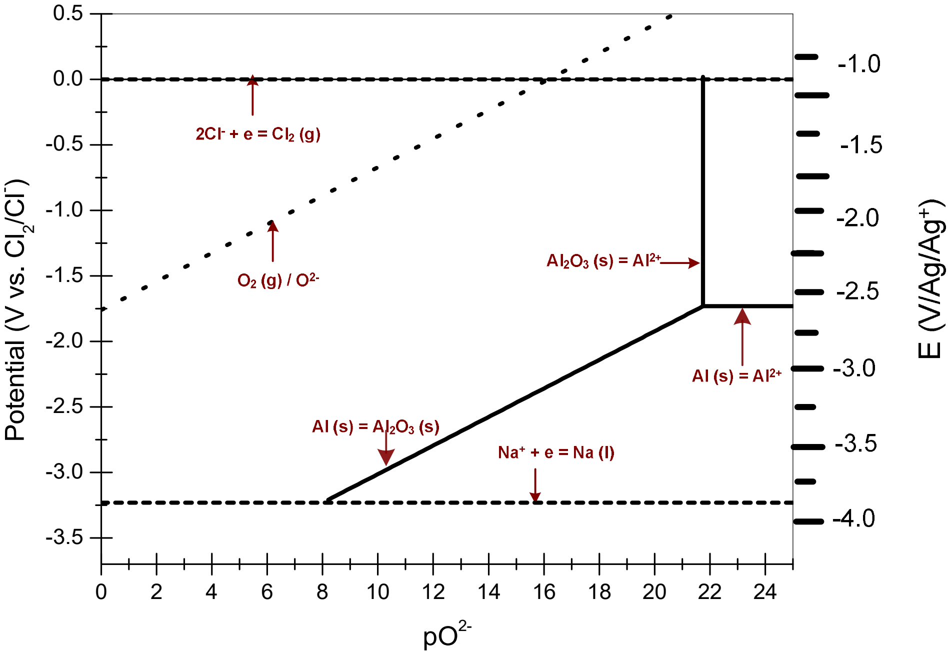

Figure 4.39: Predominance diagram for the Al-Na-O-Cl system, metal ion activity 1, at 830°C, 1 atm.

The dissolution of alumina in molten NaCl was depicted on a predominance diagram for the Al-Na-O-Cl system at 830°C (figure 4.39). This diagram was produced using the calculation method previously described by Littlewood and Trémillon, using thermodynamic data and the decomposition potential of molten NaCl from CV [189-191]. The ΔG_f for the O^{2-} ion was calculated using ΔG_f data of Na_2O (l), using the equations described previously. The formation of sodium aluminates were not considered in this calculation as described by Christie et al, 1978, as there was no visual evidence in our experiments [267]. The diagram illustrates Al_2O_3 has a low solubility in molten NaCl, governed by a low K_{sp} value for Al_2O_3 (at -log 21.2 at 830°C) (in mol fraction). [27] The diagram also illustrates that no further reactions take place in the molten salt at a high O^{2-} ion activity in the molten salt. The molten salt reactions depicted on this diagram can be found in table A6 (Appendix).

This section has shown that $CaCO_3$ and Na_2CO_3 dissolve in NaCl to produce CaO, Na_2O and CO_2, using the equations described earlier. The K_{sp} values for Na_2O and CaO were found to be -log 1.58 and -log 1.1 which indicates the MSS of cementitious compounds are suitable for industry, due to the reactants having a reasonably high solubility which is a basic requirement. These values were higher than values reported in literature for similar melts probably attributed to the evaporation of molten NaCl

---

[27] K_{sp} values calculated from thermodynamic data are in mol%

during the experiments and is therefore recommended to that the design of the cell requires improvement. The solubility of SiO_2 was low under these conditions, suggesting the limiting factor was probably the decomposition processes of $CaCO_3$ and Na_2CO_3 in molten NaCl. The Al_2O_3, glassy carbon crucible, platinum crucibles and SiO_2 calorimetric tube was found to interact with NaCl in different ways and affect the dissolution behaviour of the reactants but the Al_2O_3 crucible was found to be the most stable under our conditions.

4.6 Molten salt synthesis of cementitious compounds

The fifth stage of the investigation was to investigate the **MSS of cementitious compounds**; α-Na_2SiO_3, β-Na_4SiO_4, β-Ca_2SiO_4 and Ca_3SiO_5 from the reactants; SiO_2, $CaCO_3$, Na_2CO_3 at 830ºC and 1100ºC, using an XRD and SEM and to depict them on predominance diagrams. This will help determine which other compounds can be produced in this manner.

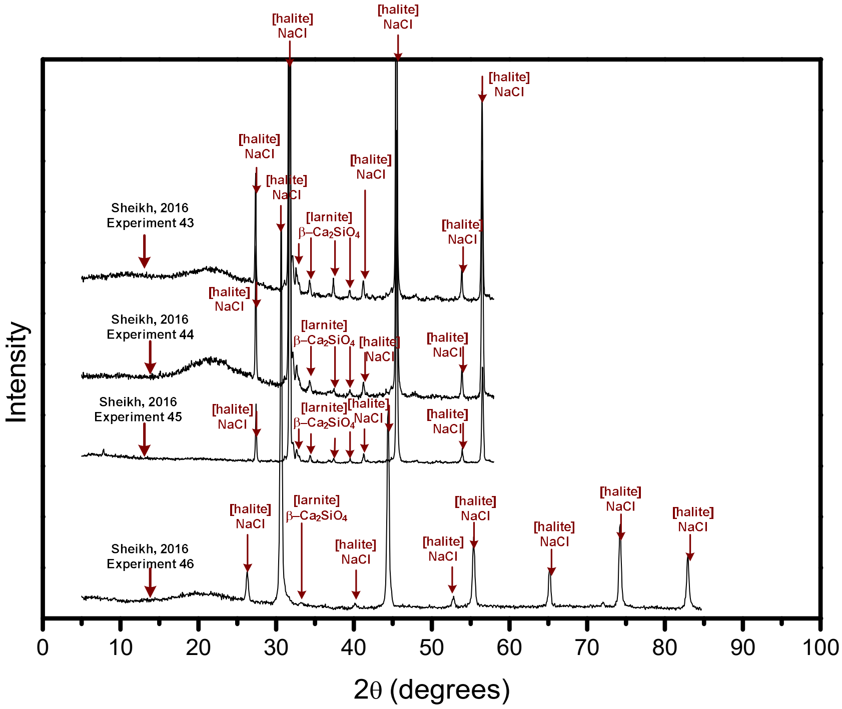

Figure 4.40: XRD pattern for the MSS of β-Ca_2SiO_4 and Ca_3SiO_5 from $CaCO_3$ and SiO_2 in NaCl at 830ºC for ~3 hours, typical operating condition; 2θ scan range of 5-110° with 150 seconds per step.

The MSS of β-Ca_2SiO_4 (experiment 43-46) and Ca_3SiO_5 (experiment 45), were investigated by filling an Al_2O_3 crucible with the reactants and heating to 830ºC, and 1100ºC for ~3 hours. A sample was then taken from the fused mixture, using the procedure described previously (Chapter 3) and taken to XRD equipment to identify the phases (figure 4.40).

The diagram shows the presence of metastable β-Ca_2SiO_4, which is in agreement with the feasibility studies described earlier. The Ca_3SiO_5 phase was not possible, indicating much larger temperatures were required (exceeding the limitations of the furnace). The CaO phase wasn't present, indicating a high extent of reaction. The absence of Al_2O_3, $SiCl_4$, $CaCl_2$ and Na_2O phases suggested there were no reactions with NaCl, Al_2O_3 crucible or O_2 from the atmosphere, which is agreement with previous experimental studies for the solubility of O_2 in molten chlorides [256].

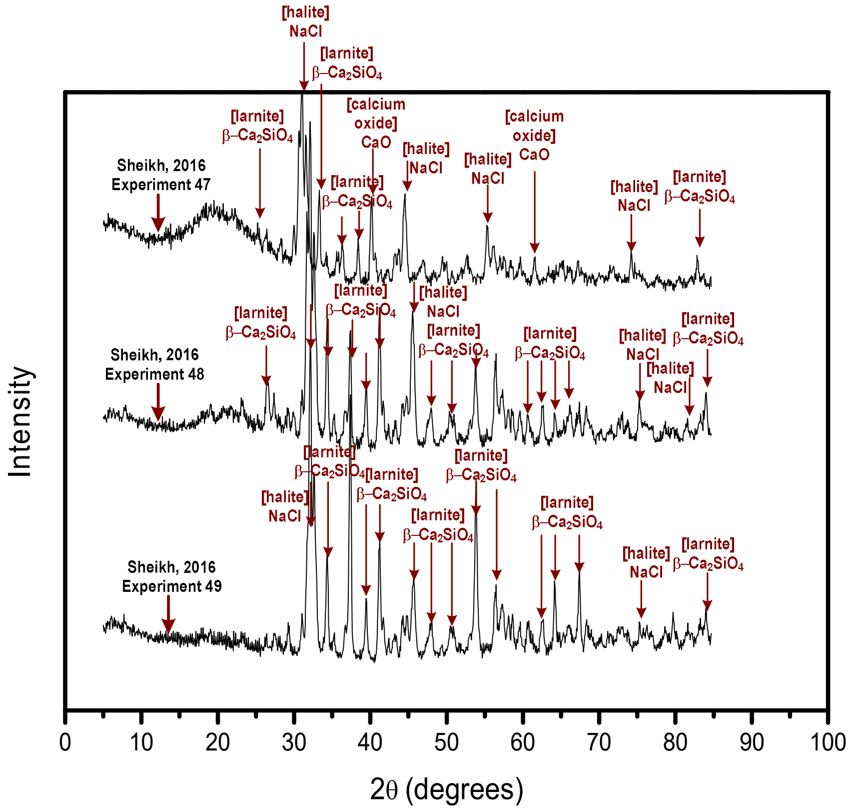

Figure 4.41: XRD pattern for the MSS of Ca_3SiO_5 and β-Ca_2SiO_4 (separation) for $CaCO_3$ and SiO_2 in NaCl at 830-1100ºC taken for ~3 hours typical operating condition; 2θ scan range of 5-110° with 150 seconds per step.

The separation of Ca_3SiO_5 (experiment 48) and β-Ca_2SiO_4 (experiment 46-47) were investigated for ~3 hours in an Al_2O_3 crucible at 1100ºC. After the experiments, each sample was taken from the fused mixture using the procedure outlined earlier and taken to XRD equipment to identify the phases (figure 4.41).

For experiment 48, the XRD pattern shows the presence of the β-Ca_2SiO_4 and CaO phases, and absence of the Ca_3SiO_5 phase, which confirms this isn't possible to achieve at 1100ºC, however in this case CaO was detected. This suggests the synthesis of Ca_3SiO_5 is a two step reaction, which is in agreement with the feasibility studies described earlier. For experiment 46-47, the XRD patterns shows only the presence of β-Ca_2SiO_4, confirming a high extent of reaction. The absence of Al_2O_3, $SiCl_4$, and $CaCl_2$ confirms limited reactions with NaCl or Al_2O_3 crucible and also suggests that CaO is not readily soluble in molten NaCl as the sample was removed from the top layer of the fused melt. No SiO_2 peaks were detected in experiment 48 which could be due to it being an amorphous solid.

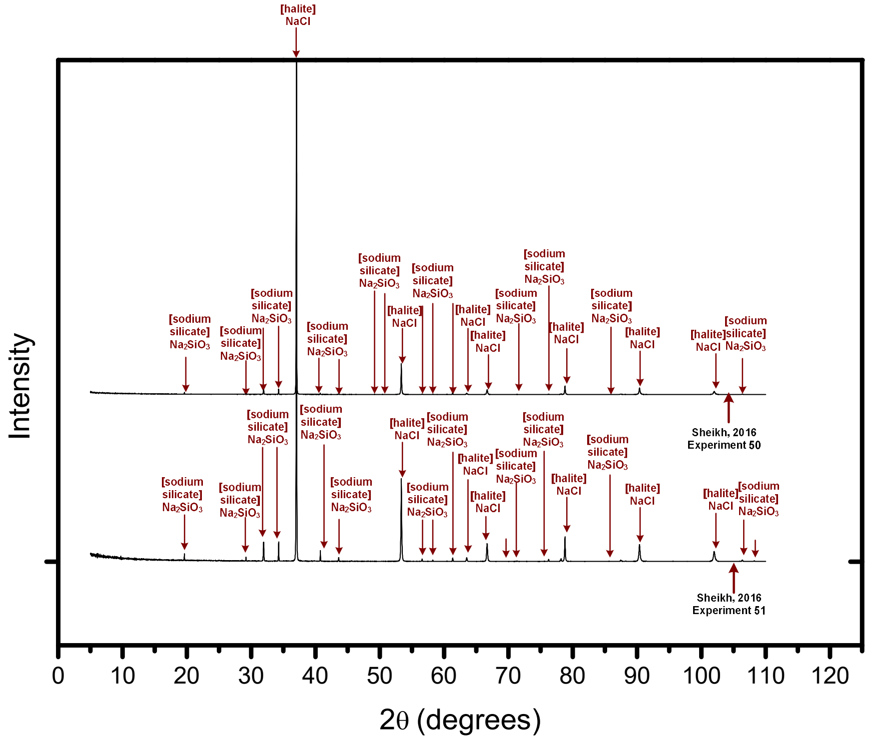

Figure 4.42: XRD pattern for the MSS of α-Na_2SiO_3 and β-Na_4SiO_4 from Na_2CO_3 and SiO_2 in NaCl for 3 hours, typical operating condition; 2θ scan range of 5-110° with 150 seconds per step, at 830℃.

The MSS for the α-Na_2SiO_3 (experiment 50) and β-Na_4SiO_4 (experiment 51) were investigated by reacting Na_2CO_3 and SiO_2 in molten NaCl, for ~3 hours in an Al_2O_3 crucible. After the experiments, each sample was taken from the fused mixture using the procedure described earlier and taken directly to XRD equipment to identify the phases (figure 4.42).

The XRD pattern shows the presence of α-Na_2SiO_3 in both cases, and absence of Na_2O indicating a high extent of reaction. The absence of the β-Na_4SiO_4 phase for experiment 51, indicates this reaction is not possible and possibly due to inadequate mixing, although the thermodynamic data supported the fact that it can be produced at 750ºC. The absence of Al_2O_3, $SiCl_4$ and Na_2O suggests there was a limited reaction with NaCl, Al_2O_3 crucible or O_2 from the atmosphere, which is agreement with previous experimental studies for the solubility of O_2 in molten chlorides [261-262].

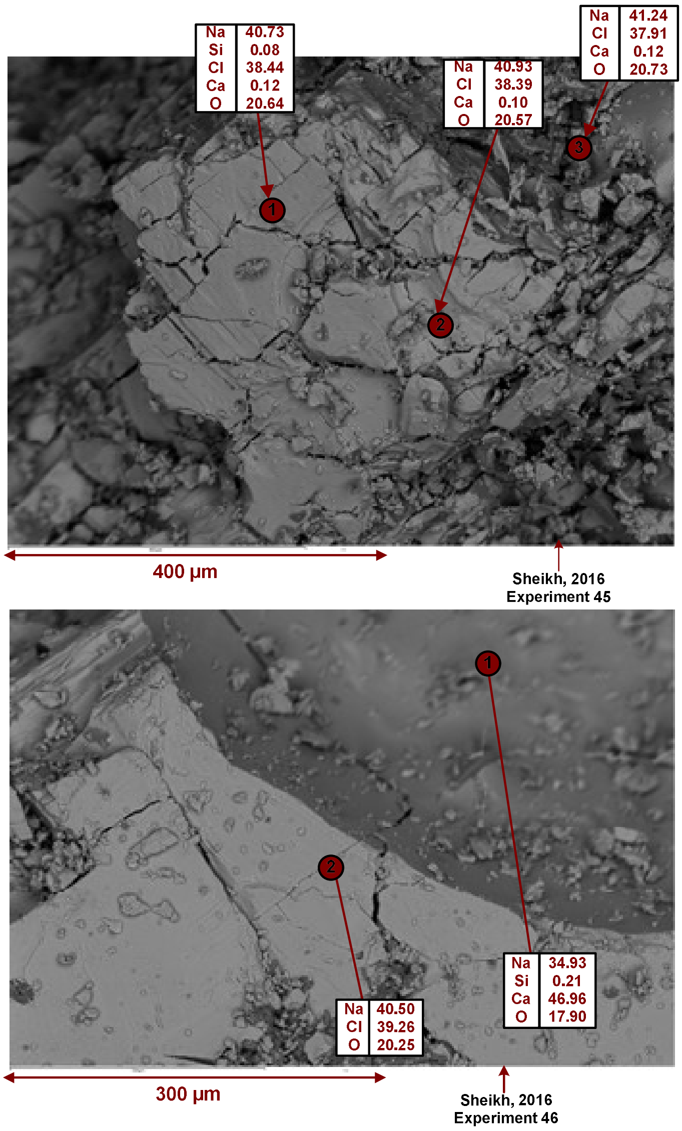

Sheikh, 2016
Experiment 45

Sheikh, 2016
Experiment 46

Figure 4.43: SEM image and EDS analysis of the MSS of Ca_3SiO_3 (top) and β-Ca_2SiO_4 (bottom) from $CaCO_3$ and SiO_2 in NaCl at 830°C for ~3 hours.

The elements and particle sizes produced during the MSS of β-Ca_2SiO_4 and Ca_3SiO_5 in NaCl (experiments 45-46), were investigated by removing samples from the Al_2O_3 crucible using the procedure described earlier and taking them to an SEM for particle size and EDS (figure 4.43).

In both cases, the EDS analysis suggested the phases β-Ca_2SiO_4, CaO, NaCl and/or their constituent ions (O^{2-} ions) were possibly present. The CaO phase was probably produced during the decomposition of $CaCO_3$ in the molten salt. No additional (hydrolysis) reactions occurred which indicates humidity levels in the laboratory were reasonably low. The particle sizes for β-Ca_2SiO_4 was reasonably low (~400 μm), which was probably due to it having a low solubility in molten NaCl.

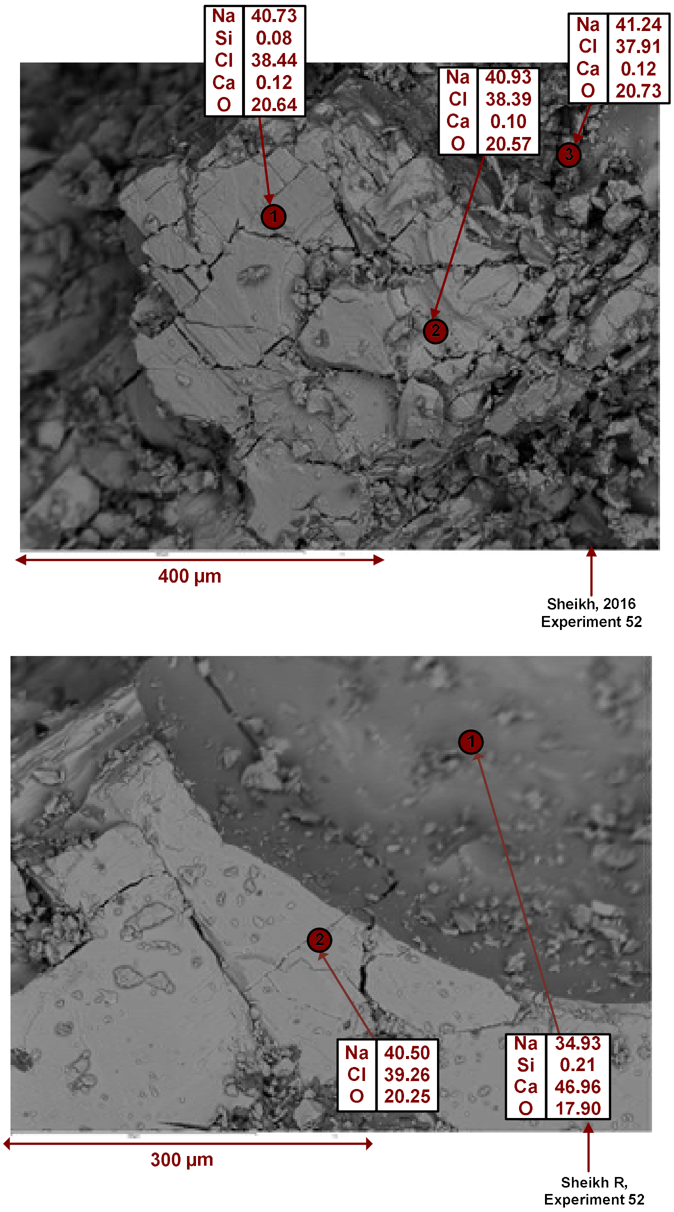

Figure 4.44: SEM image and EDS analysis for the MSS of α-Na_2SiO_3 *(top) and* β-Ca_2SiO_4 *(bottom) from* Na_2CO_3 *and* SiO_2 *in NaCl in NaCl for 3 hours at 830℃.*

The EDS analysis and particle sizes were repeated for the MSS of α-Na_2SiO_3 and β-Na_4SiO_4 experiments (experiment 52-53) and different samples taken to an SEM for particle size and EDS analysis (figure 4.44).

The EDS analysis suggested the phases; α-Na_2SiO_3, Na_2O, NaCl, β-Ca_4SiO_4, CaO and/or their constituent ions (O^{2-} ions) were possibly present demonstrating good reproducibility of the data. The presence of Na_2O and CaO can be attributed to the decomposition and dissolution of Na_2CO_3 and $CaCO_3$ in the molten salt, although these may not have been present in the molten salt. The image shows the particle sizes were ~400 µm and ~300 µm for α-Na_2SiO_3 and β-Ca_2SiO_4 respectively, indicating a high solubility in the molten salt. It is also suggests a separation stage is required to separate the products from molten NaCl.

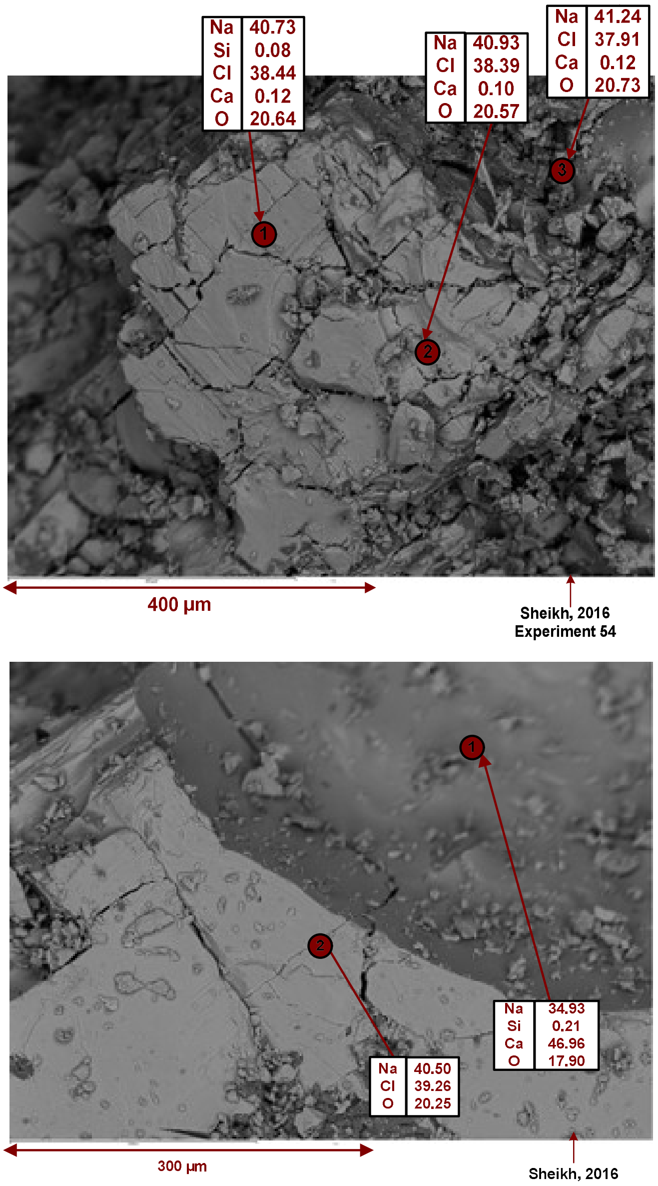

Sheikh, 2016
Experiment 54

Sheikh, 2016
Experiment 55

Figure 4.45: SEM image and EDS analysis of the separation of β-Ca_2SiO_4 from NaCl, reacted for 3 hours (top) and separated for 6 hours (bottom) at 1000°C.

The β-Ca_2SiO_4 compound was separated from molten NaCl by removing a sample from the Al_2O_3 crucible (experiment 54) and placing in an MgO crucible for ~6 hours at 1000ºC (experiment 55). These samples were then removed and taken to an SEM for particle size and EDS analysis (figure 4.45).

The EDS analysis confirms that it is possible to separate this product from molten NaCl, due to the removal of large quantities of chlorine and sodium from the final product. This can be attributed to different densities of NaCl and β-Ca_2SiO_4. There was also some evidence of aluminium and magnesium not previously seen on the XRD patterns, indicating some dissolution of the Al_2O_3 crucible and MgO cupel. The differences in the cupel weight loss were ~5 wt%, indicating most NaCl was absorbed and some lost by evaporation. The final particle size for β-Ca_2SiO_4 was ~4 mm.

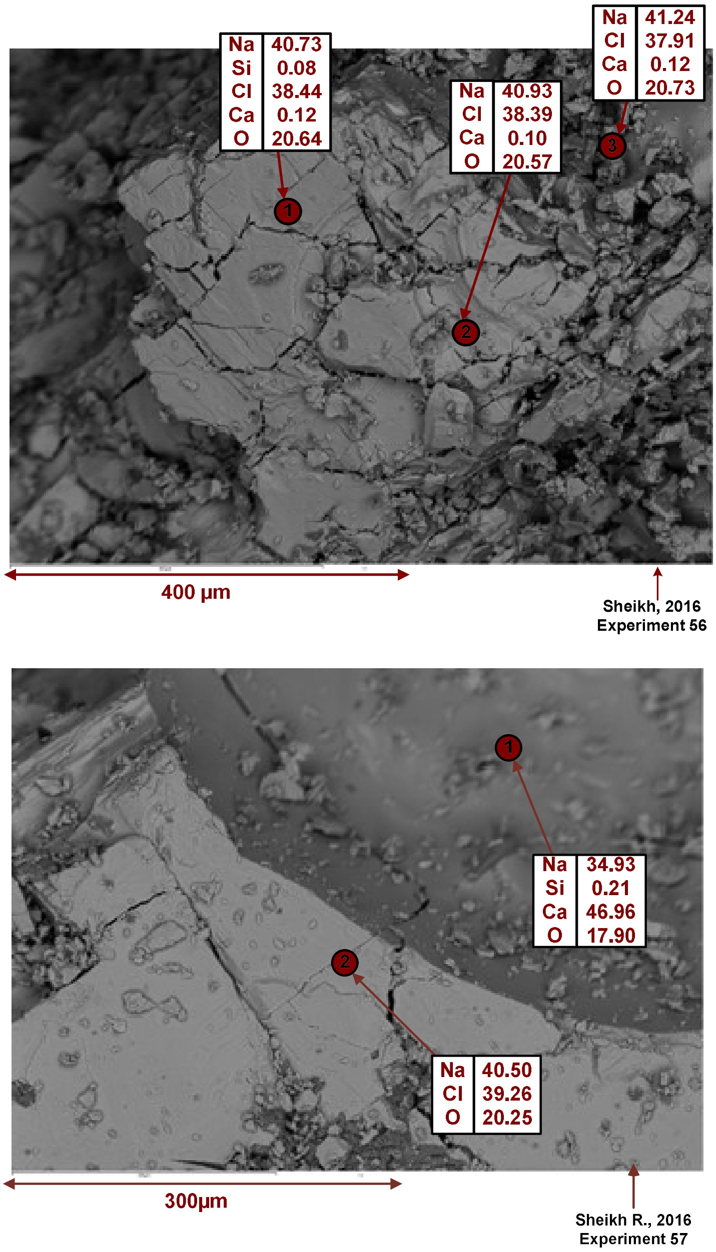

Sheikh, 2016
Experiment 56

Sheikh R., 2016
Experiment 57

Figure 4.46: SEM image and EDS analysis of the separation of α-Na_2SiO_3 from NaCl, reacted for 3 hours (top) and separated for 6 hours (bottom) at 1000°C.

The separation of α-Na_2SiO_3 from molten NaCl was investigated by removing a sample from the Al_2O_3 crucible (experiment 56) and placing in an MgO crucible for ~6 hours at 1000°C (experiment 57). These samples were then removed and taken to an SEM for particle size and EDS analysis (figure 4.46).

The EDS analysis confirms that it is possible to separate this product from molten NaCl, due to the removal of large quantities of chlorine and sodium from the final product. This can be attributed to different densities of NaCl and α-Na_2SiO_3. There was no evidence of aluminium and magnesium in the final product although this could be due the in homogeneity of the molten salt. The image shows agglomerated particles of ~between 300-400 μm. The differences in the MgO cupel weight loss were ~5 wt%, indicating most NaCl was absorbed and some lost by evaporation. The dissolution (and decomposition) of carbonates have been previously described by Cherginets, 2005 and Combes et al, 1977 [130] [263]. Using the same analogy, the MSS of β-Ca_2SiO_4 and α-Na_2SiO_3 in molten NaCl can be written in the following form;

$$Si^{4+} + 2Ca^{+} + 4O^{2-} = Ca_2SiO_4\ (s)$$ **Equation 4.23**

$$Si^{4+} + 2Na^{+} + 3O^{2-} = Na_2SiO_3\ (s)$$ **Equation 4.24**

Equation 4.23-24 describes the MSS of β-Ca_2SiO_4 (s) and α-Na_2SiO_3 (s) in molten NaCl from their constituent ions; Na^+, Si^{4+}, Ca^{2+} and O^{2-}. These arise from the dissolution (and decomposition) of $CaCO_3$ (s) and Na_2CO_3 (s) in molten NaCl. The solubility of β-Ca_2SiO_4 (s) and α-Na_2SiO_3 (s) were assumed to be low in our case, therefore only the solid phases were considered. These reactions can also be summarised in the following form;

$$SiO_2\ (s) + 2CaO\ (l) = Ca_2SiO_4\ (s)$$ **Equation 4.25**

$$SiO_2\ (s) + 2Na_2O\ (l) = Na_2SiO_3\ (s)$$ **Equation 4.26**

Equation 4.25-4.26 describes the MSS of β-Ca_2SiO_4 (s) and α-Na_2SiO_3 (s) in molten NaCl from the reactants; SiO_2 (s), CaO (l) and Na_2O (l). The solubility of SiO_2 as assumed to be low in our case, therefore only the solid phase was considered.

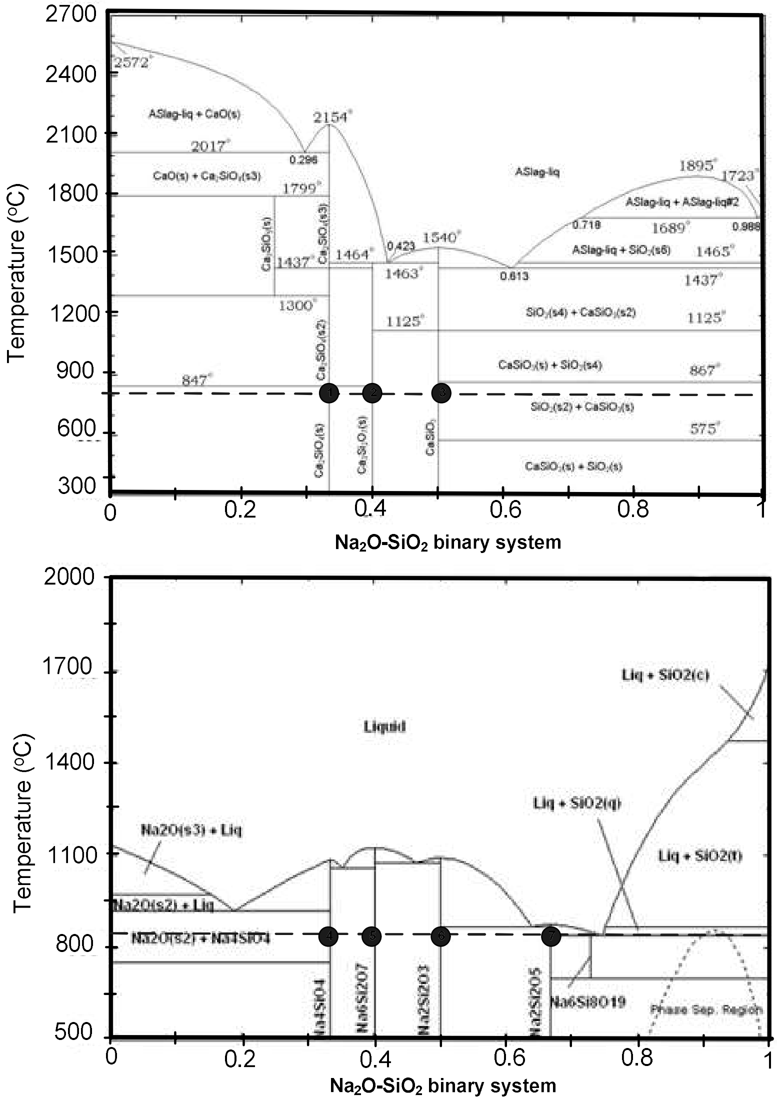

Figure 4.47: Phase diagrams of the Na_2O-SiO_2 (bottom) and CaO-SiO_2 (top) binary systems [242] [266].

The final stage of the investigation was to produce predominance diagrams for the Na-Cl-O and Ca-Si-O systems at 830°C, to illustrate the compounds in a summarising form using MSS. The compounds that can be produced in the Na_2O-SiO_2 and CaO-SiO_2 binary systems (figure 4.47) [14-15] [245-249].

These diagrams suggest that β-Ca_2SiO_4, tricalcium disilicate ($Ca_3Si_2O_7$), $CaSiO_3$, β-Na_4SiO_4, hexasodium disilicate ($Na_6Si_2O_7$), Na_2SiO_3, and disodium disilicate ($Na_2Si_2O_5$) can be produced at 830ºC. [28]

---

[28] Compounds 1-7 on figure 4.47 respectively.

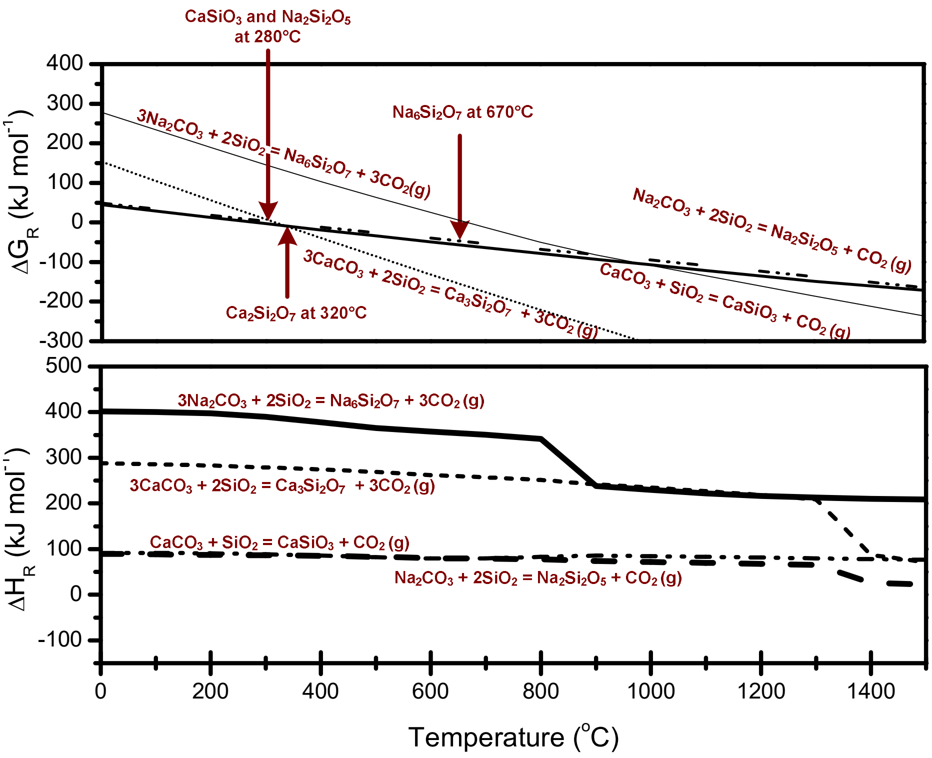

Figure 4.48: ΔH_R (bottom) and ΔG_R (top) data for the synthesis of $CaSiO_3$, $Ca_3Si_2O_7$, $Na_6Si_2O_7$ and $Na_2Si_2O_5$ as a function of temperature, 1 atm (HSC Chemistry 6.1).

The reaction temperatures required producing the cementitious compounds; $CaSiO_3$, $Ca_3Si_2O_7$, $Na_2Si_2O_5$, and $Na_6Si_2O_7$, were also found using the reaction equation module in HSC-Chemistry 6.1. This module plotted the ΔG_R and ΔH_R data as a function of temperature respectively. As the reaction temperatures for the synthesis of β-Ca_2SiO_4, α-Na_2SiO_3 and β-Na_4SiO_4 were obtained previously and therefore not required (figure 4.48).

The ΔH_R data shows these reactions are highly exothermic, producing between ~100-400 kJ mol^{-1} of energy over this temperature range. The ΔG_R data shows these reactions occur at ~280ºC, ~280ºC, ~320ºC and ~670ºC respectively (shown by negative ΔG_R values above these temperatures. This agrees with the phase diagrams provided by other authors that these compounds can be synthesised at 830ºC [14-15] [245-252].

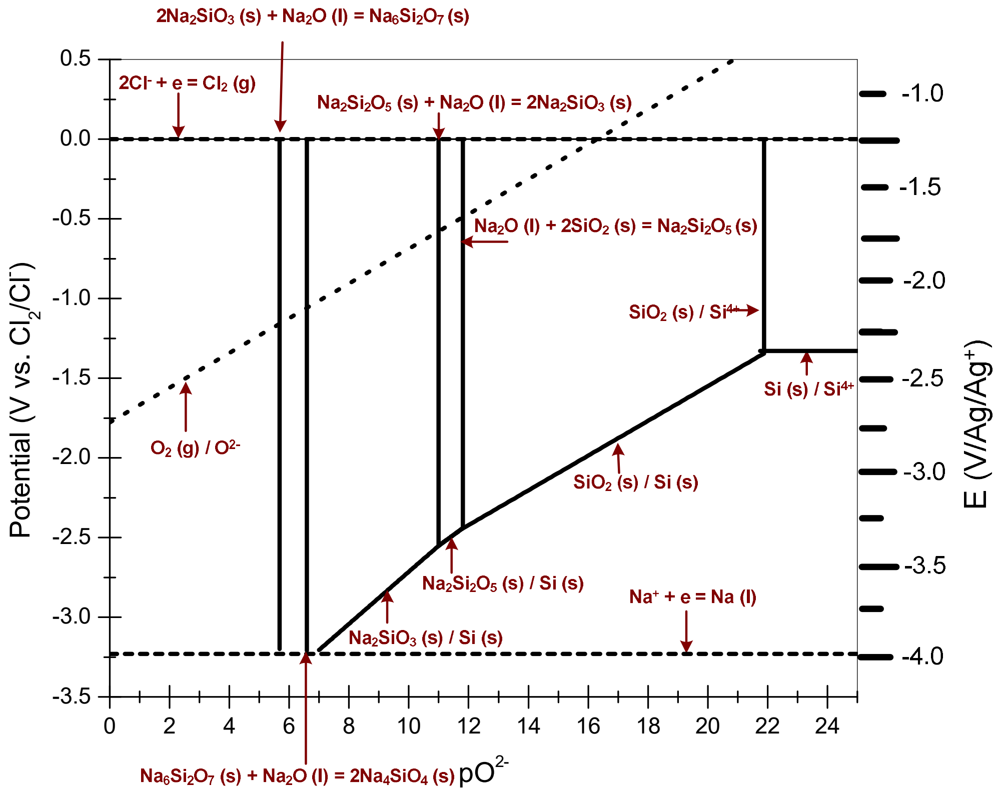

Figure 4.49: Predominance diagram for the Na-Si-O-Cl system, 1 atm.

The MSS reactions of $Na_2Si_2O_5$, α-Na_2SiO_3, β-Na_4SiO_4 and $Na_6Si_2O_7$ were depicted on a predominance diagram for the Na-Si-O-Cl system at the reaction conditions (830ºC, 1 atm) (figure 4.49). This diagram utilizes the calculation method described previously by Littlewood and Trémillon, using thermodynamic data and the decomposition potential of NaCl at 830ºC from CV [189-191].

The diagram suggests that SiO_2 has a low solubility in molten NaCl, governed by a low K_{sp} value, at -log 22 (in mole fraction) under the assumption that SiO_2 dissociates completely to Si^{4+} and O^{2-} ions. It also suggests the stability domains for α-$Na_2Si_2O_5$, Na_2SiO_3, β-Na_4SiO_4, and $Na_6Si_2O_7$ initiate at O^{2-} ion activities of -log 11.8, -log 10.9, -log 6.59, and -log 5.68 (in mole fraction). Therefore if one was to produce these compounds, one would have to mix these concentrations. The molten salt reactions depicted on this diagram can be found in table A7 (Appendix).

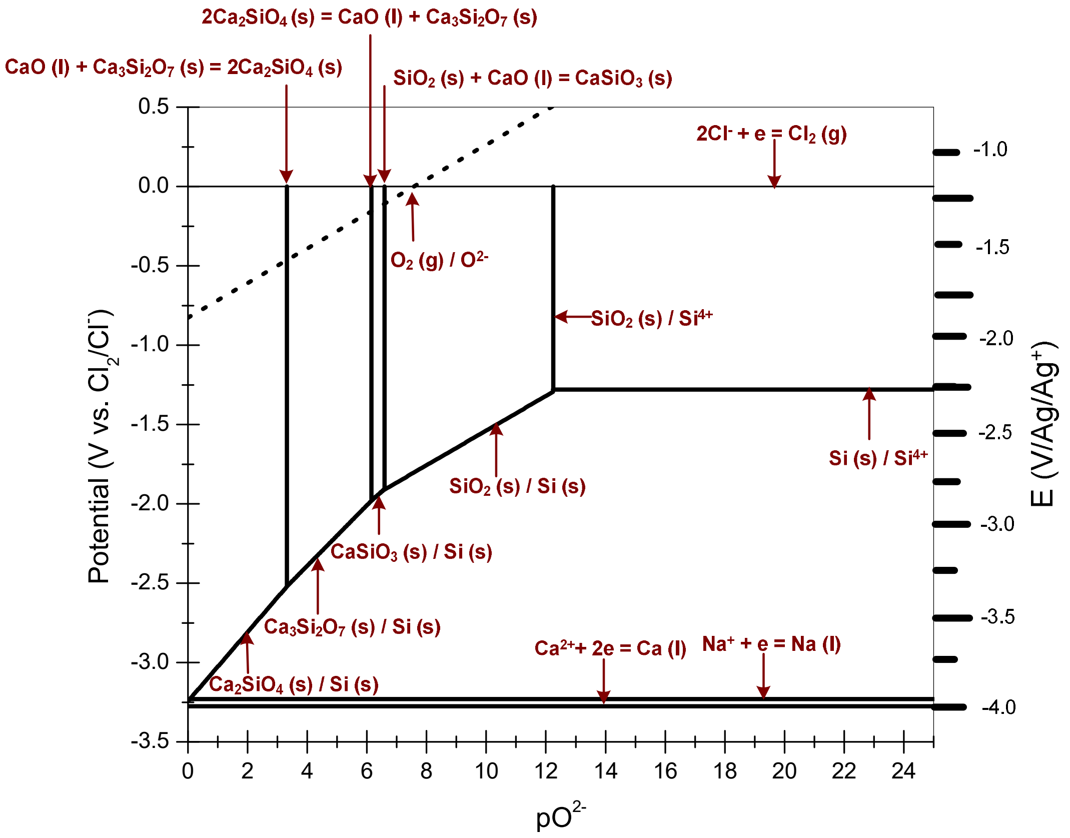

Figure 4.50: Predominance diagram for the Ca-Na-Si-O-Cl system at the reaction conditions, 1 atm.

The MSS reactions for Ca_3SiO_5, $Ca_3Si_2O_7$, $CaSiO_3$ and β-Ca_2SiO_4 were depicted on a predominance diagram for the Ca-Na-Si-O-Cl system, at the reaction conditions (830ºC, 1 atm). This diagram utilizes the calculation method described previously by Littlewood and Trémillon, using thermodynamic data and the decomposition potential of NaCl from CV [181-191] (figure 4.50). For this case, the ΔG_f for the O^{2-} ion was calculated using CaO (l) in molten NaCl via the following equations.

$$\mathrm{Ca^{2+} + 2e = Ca\ (s)}$$ **Equation 4.27** [29]

$$\mathrm{Ca(s) + \tfrac{1}{2}O_2(g) = Ca^{2+} + O^{2-}}$$ **Equation 4.28** [30]

$$\mathrm{2e + \tfrac{1}{2}O_2(g) = O^{2-}}$$ **Equation 4.29** [31]

Equations 4.27-4.29 describe the equations used to calculate the ΔG_f of the O^{2-} ion The compounds from the Na_2O-SiO_2 system were not shown under the assumption

---

[29] $\Delta G^{\circ}_{CaCl_2 \text{ at } 830ºC}$ = 631.9 kJ mol^{-1} [18-19]

[30] $\Delta G_{f\ CaO\ (l) \text{ at } 830ºC}$ = -470.23 kJ mol^{-1} [18-19]

[31] $\Delta G_{f\ O^{2-} \text{ at } 830ºC}$ = -159.5 kJ mol^{-1}

that the attraction of the Ca^{2+} ion is greater than the Na^{+} ion. The diagram suggests SiO_2 has a low solubility in the molten salt governed by a low K_{sp} value, at -log 12.2 (in mole fraction) but higher than the Na-Si-O-Cl system. It also suggests the stability domains for $CaSiO_3$, $Ca_3Si_2O_7$, β-Ca_2SiO_4 initiate at O^{2-} ion activities of -log 6.58, -log 6.16 and -log 3.32 (in mole fraction). Therefore if one was to produce these compounds, one would have to mix these concentrations. The molten salt reactions depicted on this diagram can be found in table A8 (Appendix).

This section confirmed it is possible to synthesise α-Na_2SiO_3 and β-Ca_2SiO_4 in NaCl at 830ºC and 1100ºC. α-Na_2SiO_3 was produced at lower reaction temperatures than some current industrial process and β-Ca_2SiO_4 was produced at lower temperatures than prevoious studies in literature and without the need for quenching or stabilization with foreign ions [49] [14-15]. It was not possible to produce β-Na_4SiO_4 which may have been due to inadequate mixing of the reactants. It was also not possible to produce Ca_3SiO_5 probably due to insufficient reaction temperatures at is the author's suggestion that at least 1250ºC is required to achieve this. [14-15]. No peaks for additional compounds (such as $CaCl_2$ or Al_2O_3) were observed on the XRD patterns which suggested that no significant dissolution of the Al_2O_3 crucible or reaction of the molten salt with the reactants. Upon separation however there was some evidence of aluminium and magnesium, which suggested some interaction of the Al_2O_3 crucible and MgO cupel. The complexity of these molten salt systems were described on predominance diagrams at 830ºC and 1 atm and suggested that $Ca_3Si_2O_7$, $CaSiO_3$, β-Na_4SiO_4, $Na_6Si_2O_7$ and $Na_2Si_2O_5$ could be produced using a similar methodology at 830°C.

Chapter 5

Conclusions & suggestions for future work

5.1 Introduction

This chapter reports the conclusions to the **feasibility of the synthesis of cementitious compounds, structures and purities of the reactants in the molten salt**, **behaviour of the molten salt at the reaction conditions, dissolution of the reactants in the molten salt** and **MSS of cementitious compounds.** It also describes future work for other researchers in this field.

5.2 Feasibility of the synthesis of cementitious compounds

The first stage of the investigation determined the **feasibility of the synthesis reactions of the cementitious compounds**; α-Na_2SiO_3, β-Ca_2SiO_4, Ca_3SiO_5 and β-Ca_2SiO_4, using thermodynamic data and chemical equilibrium diagrams. This was used to suggest the reaction temperatures required to produce cementitious compounds and select a suitable salt for MSS.

The ΔG_R data and chemical equilibrium module suggested it maybe possible to synthesise these compounds between 200-1250ºC. On this basis, NaCl was selected as a suitable molten salt solvent due to its stability range between ~801-1413ºC, which is in the same range as the reactions investigated in this thesis [56]. The viscosity of NaCl (1.03 Pa.s at 810ºC) is also in the same magnitude of H_2O (0.874 Pa.s at 25ºC), which suggests it can be separated from an insoluble product without requiring additional equipment and the vapour pressure of NaCl (0.302 mmHg $ºC^{-1}$ at 801ºC) was lower than H_2O (26.5 mmHg $ºC^{-1}$ at 25ºC) suggesting minimal losses of the reactant at 830°C [56].

This section could be improved by investigating the feasibility of other cementitious compounds; $Ca_2(Al, Fe)_2O_5$, and/or $Ca_2(Al, Fe)_2O_{12}$ and $Ca_3Al_2O_6$, which are found in cement ([14-15]. If the ΔG_R data and chemical equilibrium module suggests these can be formed, this could lead to obtaining the complete cement product in a molten salt solvent.

5.3 Structures and purities of the reactants in the molten salt

The second stage of the investigation determined the **structures and purities of the reactants**; Na_2CO_3, $CaCO_3$, SiO_2 and NaCl, using XRD and CV techniques. This was used to suggest the purity and phase transitions of the reactants at the reaction conditions, useful for analyzing XRD and SEM patterns at a later stage.

The Na_2CO_3, $CaCO_3$, SiO_2 and NaCl, suggested that all reactants were pure with no significant interaction with air or moisture at room temperature and pressure. The ΔC_p data suggested SiO_2 would be in its β-quartz phase, NaCl in its halite phase, $CaCO_3$ in its calcite phase and Na_2CO_3 in its α-Na_2CO_3 phase at 830ºC, and 1100ºC, which was considered upon examining the XRD patterns [18-19]. The purity of NaCl was found to be high at the reaction conditions, due to no significant peaks for electrochemical reactions on the CV curve. In addition, the ΔV_d for NaCl was found to be ~3.1 V, which was in agreement with values calculated using ΔG^o for NaCl, at 3.2 V, the difference of 0.1 V being attributed to a possible temperature gradient across the cell.

This section can be improved by heating the compounds to 830ºC and 1100ºC and investigating the phases formed using XRD. This can be performed in conjunction with quenching and stabilizing with foreign ions, as often transitional compounds revert back to their most stable phases at lower temperatures. However this information cannot truly represent an accurate scenario of the phases formed at the reaction temperatures in a molten salt solvent, therefore experiments should also accompany this.

5.4 Behaviour of the molten salt at the reaction conditions

The third stage of the investigation determined the **behaviour of the molten salt at the reaction conditions**, using a DSC technique and chemical equilibrium diagrams.[32] This was useful for describing the effects of vapour pressure upon the salt, and reaction conditions required for the experiments.

The chemical equilibrium diagram suggested that NaCl evaporates at 830°C due to its high vapour pressure. This high vapour pressure coupled with a temperature gradient across the reaction vessel would probably assist in the evaporation of salt. It was therefore recommended that all reaction vessels containing the molten salt have smaller dimensions to avoid the effects of temperature gradients and sealed to contain the molten salt. However there is some evidence to suggest that pressurized vessels can cause the partial pressure of internal gases produced to increase, however this probably would have a small impact upon the final conclusions drawn from this thesis.

This section can be improved by investigating the effect of various atmospheres (such as moisture, O_2 and N_2) upon the behaviour of molten NaCl and the effect of various drying procedures for NaCl, using a DSC. This could help the author understand the effects and mechanisms of these variables and minimize the quantity of salt evaporated.

5.5 Dissolution of the reactants in the molten salt

The fourth stage of the investigation determined the **dissolution of the reactants**; $CaCO_3$, Na_2CO_3 and SiO_2 in molten NaCl, using potentiometry, calorimetry, XRD and SEM, which subsequently led to obtaining phase diagrams, K_{sp} and ΔH_{mix} values, to determine whether MSS of cementitious compounds are possible in industry.

---

[32] The salt was selected to be NaCl

5.5.1 Phases of the reactants in the molten salt

This section determined the **dissolution reactions of the reactants**; Na_2CO_3, $CaCO_3$ and SiO_2 in molten NaCl at the reaction conditions (830ºC, 1 atm), using XRD, SEM techniques.

The XRD data suggested $CaCO_3$ and Na_2CO_3 dissolved and decomposed in NaCl at 830ºC, to produce CaO, Na_2O, CO_3^{2-}, O^{2-} ions and CO_2. The decomposition temperatures for $CaCO_3$ and Na_2CO_3 were similar to those reported by Motzfeldt, 1955, Hills, 1968 and Kim and Lee, 2001 for solid-state reactions (at 840ºC and 851ºC respectively) [258-260]. The decomposition temperature was also similar to that reported by the chemical equilibrium module (860ºC for $CaCO_3$) and thermodynamic data (825ºC for $CaCO_3$) [18-19]. The author found the decomposition of $CaCO_3$ occurred to completion, probably due to the presence of an exhaust above our muffle furnace. This suggests the decomposition rate is dependent upon the partial pressure of CO_2 in the reaction vessel. The reaction kinetics for the decomposition of Na_2CO_3 was slower than $CaCO_3$. This was probably due to a low extent of reaction for Na_2CO_3 (at 0.41 at 830^oC from HSC-Chemistry 6.1) [18-19]. This information was also confirmed by Motzfield, 1955 and Kim and Lee, 2001 [18-19] [258] [260]. The SEM data suggested SiO_2 dissolved in NaCl at 830ºC, to produce the constituent species; O^{2-} and Si^{4+} ions with an extremely low solubility. This was also evident by the appearance of solid particles on the surface of molten NaCl. This information concludes that all the reactants dissolve in molten NaCl, according to equations 4.7-4.19 and the Al_2O_3 crucible used had a limited interaction in molten NaCl. This was due to no significant Al^{3+} peaks were detected on the XRD pattern and was not expected to cause significant changes to the final phases formed.

This section can be improved by identifying the phases produced at the reaction conditions in-situ, using other analytical techniques such as neutron diffraction or XRD. These have proven useful for the phase identification in molten salts in literature and could suggest the stability domains where these reactions occur [271]. These stability domains could also be investigated by using various quenching times, reaction times and temperatures, which would probably affect the structure of the final phases formed [18-19] [112].

5.5.2 Phase diagrams of the reactants in the molten salt

This section confirmed the **dissolution reactions of the reactant;** Na_2CO_3 by obtaining the phase diagram of the Na_2CO_3-NaCl binary system, using a DSC technique. The phase diagram for the SiO_2-NaCl and $CaCO_3$-NaCl binary systems were unable to be investigated via this technique, due to their low solubilities, as described by Yasuda, 2007 [208].

The DSC data suggested the eutectic point for molten NaCl-Na_2CO_3 was 638ºC, 47 mol% Na_2CO_3, which was different to values reported by Iwasawa and Maeda, 2000, Yaokawa et al, 2007 and Lindberg et al, 2006 at 643ºC, 43 mol% Na_2CO_3. This suggests that Na_2CO_3 decomposed above 801ºC, probably due to the flow of argon above NaCl, causing the partial pressure of CO_2 to decrease. This observation also agrees with studies previously performed by Hills, 1968 and Kim and Lee, 2001 [253] [255]. A slight expansion of the Inconel^{TM} 600 crucible was also observed, which was attributed to CO_2 being released from the decomposition reaction and modifying the shape of the crucible. This information concludes that Na_2CO_3 and $CaCO_3$ decomposes in NaCl at 830ºC, and SiO_2 only dissolves according to equations 4.7-4.18

This section can be improved by obtaining the phase diagram for molten NaCl-Na_2CO_3, under CO_2. These should inhibit the decomposition of Na_2CO_3 and allow the true value of the eutectic point to be obtained. This can be compared against other eutectic points to confirm whether the reactant was truly decomposing or due to the affects of other variables. One could also determine the phase diagrams for molten $CaCO_3$-NaCl and SiO_2-NaCl using potentiometry, or software packages such as FactSage (Thermfact/CRCT and GTT-Technologies) or MTDATA (National Physical Laboratory (NPL)), which use the CALPHAD (CALculation of PHAse Diagrams) method, to provide further evidence of their dissolution in molten NaCl [210] [270-271].

5.5.3 Heats of mixing of the reactants in the molten salt

This section confirmed the **dissolution reactions of the reactant;** Na_2CO_3 by obtaining the ΔH_{mix} values the Na_2CO_3-NaCl binary system, using a drop calorimetery technique. The ΔH_{mix} values for the SiO_2-NaCl and $CaCO_3$-NaCl binary systems were unable to be investigated via this technique, due to their low solubilities, as described by Yasuda, 2007 and Cherginets, 2005 [130] [208].

The ΔH_{mix} values illustrated a positive (endothermic) contribution (~2 kJ mol^{-1}), which suggests that Na_2CO_3 decomposes at 830°C to produce CO_2 and Na_2O (equations 4.7-4.12). The average ΔH_f value for pellets of Na_2CO_3 was ~90.2 kJ mol^{-1} over three pellet drops, which was ~30% lower than its theoretical value. The average ΔH_f value for crystals of Na_2CO_3 was ~129 kJ mol^{-1} over three pellet drops, which was 1.57% higher than its theoretical value. In both cases, these values were fairly consistent over the experiments. However the ΔH_f value for pellets of Na_2CO_3 beyond the third drop was ~46.8% lower than expected and the ΔH_f value for crystals of Na_2CO_3 beyond the fourth drop was ~31% lower than expected. This ΔH_f data suggests that Na_2CO_3 decomposes probably and aided by the decrease in partial pressure of CO_2 from the flow of argon gas. The SiO_2 calorimetric tubes demonstrated significant corrosion in the drop calorimeter, probably due to the formation of sodium silicates, such as α-Na_2SiO_3. However it was unlikely this affected the ΔH_{mix} values as their interaction were mitigated from the data by subtracting the base-line upon analysis.

This section can be improved by obtaining ΔH_{mix} values for molten SiO_2-NaCl and $CaCO_3$-NaCl, using K_{sp} values in literature as a function of temperature. These values can be implemented into the Vant Hoff's equation as described by Flengas and Rideal, 1956, to obtain the ΔH_{mix} values for the liquid phase of such systems [241]. The ΔH_{mix} values can also be obtained from phase diagrams using various thermodynamic software packages such as MTDATA or FactSage, as described earlier [210] [270]. These values would provide further evidence of the dissolution of the reactants in molten NaCl. However as K_{sp} values are also a function of the sizes of the pellets and crystals, these would have to also be taken into account, as reported by Cherginets 2005 [130]. If these experiments were performed again, the SiO_2 calorimetric tubes would be replaced with Inconel^{TM} 600, which has a proven stability in molten chlorides.

5.5.4 Solubility products of the reactants in the molten salt

This section determined the **dissolution reactions of the reactants**; Na_2CO_3 and $CaCO_3$ in molten NaCl, using a potentiometric technique, which subsequently lead to obtaining the K_{sp} values for Na_2O and CaO in molten NaCl. The K_{sp} value for SiO_2 in molten NaCl was unable to be investigated via this technique, due to its low solubility, as described by Yasuda, 2007 [208].

The potentiometry technique required the construction of an electrochemical cell that was capable of producing a stable and reproducible signal at 830°C. However the construction of the cell required several modifications to its design to provide a stable and reproducible signal. These modifications included placing an Al_2O_3 disc between the crucible and cell envelope, to remove electrical contact between molten NaCl and cell envelope. This also removed the possibility of redox couples forming between the metals and metal ions in molten NaCl (denoted redox couples) which can cause galvanic corrosion and removed the possibility of junction potentials, caused by the thermoelectric effect [53] [265]. The length of the gas inlet and outlet tubes was extended to improve the circulation of argon gas over molten NaCl, and remove moisture in the cell. The Stainless steel 316L cell envelope demonstrated signs of deterioration probably due to it's interaction with O_2 and moisture from the atmosphere [241] [261]. This deterioration probably occurred due to CrO_3 Ce_2O_3 compounds being selectively removed (above 816°C) thus exposing Fe_2O_3 and FeO to the effects of oxygen and moisture. The performance of Inconel^{TM} 600 was better than Stainless Steel 316L which probably occurred due to its higher nickel content. The higher nickel content probably caused a lower thermal expansion differential between iron and the oxide layer during heating and cooling cycles, thus greatly improving its corrosion resistance [238-239]. The heating and cooling rates of the furnace were also reduced from 10°C min^{-1} to 2°C min^{-1} to avoid the YSZ membrane breaking.

The platinum crucible experienced a grey colour change on its outer surface which was different from its original silver colour from the manufacturer. The contents were also found to be slightly attached to the crucible, which was attributed to platinum reacting with O_2 in the atmosphere, to form PtO_2 or Pt_3O_4. The inner surface of the crucible remained its original silver colour, suggesting if oxide films did form, they probably dissolved in molten NaCl [234-235]. As the platinum crucible didn't experience any significant mass changes between the experiments, these effects were unlikely to impact the final K_{sp} values. Also no points of inflection on the potentiometric signal were observed, as described by Cherginets, 2003, which suggests no species such as Na_2O_2 were produced [156]. The glassy carbon crucible experienced significant mass losses between the experiments, suggesting it may have reacted with O_2 to produce CO_2. It was however unlikely these affected the K_{sp} values, due to the low reported solubility of CO_2 in molten NaCl, as reported by Hefter and Tomkins, 2004 [261]. The contents were easily removed from the glassy carbon crucible, suggesting no significant solubility of the glassy carbon crucible. The Al_2O_3 crucible experienced no mass changes between the experiments and its contents were slightly attached to the Al_2O_3 crucible. This suggested the Al_2O_3 crucible had a small solubility in molten NaCl. The dissolution of the Al_2O_3 crucible in molten NaCl was also described on a predominance diagram for the Al-Na-O-Cl system, at 830ºC. The diagram suggested that Al_2O_3 has a low solubility in molten NaCl, governed by a low K_{sp} value for Al_2O_3 (at -log 21.2 at 830°C) (in mol fraction).

The potentiometric data suggested that Na_2CO_3 and $CaCO_3$ decomposed in molten NaCl to Na_2O and CaO and CO_2. The K_{sp} values for Na_2O and CaO in NaCl at 830ºC were found by inserting an argon gas bubbler to drive the decomposition reaction to completion and ensure the complete dissolution of the pellets. The K_{sp} values were found to be -log 1.58 and -log 1.1 respectively, suggesting such compounds had high solubilities in molten NaCl in comparison to other oxides in literature [144-155]. However these values didn't take into account the evaporation of molten NaCl, suggesting their true K_{sp} values were probably slightly higher. This information concludes that Na_2CO_3 and $CaCO_3$ decompose in NaCl at 830ºC, as described by equations 4.7-4.18, suggesting the MSS of cementitious compounds is possible in industry.

This section can be improved by obtaining the evaporation rate of molten NaCl at 830ºC, using a DSC. The evaporation rate can then be used to calculate the true K_{sp}

values for Na_2O and CaO in molten NaCl, which takes into account its evaporation. The evaporation of molten NaCl could also be minimized using a ceramic lid to allow the electrochemical cell to be calibrated for low O^{2-} ion activities (in the 10^{-3} range). The equilibration times for pellets of $NaCO_3$ and $CaCO_3$ could also be reduced by decreasing the volume of the cell envelope which would reduce the volume of inet gas required to achieve a consistant partial pressure in the cell. The K_{sp} values for Na_2O and CaO in molten NaCl could also be obtained directly by heating pellets of Na_2CO_3 and $CaCO_3$ beyond their decomposition temperatures, and sintering to avoid their decomposition.

5.5 Molten salt synthesis of cementitious compounds

The fifth stage of the investigation determined the **MSS reactions of the cementitious compounds**, α-Na_2SiO_3, β-Ca_2SiO_4, Ca_3SiO_5 and β-Ca_2SiO_4, using XRD and SEM techniques at the reaction conditions (830°C 1 atm), which were depicted on predominance diagrams. This was useful to determine whether cementitious compounds can be produced in this manner.

The XRD data reported the successful synthesis of the transitional compound; β-Ca_2SiO_4 which was produced without quenching or stabilization with foreign ions, which is often a requirement for transitional compounds [49]. However the reaction temperatures were higher than those reported by previous solid-state synthesis reactions and the chemical equilibrium module, at 680ºC and 300ºC [49] [18-19]. The XRD data also reported the successful synthesis of α-Na_2SiO_3 without quenching or stabilizing with ions. These reaction temperatures were lower than industry but higher than the chemical equilibrium module, 900°C and 200°C respectively [18-19] [251].

The XRD data also reported the synthesis of Ca_3SiO_5 was not successful and instead β-Ca_2SiO_4 and CaO were produced, probably due to a higher temperature requirement, as reported by Wesselsky and Jensen, 2009 [49]. The XRD data also reported the synthesis of β-Na_4SiO_4 was not successful and instead α-Na_2SiO_3 and Na_2O were produced, probably due to inadequate mixing of the reactants. The absence of other phases such as $CaCl_2$ in the final product suggested there was limited interaction of NaCl with the reactants and products. There was however a small presence of aluminium detected by EDS analysis which suggested some interaction of the Al_2O_3 crucible.

The MSS reactions were described on predominance diagrams for the Na-Si-O-Cl and Ca-Na-Si-O-Cl systems at 830ºC. The diagrams showed that $Na_2Si_2O_5$, α-Na_2SiO_3, β-Na_4SiO_4, and $Na_6Si_2O_7$ could be produced at O^{2-} ion activities of -log 11.8, -log 10.9, -log 6.59, and -log 5.68 (in mole fraction) respectively and $CaSiO_3$, $Ca_3Si_2O_7$, β-Ca_2SiO_4 could be produced at O^{2-} ion activities of -log 6.58, -log 6.16 and -log 3.32 (in mole fraction) respectively, at 830°C. This information concludes that Na_2CO_3 and $CaCO_3$ decompose and dissolve in NaCl at 830ºC, as reported by equations 4.7-4.18, which suggests the MSS of cementitious compounds are possible in industry, and results in lower reaction temperatures, a lower energy consumption and hence CO_2 emissions.

This section can be improved by synthesising other cementitious compounds in molten NaCl, such as $Na_6Si_2O_7$, $Na_2Si_2O_5$ and $Na_6Si_2O_7$, at 830°C (from the CaO-SiO_2 and Na_2O-SiO_2 binary systems). Also the CaO-SiO_2-Al_2O_3 and Al_2O_3-Fe_2O_3-Ca_2CO_3 ternary systems could be investigated to produce the additional phases of cement; $Ca_2(Al, Fe)_2O_5$) and/or $Ca_2(Al, Fe)_2O_{12}$ and $Ca_3Al_2O_6$ phases via MSS. This would give an indication whether the complete cement product could be achieved. Also, the predominance diagram calculation procedure could be improved using the Gibbs free energy minimization method (the principle of minimum energy) to provide truly accurate scenarios whether these compounds can be formed [210].

Acknowledgements

I wish to express my gratitude to Professor D. Inman (Late) and Madame M. Gaune-Escard for their insight into molten salt electrochemistry and thermodynamics of molten salt systems. I would also like to thank Professor S. J. R. Simons and Professor D. Brett for their support on numerous occasions and seeing potential in me as a researcher. This work could not have undergone without the assistance and advice from Professor E. Fraga, Professor. Ian Wood, Dr. L. Rycerz, Dr. J. Kapala, Professor J. P. Bros and Dr. G. Photiadis on numerous occasions (which has been noted).

I would also like to express my gratitude to the Department of Chemical Engineering, the Department of Earth Sciences and the Department of Chemistry at University College London, the Department of Chemistry at Wroclaw University of Technology and École Polytechnique at University of Marseille for providing access to their facilities and allowing me to use their electroanalytical, thermoanalytical and characterization techniques.

I would also like to thank Entente Cordiale Scholarships and the Engineering Physical Sciences Research Council (EPSRC) for sponsoring this work through the project grant; EP/F014449/1, ULECeS: Ultra low energy cement synthesis A radical process change to achieve green and sustainable technologies.

The many years of effort that resulted in this work would not be spared without the support of Professor A. Maries, Dr. M. Tyrer, Professor J. Bensted, M. Vickers, E. Oroszlany, A. Blaszczyk, P. Markey, J. Bartolini, Dr. S. Barass, M. Gorecki, B. Henderson, Dr. T. Neville, Dr. I. Dedigama, Dr. M. Manage, Dr. Z. Abdullah, Dr. J. Sun, Dr. D. Strusevich, Dr. L. Brown, Z. Ebrahimji, A. Zribi and mostly my mother, father, sister and brother who have supported me throughout my journey the most.

Conferences, publications & awards

My research has been presented at the following conferences;

- UK Energy Research Centre (UKERC) Summer School, 20-25th June 2010, SPARKS Poster presentation. University of Warwick, Warwick.
- Shape of Science Symposium, 5th July 2010, Poster presentation, University of Manchester, Manchester.
- Cement and Concrete Science, 13-15th September 2010, Technical discussion, University of Birmingham, Birmingham.
- Electrochemical Innovation Lab Launch, 16th June 2011. Poster presentation, University College London, London.
- Molten Salts Chemistry and Technology, MS9. 5-9th June 2010. Poster competition, NTNU: Norwegian University of Science and Technology, Trondheim, Norway.
- European Congress and Exhibition on Advanced Materials and Processes (Euromat), 12-15th September 2011. Poster competition. Le Corum conference centre, Montpellier, France.
- 13th International Congress on the Chemistry of Cement Science, 3-8th July 2011, Palacio de Congresos de Madrid. Madrid, Spain.
- Molten Salts Discussion Group, 15th December 2014, Chemistry Centre, Royal Society Chemistry (RSC), Burlington House, London
- Royal Academy of Engineering (RAEng), SET for Britain, Poster Competition, 9th March 2015, Houses of Parliament.

I have the following publications;

- Maries A. et al, 2011. Reactions in Molten Salts as a Novel and Sustainable Route for Synthesizing Cement Compounds at Low Temperatures, 13th International Congress on the Chemistry of Cement Science.
- Sheikh R. et al, 2015. Synthesis of cementitious compounds in molten salts, Molten Salts Discussion Group (MSDG).

I have received the following awards;

- Best poster nominee UK Energy Research Centre (UKERC) Summer School, 20-25th June 2010, SPARKS Poster presentation. University of Warwick, Warwick.
- Best poster nominee Molten Salts Chemistry and Technology, MS9. 5-9th June 2010. Poster competition, NTNU: Norwegian University of Science and Technology, Trondheim, Norway.
- The Entente Cordiale Scholarship Scheme, 2011, for a 6 month study period at Aix-Marseille University. French Embassy, London.

References

[1] Jian-Bin H. et al, 2012. The Science of Global Warming. Adv. Climate Change Res. Vol. 3 (25). pp. 74-178.
doi: 10.3724/SP.J.1248.2012.00174.

[2] Handel M. and J. Risbey, 1992. An annotated bibliography on the greenhouse effect and climate change. Climatic Change. Vol. 21. pp. 97-255.
doi: 10.1007/BF00140914.

[3] Hoel M. and S. Kverndokk, 1996. Depletion of fossil fuels and the impacts of global warming. Resour. Energ. Econ. Vol. 18 (2). pp. 115-136.
doi: 10.1016/09287655(96)00005-X.

[4] Open Data Resources for Climage Change, 2015.
www.data.worldbank.org/climate-change.

[5] World Resources Institute, 2012. Earth Trends Environmental Information.
www.wri.org.

[6] Nejat P. et al, 2015. A global review of energy consumption, CO_2 emissions and policy in the residential sector (with an overview of the top ten CO_2 emitting countries). Renew. Sust. Energ. Rev. Vol. 43. pp. 843-862.
doi: 10.1016/j.rser.2014.11.066.

[7] Shi. A., 2003. The impact of population pressure on global carbon dioxide emissions, 1975-1996: evidence from pooled cross-country data. Ecol. Econ. Vol. 44 (1). pp. 29-42.
PII: S0921-8009(02)00223–9.

[8] Enerdata - ABB, 2012. The state of global energy efficiency, Global and sectorial energy efficiency trends.
www.abb-energyefficiency.com.

[9] Low Carbon Technologies for Energy-Intensive Industries, 2012. UK Parliament.
POST note 403.

[10] Ali M. B. and M. S. Hossain, 2011. A review on emission analysis in cement industries. Renew. Sustain. Energ. Rev. Vol. 15 (5). pp. 2252-2261.
doi: 10.1016/j.rser.2011.02.014.

[11] Worrel E. et al, 2001. Carbon Dioxide emissions from the Global Cement Industry, Annu. Rev. Energ. Environ. Vol. 26, pp. 303-29.
doi: 10.1146/annurev.energy.26.1.303.

[12] Lea M., 2004. Lea's Chemistry of Cement and Concrete, Fourth Edition.
ISBN: 0000750662565.

[13] World Business Council for Sustainable Development (WBCSD), 2002. Toward a sustainable cement industry, Summary report.
www.wbcsd.org.

[14] Taylor H., 1990. Cement Chemistry. Thomas Telford. Academic Press London.
ISBN: 012683900.

[15] Bye G. C., 1999. Portland Cement, Composition, Production and Properties, Thomas Telford.
ISBN: 9780727727664.

[16] Huntzinger D. N. et al, 2009. A life-cycle assessment of Portland cement manufacturing: comparing the traditional process with alternative technologies. J. Clean. Prod. Vol. 17 (7). pp. 668–675.
doi: 10.1016/j.jclepro.2008.04.007.

[17] Schneider M. et al, 2011. Sustainable cement production - present and future Cem. Conc. Res. Vol. 41 (7). pp. 642-650.
doi: 10.1016/j.cemconres.2011.03.019.

[18] Kotiranta T. and Roine A., 2009. HSC Chemistry ® 6.1 Manual – Equilibrium.
www.hsc-chemistry.net.

[19] Barin I., 2008. Thermochemical data for pure substances, VCH Verlagsgesellschaft mbH.
ISBN: 9783527287451.

[20] Afkhami B. et al, 2015. Energy consumption assessment in a cement production plant. Sustain. Energ. Tech. Assess. Vol. 10. pp. 84-89.
doi: 10.1016/j.seta.2015.03.003.

[21] Carvalho M. and D. Madivate, 1999. Theoretical energy requirement for burning clinker. Cem. Conc. Res. Vol. 29. pp. 695-698.
doi: 10.1016/S0008-8846(99)00029-0.

[22] Khurana S. et al, 2002. Energy balance and cogeneration for a cement plant. Appl. Therm. Eng. Vol. 22 (5). pp. 485-494.
PII: S13594311(01)00128-4.

[23] IPCC Fourth Assessment Report (AR4), 2007. Mitigation of Climate Change, Climate Change 2007. Working Group III.
ISBN: 9780521705981.

[24] Blobel D. et al. 2006. United Nations Framework Convention on Climate Change Handbook. Intergovernmental and Legal Affairs.
www.unfccc.int.

[25] Intergovernmental Panel on Climate Change, Emission Scenarios. 2000. Cambridge University Press.
ISBN: 9291691135.

[26] Network of Regional Governments for Sustainable Development (nrg4SD), 2011. The UNFCCC and the Kyoto Protocol, Rough Guide.
www.nrg4sd.org.int.

[27] Kyoto Protocol to the United Nations Framework Convention on Climate Change, 1998. United Nations.
www.unfccc.int.

[28] Babiker M. et al, 1999. The Kyoto Protocol and developing countries. Energ. Policy. Vol. 28 (8). pp. 525-536.
doi: 10.1016/S0301-4215(00)00033-1.

[29] Kautto N., et al, 2012. Interaction of the EU ETS and national climate policy instruments - Impact on biomass use. Biomass Bioeng. Vol. 38. pp. 117-127.
doi: 10.1016/j.biombioe.2011.02.002.

[30] Carvalho M., 2012. EU energy and climate change strategy. Energy. Vol. 40 (1). pp. 19-22.
doi: 10.1016/j.energy.2012.01.012.

[31] Zhang Y. J. and Y. M. Wei, 2010. An overview of current research on EU ETS: Evidence from its operating mechanism and economic effect. App. Energ. Vol. 87 (6). pp. 1804-1814.
doi: 10.1016/j.apenergy.2009.12.019.

[32] Soriano F. H. and F. Mulatero, 2011. EU Research and Innovation (R&I) in renewable energies: The role of the Strategic Energy Technology Plan (SET-Plan). Energ. Policy. Vol. 39 (6). pp. 3582-3590.
doi: 10.1016/j.enpol.2011.03.059.

[33] Choate W. T., 2003. Energy and Emission Reduction Opportunities for the Cement Industry, US Department of Energy.
www.1eere.energy.gov.

[34] Touil D. et al, 2006. Energy efficiency of cement finish grinding in a dry batch ball mill. Cem Conc. Res, Vol. 36 (3). pp. 416-421.
doi: 10.1016/j.cemconres.2005.12.005.

[35] Radwan A. M., 2012. Different Possible Ways for Saving Energy in the Cement Production. Adv. App. Sci. Res. Vol. 3 (2) pp. 1162-1174.
ISBN: 09768610.

[36] Wang X. and X. Han, 2012. Sustainable Cement Production with Improved Energy Efficiency and Emerging CO_2 Mitigation. Adv. Chem. Eng. Sci., Vol. 2 (1). pp. 123-128.
doi: 10.4236/aces.2012.21015.

[37] Madlool A. et al, 2013. An overview of energy savings measures for cement industries. Renew. Sust. Energ. Rev., Vol. 19. pp. 18-29.
doi: 10.1016/j.rser.2012.10.046.

[38] Varma P. G.V. and T. Srinivas, 2015. Design and analysis of a cogeneration plant using heat recovery of a cement factory. Case Studies in Thermal Engineering. Vol. 5. pp. 24-31.
doi: 10.1016/j.csite.2014.12.002.1

[39] Usón A. et al, 2013. Uses of alternative fuels and raw materials in the cement industry as sustainable waste management options. Renew. Sust. Energ. Rev., Vol. 23. pp. 242-260.
doi: 10.1016/j.rser.2013.02.024.

[40] Puertas F. et al. 2008. Ceramic wastes as alternative raw materials for Portland cement clinker production. Cem. Concr. Comp. Vol. 30 (9). pp. 798-805.
doi: 10.1016/j.cemconcomp.2008.06.003.

[41] Mokrzycki E. and A. Uliasz-Bochenczyk, 2003. Alternative fuels for the cement industry. App. Energ. Vol. 74 (1-2). pp. 95-100.
doi: 10.1016/S0306-2619(02)00135-6.

[42] Waste derived Fuels and cement kilns, 1995.
POST note 60.

[43] Vatopoulos K. and E. Tzimas, 2012. Assessment of CO_2 captures technologies in cement manufacturing process. J. Clean. Prod. Vol. 32. pp. 251-261.
doi: 10.1016/j.jclepro.2012.03.013.

[44] Freund P. 2013. Anthropogenic climate change and the role of CO_2 capture and storage (CCS). Tech. Eng. IPCC. pp. 3-25.
doi: 10.1533/9780857097279.1.3.

[45] Barker D. J. et al, 2009. CO_2 capture in the cement industry. Energ. Procedia. Vol. 1 (1). pp. 87-94.
doi: 10.1016/j.egypro.2009.01.014.

[46] Dean C. C. et al, 2011. The calcium looping cycle for CO_2 capture from power generation, cement manufacture and hydrogen production. Chem. Eng. Res. Des. Vol. 89 (6). pp. 836-855.
doi: 10.1016/j.cherd.2010.10.013.

[47] Hasanbeigi A. et al 2012. Emerging energy efficiency and CO_2 emission-reduction technologies for cement and concrete production: A technical review. Renew. Sustain. Energ. Rev. Vol.16 (8). pp. 6220-6238.
doi: 10.1016/j.rser.2012.07.019.

[48] Benhelal E. et al, 2013. Global strategies and potentials to curb CO_2 emissions in cement industry. J. Clean. Prod. Vol. 51. pp. 142–161.
doi: 10.1016/j.jclepro.2012.10.049.

[49] Wesselsky A. and O. Jensen, 2009. Synthesis of pure Portland cement phases. Cem. Concr. Res. Vol. 39 (11). pp. 973-980.
doi: 10.1016/j.cemconres.2009.07.013.

[50] Kimura T., 1991. Molten Salt Synthesis of Ceramic Powders, Chapter 4, Advances in Ceramics-Synthesis and Characterization, Processing and Specific Applications.
doi: 10.5772/20472.

[51] Trémillon D. and D. Inman, 1997. Reactions in Solution: An Applied Analytical Approach. John Wiley & Sons Inc.
ISBN: 9780471953074.

[52] Papatheodorou G. N. et al, 2004. Molten Salts for Two Centuries, Historic Perspectives of the Evolution of Electrochemical Tools, Special Volume 2002-29. Electrochemical Society Inc. pp. 253-258.
ISBN: 1566773830.

[53] Ray H., 2006. Introduction to Melts: Molten Salts, Slags and Glasses, Allied Publishers Pvt. Ltd.
ISBN: 9788177648751.

[54] Langer H. and H. Offermann, 1982. On the solubility of sodium chloride in water. J. Crystal Growth. Vol. 60 (2). pp. 389-392.
doi: 10.1016/0022-0248(82)90116-6.

[55] Mamantov G. and R. Marass, 1987. Molten Salt Chemistry: An Introduction and Selected Applications. Vol. 202.
ISBN: 9789401082174.

[56] Yaws C. L., 2001. Chemical Properties Handbook. McGraw-Hill Education.
ISBN: 0639785306160.

[57] Lovering D. G., 1982. Molten Salt Technology, Plenum Press.
ISBN: 9781475717266.

[58] McCoy H. E. et al. 1969. New Developments in Materials for molten salt reactors. Nucl. Appl. Tech. Vol. 8, pp. 118-136.
www.moltensalt.org.

[59] LeBlanc D., 2010. Molten salt reactors: A new beginning for an old idea. Nucl. Eng. Design. Vol. 240 (6). pp. 1644-1656.
doi: 10.1016/j.nucengdes.2009.12.033.

[60] Haubenreich P. N. and J. R. Engel, 1969. Experience with the Molten-Salt reactor Experiment, Nucl. App. Tech. Vol. 8. pp. 118-136.
www.moltensalt.org.

[61] Uhlíř J. 2007. Chemistry and technology of Molten Salt Reactors, history and perspectives. J. Nucl. Mater. Vol. 360 (1) pp. 6-11.
doi: 10.1016/j.jnucmat.2006.08.008.

[62] Le Brun C., 2007. Molten salts and nuclear energy production. J. Nucl. Mater. Vol. 360 (1) pp. 1-5.
doi: 10.1016/j.jnucmat.2006.08.017.

[63] U.S. Atomic Energy Commission, 1972. 1000 MW(e) Molten Salt Breeder Reactor Conceptual Design Study, Final Report - Task 1.

[64] Weinberg Foundation, 2013. Thorium-Fuelled Molten Salt Reactors. Report for the All Party Parliamentary Group on Thorium Energy.

[65] Sweeny J. R. et al 2004. Some Advances in the application of thermal battery technology. ASB Group.
www.asb-group.com.

[66] Dustmann Cord-H. et al, 2004. Advances in ZEBRA batteries. J. Power Sour. Vol. 127, (1-2). pp. 85-92.
doi: 10.1016/j.jpowsour.2003.09.039.

[67] Meridian International Research, 2005. The Sodium Nickel Chloride Zebra Battery, Battery Technologies. pp. 104-112.
www.meridian-int-res.com.

[68] Soloveichik Grigorri L., 2011. Battery Technologies for Large Scale Stationary Energy Storage. Vol. 2. pp. 203-527.
doi: 10.1146/annurev-chembioeng-061010-114116.

[69] Fujiwara S. et al, 2011. New molten salt systems for high temperature molten salt batteries: Ternary and quaternary molten salt systems based on LiF-LiCl, LiF-LiBr, and LiCl-LiBr. J. Power Sources. Vol. 196 (8). pp. 4012-4018.
doi: 10.1016/j.jpowsour.2010.12.009.

[70] GE Energy storage, Durathon Batteries, Battery Power, Reimagined.
www.renewables.gepower.com.

[71] Durathon DC System Technical Specifications, 2014. MWh Series, GE Energy Storage Durathon Battery.
www.renewables.gepower.com.

[72] Ritchie A., 1990. Molten Salt Electrolytes in High Temperature Batteries, Royal Aerospace Establishment.
AD: A229046.

[73] Dicks A. and A. Siddle, 2000. Assessment of commercial prospects of molten carbonate fuel cells, J. Power Sources. Vol. 68 (1-2). pp. 316-323.
doi: 10.1016/S0378-7753(99)00449-8.

[74] JRC, Scientific and Technical Reports, 2008. International Status of Molten Carbonate Fuel Cell MCFC Technology.
www.publications.jrc.ec.europa.eu.

[75] Bischoff M. and G. Huppmann, 2002. Operating Experience with a 250kW$_e$ molten carbonate fuel cell (MCFC) power plant. J. Power Sources. Vol. 105. (2), pp. 216-221.
doi: 10.1016/S0378-7753(01)00942-9.

[76] Huppmann G., 2005. High Temperature Fuel Cell Trigeneration for Commercial and Municipal Buildings: The MTU Carbonate Fuel Cell HotModule. MTU CFC Solutions GmbH.
www.cibse.org.

[77] FuelCell Energy, Inc, 2007. DFC 300A Molten Carbonate Fuel Cell Combined Heat and Power System. Greenhouse Gas Technology Center.
www.epa.gov.

[78] HotModule Fuel Cell onsite-energy. MTU Onsite Energy.
www.mtu-online.co.

[79] Keppler et al, 2001 "Molten salt electrolysis of alkali metals.”
U.S. Patent 6669836.

[80] Sodium Metal from France, U.S, 2008. International Trade Commission.
Publication 4045 Investigation No. 731-TA-1135.

[81] Jacobson S. E. et al, 2002. Du Pont de Nemours and Company. Low temperature alkali metal electrolysis.
US. Pat. 6787019.

[82] Winkhaus S. and S. Wilkening, 1988. Material problems in electrowinning of aluminium by the Hall-Héroult Process. J. Appl. Electrochem. Vol. 19. (4). pp. 596-604.
doi: 10.1007/BF01022120.

[83] McGeer J. P., 1986. Hall-Héroult 100 Years of Processes Evolution. JOM, Vol. 38. (11), pp. 27-33.
doi: 10.1007/BF03257618.

[84] Prasad S., 2000. Studies on the Hall-Héroult Aluminium Electrowinning Process. J. Braz. Chem. Soc. Vol. 11 (3).
doi: 10.1590/S0103-50532000000300008.

[85] Rio Tinto Alcan, Aluminium Fact Sheet, 2011.
www.riotintoalcan.com.

[86] Chen. Z. C. et al. 2000. Direct electrochemical reduction of titanium dioxide to titanium in molten calcium chloride. Nature 407 (6802). pp. 361-364.
doi: 10.1038/35030069.

[87] Oosthuizen S. J., 2011. In search of low cost titanium: the Fray Farthing Chen (FFC) Cambridge process. J. Southern African Institute Mining Metallurgy. Vol. 111. pp. 199-202.
www.saimm.co.za.

[88] Zhang W. et al. 2011. A literature review of titanium metallurgical processes. Hydromet. Vol. 108 (3-4). pp. 177-188.
doi: 10.1016/j.hydromet.2011.04.005.

[89] EHK Technologies, 2004. Summary of Emerging Titanium Cost Reduction Technologies. A study performed for the U.S. Department of Energy and Oak Ridge National Laboratory.
www.ornl.gov.

[90] Oosthuizen S. J., 2011. In search of low cost titanium, the Fray Farthing Chen Cambridge process. SAIMM. Vol. 111, pp. 199-202.
www.saimm.co.za.

[91] Dunn R., 2010. A global review of concentrated solar power storage. Proc. 48th AuSES Annu. Conf. Solar2010.
www.solar-thermal.anu.edu.au.

[92] Gaggiolia W. et al. 2014. An Innovative Concept of a Thermal Energy Storage System Based on a Single Tank Configuration Using Stratifying Molten Salts as both Heat Storage Medium and Heat Transfer Fluid and with an Integrated Steam Generator. Energ. Procedia. Vol. 49. pp. 780-789.
doi: 10.1016/j.egypro.2014.03.085.

[93] Bauer. T., 2012. Overview of Molten Salt Storage Systems and Material Development for Solar Thermal Power Plants. World Renewable Energy Forum.
www.ases.conference-services.net.

[94] Kuravi et al S. 2013. Thermal energy storage technologies and systems for concentrating solar power plants. Prog. Ener. Comb. Sci. Vol. 39. pp. 285-313.
doi: 10.1016/j.pecs.2013.02.001.

[95] Minister of Business, Innovation & Employment, 1985. The safe use of molten salt baths. New Zealand: Department of Labour.
www.mbie.govt.nz.

[96] Dexter G. W., 1989. Hardening high speed steels metallurgical benefits of salt. Precision Punch Corporation.
www.ppunch.com.

[97] Reid B., 1996. Heat treating in molten salt. Park Thermal International Corporation.
www.parkthermal.com.

[98] Cemic L, 2005. Thermodynamics in Mineral Sciences: An Introduction Springer-Verlag Berlin Heidelberg.
doi: 9783540243649 10.1007/3-540-28808-2.

[99] Atkins P. and J. de Paula, 2006. Atkins Physical Chemistry 8th edition. Oxford University Press.
ISBN: 0199543372.

[100] Kleppa O. K and L. S. Hersh, 1961. Heats of Mixing in Liquid Alkali Nitrate Systems. J. Chem. Phys. Vol. 34 (2). pp. 351-358.
doi: 10.1063/1.1700955.

[101] Holm J. L. and O. J. Kleppa. 1968. Enthalpies of Mixing in Binary Liquid Alkali Fluoride Mixtures. J. Chem. Phys. Vol. 49. pp. 2425.
doi: 10.1063/1.1670417.

[102] Hersh L. and O. Kleppa, 1965. Enthalpies of Mixing in Some Binary Liquid Halide Mixtures. J. Chem. Phys., Vol. 42. pp. 1309-1322.
doi: 10.1063/1.1696115.

[103] Andersen K., and O. Kleppa, 1976. Enthalpies of Mixing in binary liquid alkali carbonate Mixtures. Act. Chem. Scand. Vol. 30a. pp. 751-758.
doi: 10.3891/acta.chem.scand.30a-0751.

[104] Papatheodorou G. N. and O. J. Kleppa, 1967. Enthalpies of Mixing in Some Binary Alkaline Earth Chlorides. J. Chem. Phys Vol. 47 (6). pp. 2014-2020.
doi: 10.1063/1.1712231.

[105] Melnichak M. E. and O. J. Kleppa, 1970. Enthalpies of Mixing in Binary Liquid Alkali Iodide Mixtures. J. Chem. Phys. Vol. 52. pp. 1790.
doi: 10.1063/1.1673219.

[106] Dessureault Y. et al, 1990. Coupled Phase diagram - Thermodynamic Analysis of the 24 Binary Systems, A_2CO_3-AX and A_2SO_4-AX Where A=Li, Na, K and X=Cl, F, NO_3, OH. J. Phys. Chem. Ref. Data. Vol. 19 (5). pp. 1149-1178.
doi: 10.1063/1.555866.

[107] Gaune-Escard M. et al, 1994. Calorimetric investigation of $NdCl_3$-MCl liquid mixtures (where M is Na, K, Rb, Cs). Thermochim. Acta. Vol. 236. pp. 67-80.
doi: 10.1016/0040-6031(94)80256-4.

[108] Rycerz L., 2005. Enthalpy of Mixing of the $PrCl_3$-LiCl and $NdCl_3$-LiCl Molten Salt Systems Zeitschrift für Naturforschung A. Vol. 60 (3). pp. 196-200.
doi: 10.1515/zna-2005-0312.

[109] Saunders N., 1996. CALPHAD Calculation of Phase Diagrams: A Comprehensive Guide. Pergamon Materials Series.
ISBN: 9780080421292.

[110] Chang A. and W. A. Oates, 2010. Materials Thermodynamics. John Wiley & Sons, Inc.
doi: 10.1002/9780470549940.

[111] Zhao J., 2007. Methods for Phase Diagram Determination. Elsevier.
ISBN: 9780080549965.

[112] Predael B. et al, 2004. Phase Diagrams and Heterogeneous Equilibria: A Practical Introduction, Engineering Materials and Processes. Springer.
ISBN: 9783540140115.

[113] Hillbert M., 2007. Phase Equilibria, Phase Diagrams and Phase Transformations: Their Thermodynamic Basis Second Edition. Cambridge University Press.
ISBN: 9780521853514.

[114] Roth R. S., 2001. Phase Diagrams for Ceramists. Volume III Oxides National Institute of Standards and technology NIST. The American Society.
ISBN: 9780916094904.

[115] Teaching Phase Equilibria, Phase diagrams (and Pseudosections) for Petrologists.
www.serc.carleton.edu.

[116] Kuskov G. L. and O. B. Fabrichnaya, 1987. The SiO_2 polymorphs: The Equations of State and Thermodynamic Properties of Phase Transformations. Phys. Chem. Minerals. Vol.14. pp. 58-66.
doi: 10.1007/BF00311149.

[117] Okamoto H. and T. Massalsko. 1983. The Au-Si (Gold-Silicon) system. Bull. Alloy Phase Diagr. Vol. 4 (2). pp. 190-198.
doi: 10.1007/BF02884878.

[118] Teeriniemi J. et al. 2015. First-principles investigation of the Cu-Ni, Cu-Pd, and Ni-Pd binary alloy systems. Intermetallics. Vol. 57. pp. 41-50.
doi: 10.1016/j.intermet.2014.09.006.

[119] Burton P. and A. Walle. 2006., First-principles Phase Diagram Calculations for the System NaCl-KCl: The role of excess vibrational entropy. Chem. Geol. Vol. 225 (3-4). pp. 222-229.
doi: 10.1016/j.chemgeo.2005.08.016.

[120] Yaokawa J. et al., 2007. Thermodynamic assessment of the KCl-K_2CO_3–NaCl–Na_2CO_3 System. Calphad. Vol. 31 (2). pp. 155-163.
doi: 10.1016/j.calphad.2007.01.004.

[121] Lindberg D. et al., 2006. Thermodynamic evaluation and optimization of the (Na_2CO_3 + Na_2SO_4 + Na_2S + K_2CO_3 + K_2SO_4 + K_2S) system. J. Chem. Thermodynamics. Vol. 39 (6). pp. 942-960.
doi: 10.1016/j.jct.2006.11.002.

[122] Paul A, 1990. The Chemistry of Glasses, Chapman and Hall.
ISBN: 0412230208.

[123] Kochkarov Z. A. et al, 2011. $NaBO_2$-NaCl–Na_2CO_3, $NaBO_2$–Na_2CO_3–$NaMoO_4$ Ternary Systems. Zh. Obshch. Khim. Vol. 56 (6). pp. 946-953.
doi: 10.1134/S0036023611060106.

[124] Iwasawa K. and M. Maeda, 2000. Phase Diagram Study for the Alkali Metal-Oxychloride System. Metall. Mater. Trans. B. Vol. 31 (4). pp. 795-799.
doi: 10.1007/s11663-000-0116-x.

[125] Yaokawa J. et al, 2007. Thermodynamic assessment of the KCl-K_2CO_3-NaCl-Na_2CO_3 system. Calphad. Vol. 31 (2). pp. 155-163.
doi: 10.1016/j.calphad.2007.01.004.

[126] Lindberg D. et al. 2007. Thermodynamic evaluation and optimization of the ($NaCl + Na_2SO_4 + Na_2CO_3 + KCl + K_2SO_4 + K_2CO_3$) system. J. Chem. Therm., Vol. 39 (7). pp. 1001-1021.
doi: 10.1016/j.jct.2006.12.018. 1021.

[127] Kochkarov Z. et al, 2011. $NaBO_2$-NaCl-Na_2CO_3, $NaBO_2$-Na_2CO_3-$NaMoO_4$, $NaBO_2$-Na_2CO_3-$NaWO_4$ and $NaBO_2$-NaCl-Na_2WO_4 ternary systems. Russ. J. Inorg. Chem. Vol. 56 (6). pp. 946-953.
doi: 10.1134/S0036023611060106.

[128] Ye. L. et al, 2014. The thermal physical properties and stability of the eutectic composition in a Na_2CO_3-NaCl binary system. Thermochim. Acta. Vol. 597 (20). pp. 14-20.
doi: 10.1016/j.tca.2014.07.002.

[129] Cherginets V. L. 1996. On studies of oxide solubilities in melts based on alkaline halides. Electrochim. Acta. Vol. 42 (23-24). pp. 3619-3627.
doi: 10.1016/S0013-4686(97)00031-5.

[130] Cherginets V. L. 2005. Oxoacidity: Reactions of Oxo-Compounds in Ionic Solvents (Comprehensive Chemical Kinetics). Elsevier.
ISBN: 9780444517821.

[131] Cherginets V. L. and G. Wypych 2001. Oxide Solubilities in Ionic Melts, Handbook of Solvents. Chemtec Publishing. 2001. pp. 1484-1495.
ISBN: 9781895198-65-2.

[132] Delarue G., 1960. Propértés chimiques dans l'eutectique LiCl-KCl fondu 1. Oxydes métalliques. J. Electroanal. Chem. Vol. 1 (1). pp. 285-300 (In French).
doi: 10.1016/0022-0728(60)85029-2.

[133] Laitinen H. A. and B. B. Bhatia, 1960. Electrochemical Study of Metallic Oxides in Fused lithium Chloride-Potassium Chloride Eutectic. J. Electrochem. Soc. Vol. 107 (8). pp. 73-276.
doi: 10.1149/1.2427812.

[134] Picard G. et al. 1978. Oxoacidity reactions in molten LiCl+KCl (at 470ºC): Potentiometric study of the equilbria of exchange of O^{2-} between Al(III) systems and carbonate and water systems. J. Electroanal. Chem. Vol. 102 (1). pp. 65-75.
doi: 10.1016/S0022-0728(79)80030-3.

[135] Martinot L. and Fuger J, 1986. Determination of solubility products of various actinide oxides in the Na-K (Cl) and Li-K (Cl) eutectics and calculation of new potential-pO^{2-}diagrams. J. Less. Common. Met. Vol. 120 (2). pp. 255-266.
doi: 10.1016/0022-5088(86)90650-8.

[136] Rouault-Rogez H. et al, 1995. Zinc oxoacidity properties in molten LiCl-KCl eutectic at 450ºC. J. App. Electrochem. Vol. 25 (2). pp 166-172.
doi: 10.1007/BF00248174.

[137] Cherginets V. L. and T. P. Rebrova, 1999. Studies of some acid-base equilibria in the molten eutectic mixture KCl-LiCl at 700ºC. Electrochim. Acta. Vol. 45 (3). pp. 469-476.
doi: 10.1016/S0013-4686(99)00274-1.

[138] Caravaca C. et al, 2001. Solubilization studies of rare earth oxides and oxohalides. Application of electrochemical, techniques in pyrochemical processes. 6th Information Exchange Meeting on Actinide and Fission Product Partitioning and Transmutation Nuclear Energy Agency. Vol. 958 (6). pp. 625-636.
RN: 32052976.

[139] Casterillego Y. et al, 2003. Solubilization of rare earth oxides in the eutectic LiCl-KCl mixtures at 450ºC and in the equimolar $CaCl_2$-NaCl melt at 550ºC. J. Electroanal. Chem. Vol. 546. pp. 141-157.
doi: 10.1016/S0022-0728(03)00092-5.

[140] Cherginets V. L. et al 2004. Potentiometric study of acid–base equilibria in the {KCl + LiCl} eutectic melt at temperatures in the range (873 to 1073) K. J. Chem. Therm. Vol. 36 (2). pp. 115-120.
doi: 10.1016/j.jct.2003.09.007.

[141] Cordoba G. De. and C. Caravaca 2006. Potentiometric study of Sm-O compounds formation in the molten LiCl-KCl eutectic at 450ºC and determination of a E-pO^{2-} stability diagram. J. Phys. Chem. Sol. Vol. 67 (8). pp. 1862-1868.
doi: 10.1016/j.jpcs.2006.04.011.

[142] Kado Y. et al, 2008. Dissolution Behavior of Lithium Oxide in Molten LiCl-KCl Systems. J. Chem. Eng. Data. Vol. 53 (12). pp. 2816-2819.
doi: 10.1021/je800540c.

[143] Osipenko A. et al, 2012. Electrochemistry of Curium in Molten Chlorides. Chapter 1, Recent Trend in Electrochemical Science and Technology.
doi: 10.5772/38935.

[144] Naumann D. and G. Reinhardt, 1966. Die Loslichkeit von Erdalkalioxiden in Alkalichloride-Schmelzen. Z. Anorg. Allg. Chem., Vol. 343 (3-4). pp 165-173 (in German).
doi: 10.1002/zaac.19663430308.

[145] Combes R. et al, 1975. Mesure de pO^{2-} au moyen d'une electrode a membrane de zircone stabilisee et determination potentiometrique de constantes d'equilibre d'echange de O^{2-} dans le melange equimolaire NaCl-KCl fondu. Electrochim. Acta. Vol. 20 (3). pp. 191-200 (in French).
doi: 10.1016/0013-4686(75)85024-9.

[146] Combes R. et al, 1975. Mesure de pO^{2-} au moyen d'une electrode a membrane de zircone stabilsee et determination potentiometrique de constantes d'equilibre d'echange de O^{2-} dans le melange equimolaire NaCl-KCl fondu. Electrochim. Acta. Vol. 50 (3). pp. 191-200 (in French).
doi: 10.1016/0013-4686(75)85024-9.

[147] Combes R. et al, 1978. Conditional solubility versus pO^{2-} of cerium(III) oxide in molten equimolar NaCl+KCl at 727ºC. J. Electroanal. Chem. Vol. 91 (1). pp. 125-131.
doi: 10.1016/S0022-0728(78)80256-3.

[148] Combes R. et al, 1979. Dissociation and solubility variation pO^{2-} of some alkaline earth oxides in molten NaCl-KCl (at 1000K). Electrochim. Acta., Vol. 25 (4). pp. 371-374.
doi: 10.1016/0013-4686(80)87025-3.

[149] Stern K. H. and M. L. Deanhardt, 1981. Solubility Products of Metal Oxides in Molten Salts by Coulometric Titration of Oxide Ion through Zirconia Electrodes. J. Electrochem. Soc. Vol. 128 (12). pp. 2577-2582.
doi: 10.1149/1.2127295.

[150] Volkovitch V., 1991. Interaction of Oxides of Alkaline Earth Metals with the Melt of Equimolar Mixture of Chlorides of Sodium and Potassium. Rasplavy. Vol. N4. pp. 24-30 (in Russian).

[151] Watson R. F. and G. S. Perry, 1991. Solubility of ZnO and Hydrolysis of $ZnCl_2$ in KCl Melts. J. Chem. Soc. Faraday Trans., Vol. 87 (18). pp. 2955-2960.
doi: 10.1039/FT9918702955.

[152] Koeller S. L. and R. L. Combes, 2000. Solubilidade do SrO em NaCl KCl fundido a 727ºC. Quím. Nova. Vol. 23 (1) (in Portuguese).
doi: 10.1590/S0100-40422000000100008.

[153] Barbin N. M. and V. N. Nekrasov, 1999. The physicochemical and electrochemical behavior of lithium oxide in the equimolar NaCl-KCl melt. Electrochim. Acta. Vol. 44 (25). pp. 4479-4488.
doi: 10.1016/S0013-4686(99)00179-6.

[154] Koeller S. L. and R. L. Combes, 2002. Estudo de Algumas Reacoes Oxoacidobasicas no Solvente NaCl Fundido Entre 1100K e 1200K. Quim. Nova., Vol. 25 (2). pp. 226-230 (in Portuguese).
doi: 10.1590/S0100 40422002000200010.

[155] Cherginets V. L. et al. 2002. Potentiometric investigation of oxide solubilities in molten KCl-NaCl eutectic. The effect of surface area of solid particles on the solubilities. J. Electroanal Chem Vol. 531 pp. 171-178.
doi: 10.1016/S0022-0728(02)01061-6.

[156] Cherginets V. L. and T. Rebrova, 2003. Equilibrium Constants of Some Acid-Base Reactions in Molten Sodium Chloride. International Symposium on Ionic Liquids in honour of M. Gaune-Escard.
ISBN 0873391276.

[157] Casterillejo Y. et al, 1997. Oxoacidity reactions in equimolar molten $CaC1_2$-NaCl mixture at 575ºC. Electrochim. Act. Vol. 42 (10). pp. 1489-1494.
doi: 10.1016/S0013-4686(96)00305-2.

[158] Martinez A. M. et al, 1998. Chemical and electrochemical study of titanium ions in the molten equimolar $CaCl_2$+NaCl mixture at 550ºC. J. Electroanal. Chem., Vol. 449 (1-2). pp. 67-80.
doi: 10.1016/S0022-0728(97)00413-0.

[159] Lambertin D. et al, 2002. Determination of the solubility product of plutonium sesquioxide in the NaCl-$CaCl_2$ eutectic and calculation of a potential-pO^{2-} diagram. Electrochem. Comm. Vol. 4 (5). pp. 447-450.
doi: 10.1016/S1388-2481(02)00334-X.

[160] Wang S. et al, 2008. CaO solubility and activity coefficient in molten salts $CaCl_2$–x (x = 0, NaCl, KCl, $SrCl_2$, $BaCl_2$ and LiCl). Thermochim Acta. Vol. 470 (1-2). pp. 105-107.
doi: 10.1016/j.tca.2008.02.007.

[161] Segal. D., 1997. Chemical synthesis of ceramic minerals. J. Mater. Chem. Vol. 7 (8). pp 1297-1305.
doi: 10.1039/A700881C.

[162] Garcia J. C. et al. 2006. Structural, electronic, and optical properties of ZrO_2 from ab initio calculations. J. Appl. Phys. Vol. 100.
doi: L 10.1063/1.2386967.

[163] Kerridge D. H. et al., 1975. Molten lithium nitrate-potassium nitrate eutectic: the reaction of compounds of titanium. J. Inorg. Nucl. Chem. Vol. 37 (11). pp. 2257-2260.
doi: 10.1016/0022-1902(75)80722-6.

[164] Raihani H. et al, 1994. Zirconia Formation by reaction of zirconium sulfate in molten alkali-metal nitrates or nitrites. J. Mater. Chem. Vol. 4 (8). pp. 1331-1336.
doi: 10.1039/JM9940401331.

[165] Afanasiev P. and C. Geantet, 1988. Synthesis of solid materials in molten nitrates. Coord. Chem. Rev., Vol. 178-180 (2). pp. 1725-1752.
doi: 10.1016/S0010-8545(98)00154-4.

[166] Du Y. and D. Inman. 1995. Reactions of $Zr(SO_4)_2$ in molten nitrite and nitrate systems. J. Mater. Chem. Vol. 5 (11). pp. 1927-1930.
doi: 10.1039/JM9950501927.

[167] Du Y. and D. Inman, 1996. Preparation of zirconia powders from molten nitrites and nitrates. J. Mater. Sci. Vol. 31 (20). pp. 5505-5511.
doi: 10.1007/BF01159324.

[168] Du Y. et al., 1996. The acidic/basic effects on preparation of zirconia powders from molten salts. J. Mater. Sci. Vol. 31. pp. 3361-3364.
doi: 10.1007/BF00360735.

[169] Afanasiev P. and C. Geantet, 1995. Effect of alkali metal cations on the properties of zirconia prepared in molten nitrates. Maters. Chem. Phys. Vol 41. pp. 18-27.
doi: 10.1016/0254-0584(95)01494-2.

[170] Marato P. et al, 2002. Reactions of Metals Salts and Alkali Metal Nitrates. Role of the Metal Precursors and Alkali Metal Ions in the Resulting Phase of Zirconia. J. Sol. State Chem. Vol. 163 (1). pp. 202-209.
doi: 10.1006/jssc.2001.9393.

[171] Finch B. and P. Becher, 1982. Growth of monoclinic macrocrystalline ZrO_2 by hydrolysis of ZrF_4-LiF-NaF melts at 650-800°C. J. Cryst. Growth. Vol. 60 (2). pp. 32-324.
doi: 10.1016/0022-0248(82)90105-1.

[172] Kerridge D. H. and S. Shakir, 1991. Molten lithium nitrate-potassium nitrate eutectic: the reactions of aluminium, gallium and thallium. Thermochim. Acta. Vol. 182 (1). pp. 107-122.
doi: 10.1016/0040-6031(91)87012-L.

[173] Du Y. and D. Inman. 1996. Precipitation of finely divided Al_2O_3 powders by a molten salt method. J. Mater. Chem. Vol. 6 (7). pp. 1239-1240.
doi: 10.1039/JM9960601239.

[174] Hashimoto S. and A. Yamaguchi, 1999. Formation of porous aggregations composed of Al_2O_3 platelets using potassium sulfate flux. J. Euro. Ceram. Soc., Vol. 19 (3). pp. 335-339.
doi: 10.1016/S0955-2219(98)00202-7.

[175] Hashimotoa S. and A. Yamaguchi, 1999. Synthesis of α-Al_2O_3 platelets using sodium sulfate flux. J. Mater. Res. Vol. 14 (12). pp. 4667-4672.
doi: 10.1557/JMR.1999.0631.

[176] Zhu. L. et al., 2008. Synthesis of plate-like α-Al_2O_3 single-crystal particles in NaCl-KCl flux using $Al(OH)_3$ powders as starting materials. Ceram. Int. Vol. 34 (7). pp. 1729-1733.
doi: 10.1016/j.ceramint.2007.05.011.

[177] Zhu. L. and H. Qing-wei, 2011. Morphology control of α-Al_2O_3 platelets by molten salt synthesis. Ceram. Int. Vol. 37 (1). pp. 249-255.
doi: 10.1016/j.ceramint.2010.09.021.

[178] Zhu. L. et al, 2012. Molten salt synthesis of α-Al_2O_3 platelets using $NaAlO_2$ as raw material. Ceram. Int. Vol. 38 (2). pp 901-908.
doi: 10.1016/j.ceramint.2011.08.008.

[179] Kerridge D. H. and J. C. Rey, 1977. Molten lithium nitrate-pottasium nitrate eutectic: the reactions of two compounds of zirconium. J. Nucl. Chem. Vol. 39. pp. 405-407.
doi: 10.1016/S0010-8545(98)00154-4.

[180] Afanasiev P., 2006. Molten salt syntheses of alkali metal titanates. J. Mater. Sci. Vol. 41 (4). pp. 1187-1195.
doi: 10.1007/s10853-005-3656-2.

[181] Kožáková Z. et al, 2011. Preparation of TiO_2 powder by microwave-assisted molten salt synthesis. 2011 Nanocon.
www.konsys-t.tanger.cz.

[182] Han Y. et al., 2012. Preparation of titanium dioxide from titania-rich slag by molten NaOH method. Int. J. Min Met. Mater. Vol. 19 (3). pp. 205-2011.
doi: 10.1007/s12613-012-0539-9.

[183] Wu R. et al 2014. Synthesis of Ultra-long TiO_2 Microrods via Molten Salt Method. Integ. Ferroelectrics. 12th China Int. NanoScience Tech. Sym., Vol. 153 (1). pp. 151-155.
doi: 10.1080/10584587.2014.903131.

[184] Peining Z. et al. 2012. TiO_2 nanoparticles synthesized by the molten salt method as a dual functional material for dye-sensitized solar cells. RSC Advan. Vol. 2 (12). pp. 5123-5126.
doi: 10.1039/C2RA00041E.

[185] Photiadis G. et al, 2009. Molten Salt Synthesis of the cement compound dicalcium silicate. 8th World Congress of Chemical Engineering. **www.wcce8.com.**

[186] Photiadis G. et al, 2009. Low energy synthesis of cement compounds in molten salt. Adv. Appl. Ceram. Vol. 110 (3). pp. 137-141. **doi: 10.1179/1743676110Y.0000000018.**

[187] Maries A. et al, 2012. A Sustainability Analysis of a Potential Low Energy Route to Cement production by synthesis in molten salts. Proceedings of 13th International Congress on the Chemistry of Cement. 3rd 8th July 2011. **www.cementscience.com.**

[188] Phodiadis G. 2015, A study of Various Aspects of Cement Chemistry and Industry Relevant to Global Warming and the Low Carbon and Low Energy Molten Salt Synthesis of Cement Compounds Chapter 8. Global Warming - Causes, Impacts and Remedies. **doi: 10.5772/59771.**

[189] Littlewood R., 1962. Diagrammatic Representation of the Thermodynamics of Metal-Fused Chloride Systems. Vol. 109 (6). pp. 525-533. **doi: 10.1149/1.2425462.**

[190] Trémillon B., 1974. Chemistry in Non-Aqueous Solvents. Reidel Publishing Company. **ISBN: 10: 9027703892.**

[191] Trémillon B., 1971. Diagrammes d’equilibre potential-acidité (E-pO^{2-}) dans les sels et hydroxydes alcalins fondus. Pure Appl. Chem. Vol. 25 (2). pp. 395-428 (in French). **doi: 10.1351/pac197125020395.**

[192] McCafferty E., 2010. Introduction to Corrosion Science. Thermodynamics of Corrosion: Pourbaix Diagrams. Springer. pp. 95-117.
doi: 10.1007/978-1-4419-0455-36.

[193] Verink E. D. and R. W. Reev. Simplified Procedure for Constructing Pourbaix Diagrams. Uhlig 's Corrosion Handbook, Second Edition,
ISBN: 047115777-5.

[194] Nishikata A. et al. 1991. Electrochemistry of molten salt corrosion. Mater. Sci. Eng., A. Vol. 146 (1-2). pp. 15-31.
doi: 10.1016/0921-5093(91)90265-O.

[195] Ishitsuka T. and K. Nose, 2000. Solubility study on protective oxide films in molten chlorides created by refuse incineration environment. Mater. Corr. Vol. 51 (3). pp. 177-181.
doi: 10.1002/(SICI)1521-4176(200003).

[196] Lambertin D. et al, 2005. Plutonium chemical properties in NaCl-KCl and $CaCl_2$ at 1073 K. J. Nucl. Mater. Vol. 341 (2-3). pp. 124-130.
doi: 10.1016/j.jnucmat.2005.01.010.

[197] Takahashi M. et al, 1975. The passivation phenomenon of platinum in fused lithium chloride + potassium chloride eutectic: 1. Effect of oxide ions on the passivation. J. Electroanal. Chem. Interfac. Electrochem. Vol. 62 (2). pp. 363-371.
doi: 10.1016/0022-0728(75)80004-0.

[198] Uchida I. et al, 1981. Electrochemical Study of UO_2^{2+}-UO_2^{+}-UO_2 system in molten LiCl+KCl eutectic. J. Electroanal. Chem. Vol. 124 (1-2). pp. 165-177.
doi: 10.1016/S0022-0728(81)80294-X.

[199] Landresse G. and G. Duyckaerts. 1973. Diagramme potential/pO^{2-} de l'uranium dans l'eutectique LiCl-KCl fondu. J. Anal. Chim. Acta., Vol. 65 (1). pp. 245-247.
doi: 10.1016/S0003-2670(01)80190-2.

[200] Seon F. et al, 1982. Stability of ferrous oxide in molten LiCl+KCl eutectic at 470ºC. J. Electroanal. Chem. Interfac. Electrochem., Vol. 138 (2). pp. 315-324.
doi: 10.1016/0022-0728(82)85085-7.

[201] Rouquette-Sanchez S. and G. Picard, 2004. Chalcogenide chemistry in molten salts. I. Selenium(IV) acido-basic and redox properties in the LiCl-KCl eutectic melt at 450, 500, 550 and 600ºC. J. Electroanal. Chem. Vol. 572 (1). pp.173-183.
doi: 10.1016/j.jelechem.2004.06.010.

[202] Hayashi H. and K. Minato, 2005. Stability of lanthanide oxides in LiCl-KCl eutectic melt. J. Phy. Chem. Solids., Vol. 66 (2-4). pp. 422-426.
doi: 10.1016/j.jpcs.2004.06.054.

[203] Caravaca C., 2008. Determination of the E-pO^{2-} stability diagram of plutonium in the molten LiCl-KCl eutectic at 450^{o}C. J. Nucl, Mater. Vol. 377. pp. 340-347.
doi: 10.1016/j.jnucmat.2008.01.03.1

[204] Brown L. D. 2013. Predominance diagrams of uranium and plutonum species in both lithium chloride-potassium chloride eutectic and calcium chloride. J. Appl. Electrochem. Vol. 43. pp. 1235-1241.
doi: 10.1007/s10800-013-0611-9.

[205] Martinez A. et al, 2000. Chemical and electrochemical behaviour of chromium in molten chlorides. J. Electroanal. Chem., Vol. 493 (1-2). pp. 1-14.
doi: 10.1016/S0022 0728(00)00298-9.

[206] Dring K. et al, 2005. Predominance Diagrams for Electrochemcial Reduction of Titanium Oxides in molten $CaCl_2$. J. Electrochem. Soc. Vol. 152 (10). pp. 184-190.
doi: 10.1149/1.2034552.

[207] Dring K. et al, 2006. Direct electrochemical production of Ti–10W alloys from mixed oxide preform precursors. J. Alloys. Comp., Vol. 419 (1-2). pp. 103-109.
doi: 10.1016/j.jallcom.2005.10.029.

[208] Yasuda K. et al. 2007. Diagrammatic Representation of Direct Electrolytic Reduction of SiO_2 in Molten $CaCl_2$. J. Electrochem. Soc. Vol. 154 (7). pp. 95-101.
doi: 10.1149/1.2736641.

[209] Bale C. W. 2009. FactSage thermochemical software and databases - recent developments. Calphad. Vol 33 (2). pp. 295-311.
doi: 10.1016/j.calphad.2008.09.009.

[210] Zhihend H. et al, 2008. A computational interface for thermodynamic calculations software MTDATA. Calphad. Vol 32 (1). pp. 129-134.
doi: 10.1016/j.calphad.2007.07.003.

[211] Factoria de Cristalizacion, 2012.
www.lafactoria.lec.csic.es.

[212] Zschornack G., 2007. Handbook of X-Ray Data. Springer.
ISBN: 9783540286196.

[213] Scintag Inc, 1999. Basics of X-Ray diffraction, Chapter 7.
www.scintag.com.

[214] Cockcroft J., 1997. Powder Diffraction on the WEB. Christopher Ingold Laboratories.
www.pd.chem.ucl.ac.uk.

[215] International Centre for Diffraction Database - ICDD.
www.icdd.com.

[216] Reimer L., 1998. Scanning electron microscopy. Physics of Image Formation and Microanalysis. Springer.
ISBN: 978-3-540-38967-5.

[217] Smith, K. C. A. and C. W. Oatley, 1955. The scanning electron microscope and its fields of application. J. Appl. Phys. Vol. 6. pp. 391-399.
doi: 10.1088/0508-3443/6/11/304.

[218] McMullan D, 1995. Scanning Electron Microscopy 1928-1965. J. Scan. Micro. Vol. 17 (3). pp. 175-185.
doi: 10.1002/sca.4950170309.

[219] The electron gun, 2013. Australlian Microscopy and Microanalysis Research Facility.
www.ammrf.org.au.

[220] Rycerz L., 2003. High temperature Characterization of LnX_3 and LnX_3-AX solid and liquid systems (Ln = Lanthanide, Alkali, X = Halide): Thermodynamics and Electrical Conductivity These. Université d'Aix-Marseille.

[221] Gaune-Escard M., 2001. Molten Salts: From Fundamentals to Applications. Proceedings of the NATO Advanced Study Institute on Molten Salts. Springer.
ISBN: 9781402004599.

[222] Brown M. E. and P. K. Gallagher, 2008. Handbook of Thermal Analysis and Calorimetry: Recent advances Techniques and Applications. Vol. 5. Elsevier Science.
ISBN: 978044453123-0.

[223] Herwaarden S., 2000. Calorimetry Measurement. Chapter 17. CRC Press LLC.
www.engnetbase.com.

[224] FlukeView Software.
www.fluke.com.

[225] OriginPro 8.
www.origin.com.

[226] Netszsch Group.
www.netzsch-thermal-analysis.com.

[227] Setaram Instrumentation - Calorimetry & Thermal Analysis.
www.setaram.com.

[228] Calisto Thermal Analysis Software.
www.setaram.com.

[229] Proteus Thermal Analysis Software.
www.netzsch-thermal-analysis.com.

[230] Gale R. J. and D. G. Lovering, 1991. Molten Salt Techniques Volume 4. Plenum Press New York and London.
ISBN: 9780306435546.

[231] Abelard P. and J. Baumard. 1995. The electrical conductivity of cubic stabilized zirconia. The Results of an IUPAC Collaborative Study. Pure Appl. Chem. Vol. 67 (11). pp. 1891-1904.
doi: 10.1111/j.1151-2916.1996.tb08951.x.

[232] Science and Technology of Ceramic Fuel Cells, N.Q. Minh, T. Takahashi Elsevier.1995.
ISBN: 044489568X.

[233] Braunstein J. et al, 2013. Advances in Molten Salt Chemistry. Vol. 2. Springer.
ISBN: 978147570506-5.

[234] Chaston J. C. 1975. The Oxidation of the Platinum Metals. Platinum Metals Rev., Vol 19 (4), pp. 135-140.
www.technology.matthey.com.

[235] Jehn H. 1984. High temperature behaviour of platinum group metals in oxidising atmospheres. J. Less-Common MET.
doi: 10.1016/0022-5088(84)90072-9.

[236] British Stainless Steel Association, Melting temperature ranges for stainless steels.
www.bssa.org.uk.

[237] Special Metals, Inconel alloy 600.
www.specialmetals.com.

[238] Davis J., 1954. ASM Specialty Handbook: Heat-Resistant Materials, ASM International 1997.
ISBN: 9780871705969.

[239] Indacochea J. et al, 2000. High-Temperature Oxidation and Corrosion of Structural Materials in Molten Chlorides. Oxidation of Metals. Vol. 55 (1/2).
doi: 10.1023/A:1010333407304.

[240] Hanf N. W. and M. J. Sole. 1970. High-temperature hydrolysis of sodium chloride. Trans. Faraday Soc. Vol. 66. pp. 3065-3074.
doi: 10.1039/TF9706603065.

[241] Flengas S. N. and E. Rideal. 1956. On Electrometric Titration in Fused Salts Proc. A. Royal Soc. Lond. Vol. 233, pp. 443-454.
doi: 10.1098/rspa.1956.0002.

[242] Compton R. and C. Banks, 2011. Understanding Voltammetry, 2nd Edition. Imperial College Press.
ISBN: 97818165854.

[243] Metrohm Autolab, 2013.
www.ecochemie.nl.

[244] Specac IR Sampling Accessories and Press Solutions
www.specac.com.

[245] Kracek. F. C. 1930. The System Sodium-Oxide-Silica. J. Phys. Chem. Vol. 34 (7). pp. 1583-1598.
doi: 10.1021/j150313a018.

[246] Ryś M. and M. Müller, 2010. Thermal analysis of the Na_2O-rich concentration region of the quasi-binary system Na_2O-SiO_2. Thermochim. Acta. Vol. 502 (1-2). pp. 8-13.
doi: 10.1016/j.tca.2010.01.017.

[247] Halter W. et al, 2004. Melt speciation in the system Na_2O-SiO_2. Chemical Geology. Vol. 213, pp 115-123.
doi: 10.1016/j.chemgeo.2004.08.036.

[248] CRCT, Center for Research in Computational Thermochemistry, 2015. FToxid – Oxide Phase Diagrams.
www.crct.polymtl.ca.

[249] Zhang L. et al, 2013. Thermodynamic description of the M_2O–SiO_2 (M = K, Na) systems Computational Materials Science. Vol. 66. pp. 20-27.
doi: 10.1016/j.commatsci.2012.04.040.

[250] Tan Y. et al, 2010. Comparing three methods for the synthesis of pure β-dicalcium silicate. 4th Int. iCBBE, 2010. pp. 1-4.
doi: 10.1109/ICBBE.2010.5515290.

[251] CEES, 2013. Centre Euopeen d'etudes des silicates.
www.cees-silicates.org.

[252] Ryś M., 2007. Investigation of Thermodynamic Properties of Alkali Metals in Oxide Systems Relevant to Coal Slags**.** Diese Dissertation (in German).
www.darwin.bth.rwth-aachen.de.

[253] Monroe E. A. et al, 1969. Stacking faults and polytypism in opal, $SiO_2.nH_2O$. Acta. Cryst. Vol. 25 (4). pp. 579-580.
doi: 10.1107/S0567739469001227.

[254] Stern K. 2001. High Temperature Properties and Thermal Decomposition of Inorganic Salts. CRC Press LLC.
ISBN: 9780849302565.

[255] Clifford Y. T. and F. B. Chen, 1998. Polymorphism of $CaCO_3$, precipitated in a Constant-Composition environment. Clifford Vol. 44 (8). pp. 1790-1798.
doi: 10.1002/aic.690440810.

[256] Faraday constant 2015. The NIST Reference on Constants, Units, and Uncertainty. US National Institute of Standards and Technology.
www.physics.nist.gov.

[257] Plambeck J. A. 1967. Electromotive Force Series in Molten Salts. J. Chem. Eng. Data. Vol. 12 (1). pp. 77-82.
doi: 10.1021/je60032a023.

[258] Motzfeldt. K, 1955. The Thermal Decomposition of Sodium Carbonate by the Effusion Method. J. Phys. Chem. Vol. 59 (2). pp. 139-147.
doi: 10.1021/j150524a011.

[259] Hills A. W. D. 1968. The mechanism of the thermal decomposition of calcium carbonate. Chem. Eng. Sci. Vol. 23 (4). pp. 297-320.
doi: 10.1016/0009-2509(68)87002-2.

[260] Kim J. and H. Lee. 2001. Thermal and Carbothermic Decomposition of Na_2CO_3 and Li_2CO_3. Met. Mater. Trans. B. Vol. 32 (1). pp. 17-24.
doi: 10.1007/s11663-001-0003-0.

[261] Hefter G. T. and R.P.T. Tomkins, 2004. Solubility of Gases in Molten Salts and Molten Metals. The experimental determination of solubilities. Vol.6 pp. 173-217.
doi: 10.1002/0470867833.ch5 2004.

[262] Grjotheim K. et al, 1962. On the Solubility of Carbon dioxide in Molten Halides Acta. Chemica. Scandinavica. Vol. 16. pp. 689-694.
doi: 10.3891/acta.chem.scand.16-0689.

[263] Combes R. et al 1977. Dissociation of Carbonate in molten NaCl-KCl. Electroanal. Chem. Vol. 83. pp. 383-385.
doi: 10.1016/S0022-0728(77)80184-8.

[264] Mersen Group, 2015.
www.mersen.com.

[265] Bach H., 2001. Electrochemistry of Glasses and Glass Melts, including Glass Electrodes. Springer.
ISBN: 3540586083.

[266] Jacobson N. S and Kang N. L. J, 1996. Corrosion of Mullite by Molten salts. J. Am. Ceram. Soc. Vol. 79 (8). pp. 2161-2167.
doi: 10.1111/j.1151-2916.1996.tb08951.x.

[267] Christie J. R. et al, 1978**.** Reaction of molten sodium carbonate with aluminum oxide. J. Phys. Chem. Vol. 82 (1). pp 33-37.
doi: 10.1021/j100490a009.

[268] Kotz J. et al, 2009. Chemistry and Chemical Reactivity Vol 1. Cenage Learning.
ISBN: 9780495387039.

[269] Inman. D. et al. 1978. II. A potentiometric study of alumina solubility and the influence of complexing by fluoride ions in LiCl-KCl. J. Applied Electrochem. Vol. 8. pp. 273-276.
doi: 10.1007/BF00616431.

[270] Bale. W. et al, 2002. FactSage thermochemical software and database. Calphad Vol 26 (2). pp. 189-228.
doi:10.1016/S0364-5916(02)00035-4.

[271] Iwadate Y., 2013. Raman Spectroscopy and Pulsed Neutron Diffraction of Molten Salt Mixtures Containing Rare-Earth Trichlorides: Trial Approaches from Fundamentals to Pyrochemical Reprocessing. Chapter 2. pp. 17-31.
doi:10.1016/B978-0-12 398538-5.00002-0.

Appendix

Compound	Phase	Crystal system	a (Å)	b (Å)	c (Å)	α (°)	β (°)	γ (°)	V (Å^3)	Z
Ca_3SiO_5	R	Rhombohedral	7.15	7.15	25.6	90.0	90.0	120.0	1130	9.00
	M_3	Monoclinic	33.1	7.07	18.6	90.0	94.2	90.0	4330	36.0
	M_2	Pseudohexagonal	7.13	7.14	25.1	90.0	90.0	120	-	-
		Orthorhombic	12.3	7.14	25.4	90.0	90.0	90.0	2240	-
Ca_3SiO_5	M_1	Pseudohexagonal	7.12	7.14	25.4	90.1	90.1	120	-	-
		Monoclinic	12.3	7.14	25.4	90.0	90.1	90.0	2240	-
Ca_3SiO_5	T_3	Triclinic	24.6	14.3	25.4	90.1	89.9	89.9	8950	-
	T_2	Triclinic	24.5	14.3	25.3	90.0	89.8	89.8	8854	-
	T_1	Triclinic	24.4	14.2	25.1	90.1	90.7	89.7	8704	-
Ca_2SiO_4	A	Orthorhombic	9.58	5.58	7.15	90.0	90.0	120	193	2.00
	$\acute{\alpha}_H$	Orthorhombic	5.59	9.54	6.86	90.0	90.0	90.0	366	4.00
	$\acute{\alpha}_L$	Orthorhombic	11.2	19.0	6.84	90.0	90.0	90.0	1450	16.0
	B	Monoclinic	9.31	6.76	5.51	90.0	94.5	90.0	345	4.00
	Γ	Orthorhombic	5.08	11.2	6.76	90.0	90.0	90.0	387	4.00
Na_2SiO_3	A	Hexagonal	6.08	6.08	4.83	90.0	90.0	120	154	-
	B	Orthorhombic	10.5	6.07	4.82	90.0	90.0	90.0	307	4.00
Na_4SiO_4	A	Monoclinic	5.58	6.19	8.51	103	95.6	124	229	2.00
	β	Orthorhombic	12.9	11.8	11.0	90.0	90.0	90.0	1670	8.00
Na_2CO_3	α	Hexagonal	5.22	5.22	6.58	90.0	90.0	120	155	2.00
	β	Monoclinic	8.90	5.24	6.04	90.0	101	90.0	276	4.00
	γ	Monoclinic	9.01	5.24	6.32	90.0	96.9	90.0	296	4.00
CO_2	-	Cubic	5.62	5.62	5.62	90.0	90.0	90.0	178	4.00
Na_2O	-	Cubic	5.56	5.56	5.56	90.0	90.0	90.0	172	4.00
Na	-	Cubic	4.29	4.29	4.29	90.0	90.0	90.0	79.0	2.00
O_2	-	Monoclinic	5.40	3.49	5.09	90.0	133	90.0	69.4	2.00
$CaCO_3$	Calcite	Monoclinic	6.33	4.95	8.03	90.0	108	90.0	239	4.00
	Aragnoite	Orthorhombic	4.96	7.97	5.74	90.0	90.0	90.0	227	4.00
	Vaterite	Hexagonal	4.13	4.13	8.58	90.0	90.0	120	127	2.00
CO_2	-	Monoclinic	5.63	5.63	5.63	90.0	90.0	90.0	179	4.00
CaO	-	Cubic	4.80	4.80	4.80	90.0	90.0	90.0	110	4.00
SiO_2	β – cristoballite	Cubic	7.12	7.12	7.12	90.0	90.0	90.0	361	8.00
	β – trydimite	Monoclinic	9.93	17.2	18.9	90.0	90.0	90.0	3500	320
	β –quartz	Hexagonal	5.00	5.00	5.45	90.0	90.0	120	118	3.00
	α –quartz	Hexagonal	4.90	4.90	5.40	90.0	90.0	120	112	3.00
NaCl		Cubic	5.63	5.63	5.63	90.0	90.0	90.0	178	2.16

Table A1: Lattice parameters for compounds of interest (including polymorphic transitions) [248].

Material/Equipment	Details	Supplier	Address
High temperature furnace.	Temperature limit, 1100ºC	Vecstar Ltd.	Units 11 & 12, Foxwood Road, Dunston Trading Estate, Chesterfield
Alumina crucible.	Purity ≥ 99.9%.	Dynamic ceramic	Crewe Hall, Weston Road, Crewe, CW1 6UA.
Magnesia cupel.	-	Cerex Ltd.	46 Bannerdale Road Sheffield, South Yorkshire, S7 2DP.
Sodium chloride.	Purity ≥ 99%.	Sigma-Aldrich.	The Old Brickyard, New Road Gillingham, Dorset, SP8 4XT.
Silicon dioxide.	Purity ≥ 99%.		
Calcium carbonate.	Purity ≥ 99%.		
Sodium carbonate.	Purity ≥ 99.9%.		
Evaporation furnace.	Temperature limit, 300ºC.	Carbolite.	Parsons Lane, Hope, Hope Valley, S33 6RB.
Stainless steel 316L.	18 wt% Cr, 10 wt% Ni, 70 wt% Fe, 2 wt% Mo.	Berkley's Stainless Steel.	Unit 15, Premier Business Park, Dencora Way, Luton, Bedfordshire
Inconel™ 600.	22 wt% Cr, 61 wt% Ni, 8 wt% Fe, 9 wt% Mo.	Philip Cornes	The Cofton Centre, Groveley Lane, Longbridge, Birmingham, B31 4PT.
Platinum crucible.	Purity ≥ 99%.	-	-
Potentiostat.	PGSTAT30.	Autolab.	Metrohm UK. Limited, Metrohm House, Evenwood Close, Daresbury Court, Runcorn Cheshire, WA7 1LZ.
Yttria-stabilised zirconia membrane.	Purity ≥ 99%.	Dynamic ceramic.	Homefield Road Business Park Homefield Road, Haverhill, CB9 8QP.
Mullite membrane.	-		
Carbon rod.	6 mm diameter.	Alfa Aesar.	Alfa Aesar Shore Road Port of Heysham Industrial Park Lancashire LA3 2XY.
Glassy carbon crucible.	-		
Nickel wire.	1 mm diameter.	-	-
Platinum wire.	1 mm diameter.	-	-
Calcium chloride.	Purity ≥ 99.9%.	Sigma-Aldrich.	The Old Brickyard, New Road Gillingham, Dorset, SP8 4XT.
Calorimetric tube.	Purity ≥ 99%.	-	-
Graphite crucible.	6 mm diameter.	-	Ecole Polytechnique, University of Marseille, CNRS UMR 6595, Technopôle de Chateau Gombert, 5
DSC.	Temperature limit, 830ºC.	Setaram.	7, rue de l'Oratoire 69300 Caluire, France.
BOC.	-	-	10 Priestley Road Surrey Research Park, Guildford Surrey GU2 7XY.
XRD.	-	Stoe.	Hilpertstrasse 10 64295 Darmstadt Germany.
	-	PANalytical.	7310 Ground Floor Beach Drive Waterbeach Cambridge CB25 9AY.
Thermocouple.	N-type.	RS Components.	RS Components, Birchington Road, Corby, Northants, NN17 9RS, UK.
Voltmeter.	-	Uni-trend.	83 Baker Street 5th Floor London W1U 6AG.

Table A2: Supplier list.

NaCl (mol %)				**Na_2CO_3 (mol %)**				**Temperature (°C)**			
DSC	**Ref 124**	**Ref 125**	**Ref 126**	**DSC**	**Ref 124**	**Ref 125**	**Ref 126**	**DSC**	**Ref 124**	**Ref 125**	**Ref 126**
100	100	100	100	0	0	0	0	801	801	801	801
	95	98	98		5	2	2		786	792	792
80	85	92	95	20	15	8	5	729	752	774	782
	75	87	82		25	13	18		716	755	736
60	65	78	76	40	35	22	24	698	678	722	717
	60	67	72		40	33	28		658	680	702
	55	53	68		45	47	32		644	632	686
	45	50	61		55	50	39		705	658	659
	35	32	55		65	68	45		729	737	631
	25	11	49		75	89	51		751	792	659
	15	10	43		85	90	57		806	820	687
	5	3	10		95	97	90		834	848	819
	0	0	0		100	100	100		851	851	858

Table A3: Liquidus points for molten NaCl-Na_2CO_3 [124-126].

NaCl (mol %)				**Na_2CO_3 (mol %)**				**Temperature (°C)**			
DSC	**Ref 124**	**Ref 125**	**Ref 126**	**DSC**	**Ref 124**	**Ref 125**	**Ref 126**	**DSC**	**Ref 124**	**Ref 125**	**Ref 126**
		100	100			0	0			634	634
		98	98			2	2			634	634
80	75	92	95	20	25	8	5	637	636	634	634
70	65	87	82	30	35	13	18	638	632	634	634
60	60	78	76	40	40	22	24	638	634	634	634
40		67	72	60		33	28	635		634	634
50	45	53	68	50	55	47	32	637	632	634	634
	35	50	61		65	50	39		637	634	634
		32	55			68	45			634	634
		11	49			89	51			634	634
		10	43			90	57			634	634
		3	10			97	90			634	634
		0	0			100	100			634	634

Table A3: Liquidus points for molten NaCl-Na_2CO_3 [124-126].

Molten salt reactions	**Equilibrium expression**	**Standard potentials (V vs Cl_2/Cl^-)**
$Cl_2\ (g) + 2e = 2Cl^-$	$E_{Cl_2/Cl^-} = E^O{}_{Cl_2/Cl^-} - \frac{2.3RT}{2F}\log P_{Cl_2}$	$E^O{}_{Cl_2/Cl^-} = 0$
$Na^+ + e = Na\ (l)$	$E_{Na^+/Na} = E^O{}_{Na^+/Na} - \frac{2.3RT}{F}\log a_{Na}$	$E^O{}_{Na^+/Na} = -3.21$
$O_2\ (g) + 4e = 2O^{2-}$	$E_{O2} = E^O{}_{O_2/O^{2-}} - \frac{2.3RT}{4F}pO^{2-}$	$E^O{}_{O_2/O^{2-}} = -1.89$

A5: Molten salt reactions for the Na-O-Cl system, at 830℃, 1 atm.

Molten salt reactions	**Equilibrium expression**	**Standard potentials (V vs Cl_2/Cl^-)**
$Cl_2 + 2e = 2Cl^-$	$E_{Cl} = E^O{}_{Cl_2/Cl^-} - \frac{2.3RT}{2F}\log P_{Cl_2}$	$E^O{}_{Cl_2/Cl^-} = 0$
$Na^+ + e = Na\ (l)$	$E_{Na} = E^O{}_{Na^+/Na} - \frac{2.3RT}{F}\log a_{Na}$	$E^O{}_{Na^+/Na} = -3.21$
$O_2\ (g) + 4e = 2O^{2-}$	$E_{O2} = E^O{}_{O_2/O^{2-}} - \frac{2.3RT}{4F}pO^{2-}$	$E^O{}_{O_2/O^{2-}} = -1.89$
$Al^{3+} + 3e = Al\ (s)$	$E_{Al^{3+}/Al} = E^O{}_{Al^{3+}/Al} - \frac{2.3RT}{3F}\log a_{AlCl_3}$	$E^O{}_{Al^{3+}/Al} = -1.75$
$Al_2O_3\ (s) + 6e = 2Al\ (s) + 3O^{2-}$	$E_{Al_2O_3/Al} = E^O{}_{Al_2O_3/Al} - \frac{2.3RT}{6F}pO^{2-}$	$E^O{}_{Al_2O_3/Al} = -4.12$

A6: Molten salt reactions for the Al-Na-O-Cl system, metal ion activity 1, at 830℃, 1 atm.

Molten salt reactions	**Equilibrium expression**	**Standard potentials (V vs Cl_2/Cl^-)**
$Cl_2 + 2e = 2Cl^-$	$E_{Cl} = E^O{}_{Cl_2/Cl^-} - \frac{2.3RT}{2F}\log P_{Cl_2}$	$E^O{}_{Cl_2/Cl^-} = 0$
$Na^+ + e = Na\ (l)$	$E_{Na} = E^O{}_{Na^+/Na} - \frac{2.3RT}{F}\log a_{Na}$	$E^O{}_{Na^+/Na} = -3.21$
$O_2\ (g) + 4e = 2O^{2-}$	$E_{O2} = E^O{}_{O_2/O^{2-}} - \frac{2.3RT}{4F}pO^{2-}$	$E^O{}_{O_2/O^{2-}} = -1.89$
$SiO_2\ (s) + 2e = Si\ (s) + O^{2-}$	$E_{SiO_2/Si} = E^O{}_{SiO_2/Si} - \frac{2.3RT}{2F}pO^{2-}$	$E^O{}_{SiO_2/Si} = -3.73$
$Si^{4+} + 4e = Si\ (s)$	$E_{Si^{4+}/Si} = E^O{}_{Si^{4+}/Si} - \frac{2.3RT}{4F}pO^{2-}$	$E^O{}_{Si^{4+}/Si} = -1.33$
$Na_4SiO_4\ (s) + 4e = Si\ (s) + Na^+ + 4O^{2-}$	$E_{Na_4SiO_4/Si} = E^O{}_{Na_4SiO_4/Si} - \frac{2.3RT}{4F}pO^{2-}$	$E^O{}_{Na_4SiO_4/Si} = - - 4.69$
$Na_2Si_2O_5\ (s) + 8e = 2Si\ (s) + 2Na^+ + 5O^{2-}$	$E_{Na_2Si_2O_5/Si} = E^O{}_{Na_2Si_2O_5/Si} - \frac{2.3RT}{8F}pO^{2-}$	$E^O{}_{Na_2Si_2O_5/Si} = -4.05$
$Na_6Si_2O_7\ (s) + 8e = 2Si\ (s) + 6Na^+ + 7O^{2-}$	$E_{Na_6Si_2O_7/Si} = E^O{}_{Na_6Si_2O_7/Si} - \frac{2.3RT}{8F}pO^{2-}$	$E^O{}_{Na_6Si_2O_7/Si} = -4.51$
$Na_2SiO_3\ (s) + 4e = Si\ (s) + 2Na^+ + 3O^{2-}$	$E_{Na_6Si_2O_7/Si} = E^O{}_{Na_6Si_2O_7/Si} - \frac{2.3RT}{8F}pO^{2-}$	$E^O{}_{Na_2SiO_3/Si} = -4.55$

A7: Molten salt reactions for Na-Si-O-Cl system, metal ion activity 1, at 830℃, 1 atm.

Molten salt reactions	Equilibrium expression	Standard potentials (V vs Cl_2/Cl^-)
$Cl_2 + 2e = 2Cl^-$	$E_{Cl} = E^{O}{}_{Cl_2/Cl^-} - \frac{2.3RT}{2F} \log P_{Cl_2}$	$E^{O}{}_{Cl_2/Cl^-} = 0$
$Na^+ + e = Na\ (l)$	$E_{Na} = E^{O}{}_{Na^+/Na} - \frac{2.3RT}{2F} \log a_{Na}$	$E^{O}{}_{Na^+/Na} = -3.21$
$O_2\ (g) + 4e = 2O^{2-}$	$E_{O2} = E^{O}{}_{O_2/O^{2-}} - \frac{2.3RT}{4F} pO^{2-}$	$E^{O}{}_{O_2/O^{2-}} = -0.83$
$CaSiO_3\ (s) + 4e = Si\ (s) + Ca^{2+} + 3O^{2-}$	$E_{CaSiO_3/Si} = E^{O}{}_{CaSiO_3/Si} - \frac{2.3RT}{4F} pO^{2-}$	$E^{O}{}_{CaSi\ \ _3/Si} = -2.99$
$Ca_3Si_2O_7(s) + 8e = 2Si\ (s) + 3Ca^{2+} + 7O^{2-}$	$E_{Ca_3Si_2O_7/Si} = E^{O}{}_{Ca_3Si_2O_7/Si} - \frac{2.3RT}{8F} pO^{2-}$	$E^{O}{}_{Ca_3Si_2O_7/Si} = -3.15$
$Ca_2SiO_4(s) + 4e = Si\ (s) + 2Ca^{2+} + 4O^{2-}$	$E_{Ca_2SiO_4/Si} = E^{O}{}_{Ca_2SiO_4/Si} - \frac{2.3RT}{4F} pO^{2-}$	$E^{O}{}_{Ca_2SiO_4/Si} = -3.24$
$SiO_2\ (s) + 4e = Si\ (s) + 2O^{2-}$	$E_{SiO_2/Si} = E^{O}{}_{SiO_2/Si} - \frac{2.3RT}{4F} pO^{2-}$	$E^{O}{}_{SiO_2/Si} = -2.63$
$Si^{4+} + 4e = Si\ (s)$	$E_{Si^{4+}/Si} = E^{O}{}_{Si^{4+}/Si} - \frac{2.3RT}{4F} pO^{2-}$	$E^{O}{}_{Si^{4+}/Si} = -1.28$
$Ca^{2+} + 2e = Ca\ (l)$	$E_{Ca^{2+}/Ca} = E^{O}{}_{Ca^{2+}/Ca} - \frac{2.3RT}{2F} pO^{2-}$	$E^{O}{}_{Ca^{2+}/Ca} = -3.28$

A8: Molten salt reactions for the Ca-Na-Si-O-Cl system, metal ion activity 1, at 830°C, 1 atm.